High-Order Numerical Methods for Shock-Bubble Interaction Computations

Ksenia Kozhanova

THÈSE

Pour l'obtention du grade de

DOCTEUR DE L'ÉCOLE NATIONALE SUPÉRIEURE DE MÉCANIQUE ET D'AÉROTECHNIQUE

(Diplôme National - Arrêté du 25 Mai 2016)

École Doctorale : Sciences et Ingénierie en
Matériaux, Mécanique, Energétique

Secteur de Recherche : MÉCANIQUE DES MILIEUX FLUIDES

Présentée par

Ksenia KOZHANOVA

High-order numerical methods for shock-bubble interaction computations

Directeur de thèse : **M. Eric Goncalves**
Co-directeur : **M. Yannick Hoarau**

Soutenue le 11 Février 2022 devant la Commission d'Examen

JURY

Ashwin Chinnayya	Professeur, ENSMA, Institut Pprime	Président
Philippe Helluy	Professeur, Université de Strasbourg, IRMA	Rapporteur
Alistair Revell	Professor, University of Manchester	Rapporteur
Christian Tenaud	DR CNRS, Centrale-Supélec, EM2C	Rapporteur
Marica Pelanti	Maître de conférences, ENSTA, IMSIA	
Eric Goncalves	Professeur, ENSMA, Institut Pprime	
Yannick Hoarau	Professeur, Université de Strasbourg, ICUBE	

Remerciements

This part of the manuscript is written last. However, by no means it is the last in order of importance. Indeed, without having reasons to write it, the experience of these past three years (and two months) would not be the same. Thus, I allow myself at last to pay all my attention to all those who made this thesis possible to happen.

Firstly, I would like to express my sincere gratitude to my Supervisor with a capital S, Eric Goncalves. That is, I say a huge 'THANK YOU' to Eric for this amazing experience, a 'THANK YOU' for giving me this chance and giving me a space to think, to work and to exercise my creativity if you wish. I say 'thank you' for always being there for me and your guidance and sometimes a gentle (and sometimes not so gentle) push towards the right decision or harder work. Furthermore, I want to mention that this thesis took place at the time of several lockdowns and I know how hard it has been for many to pursue the work during this challenging period. As for me, I felt nothing of this sort. Quite the opposite, not only Eric was there for me for all the virtual meetings, but he was also patiently listening to all my complaints about the restrictions and nuisances which it caused to my lifestyle. Now, after this PhD is over, I can say with absolute sincerity that I could not wish a better supervisor for myself.

Secondly, I would like to thank my co-supervisor, Yannick Hoarau. Thank you for your warm welcome in Strasbourg, for your useful work-related comments and always a positive mood and environment even on the rare occasions we had a chance to meet. Further, I am very grateful to the jury board, the members of which kindly agreed to dedicate their precious time to my work. I thank Ashwin Chinnayya, the president of the juries who, moreover, happened to be an excellent listener and sometimes scientific adviser of how this work could be improved. The three rapporteurs of my manuscript, Philippe Helluy, Christian Tenaud and Alistair Revell, many thanks for your contribution and very useful remarks for present manuscript. While not all of your suggestions could be precisely implemented, I found them very constructive and will try to use many of your comments in my future work. Marica Pelanti, thank you very much for being with us on the big day even if only virtually, thank you for your questions and comments and of course, for your time.

Now, with scientific 'thank you's out of hand, I will dedicate the rest of this Chapter to people who did the mental contribution, which is, and it is my strong belief, at least 50% of success! My friends from ENSMA, MY FRIENDS, thank you for everything. Thank you for listening my endless stories, for so many moments we shared together and so many jokes, which only us can understand. Thank you for being weird:) Thank you for being what you are. And you definitely are some individualities! Here, I have to mention everyone by specific order which has been earned during these three years (just kidding). Di Bao, Di, Di the chief engineer, Di the "give me ten euros", Di the "my bike is better than yours", I could not wish to have a better office mate and better companion for Grand Frais shopping and many other things. My stomach has been sometimes in pain from all the laughing with you. You are missed tremendously in my new office. Arun aka Tamara with whom 'my hodim paroy', what could I do without you all these years in Poitiers? Thank you for all your support and the time you dedicated to me. You are a very special person and I am proud to be among your many many friends (each of whom you absolutely deserve). Yann, the definition of generally talented person in everything he does, thank you for our sometimes VERY heated discussions, thank you for your amazing home made food we shared (wish you cooked more often tho!) and all your advises and positive contributions to my stay. I hope we will share many cherries hunts in the years to come. Gabriel, I should confess, it was not always the easiest to find a right path of conversation which would not lead to the argument with

you:) However, now I understand, sometimes a friendship and mutual understanding take time, and my friendship with you is, thus, even more so valuable. This group of ours would never be the same without you, and I thank you for hours you spent listening to me and supporting me in very difficult moments. Armando, I mention you the last not because you're the last in the list:) It is rather to emphasise on you. Armando, we had different moments during the times we shared the office, however, at the end it does not affect anything good we had. When you were leaving Poitiers, you said that we are your family there, and I agree with you 110%. Guys, I'm looking forward to have endless laughing on many more occasions. You are truly the best, and I miss you already. I also would like to thank all other people who make ENSMA what it is. All personnel of FTC team, particularly, Jean-Marc Breux, who can virtually solve any problem and has everything in his cave, François Paillé, who has (and probably is not even aware of it!) the internal grade of being the kindest person in ENSMA, Jacques Borée, who is a definition of 'the best supervisor in the world' according to his students (sorry Di to reveal your secrets here), Valérie Picquet, who professionally supports the team's smooth work. I thank the fellow PhD students, Clement and Clement, Lucas and Lucas, Miguel for, if only shortly, sharing some nice lab moments with me.

Lastly, but most importantly, I thank the people who were always behind the scenes. My parents, my papa and my mama, who defined the base of my being, of my personality, of my stubbornness and of my, sometimes, audacity (the last one I especially dedicate to my father). I would like to mention that all this happened a bit against my father's predictions. However, we (my dad and I) both know that there is still a good chance for his predictions to happen:) Papan, I know that even if you always hold it to yourself how much you supported me during my all, often absolutely reckless, affairs and I thank you that all these affairs are actually always happening:) Everyone among my friends knows how much my father means to me and I could write endlessly about him here. However, the space is limited and I just want to say that nothing of this would be possible without my amazing (best of a kind) dad. Thank you papa! I also thank my partner, Vedat, who knows better than anyone else how long ago this journey has started, who has been with me at the times when I did not even dream of doing what I am doing now and who is still with me through all the evolution of my personality and lifestyle. You have been my example of persistence in many moments of these past years. Sergey, my soul mate, explanations are not necessary between us, just a huge thank you for everything you have done for me during my thesis (and before). My unofficial professor and just a friend, Momo Traore, thank to you too for all your education sessions, work and life related. My other long term friend, Shahid, thank you for your, so always needed, mental support and guidance.

I used to believe that I am the person who prefers to be alone, prefers to do everything without help and support. I used to think that being solitary and independent is somehow my strength. Well, if anything I learned during my PhD (except the methods to resolve the problems with strong shocks and discontinuities) is that my absolute strength is people around me. I will never forget this experience and warm memories of it will always live with me.

Yours sincerely,
Ks Ko

Résumé étendu

Un résumé étendu en langue française du manuscrit est donné dans les pages suivantes. Il reprend les princaux éléments et résultats de chaque chapitre accompagnés des figures clés du manuscrit.

Chapitre 1. Une introduction au sujet de l'interaction choc-bulle

L'érosion par cavitation est un problème important qui doit être résolu dans de nombreux domaines, tels que les applications hydrauliques et marines. Ce processus se produit à la suite de l'effondrement des bulles à proximité des parois solides, ce qui endommage les matériaux. Le processus physique de ces phénomènes a été étudié dans de nombreuses recherches expérimentales et numériques. Par exemple, Haas & Sturtevant (1987) a réalisé une étude expérimentale où la bulle de gaz a été affectée par l'onde de choc faible plane. Les auteurs ont présenté la géométrie de la déformation de la bulle, ce qui a permis de valider de nombreuses études numériques utilisant cette configuration. D'autre part, Johnsen & Colonius (2009) a réalisé une simulation numérique de l'effondrement d'une bulle de gaz immergée dans un champ libre et à proximité d'une paroi, en comparant les résultats obtenus aux données expérimentales disponibles. Cette étude est la première où la validation de la solution numérique a été faite quantitativement contre celles obtenues par des expériences. La réponse du matériau solide causée par un tel effondrement de bulle a été étudiée numériquement dans Gong & Klaseboer (2016), où les auteurs ont effectué un couplage des méthodes pour étudier l'évolution de la bulle avec des méthodes pour analyser quantitativement l'effet de la pression impulsive, causée par l'effondrement de la bulle, sur le matériau solide. Du point de vue des calculs numériques, le phénomène de cavitation nécessite une modélisation de l'écoulement diphasique compressible. La contribution à ce besoin est faite dans Goncalves & Zeidan (2018) où un solveur multiphase compressible a été implémenté pour étudier les écoulements de type liquide-gaz avec la présence d'ondes de choc et d'expansion qui provoquent le processus de cavitation. Cependant, ce type de calculs reste un défi pour les mathématiques appliquées et les méthodes numériques, même si la demande industrielle d'une telle modélisation est élevée. Cette complexité est due aux fortes variations des propriétés thermodynamiques, aux fortes ondes de pression et à leur interaction avec les interfaces et la dynamique rapide impliquée.

Il existe plusieurs stratégies largement utilisées pour ces problèmes à deux phases. L'une des plus utilisées est une méthode basée sur une approche moyenne. Cette méthode a conduit au développement d'une variété de perspectives différentes basées sur les hypothèses physiques pour la condition de glissement entre les phases et l'équilibre mécanique et thermodynamique. L'approche de modélisation la plus complète est connue pour être le modèle à deux fluides Baer & Nunziato (1986), qui présente une grande complexité de calcul puisqu'il se compose de sept équations. Une méthode alternative, plus adaptée aux applications pratiques, est un modèle réduit à cinq équations avec l'hypothèse sous-jacente d'un équilibre de pression et de vitesse entre les phases Kapila *et al.* (2001); Saurel *et al.* (2008). En outre, ce modèle peut être réduit en utilisant l'hypothèse d'équilibre thermique. Un tel modèle consiste en trois équations pour les lois de conservation et une quatrième pour le taux de vide Goncalves & Parnaudeau (2020).

L'un des domaines importants et difficiles de l'étude des écoulements compressibles diphasiques est celui des méthodes numériques appropriées. Un défi provient de la structure caractéristique des ondes du système hyperbolique décrivant ce phénomène physique, ce qui donne lieu à des simulations instables. De plus, le problème des discontinuités des variables thermodynamiques et des équations d'état dues aux interfaces matérielles pose des difficultés dans la dérivation des

solveurs de Riemann. La composante vitesse du son constitue également un défi. En raison des grandes différences entre ses valeurs dans le mélange et les phases liquides, de grandes variations sont présentes et provoquent un comportement non lisse et des imprécisions dans la solution. Ainsi, des oscillations non physiques peuvent apparaître dans la solution de la structure entière de l'onde Abgrall (1996). La dissipation numérique des schémas numériques qui est nécessaire pour suivre la loi thermodynamique est également un résultat de ces imprécisions de la modélisation. En général, le processus complet d'établissement du modèle numérique peut être divisé en trois parties. La première est une discrétisation de base, où le cadre global de la discrétisation spatiale et temporelle est défini. La deuxième partie est une amélioration de ces méthodes globales afin d'obtenir une plus grande précision de reconstruction dans les parties lisses de la solution. La dernière partie est liée à l'observation du coût de calcul qui devient généralement rapidement prohibitif lorsque l'ordre de précision et la grille fine requise du problème augmentent. Par conséquent, des méthodes supplémentaires de réduction du temps de calcul sont nécessaires.

En termes de discrétisation numérique de base, trois méthodes sous-jacentes sont principalement utilisées : celles basées sur des maillages lagrangiens, lagrangiens-eulériens arbitraires (ALE) et eulériens. Les deux premières méthodes utilisent le suivi de l'interface des matériaux en utilisant le maillage mobile. L'inconvénient d'une telle approche réside dans sa grande complexité de calcul et sa mise en œuvre difficile en raison de la nécessité de réinitialiser fréquemment le maillage pour tenir compte de sa déformation lorsque l'écoulement se déplace. La méthode eulérienne, en revanche, utilise les marqueurs lagrangiens pour suivre l'interface matérielle et capture cette interface en utilisant un scalaire supplémentaire avec le terme d'advection requis. L'introduction du scalaire lui-même est encore divisée en deux sous-catégories de méthodes : les méthodes à interface nette et à interface diffuse.

Une autre partie de la discrétisation de base consiste à choisir le solveur à utiliser pour les méthodes de volumes finis. Une des formulations habituelles est le Harten-Lax-van Leer-Contact (HLLC) initialement introduit dans Toro *et al.* (1994). Elle a été utilisée dans de nombreuses études où la reconstruction d'ordre élevé a été réalisée avec succès, par exemple Johnsen & Colonius (2006, 2009); Wang *et al.* (2018) parmi beaucoup d'autres. Un autre choix populaire est celui des schémas upwind, où le solveur de Riemann et la décomposition caractéristique sont les techniques sous-jacentes. Ces méthodes s'inspirent des schémas de Godunov et, là encore, elles ne sont pas faciles à mettre en œuvre dans le cadre des écoulements multiphasiques. Un autre type de méthodes est celui des schémas centraux qui sont avantageux en raison de leur indépendance de la structure propre du problème considéré. Quelques exemples de tels schémas sont le schéma de Lax-Friedrichs Lax (2005) et le schéma de Nessyahu-Tadmor Nessyahu & Tadmor (1990). La combinaison des deux schémas, ascendant et central, est une méthode discutée dans Spina & Vitturi (2012), qui est abordée comme la formulation KNP. Cette méthode prend un point avantageux des deux côtés, l'indépendance de la décomposition caractéristique et la nature upwind retenue en raison du calcul de type unilatéral des valeurs propres requises dans la formulation.

La complexité des phénomènes physiques de cavitation exige une amélioration de l'ordre de précision des solveurs de volumes finis, c'est-à-dire que des méthodes de reconstruction d'ordre élevé doivent être utilisées. Bien qu'il existe de nombreux schémas de ce type, le choix n'est pas simple. Les méthodes utilisées pour améliorer la précision de la solution doivent satisfaire plusieurs exigences : stabilité dans les régions non lisses de la solution, reconstruction nette des régions de discontinuité et comportement non oscillatoire. Selon Johnsen & Colonius (2006), les instabilités numériques dues à l'interface matérielle, par exemple, peuvent être améliorées en utilisant la reconstruction de variables primitives par opposition aux variables conservatrices qui sont normalement les valeurs de reconstruction par défaut dans les méthodes de volumes finis. Les auteurs ont appliqué avec succès la méthode Weighted Essentially Non-Oscillatory (WENO) pour les problèmes diphasiques gaz-gaz. Cependant, cette stratégie n'est pas aussi adaptée lorsqu'un rapport de densité important entre les phases est présent, ce qui entraîne des gradients élevés dans l'écoulement. En effet, il a été démontré que les schémas d'ordre élevé peuvent conduire à des oscillations parasites lorsqu'ils sont appliqués à des écoulements diphasiques compressibles rigides. Deux méthodes ont été proposées pour résoudre ce problème dans Coralic & Colonius (2014). L'une d'entre elles, la construction hybride du schéma, où le WENO d'ordre 5 est localement réduit à la reconstruction d'ordre 2 près de l'interface. Une autre méthode consiste à lisser l'interface

matérielle en tant que partie de la condition initiale. Cependant, les deux stratégies présentent des inconvénients. La première méthode est dépendante du problème, puisque la condition de l'interface est différente en fonction des phénomènes physiques impliqués. D'autre part, la deuxième méthode présente le problème d'épaissir artificiellement l'interface, ce qui peut provoquer d'autres instabilités numériques. Afin d'éviter ces problèmes, une méthode alternative a été suggérée par Wang et al. Wang *et al.* (2018), où un pochoir incrémental à 2 et 3 points est utilisé pour obtenir un schéma WENO d'ordre 5. Ce choix entre le pochoir le plus petit et le plus grand est conditionné par le critère de discontinuité.

La classe de méthodes WENO mentionnée ci-dessus est l'une des plus utilisées dans la recherche moderne dans le contexte de la variété de l'écoulement diphasique compressible. Initialement introduite par Liu *et al.* (1994), où le schéma essentiellement non-oscillatoire pour la capture des chocs a été proposé sur la base de la combinaison convexe de candidats polynomiaux interpolants, cette méthode a fait l'objet de nombreuses études. Les résultats numériques préliminaires ont montré une tendance prometteuse sur divers problèmes, y compris le problème du tube de choc. La plus grande amélioration de cette méthode a été suggérée dans Jiang & Shu (1996*a*). La nouvelle méthode de mesure de la régularité de la solution a été dérivée, ce qui a conduit à un ordre supplémentaire de précision et a abouti à un schéma d'ordre 5. La principale caractéristique de ce nouveau schéma est son efficacité, puisqu'un ordre amélioré du schéma est dérivé de telle sorte qu'il est deux fois plus rapide que son homologue précédent. Cette version de WENO a été testée dans de nombreux cadres numériques, notamment un problème d'interaction d'onde de choc entropique en 2D. Les auteurs ont démontré que la nouvelle mesure de lissage est un outil capable de résoudre les chocs complexes. De nombreuses autres améliorations de WENO de cinquième et troisième ordre ont suivi. Outre l'amélioration déjà mentionnée dans Wang *et al.* (2018), il y a eu Henrick *et al.* (2005) avec l'observation que la convergence du schéma n'est pas satisfaisante près des points critiques et la suggestion d'améliorer cet inconvénient avec une technique de mappage spéciale pour garder les poids non linéaires en accord avec les linéaires partout où la discontinuité est détectée. Une inspiration de cette idée a été prise par Borges *et al.* (2008) et une autre version du schéma a été introduite avec une mesure d'indicateur de lissage supérieure qui a conduit à des résultats supérieurs avec un coût de calcul similaire. De plus, la formulation arbitraire convenant à tous les ordres impairs de précision a été dérivée dans Castro *et al.* (2011). Une conception améliorée et une nouvelle conception de la fonction d'indicateur de lissage de WENO ont été principalement axées sur la précision de la méthode aux points critiques et sont basées sur l'attribution de poids plus importants aux pochoirs moins lisses avec la préservation de la propriété essentiellement non oscillatoire (ENO). Ce type de méthodes s'est avéré efficace pour résoudre des problèmes présentant de forts chocs et des discontinuités.

Si les méthodes WENO sont extrêmement populaires, d'autres méthodes retiennent occasionnellement l'attention dans la littérature. Une méthode assez proche est proposée dans Suresh & Huynh (1997) qui a développé un schéma de préservation de la monotonicité, où la reconstruction polynomiale d'ordre élevé est limitée sur la base de la détection de discontinuité. Les auteurs ont fourni la validation basée sur l'équation d'advection linéaire que la méthode préserve la monotonicité et maintient l'ordre élevé uniformément. Une méthode beaucoup moins disponible dans le contexte des écoulements diphasiques compressibles et une classe différente de reconstruction numérique d'ordre élevé est une méthode parabolique par morceaux (PPM). Ce schéma a été initialement discuté dans Colella & Woodward (1984) et conçu pour les problèmes de gaz idéal monophasique. Ce schéma a été étendu et appliqué avec succès dans Zheng & Lee (2013) dans le cadre d'un système d'équations inviscides avec une détection appropriée des discontinuités de contact pour les EOS raidis et un algorithme d'aplatissement simplifié. La version modifiée a donné à la méthode la capacité de résoudre des problèmes avec de fortes discontinuités et des gradients aigus mieux résolus. La stratégie PPM a également été redéfinie dans le contexte des limiteurs préservant les extremums dans Colella & Sekora (2008), où les auteurs ont proposé une modification conduisant à la préservation de la précision des extrema lisses. Cette méthode modifiée a été conçue à nouveau pour les problèmes de type dynamique des gaz.

Bien que les méthodes numériques d'ordre supérieur améliorent la résolution de phénomènes physiques complexes, il est toujours nécessaire de disposer de maillages très fins. Ainsi, en plus d'un plus grand stencil de calcul normalement nécessaire pour atteindre un ordre de précision plus

élevé, la complexité de calcul augmente également en raison du nombre de points dans le domaine de calcul. Alors que les problèmes avec des solutions lisses peuvent être optimisés en utilisant des schémas numériques d'ordre élevé avec un nombre de points réduit, les cas impliquant de forts chocs et des discontinuités ne suivent pas nécessairement cette règle. Le besoin de stratégies permettant de réduire le coût de calcul tout en préservant la précision de la solution se fait sentir. L'une d'entre elles est l'introduction de maillages non-uniformes.

Plusieurs méthodes de réduction de maillage existent. Le raffinement de maillage adaptatif (AMR), l'une des plus utilisées dans la littérature récente, est une méthode où la précision de la solution est adaptée en fonction de l'emplacement de certaines composantes critiques de la solution. L'idée principale sous-jacente de cette méthode est d'appliquer une précision numérique plus élevée au moyen d'un maillage plus fin dans les zones du domaine de calcul où les gradients élevés sont détectés et de réduire cette précision dans le cas contraire. L'algorithme AMR original a été présenté dans Berger & Joseph (1984) et Berger & Colella (1989) où les auteurs ont présenté un maillage dynamique ou un raffinement adaptatif local du maillage. Une autre méthode de maillage non uniforme est l'étirement du maillage. L'étirement du maillage peut être réalisé par l'introduction d'une fonction quelconque pour distribuer les points de manière non uniforme. La fonction la plus simple peut être basée sur la progression géométrique et la plus complexe sur des fonctions plus lisses, comme le sinus, le tan, etc. Les études analytiques de ces fonctions adaptées à la génération de grille ont été étudiées dans Thompson *et al.* (1985); Vinokur (1983); Pierson & Kutler (1980); Gough *et al.* (1975).

Bien que les deux techniques de réduction de maillage aient été utilisées avec succès pour introduire un maillage non uniforme, certaines difficultés peuvent survenir. En effet, la pertinence des schémas numériques pour de tels maillages peut être remise en question, puisque la majorité des schémas sont dérivés pour les maillages uniformes. La dérivation modifiée de la reconstruction d'ordre supérieur est nécessaire si elle est utilisée avec un espacement de grille non égal. Il est intéressant de noter que la méthode PPM a été présentée dans Colella & Woodward (1984) avec la prise en compte de la grille non uniforme, ce qui facilite considérablement son utilisation sur les mailles non homogènes. D'autre part, les méthodes WENO ont été abordées dans le cadre de la grille non uniforme dans Wang *et al.* (2008).

En ce qui concerne l'aperçu ci-dessus, la présente thèse se concentre sur les méthodes numériques d'ordre élevé appropriées pour résoudre avec une grande précision le problème de l'effondrement d'une bulle induit par un choc eau-air près d'un mur. La méthode de modélisation d'un tel problème est basée sur le modèle à quatre équations présenté dans Goncalves & Charriere (2014). On considère une bulle de gaz immergée dans l'eau et s'effondrant sous l'incidence d'une onde de choc soit en champ libre Nourgaliev *et al.* (2006) soit à proximité d'une paroi. Le second problème est particulièrement important pour l'étude de l'endommagement des matériaux conduisant à l'érosion et est basé sur l'étude de Paquette *et al.* (2018).

Les objectifs suivants ont été établis pour cette étude et peuvent être divisés en trois parties.

- **La discrétisation de base et les schémas numériques d'ordre élevé.** Cette partie est destinée à étudier le modèle mathématique sous-jacent et la discrétisation numérique de base. Plus précisément, les méthodes appropriées pour les problèmes qui impliquent de forts chocs et des discontinuités doivent être examinées en se concentrant sur les techniques qui ont été validées dans le contexte des écoulements diphasiques compressibles. Une attention particulière doit être accordée à l'existence d'un terme source dans le modèle mathématique sous-jacent. En plus de la discrétisation spatiale de base, l'intégration temporelle doit être choisie en préservant les caractéristiques des autres méthodes numériques choisies. Enfin, les méthodes numériques d'ordre supérieur doivent être examinées dans le cadre du problème considéré. Les techniques appropriées doivent être validées sur les problèmes qui peuvent démontrer la compatibilité des schémas des phénomènes impliqués.

- **Maillage non-uniforme.** Cette partie de la thèse traite des techniques de réduction des coûts de calcul au moyen de techniques d'étirement de maillage. Les méthodes d'étirement de maillage ont été examinées et des méthodes appropriées ont été mises en œuvre et testées. Les stratégies d'étirement de maillage dépendantes du problème doivent être proposées, testées et validées. Le cadre final de l'étirement des mailles doit être établi.

- **Calculs 3D.** L'objectif final de cette thèse est une extension des méthodes numériques proposées calculées sur le maillage non-homogène avec la résolution nécessaire au problème de l'effondrement des bulles de choc à proximité de la paroi en 3D. Le coût élevé de tels calculs nécessite l'introduction d'un solveur entièrement parallélisé et une mise en œuvre parallèle efficace des schémas numériques d'ordre élevé. Une attention supplémentaire doit être accordée à l'implémentation du maillage non-uniforme dans le cadre d'un environnement de calcul parallélisé. La stratégie finale appropriée en termes de méthode numérique d'ordre élevé et de maillage non uniforme doit être suggérée.

Cette thèse aborde les objectifs ci-dessus dans le schéma suivant. Le chapitre 2 présente le modèle mathématique sous-jacent utilisé dans cette étude et développe la discrétisation numérique de base. Le chapitre 3 traite de l'extension de la discrétisation de base aux schémas numériques d'ordre élevé et passe en revue les principales méthodes numériques disponibles. Ces méthodes sont ensuite validées au chapitre 4, où trois problèmes 1D sont utilisés par ordre hiérarchique en termes de rigidité. La validation est finalisée par l'utilisation de schémas sélectionnés dans le problème 2D de l'interaction choc-bulle air-hélium. Le chapitre 5 présente une extension de ces méthodes aux problèmes d'effondrement de bulles induit par un choc dans un champ libre et près d'une paroi. Nous améliorons ces méthodes en termes de réduction des coûts de calcul en introduisant un maillage non-uniforme. Ces techniques sont discutées dans le chapitre 6 et validées pour les calculs 2D dans le chapitre 7. Enfin, nous présentons des calculs 3D en utilisant des schémas appropriés et un maillage non uniforme dans le chapitre 8. Le résumé général de ce travail et ses perspectives sont donnés dans le chapitre 9.

Chapitre 2. Modèle mathématique et discrétisation de base

Dans cette étude, nous nous concentrons sur un modèle à quatre équations qui constitue la première partie du travail d'établissement de l'effet du schéma numérique sur la base de simulations inviscides. Le système à quatre équations comprend trois lois de conservation pour les quantités de mélange et une équation de transport supplémentaire pour la fraction de vide. Le solveur est basé sur les méthodes explicites de volumes finis utilisant deux approximations de flux différentes (HLLC et KNP) avec différentes approches de résolution dans le temps et des techniques de limitation dans l'espace.

Nous commençons par présenter le problème mathématique et les équations gouvernantes, puis nous décrivons les schémas d'approximation numérique mis en œuvre et testés. Il est employé sur la base de l'approche du mélange à un seul fluide avec les hypothèses suivantes:

- couplage fort des phases avec la même vitesse
- équilibre thermique et mécanique entre les phases
- état de saturation du liquide
- les effets visqueux et la tension superficielle sont négligés

Le modèle utilise un système à quatre équations dont trois sont des lois de conservation pour les quantités de mélange et la quatrième est l'équation de transport du taux de vide Goncalves & Zeidan (2018). La discrétisation de base est effectuée en utilisant la méthode des volumes finis avec intégration temporelle explicite. En utilisant la représentation des variables conservatives, c'est-à-dire $w = (\rho, \rho\overrightarrow{V}, \rho E)$ et la fraction volumique du gaz α), le système inviscide 2D peut être écrit comme suit,

$$\begin{aligned} \frac{\partial \rho}{\partial t} + \mathrm{div}(\rho \overrightarrow{V}) &= 0 \\ \frac{\partial (\rho \overrightarrow{V})}{\partial t} + \mathrm{div}(\rho \overrightarrow{V} \otimes \overrightarrow{V} + PId) &= 0 \\ \frac{\partial (\rho E)}{\partial t} + \mathrm{div}(\rho \overrightarrow{V} H) &= 0 \\ \frac{\partial \alpha}{\partial t} + \overrightarrow{V}.\mathrm{grad}(\alpha) &= \mathrm{Kdiv}(\overrightarrow{V}) \end{aligned} \tag{1}$$

où $\overrightarrow{V} = (u, v)$ désigne la vitesse du centre de masse, $E = e + V^2/2$ est l'énergie totale du mélange et $H = h + V^2/2$ est l'enthalpie de ce mélange. Le reflet de la variation du volume de chaque phase et de la vitesse du son des phases pures c_k sont inclus dans le terme K, qui est dérivé selon la formulation suivante,

$$K = \frac{\rho_l c_l^2 - \rho_v c_v^2}{\frac{\rho_l c_l^2}{1-\alpha} + \frac{\rho_v c_v^2}{\alpha}}$$

où l'indice g représente la phase gazeuse et l la phase liquide. Plusieurs études menées par Wermelinger *et al.* (2018) et Schidmayer *et al.* (2020) ont démontré un effet de ce terme dans le cadre de l'étude du modèle à cinq équations avec et sans terme K. Il a été établi que ce terme améliore la précision du comportement thermodynamique dans le mélange.

Une équation d'état (EOS) pour le mélange est nécessaire pour fermer le système. La formulation est déduite de l'EOS des gaz raidis convexes LeMétayer *et al.* (2004) pour les deux phases et obtenue à partir de l'hypothèse de l'équilibre thermique et mécanique. Les équations pour la pression et la température sont,

$$P(\rho, e, \alpha, Y) = (\gamma(\alpha) - 1)\rho(e - q(Y)) - \gamma(\alpha) P_\infty(\alpha) \tag{2}$$

$$T(\rho, h, Y) = \frac{h - q(Y)}{C_p(Y)} \tag{3}$$

with

$$\begin{aligned} \frac{1}{\gamma(\alpha) - 1} &= \frac{\alpha}{\gamma_v - 1} + \frac{1 - \alpha}{\gamma_l - 1} \\ q(Y) &= Y q_v + (1 - Y) q_l \\ C_p(Y) &= Y C_{p_v} + (1 - Y) C_{p_l} \end{aligned} \tag{4}$$

$$P_\infty(\alpha) = \frac{\gamma(\alpha) - 1}{\gamma(\alpha)} \Big[\alpha \frac{\gamma_v}{\gamma_v - 1} P_\infty^v + (1 - \alpha) \frac{\gamma_l}{\gamma_l - 1} P_\infty^l \Big] \tag{5}$$

où C_p et C_v sont les capacités thermiques, q est l'énergie de formation, $\Gamma = C_p/C_v$ est le rapport des capacités thermiques et $Y = \alpha\rho_v/\rho$ est la fraction massique de gaz. La quantité P_∞ désigne une pression de référence constante.

Le présent système est hyperbolique et les valeurs propres sont $\lambda_1 = u - c_{wallis}$, $\lambda_{2,3,4} = u$, $\lambda_5 = u + c_{wallis}$, où c_{wallis} correspond à la propagation des ondes acoustiques sans transfert de masse et de chaleur et a la formulation suivante,

$$\frac{1}{\rho c_{wallis}^2} = \frac{\alpha}{\rho_v c_v^2} + \frac{1 - \alpha}{\rho_l c_l^2} \tag{6}$$

où c_v et c_l sont les vitesses du son des phases vapeur et liquide, respectivement.

Afin d'appliquer la discrétisation, le système 2.1 doit être réécrit sous forme 1D comme suit,

$$\frac{\partial U}{\partial t} + \frac{\partial G(U)}{\partial x} + B(U)\frac{\partial u}{\partial x} = 0 \tag{7}$$

où $U = \begin{pmatrix} \mathbf{w} \\ \alpha \end{pmatrix}$, $G(U) = \begin{pmatrix} F(\mathbf{w}) \\ \alpha u \end{pmatrix}$, $B(U) = \begin{pmatrix} 0 \\ -K - \alpha \end{pmatrix}$, et F désigne le flux convectif.

Cette nouvelle formulation 1D peut ensuite être utilisée pour le fractionnement directionnel lors de la résolution de problèmes en plusieurs dimensions. Les domaines spatial et temporel de calcul sont divisés en mailles régulières de longueur uniforme Δx et d'intervalles uniformes Δt, respectivement. La forme discrète reformulée de (2.1) est obtenue en utilisant la méthode des volumes finis. Le système peut être exprimé comme suit,

$$\Delta x \frac{U_i^{n+1} - U_i^n}{\Delta t} + G_{i+1/2}^n - G_{i-1/2}^n + \int_{x_{i-1/2}}^{x_{i+1/2}} B(U) \frac{\partial u}{\partial x} = 0 \tag{8}$$

La discrétisation du terme non-conservatif est discutée ci-dessous. La discrétisation a pour but d'approximer le flux numérique $G_{i+1/2}^n$, $G_{i-1/2}^n$ en utilisant la solution du problème de Riemann ou toute autre technique numérique. Alors que de nombreuses formulations sont disponibles pour l'estimation du flux numérique, telles que le type Roe Gallouet *et al.* (2002), le type AUSM Kitamura *et al.* (2014), le type Jameson-Schmidt-Turkel Jameson *et al.* (1981), deux formulations sont considérées dans cet article : HLLC Toro *et al.* (1994) et KNP Spina & Vitturi (2012). Le schéma HLLC a été largement utilisé dans la plupart des publications récentes et il a été démontré qu'il était adapté aux problèmes impliquant des chocs forts. La formulation KNP, d'un autre côté, plus spécifiquement la formulation de l'unpwind central, a été implémentée dans le schéma prédicteur-correcteur de Hancock et testée pour des écoulements compressibles, ce qui est effectivement le problème considéré dans cette thèse.

Ce chapitre a examiné le modèle mathématique à quatre équations qui est à la base de tous les calculs à venir. L'EOS pour le gaz raidi a été énoncé. Ensuite, deux formulations pour la discrétisation spatiale de base ont été proposées. L'une d'entre elles, HLLC, est basée sur le solveur de Riemann et est l'une des formulations les plus utilisées pour les problèmes où des chocs et des discontinuités sont présents. La deuxième méthode est KNP, qui a été appliquée avec succès dans le contexte de l'écoulement diphasique compressible avec la présence du terme source et a été particulièrement testée dans le cadre du schéma prédicteur-correcteur MUSCL-Hancock. Par conséquent, le schéma MUSCL-Hancock a été décrit étape par étape avec la description du traitement de la source. Le choix des variables de reconstruction a été discuté et l'étape de transformation entre les variables primitives et caractéristiques a été énoncée. Les techniques des limiteurs MUSCL et TVD qui peuvent être utilisées comme première étape de l'amélioration de l'ordre spatial sont passées en revue et les dérivations clés sont présentées. Le traitement des conditions aux limites est discuté.

Chapitre 3. Méthodes numériques d'ordre élevé

La discrétisation de base basée sur le solveur de volumes finis avec le schéma prédicteur-correcteur MUSCL-Hancock conduit généralement à une précision du second ordre dans l'espace et le temps. Toutefois, il convient de noter que la partie non conservative dans 2.24 est toujours reconstruite avec le premier ordre dans le temps. Afin de réaliser la reconstruction détaillée de phénomènes physiques complexes, une telle approche numérique nécessiterait une grille extrêmement fine, ce qui pourrait être irréaliste pour les calculs en 3D. Une précision similaire avec moins de points dans le domaine de calcul peut être obtenue en utilisant des schémas numériques d'ordre supérieur, en raison de leurs propriétés formelles de convergence plus rapide.

L'ordre supérieur de précision peut être obtenu par deux moyens: Les techniques de TVD MUSCL, telles que discutées dans la section 2.2, pour obtenir une convergence de deuxième ou troisième ordre dans l'espace et des méthodes numériques plus avancées, abordées ici comme des méthodes numériques d'ordre supérieur. Le premier choix, c'est-à-dire la TVD MUSCL, nécessite des procédures de limitation supplémentaires, telles que les limiteurs de pente qui sont destinés à réduire les oscillations non physiques et, par conséquent, pourraient conduire à une solution diffusive autour des régions de discontinuité. Le deuxième choix, d'autre part, les schémas numériques d'ordre élevé, ont des techniques plus complexes pour définir les zones de la solution où un traitement spécial est requis et peuvent changer l'ordre de la solution dans ces zones pour conduire à des

résultats monotones et non oscillants. Cependant, ces méthodes peuvent présenter l'inconvénient d'une complexité de calcul élevée, de méthodes de mise en œuvre difficiles et du traitement de régions critiques qui peuvent être soit trop diffusives, soit trop oscillantes. Ainsi, le choix des méthodes d'ordre élevé, qui est une préoccupation principale du présent chapitre, est basé sur ces critères. En particulier, les méthodes considérées doivent conduire à un ordre uniforme formel de précision supérieur à 2, les propriétés de monotonicité doivent être préservées et des algorithmes non oscillants doivent être envisagés. De plus, les schémas doivent être capables de travailler avec des problèmes avec de forts chocs et discontinuités et avoir des propriétés de stabilité sur le maillage avec une petite valeur du pas spatial dx.

Le domaine de recherche de la dynamique des fluides computationnelle est souvent caractérisé par des problèmes où la solution uniforme est perturbée par des discontinuités. Le défi consiste donc à trouver des schémas d'ordre élevé qui préservent la reconstruction nette et non oscillatoire autour des discontinuités tout en étant précis dans les régions lisses. L'une des toutes premières tentatives pour résoudre ce problème a été présentée par Colella & Woodward (1984), où les auteurs ont présenté une méthode parabolique par morceaux utilisant le stencil centré à quatre points pour la dérivation de la valeur d'interface. Cette méthode utilise ensuite des procédures de limitation pour réduire les oscillations dans les régions de discontinuités. D'autres techniques d'ordre supérieur couplées à des algorithmes de limitation ont été introduites, par exemple, par Leonard (1991). Cependant, cette classe de méthodes présente l'inconvénient de réduire l'ordre du schéma local près des extrema.

Une approche alternative à la technique de réduction de l'ordre local est une technique de stencil adaptatif introduite pour la première fois par Harten *et al.* (1987) dans le cadre de ses schémas essentiellement non-oscillatoires ENO, où les données les plus "lisses" sont utilisées pour éviter les interpolations dans les régions discontinues. Cette méthode, cependant, n'utilise pas toutes les données disponibles par rapport au schéma ENO pondéré de Liu *et al.* (1994) et Jiang & Shu (1996*b*), où les auteurs dérivent la valeur d'interface en utilisant la moyenne pondérée des valeurs d'interface de tous les pochoirs disponibles. L'idée derrière cette méthode est d'utiliser la moyenne pondérée de tous les pochoirs autour des zones lisses de la solution et seulement le pochoir le plus "lisse" dans les régions discontinues. Néanmoins, les versions précédentes des schémas ENO et WENO sont considérées comme des schémas diffusifs et, par conséquent, ces schémas ont tendance à maculer les régions discontinues.

Une autre technique est introduite par Suresh & Huynh (1997), où l'approche limitative mentionnée ci-dessus est utilisée. La base de ce schéma est la reconstruction du stencil en cinq points. L'avantage de cette technique numérique est un pochoir plus grand (par rapport à la méthode PPM), ce qui réduit l'effet d'escalier dû à la nature dissipatrice du schéma. Selon les auteurs de la méthode, ce schéma présente plusieurs différences principales par rapport à ceux mentionnés ci-dessus : la monotonicité et la précision sont préservées, la conception spécifique pour l'échelonnement temporel Runge-Kutta et la faible complexité de calcul due aux procédures de limitation plus simples.

Les méthodes numériques d'ordre supérieur sont introduites dans le cadre du solveur de Riemann HLLC Hancock ou du solveur de Hancock KNP. Ceci est réalisé en modifiant le calcul du limiteur de pente $\delta\mathbf{W}_j$ dans l'algorithme de Hancock.

Ce chapitre a défini la motivation des schémas numériques d'ordre élevé et les exigences que ces méthodes doivent satisfaire. Il s'agit, entre autres, de la préservation de la monotonicité, de l'uniformité de l'ordre élevé, de la stabilité sur les mailles fines et du comportement non oscillant. Le bref aperçu de ces schémas dans la section 1 a été suivi de présentations détaillées de techniques numériques satisfaisant formellement et parfois pratiquement à ces exigences. Ces schémas sont PPM, MP5 et WENO.

La section 2 propose la dérivation du schéma PPM avec plusieurs développements récents disponibles. L'algorithme de monotonie, la technique d'aplatissement et la détection des discontinuités sont intégrés dans le schéma. La technique de préservation des extrema est proposée. La méthode PPM est adaptée au maillage non uniforme. La précision du quatrième ordre formel dans les solutions lisses peut être obtenue en utilisant cette stratégie.

La section 3 présente la technique MP5. Cette méthode a été validée sur l'équation d'advection linéaire et a conduit aux solutions uniformes d'ordre élevé. La technique de limitation TVD est

utilisée dans la base de la méthode. La méthode MP5 permet d'obtenir une précision formelle d'ordre 5.

Enfin, la section 4 est consacrée à la classe des méthodes WENO. Celles-ci sont discutées dans le contexte du troisième et du cinquième ordre de précision. Certaines améliorations récentes de ces schémas sont proposées. Ce type de méthodes est le plus prometteur par rapport à ses homologues PPM et MP5 en raison de l'énorme quantité de recherches axées sur ce type de technique et de son application à de nombreux problèmes d'écoulement diphasique compressible. Afin de différencier la variété des méthodes discutées, les notations suivantes seront utilisées tout au long de la thèse.

- WENO3-JS et WENO5-JS sont les méthodes de troisième et cinquième ordre de précision, respectivement, basées sur les études de Liu *et al.* (1994) et Jiang & Shu (1996*b*).
- WENO3-Z et WENO5-Z sont des modifications proposées par Borges *et al.* (2008)
- WENO3-P est une méthode de précision de troisième ordre proposée dans Xu & Wu (2017)
- OWENO3 est une amélioration discutée dans Baeza *et al.* (2013)
- WENO5-SZ est une méthode améliorant la précision du cinquième ordre présentée par Shen (2009)
- WENO5-IS est une autre version modifiée d'ordre 5 proposée par Wang *et al.* (2018).
- c représente la reconstruction des variables caractéristiques.

Les méthodes discutées dans ce chapitre seront soumises à la procédure de validation numérique afin de confirmer leur compatibilité formelle pour résoudre les problèmes avec de forts chocs et discontinuités.

Chapitre 4. La validation numérique

L'ordre formel des schémas numériques peut être dérivé analytiquement pour certains problèmes simples. Cependant, une telle dérivation est presque impossible pour la majorité des cas pratiques impliqués dans la dynamique des fluides numérique. Bien que toutes les méthodes numériques présentées dans cette thèse aient été validées par l'ordre formel de précision dans différentes études, l'ordre réel dépend fortement du problème qui est résolu. Certains facteurs qui peuvent réduire la précision du schéma sont la présence de discontinuités et de chocs. Ainsi, même si les schémas numériques considérés sont d'ordre élevé, par exemple du troisième, quatrième ou cinquième ordre, cela ne signifie pas nécessairement que lorsqu'ils sont appliqués au problème de l'interaction choc-bulle, l'ordre de précision analytique est conservé. De nombreux auteurs ont observé que dès que le problème présente des discontinuités, l'ordre de précision numérique de la majorité des schémas se détériore en raison du phénomène bien connu de Gibbs. Il a été démontré Majda & Osher (1977); Lax & Mock (1978); Toro (1999) que l'approximation de solutions discontinues par des méthodes d'ordre élevé ne donne, en général, qu'une précision de premier ordre, car l'information passant par le choc le long des caractéristiques est dégradée.

La validation de l'ordre de précision théorique pour un problème réel de dynamique de calcul peut être une tâche difficile. Alors que les schémas sont normalement présentés avec une dérivation de la précision basée sur des problèmes "jouets", l'ordre réel de précision peut être démontré numériquement en utilisant un problème simple avec une solution analytique disponible. Ces cas d'essai sont normalement basés sur l'approximation de la dérivation et l'équation d'advection linéaire. Cependant, cette tâche devient un défi lorsque des problèmes plus difficiles sont résolus et que les solutions analytiques sont soit difficiles à obtenir, soit inconnues. De plus, l'ordre de précision pour le cas d'essai simple de l'approximation dérivée n'est pas nécessairement une prédiction exacte pour les solutions impliquées dans les écoulements diphasiques compressibles. Ainsi, des méthodes de validation alternatives sont nécessaires pour avoir une idée de la performance des schémas.

La procédure classique d'analyse de la performance des méthodes numériques repose sur le calcul de l'erreur entre les solutions numériques et analytiques et la démonstration de la vitesse à laquelle cette erreur diminue avec l'augmentation du nombre de points dans le domaine de calcul. Cependant, que se passe-t-il si la solution analytique n'est pas disponible?

L'inspiration pour un tel cas est présentée par Spina & Vitturi (2012). Le travail de ces auteurs démontre la validation numérique basée sur la solution numérique de référence calculée. Cette solution de référence est obtenue par des calculs sur un maillage considérablement plus fin que les solutions numériques comparées. L'estimation de l'erreur E_{est} et le taux de convergence R sont calculés de la manière suivante,

$$E_{est}(sol_N, sol_{ref}) = \frac{\sum_j (sol_N(x_j) - sol_{ref}(x_j))^2}{\sum_j (sol_{ref}(x_j))^2} \tag{9}$$

$$R(sol_N, sol_{2N}, sol_{ref}) = \frac{\sum_j |(sol_N(x_j) - sol_{ref}(x_j))|}{\sum_j |(sol_{ref}(x_j))|} \tag{10}$$

où sol_{ref} est une solution de référence calculée sur le maillage fin et sol_N désigne la solution calculée sur le maillage avec N nombre de points.

L'erreur et le taux de convergence sont estimés pour le problème du tube-choc. L'intérêt particulier du problème du tube-choc est dû aux plusieurs types de phénomènes physiques impliqués, à savoir l'onde de dilatation, le choc et la discontinuité de contact. Ainsi, le comportement des schémas peut être correctement évalué pour chacun de ces processus physiques. La solution de référence est calculée sur 128 000 nœuds dans le cadre du solveur HLLC Hancock avec une reconstruction WENO5-IS.

Les schémas sont ensuite testés pour les problèmes de tube d'expansion avec des vitesses faibles et élevées. Les discontinuités plus fortes impliquées dans le problème permettent d'accéder à la performance des schémas numériques. Les solutions sont comparées qualitativement.

La validation est conclue par le cas 2D air-hélium. Ce problème est choisi comme un bon point de départ pour accéder à la performance des schémas en 2D et à la disponibilité des données expérimentales. La validation basée sur ce problème est effectuée en analysant la convergence de la composante de pression maximale de la solution P_{max} convergeant vers la valeur obtenue sur le maillage le plus fin. L'évaluation qualitative du contour du gradient de densité permet de conclure à un degré de reconstruction détaillée de la déformation des bulles.

Sauf indication contraire, la reconstruction est effectuée sur des variables primitives et le solveur HLLC Hancock est utilisé par défaut.

Le premier cas considéré a été introduit dans Murrone & Guillard (2005) et est un tube de choc d'un mètre de long avec une discontinuité dans la fraction volumique, avec le côté droit ($x > 0.7$) rempli d'air et le côté gauche d'eau liquide à haute pression. Les fractions volumiques sont de 0,8 et 0,2, pour $x > 0,7$ et $x > 0,7$, respectivement. Les deux fluides sont initialement au repos et décrits par l'équation d'état (EOS) des gaz raidis. La partie remplie d'air est à basse pression $10^5 Pa$, tandis que la partie d'eau est à haute pression $10^9 Pa$. Les paramètres EOS pour ce test sont,

$$\begin{pmatrix} \Gamma \\ P_\infty \\ \rho \end{pmatrix}_{Water} = \begin{pmatrix} 4.4 \\ 6 \times 10^8 \text{ Pa} \\ 1000 \text{ kg/m}^3 \end{pmatrix} \text{ et } \begin{pmatrix} \Gamma \\ P_\infty \\ \rho \end{pmatrix}_{Air} = \begin{pmatrix} 1.4 \\ 0 \text{ Pa} \\ 1 \text{ kg/m}^3 \end{pmatrix}$$

Les calculs ont été effectués sur le maillage de 1000 cellules avec un pas de temps fixe dt=10^{-7} s. Nous comparons les résultats au temps final $t_{final} = 0.2$ μ s. Les résultats calculés sont obtenus par un solveur basé sur HLLC Hancock ou KNP Hancock. Un Runge-Kutta à trois étapes a été utilisé pour comparer la solution avec une résolution temporelle plus élevée. Bien que notre préoccupation principale soit les schémas d'ordre élevé, la méthode MUSCL TVD de second ordre est utilisée à des fins de comparaison. Sauf indication contraire, le limiteur de pente van Albada est utilisé dans le cadre de la méthode MUSCL TVD.

Le tableau 4.1 présente les estimations d'erreur et de convergence avec CFL=0.4 fixe. L'estimation de l'erreur E_{est} a démontré que les schémas d'ordre supérieur, par exemple WENO5 et PPM, conduisent effectivement à une solution plus précise. En général, il a été constaté que l'erreur est plus

faible pour les schémas d'ordre supérieur et qu'elle diminue à mesure que le maillage est raffiné. Le taux de convergence R calculé en utilisant (4.2) est estimé en raffinant le maillage à partir de 1 000 nœuds et jusqu'à 8 000 nœuds avec le pas 1 000. Tous les schémas ont donné lieu à une convergence d'environ second ordre, contrairement à la précision théorique plus élevée. Cependant, si les formulations classiques de dérivation d'ordre sont utilisées (c'est-à-dire une différence de norme), le premier ordre de convergence est observé dans tous les schémas en raison des discontinuités présentes dans la solution. En effet, l'ordre de précision des méthodes d'ordre élevé diminue pour les problèmes où une forte discontinuité est présente (voir Toro (1999); Schidmayer *et al.* (2020)).

Table 1: Problème du tube de choc : erreur relative (à gauche) et taux de convergence (à droite).

Relative error				Convergence rate		
N	WENO5SZ	WENO5IS	PPM	WENO5SZ	WENO5IS	PPM
8000	3.9×10^{-6}	4.5×10^{-6}	5.3×10^{-6}	2.3	2.3	2.2
4000	1.9×10^{-5}	1.9×10^{-5}	2.4×10^{-5}	2.1	2.1	2.1
2000	9.3×10^{-5}	9.2×10^{-5}	1.0×10^{-4}	2.1	2.1	2.1
1000	3.9×10^{-4}	3.9×10^{-4}	4.2×10^{-4}	-	-	-
N	WENO3JS	WENO3Z	WENO3P	WENO3JS	WENO3Z	WENO3P
8000	4.4×10^{-6}	4.4×10^{-6}	4.3×10^{-6}	2.3	2.3	2.3
4000	1.8×10^{-5}	1.9×10^{-5}	1.9×10^{-5}	2.2	2.1	2.1
2000	8.4×10^{-5}	9.2×10^{-5}	9.2×10^{-4}	2.1	2.1	2.1
1000	3.5×10^{-4}	3.9×10^{-4}	3.9×10^{-4}	-	-	-

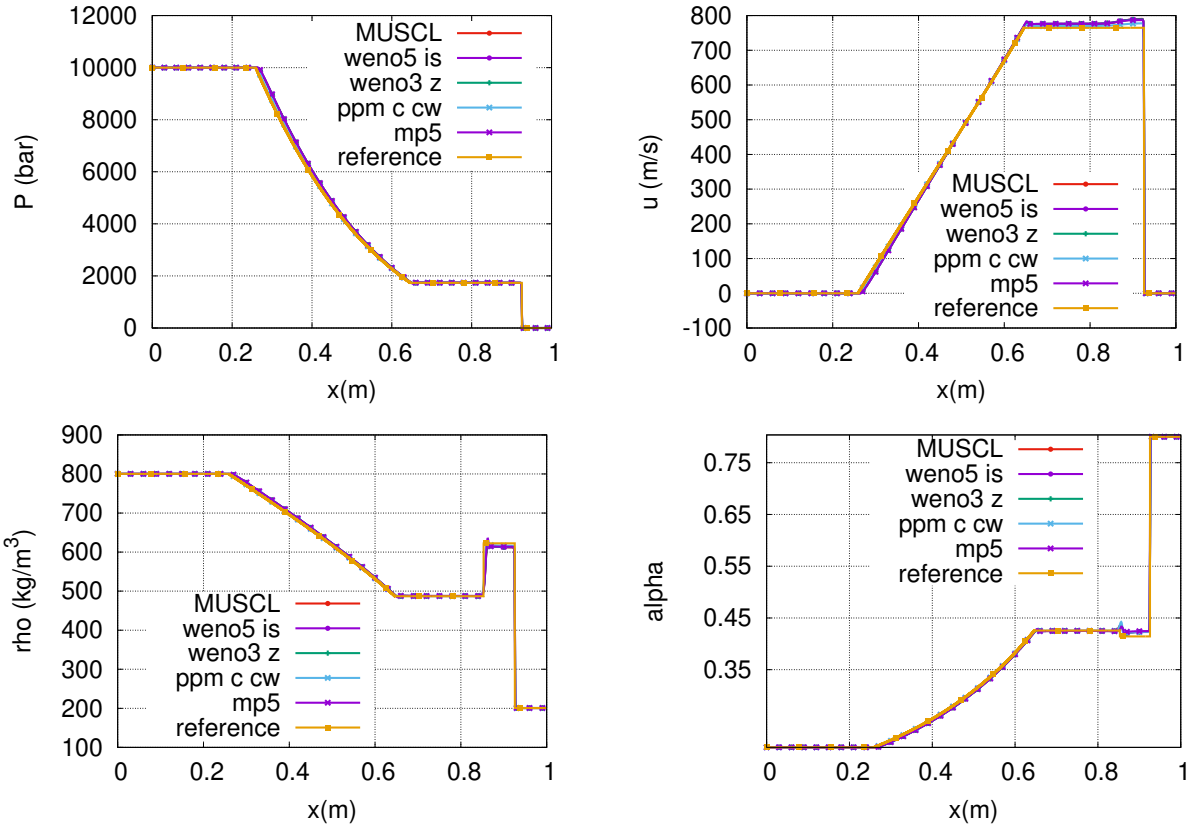

Figure 1: Problème de tube de choc eau-gaz, comparaison des schémas numériques, maillage 1000 cellules, t_{final}=0.2 μs. Profils de pression et de vitesse (en haut), de densité du mélange et de taux de vide (en bas) le long du tube.

Enfin, la comparaison des solutions entre les principaux schémas numériques est proposée sur la figure 4.9 où sont présentés les résultats obtenus en utilisant MUSCL, PPM, MP5, WENO3-Z et WENO5-IS. Le schéma PPM a conduit à une légère variation près de la discontinuité du contact

pour le profil du taux de vide. La méthode MP5 a un résultat oscillant pour la densité du mélange dans la zone post-choc. Sinon, tous les schémas ont conduit à une solution précise en accord étroit avec la solution de référence.

Le problème du tube de choc eau-gaz est le point de départ du processus de validation. Les performances des schémas sont estimées. La plupart des schémas ont conduit à une solution précise, à l'exception de WENO5-JS, MP5 et PPM-CW où des oscillations sont observées dans la zone post-choc.

La première partie du processus de validation des schémas numériques utilisés dans cette étude a commencé par des calculs 1D pour les tests du tube de choc eau-gaz et du tube de détente avec des vitesses initiales faibles et élevées.

Tout d'abord, les calculs du problème du tube de choc montrent que la plupart des techniques de reconstruction fournissent des résultats en bon accord avec la solution de référence. La solution de référence est calculée en utilisant HLLC avec WENO5-IS méthode de Hancock. Cependant, certaines divergences ont été constatées. Par exemple, le schéma WENO5-SZ présente une oscillation pour la densité du mélange autour de la zone de discontinuité, qui n'est observée ni dans les autres méthodes WENO5, ni dans la solution de référence. Cette oscillation a été éliminée en utilisant la reconstruction des variables caractéristiques. D'autre part, les schémas WENO3 ont conduit à une reconstruction précise et lisse de toutes les variables, à l'exception de la formulation OWENO, où une légère divergence est notée pour la densité du mélange dans la zone de discontinuité. De plus, la méthode PPM produit des oscillations de la solution dans la zone post-choc en utilisant la reconstruction des variables primitives (PPM CW). Ce problème est résolu en utilisant des variables caractéristiques. Ce test n'a pas démontré de différence entre les solveurs HLLC et KNP. L'analyse numérique en utilisant la solution de référence calculée sur la grille fine a été effectuée et un second ordre de convergence approximatif est obtenu en utilisant tous les schémas.

Deuxièmement, deux tests de tubes d'expansion ont été effectués. Ici, la vitesse initiale établie avec des valeurs faibles et élevées permet d'examiner le comportement du schéma lorsque des vagues plus fortes sont impliquées. La solution de référence a été obtenue en utilisant la méthode HLLC WENO5-IS de Hancock avec 128 000 points pour la vitesse faible et la méthode HLLC MUSCL-Hancock avec une taille similaire de dx pour la vitesse élevée. En effet, d'autres variations de la solution numérique ont été illustrées. Par exemple, le schéma WENO5-JS a conduit à des oscillations symétriques le long des ondes d'expansion dans les deux essais pour la pression. Contrairement au problème du tube à choc, ces tests ont également montré une différence dans l'évolution de la pression en utilisant WENO3-τ_N et WENO3-τ_P, où le premier a conduit à la reconstruction inexacte des ondes de raréfaction pour le cas avec une vitesse initiale plus forte. En outre, toutes les méthodes PPM produisent des oscillations pour les profils de densité du mélange et de taux de vide, même avec une reconstruction caractéristique, soit au milieu du tube pour le cas de faible vitesse initiale, soit le long des ondes d'expansion pour le cas de vitesse élevée. De plus, la méthode PPM avec reconstruction primitive présente une grande oscillation non symétrique dans la zone de raréfaction pour le cas avec une vitesse initiale élevée, qui n'est pas présente dans des calculs similaires avec reconstruction caractéristique. Enfin, ces tests ont présenté les divergences dans la solution pour la variable de pression en utilisant le solveur KNP.

Ces premiers résultats donnent une indication du comportement des schémas lorsque de forts chocs ou des ondes d'expansion sont impliqués. Nous pouvons conclure de manière préliminaire que la méthode PPM fournit une solution plus précise lorsqu'elle est appliquée aux variables caractéristiques, puisque la plupart des problèmes sont éliminés par rapport à la reconstruction des variables primitives. En outre, la formulation WENO5-JS devient oscillante si un choc important est impliqué et, par conséquent, ne devrait probablement pas être utilisée dans de tels problèmes. En revanche, le schéma WENO5-IS a donné des résultats précis dans tous les tests. De même, la tendance à la détérioration de la solution est notée pour certains schémas WENO3, c'est-à-dire que la méthode OWENO3 oscille même pour le cas du tube à choc et que WENO3-τ_P n'est pas précis pour les problèmes impliquant une forte onde d'expansion. Enfin, nous notons une détérioration de la solution du solveur KNP, alors que la formulation HLLC est un choix préférentiel préliminaire pour les calculs de tels cas.

La deuxième partie de la validation est une interaction choc-bulle 2D : une bulle d'hélium immergée dans l'air est impactée et accélérée par une onde de choc. Ce problème particulier a été

choisi en raison de l'existence d'études expérimentales menées par Haas & Sturtevant (1987) et plus récemment par Layes *et al.* (2009). Cela implique que les visualisations des données expérimentales peuvent être utilisées pour une évaluation qualitative.

La bulle d'hélium a un diamètre initial de 4 cm et est impactée par une onde de choc normale se déplaçant à un nombre de Mach de 1,175. Les paramètres EOS et post-choc sont indiqués dans le tableau 4.2. La fraction volumique α représente ici le rapport entre le gaz le plus léger et le gaz porteur.

Table 2: Paramètres EOS de l'air et de l'hélium et conditions post-chocs

	γ	P_∞	ρ
air	1.4	0 Pa	1.163 kg/m^3
helium	1.648	0 Pa	0.16 kg/m^3
	P	ρ	u
post-shock	1.444 10^5 Pa	1.51 kg/m^3	93.65 m/s

Les calculs sont effectués sur un demi-domaine en raison de la symétrie du problème. Sauf indication contraire, les résultats ont été obtenus en utilisant une discrétisation à maillage uniforme de 4000×400 cellules, un pas de temps de 2,5 $\times 10^{-9}$ s et la formulation de flux HLLC. Dans les présents calculs, la méthode PPM est utilisée avec des variables caractéristiques avec détection des discontinuités de contact. La notation WENO3-P désigne la formulation avec l'indicateur de lissage de référence selon 3.46, qui n'oscille pas dans le problème du tube de détente avec une vitesse initiale élevée.

Tout d'abord, l'évolution du gradient de densité par rapport aux visualisations expérimentales est présentée dans les figures 4.15 et 4.16 pour les simulations effectuées en utilisant la reconstruction WENO5-IS. Les solutions numériques et expérimentales sont comparées à des moments approximativement similaires. La déformation de la bulle commence par son aplatissement dans la direction de l'onde de choc et prend finalement la forme d'un rein en raison de la formation d'un jet d'air à grande vitesse situé à l'interface amont. D'autre part, le jet de l'interface aval conduit à l'apparition de tourbillons contrarotatifs qui provoquent l'allongement de la bulle. Les calculs obtenus avec tous les schémas sont capables de reproduire les principaux éléments de l'évolution de la forme des bulles par rapport aux données expérimentales.

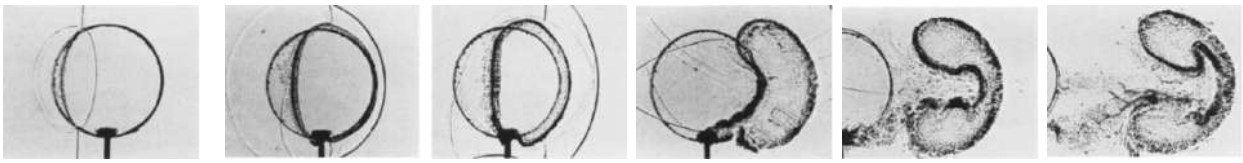

Figure 2: Visualisation expérimentale par Haas et Sturtevant, extraite de Haas & Sturtevant (1987).

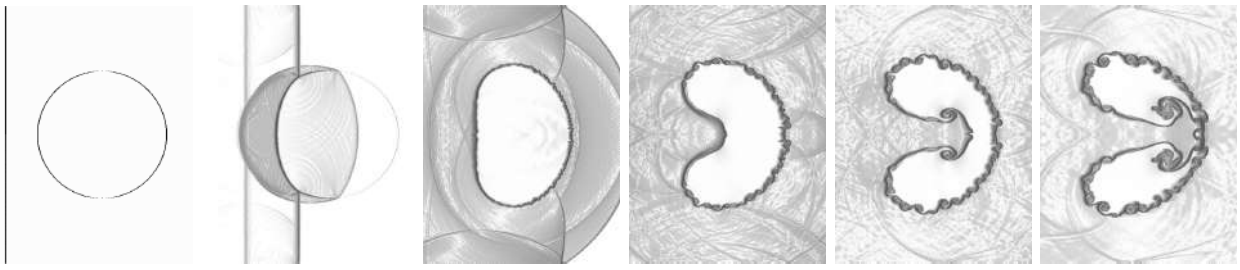

Figure 3: Résultats numériques calculés sur 4000×400 nœuds, dt=2,5 $\times$ 10^{-9} s, HLLC Hancock WENO5-IS.

L'étude de la convergence du maillage des schémas a été réalisée sur la composante de pression maximale calculée au temps final t_{final}=0,05 μs avec CFL=0,3 en utilisant les méthodes de reconstruction MUSCL, WENO3-Z, PPM et WENO5-IS. L'évolution de la pression maximale atteinte au cours du processus est représentée sur la figure 4.20 (partie gauche). La solution de la

pression maximale présente trois pics principaux. Le premier, d'une valeur approximative de 1,8 bar, se produit au temps 0,3 μs. Tous les schémas ont conduit à des valeurs de pression similaires. Le deuxième pic, le plus élevé, de 2,2 bar, se produit au temps 1,2 μs, qui a été correctement reconstruit par tous les schémas avec la formulation HLLC et a été retardé et lissé en utilisant la formulation KNP. Enfin, le troisième pic de 1,9 bar en deux parties se produisant à des moments compris entre 2,9 et 3,5 μs a été légèrement diminué en intensité en utilisant la reconstruction PPM avec la formulation HLLC et décalé dans le temps et sans l'intensité exacte en utilisant la formulation KNP.

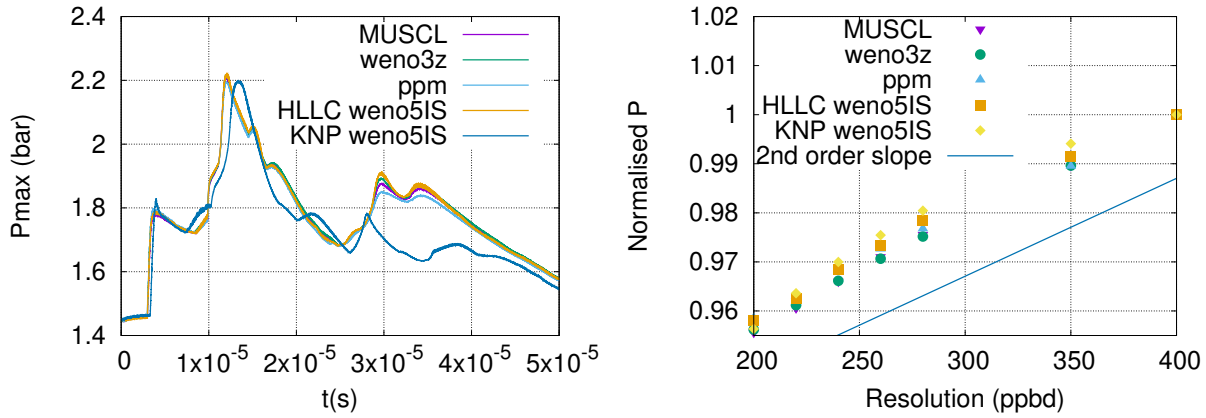

Figure 4: Interaction choc-bulle air-hélium, comparaison de la pression maximale, maillage : 4000×400 (gauche), convergence de la pression maximale (droite). CFL=0.3

La valeur de pression normalisée du pic le plus élevé (estimée en utilisant la solution calculée sur le maillage le plus fin de 4000×400 nœuds avec la formulation WENO5-IS) est représentée sur la figure 4.20 (partie droite) en fonction de l'augmentation progressive de la résolution du maillage indiquée par le nombre de points par diamètre de bulle (ppbd). Le pic de pression le plus élevé se produit approximativement au même moment, 0,012 ms, et est obtenu en utilisant le schéma WENO5-IS. La convergence du second ordre approximatif est vérifiée en calculant l'erreur approximative liée à la valeur de pression de la maille la plus fine. Cela confirme la précision numérique des schémas obtenus dans les essais 1D du tube à choc discutés précédemment.

L'étude de validation en 2D a mis en évidence une assez bonne performance de tous les schémas numériques. Le solveur HLLC s'avère plus adapté aux calculs actuels, tandis que la formulation du flux KNP est diffusive. L'effet de la reconstruction d'ordre élevé par rapport à la reconstruction MUSCL de second ordre est illustré. Les formulations standard de WENO3-JS et WENO5-JS sont plus diffusives que leurs équivalents modifiés, par exemple WENO3-Z et WENO5-SZ,IS. La variation entre la reconstruction primitive et la reconstruction caractéristique est négligeable, la reconstruction primitive est donc préférée en raison de sa dérivation et de sa mise en œuvre plus simples.

L'objectif du processus de validation a été fixé pour définir les performances des schémas sur la base de différents problèmes. Trois problèmes en 1D (problèmes de tube-choc et de deux tubes d'expansion) et un problème en 2D (interaction air-hélium choc-bulle) ont été définis comme des tests appropriés pour examiner la réponse des schémas numériques aux phénomènes de chocs, de discontinuités de contact et d'ondes d'expansion. Les problèmes ont été testés dans l'ordre hiérarchique du plus facile au plus difficile en 1D : tube-choc, tube d'expansion à faible vitesse, tube d'expansion à grande vitesse. La conclusion suivante peut être tirée :

- **Ordre de précision.** Bien que les schémas numériques présentés dans cette thèse aient un ordre de précision formel élevé, cet ordre ne peut être atteint lorsque des discontinuités dans la solution sont présentes. Ceci a été observé dans la littérature et a été validé dans notre étude du taux de convergence en utilisant le problème du tube de choc et une solution de référence approximative. La précision moyenne du second ordre est estimée pour tous les schémas considérés.

- **Flux formulation.** Le choix de la formulation du flux est crucial car nous avons calculé des cas plus complexes. Ainsi, alors que le problème du tube de choc n'a pas illustré de différences dans la solution, des divergences apparaissent dans le profil de pression pour le tube d'expansion. De plus, la solution obtenue avec le schéma KNP pour l'interaction choc-bulle en 2D est fortement diffusive. Par conséquent, nous pensons qu'à cet égard, le solveur HLLC est préférable.

- **Variables de reconstruction.** L'effet des variables de reconstruction n'a pas été démontré comme étant important. Bien que plusieurs schémas répondent mieux aux variables caractéristiques (PPM en particulier), nous avons remarqué que les schémas généralement stables, tels que WENO5-IS, WENO3-Z, WENO3-P ont une solution similaire avec des variables primitives et caractéristiques. Globalement, la reconstruction à l'aide de variables primitives est plus simple en termes de dérivation analytique et de mise en œuvre. Il est donc logique de choisir les schémas où le choix des variables n'est pas crucial. Néanmoins, d'après nos tests, la méthode PPM devrait être utilisée avec des variables caractéristiques.

- **Reconstruction d'ordre élevé.** Nous avons testé une variété de schémas numériques d'ordre élevé et plusieurs méthodes ont démontré de meilleurs résultats globaux dans tous les problèmes considérés. Ces schémas sont les suivants : WENO5-IS, WENO3-Z, WENO3-P. La méthode PPM fonctionne bien avec la reconstruction caractéristique et peut être utilisée de cette manière. La méthode MP5 oscille dans tous les problèmes. Le schéma MUSCL est toujours stable mais présente beaucoup moins de détails dans la reconstruction, selon notre évaluation qualitative.

Chapitre 5. 2D Effondrement des bulles induit par un choc

Ce chapitre traite du problème de l'effondrement d'une bulle induit par un choc liquide-gaz. Deux problèmes sont proposés : premièrement, l'effondrement de la bulle en champ libre et, deuxièmement, le problème similaire à proximité d'une paroi (qui peut conduire à l'érosion du matériau solide).

L'objectif de ce chapitre est d'établir l'effet des schémas numériques d'ordre élevé sur la reconstruction de la solution. Plus précisément, les solutions de la pression maximale à l'intérieur du fluide P_{max} dans le cas de l'effondrement d'une bulle dans un champ libre et, en outre, de la pression maximale près de la paroi $Pwall_{max}$ dans le cas de l'effondrement d'une bulle près d'une paroi sont examinées du point de vue de la reconstruction globale précise et, plus important encore, de la récupération précise des pics de pression. L'étude de la convergence des pics d'intensité de pression est présentée. L'examen qualitatif des contours des gradients de densité est proposé. Nous visons à quantifier l'impact des schémas numériques sur les solutions et à tirer une conclusion préliminaire pour des calculs 3D supplémentaires.

Le premier test est basé sur celui présenté dans Bourne & Field (1992) et calculé par divers auteurs (par exemple Nourgaliev *et al.* (2006)). Une bulle d'air de diamètre 6 mm, immergée dans l'eau au repos, est impactée par une onde de choc normale pour laquelle le nombre de Mach M_{sh}=1.7. Les conditions physiques sont initialisées comme suit : $P = 10^5$ Pa, $\rho_{air} = 1$ kg/m^3 et ρ_{eau} 1000 kg/m^3. Seule une moitié de la bulle est considérée en raison de la symétrie du problème. Les frontières supérieure et inférieure du domaine sont définies comme des parois de glissement, tandis que les frontières gauche et droite sont soumises à des conditions de non-réflexion. Les calculs sont effectués avec une discrétisation spatiale de 2000×1000 nœuds en utilisant soit un pas de temps fixe $dt = 10^{-9}$ s, soit un nombre fixe de LFC. Les paramètres EOS et la condition post-choc sont indiqués dans le tableau 5.1.

Table 3: Paramètres EOS eau-air et conditions post-chocs

	γ	P_∞	C_p
air	1.4	0 Pa	4180 J/K.kg
water	4.4	6×10^8 Pa	1487 J/K.kg
	P	ρ	u
post-shock	1.9×10^9 Pa	1323.65 kg/m^3	681.58 m/s

Tout d'abord, une description des principaux phénomènes physiques est proposée dans la Figure 5.1 où sont tracés le module du gradient de densité (en haut du graphique) et le champ de pression (en bas du graphique) obtenus à l'aide du schéma WENO5-IS. La collision du choc avec la bulle provoque la réflexion d'une forte onde de raréfaction dans la direction arrière et la pénétration d'une faible onde de choc dans la bulle (au temps t=2 μs). La différence de pression entraîne une déformation de la bulle qui prend la forme d'un rein (au moment t=3 μs). Cette forme particulière est le résultat de la vorticité qui se produit au bord de la bulle en raison du jet d'eau provoqué par le passage de l'onde de choc. La zone de haute pression est générée lorsque ce jet d'eau frappe l'eau stagnante devant la bulle, provoquant l'émission d'une forte onde de choc (temps $t = 4$ μs). De plus, la poursuite de la propagation du jet d'eau et sa vitesse élevée entraînent une expansion asymétrique du front de souffle. Enfin, une zone de haute pression est générée au moment t=4,8 μs en raison de la recollapse des morceaux de bulles par le front gauche de l'onde de souffle. Alors que l'onde de souffle continue de s'étendre, la cavité se rétrécit et les champs de basse pression sont observés au cœur des tourbillons.

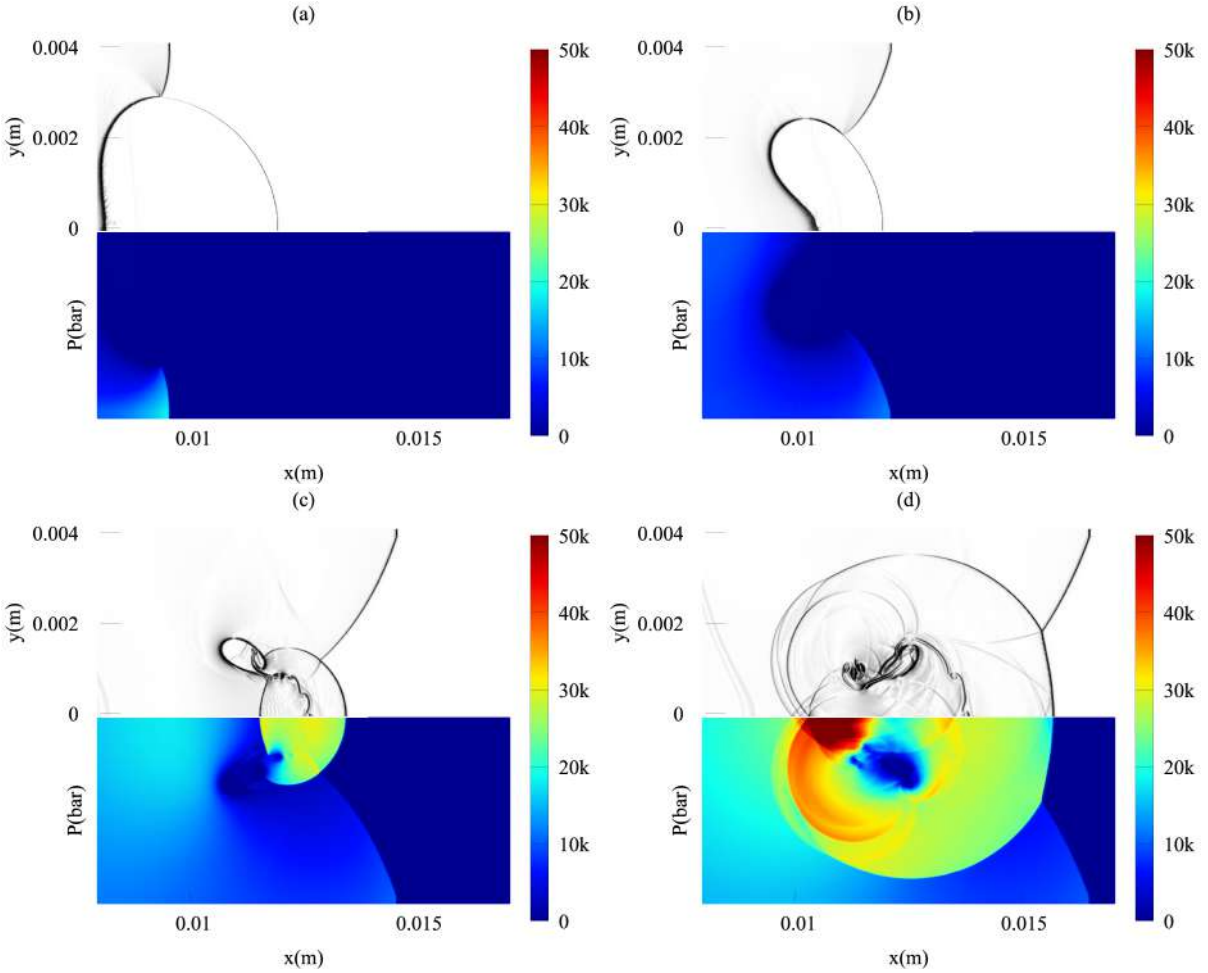

Figure 5: Évolution du temps d'effondrement des bulles, (a) 2 μs, (b) 3 μs, (c) 4 μs, (d) 4.8 μs, HLLC Hancock WENO5-IS, maillage 2000 × 1000, CFL=0.3.

Le temps et l'intensité des pics de pression maximale atteints pendant l'effondrement sont analysés. La convergence du maillage est attestée par l'évolution du pic de pression le plus élevé. La figure 5.2 (gauche) présente l'évolution de la pression maximale où trois pics principaux sont observés (voir tableau 5.2). Le premier pic se produit à environ 3,6 μs en raison de la génération de l'onde de choc et les valeurs les plus élevées sont obtenues en utilisant WENO3-Z et WENO5-IS, c'est-à-dire 50,600 bar et 50,700 bar respectivement. Le deuxième pic se produit au moment approximatif de 4,4 μs en raison de la génération d'une autre forte onde de choc dans le liquide lorsque le choc du gaz expulsé se concentre sur le point le plus en amont de la bulle. Enfin, le troisième pic, le plus fort, est observé à un moment approximatif de 4,7-4,8 μs et est dû à la recollapse des fragments de la bulle. Ce pic présente le plus de déviations en solution. La méthode PPM donne lieu à la plus forte intensité de pic, autour de 98 000 bar, qui est presque 10% plus élevée que les deux autres schémas. La différence entre les intensités de pression obtenues par WENO3-Z et WENO5-IS à ce pic est d'environ 3 000 bar, la valeur la plus élevée étant calculée en utilisant WENO5-IS. Cela correspond à une différence d'environ 3%. Une variation similaire de la solution a été notée en utilisant la méthode MUSCL qui a conduit à une intensité de pression inférieure d'environ 3%.

Table 4: Effondrement des bulles induit par un choc, comparaison des pics de pression maximale P_{max}.

Water-air shock-bubble, Pmax (bar)						
Scheme	t1	P1	t2	P2	t3	P3
MUSCL	3.6μs	49,900	4.4μs	58,100	4.8μs	86,600
WENO3-Z	3.6μs	50,600	4.4μs	59,600	4.8μs	86,300
PPM	3.7μs	51,506	4.39μs	65,950	4.7μs	97,930
WENO5-IS	3.6μs	50,700	4.4μs	67,300	4.8μs	89,300

La convergence des schémas est étudiée en affinant le maillage et en examinant l'intensité du troisième pic de pression. La figure 5.2 (droite) présente la convergence en utilisant la reconstruction MUSCL de second ordre et les méthodes d'ordre supérieur, WENO3-Z et WENO5-IS. Les valeurs ont été normalisées par la valeur de pression obtenue sur le maillage le plus fin, c'est-à-dire 2000×1000 nœuds. Les calculs ont été effectués en utilisant la valeur fixe CFL=0.1 qui a été choisie sur la base des études préliminaires de l'effet CFL. La nature oscillante de la solution est notée dans tous les schémas, ce qui rend problématique l'étude de la convergence numérique. C'est particulièrement le cas pour le schéma PPM qui a conduit au résultat le plus oscillant. Ainsi, afin d'effectuer une étude de convergence approximative, le filtre de Savitsky-Golay de quatrième ordre avec 100 points est utilisé pour lisser les données : Savitzky & Golay (1964). La reconstruction PPM n'est pas incluse dans cette analyse en raison des fortes oscillations. La meilleure convergence des schémas d'ordre supérieur WENO3-Z et WENO5-IS est notée par rapport au schéma MUSCL de second ordre, où une légère divergence est observée. La solution indépendante du maillage est obtenue à environ 500 points par diamètre de bulle, ce qui correspond à un maillage de 2000×1000 nœuds.

Le problème de l'effondrement d'une bulle de choc dans un champ libre est caractérisé par un saut de pression important au moment de la recollapse des fragments de la bulle. On s'attend à ce que les schémas numériques d'ordre élevé soient capables de récupérer la valeur d'une telle intensité de pression avec plus de précision que les méthodes MUSCL. De plus, la complexité des phénomènes physiques impliqués dans ce problème ne peut être reconstituée qu'en utilisant un maillage très fin pendant les calculs. Les résultats présentés dans cette section ont illustré un effet de la reconstruction d'ordre élevé. En effet, les solutions obtenues en utilisant WENO3-Z et WENO5-IS ont une meilleure précision par rapport au schéma MUSCL en utilisant le même maillage. La méthode PPM présente une variation qui n'est pas observée avec les autres schémas. Le pic de pression le plus élevé et son intensité pourraient être le résultat de la nature oscillante de la méthode.

Le deuxième test a été proposé par Paquette Paquette *et al.* (2018) pour étudier les dommages potentiels aux murs dus à l'effondrement des bulles. Une paroi est placée derrière la bulle. Une onde de choc normale initialement située à 0,1 mm se déplace avec un nombre de Mach M_{sh}=1,09 provoquant l'effondrement de la bulle. Les paramètres EOS restent les mêmes et les conditions

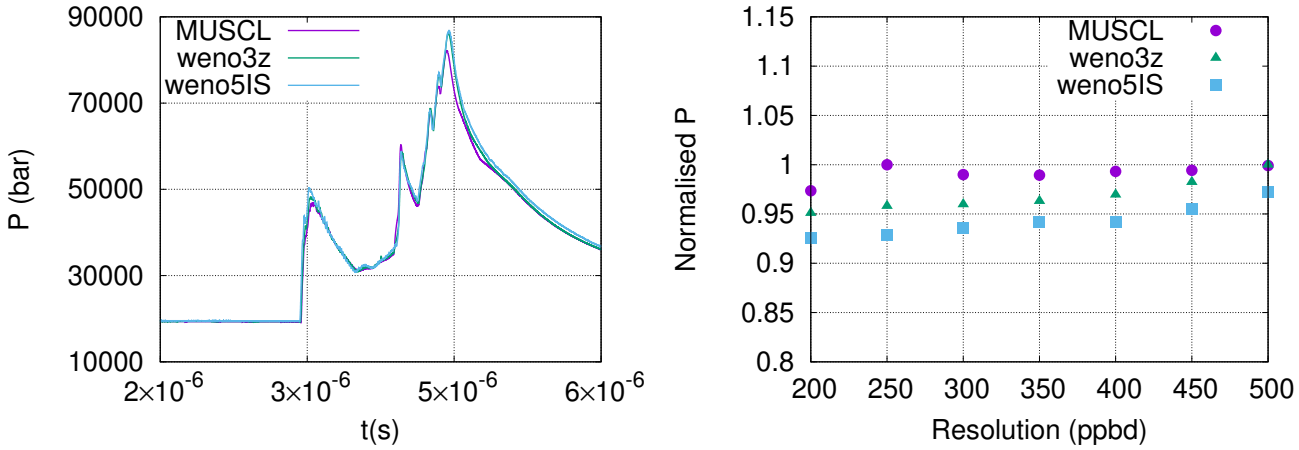

Figure 6: Effondrement des bulles induit par un choc, pression maximale filtrée par la méthode de Savitsky-Golay, maillage 2000 × 1000 (gauche), convergence du troisième pic de pression (droite), CFL=0.1.

post-choc sont indiquées ci-dessous:

$$\begin{pmatrix} P \\ \rho \\ u \end{pmatrix}_{post-shock} = \begin{pmatrix} 1.2 \times 10^8 \text{ Pa} \\ 1049 \text{ kg/m}^3 \\ 75 \text{ m/s} \end{pmatrix} \tag{11}$$

Le domaine de calcul est d'une taille de 0,3×0,5 mm et le diamètre initial de la bulle est de 0,1 mm avec son emplacement initial à (0,2,0) mm. Le rapport L/R_0 entre la position du centre de la bulle par rapport à la paroi et le rayon initial de la bulle est un paramètre majeur qui régit la dynamique d'effondrement de la bulle. Comme le suggère l'étude de Johnsen et Colonius Johnsen & Colonius (2009), la bulle initialement située à une distance inférieure à $L/R_0 = 2$ présente un potentiel élevé de causer des dommages. Nous considérons dans cette section uniquement le cas où le rapport $L/R_0 = 2$.

Les calculs sont effectués avec CFL=0.1 et 650 points par diamètre de bulle, ce qui correspond à une discrétisation spatiale de 1908×3180 nœuds. Les solutions sont obtenues en utilisant MUSCL, WENO3-Z, WENO3-P, PPM et WENO5-IS.

La convergence du maillage est vérifiée sur l'évolution des pics de pression maximale à partir des solutions obtenues avec MUSCL, WENO3-Z et WENO5-IS. Le maillage est compris entre 750×1250 et 1908×3180 (250 à 650 points par diamètre de bulle). Trois pics principaux sont observés dans la solution de pression. Le premier, de plus faible intensité, se produit au temps 0,13 μs et est dû à l'impact de l'onde de choc incidente sur la paroi. La deuxième est observée au temps 0,28 μs et résulte de l'impact de l'onde de choc générée sur le mur. La troisième, au temps 0,36 μs, est causée par l'impact d'une onde secondaire émise par la recollapse de la bulle. Tous les schémas numériques conduisent à des temps approximativement similaires pour ces pics. L'intensité du pic en fonction du schéma numérique employé est présentée dans le tableau 5.3. Les tests ont montré la convergence de tous les schémas avec une solution indépendante du maillage obtenue en utilisant 500 points par diamètre de bulle. Cependant, la forte dépendance du troisième pic de pression par rapport au nombre de LFC a été établie. Les premier et deuxième pics de pression convergent plus rapidement même avec des nombres CFL plus élevés.

Table 5: Effondrement d'une bulle près d'une paroi, comparaison des pics de pression maximale P_{max}.

Water-air shock-bubble with a wall, maximum pressure P_{max} (bar)						
Scheme	t_1	P_1	t_2	P_2	t_3	P_3
MUSCL	0.13μs	2,573	0.28μs	9,444	0.36μs	8,829
weno3-Z	0.13μs	2,565	0.28μs	9,453	0.36μs	8,938
weno3-P	0.13μs	2,565	0.28μs	9,440	0.36μs	9,158
PPM	0.13μs	2,553	0.28μs	9,449	0.36μs	9,070
weno5-IS	0.13μs	2,563	0.28μs	9,456	0.35μs	9,138

Le troisième pic de pression le plus élevé a été obtenu en calculant la solution avec les schémas d'ordre supérieur, c'est-à-dire WENO5-IS, PPM et WENO3-P, tandis que les premier et deuxième pics de pression ne présentent qu'une légère différence due au schéma numérique. Les figures 5.5 et 5.6 présentent la convergence du maillage des schémas MUSCL, WENO3-Z et WENO5-IS.

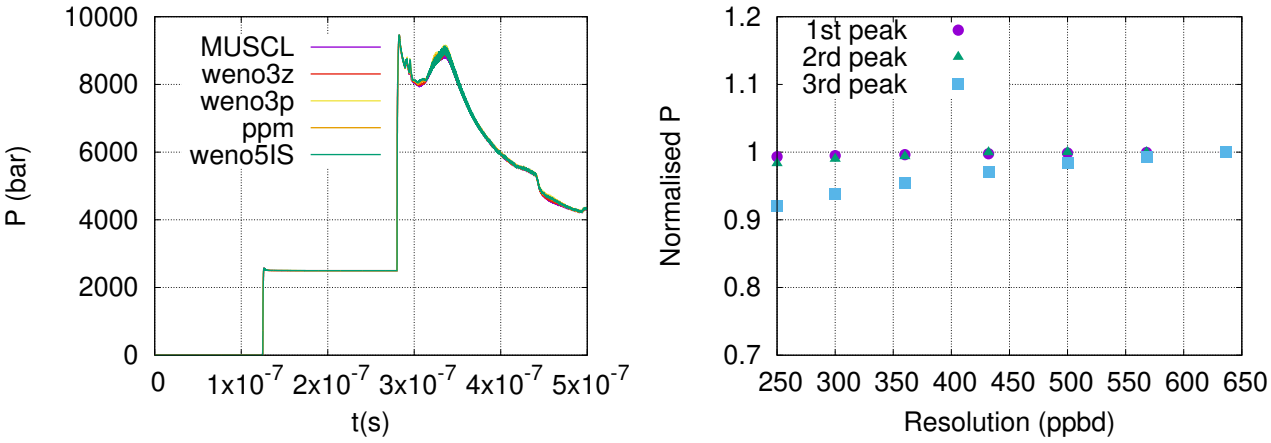

Figure 7: Effondrement de la bulle près d'une paroi, pression maximale de la paroi obtenue avec le maillage 1908 × 3180 nœuds, CFL=0.1 (à gauche), convergence des pics de pression maximale P_{max} obtenus avec MUSCL, CFL=0.1 (right).

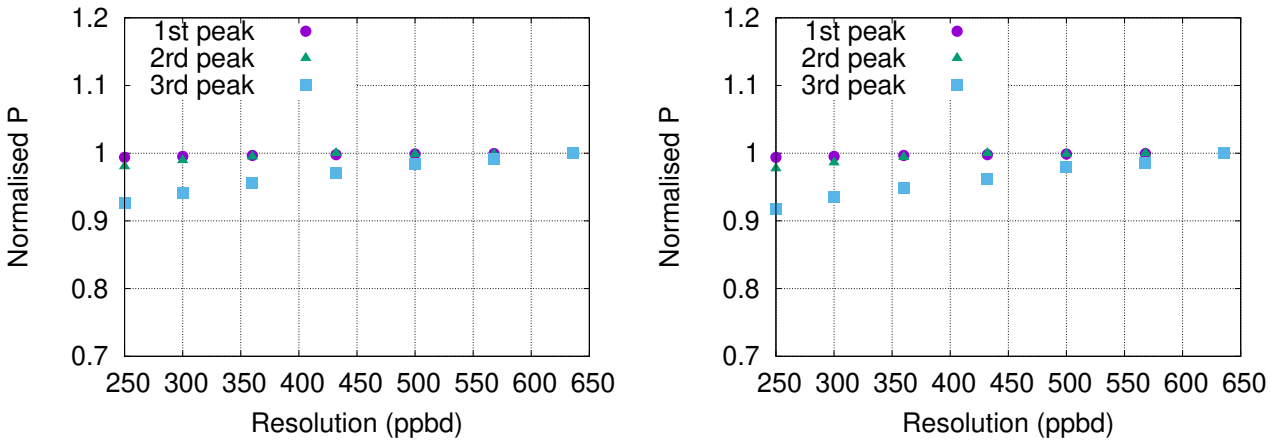

Figure 8: Effondrement des bulles près d'une paroi, convergence des pics de pression maximaux P_{max}, CFL=0.1, WENO3-Z (gauche), WENO5-IS (droit).

Le temps de calcul des solutions obtenues en utilisant les principaux schémas numériques (à savoir MUSCL, WENO3-Z, WENO5-IS) est indiqué dans le tableau 5.4. Le coût a augmenté de 40% entre les schémas MUSCL et WENO5-IS. Ce coût de calcul est critique pour les calculs à haute résolution et, en particulier, pour les problèmes 3D.

Table 6: Coût du CPU, effondrement de la bulle près d'un mur. Maillage: 1908×3180. CFL=0.1.

Scheme	CPU (h)	ratio
MUSCL	94.7	1
WENO3-Z	121.6	1.28
WENO5-IS	133.7	1.41

L'objectif de ce chapitre est de définir l'effet des schémas numériques d'ordre élevé et de définir

une stratégie pour les calculs 3D ultérieurs. Deux tests ont été effectués: l'effondrement d'une bulle de choc dans un champ libre et à proximité d'un mur.

La réponse des schémas numériques au grand saut de pression généré par la recollapse des fragments de bulles dans le premier cas a été observée. En effet, une reconstruction supérieure de l'intensité de la pression a été observée en utilisant les schémas WENO5-IS et WENO3-Z par rapport à la reconstruction MUSCL de second ordre. En outre, l'examen qualitatif du gradient de densité a mis en évidence une solution plus détaillée. La méthode PPM, bien que conduisant à la valeur d'intensité de pression la plus élevée, est considérée comme moins précise et ces valeurs sont dues à la nature oscillante.

Les résultats obtenus à partir des calculs de l'effondrement des bulles près d'un mur ont montré une tendance similaire. Les résultats les plus précis ont été obtenus en utilisant le schéma WENO5-IS. La solution a été considérablement améliorée par rapport à la technique MUSCL de second ordre.

L'objectif de ce chapitre était cependant en partie de quantifier les résultats des schémas numériques d'ordre élevé. Les calculs d'une solution de référence n'étant pas réalisables, cette quantification est basée uniquement sur deux éléments: l'ampleur des pics de pression et le coût de calcul. La première partie est de savoir combien d'intensité de pression supplémentaire a été récupérée en utilisant des schémas d'ordre élevé. La seconde partie est la quantité de puissance de calcul supplémentaire utilisée pour obtenir ce gain.

Il est intéressant de noter qu'en examinant uniquement les composantes de pression maximale de la solution (pression maximale à côté d'une paroi dans le cas d'un effondrement de bulle à proximité d'une paroi), nous n'observons pas une énorme différence. En particulier, une amélioration de seulement 3% est notée en utilisant WENO5-IS pour le premier problème. D'autre part, l'effondrement d'une bulle à côté d'un mur illustre des valeurs d'intensité de pression très similaires par toutes les méthodes. Par conséquent, la plupart des conclusions peuvent être tirées d'observations qualitatives.

Bien que ces observations mènent effectivement à la conclusion de meilleurs résultats obtenus avec les schémas WENO5-IS et WENO3-Z, l'évaluation de la solution numérique n'est pas complète sans la comparaison du coût du CPU. En effet, une augmentation du coût du CPU est présente lorsque l'ordre de la méthode s'améliore, en particulier en raison de l'augmentation de la taille du stencil de calcul. Le coût a été augmenté de 40% en utilisant le schéma WENO5-IS par rapport à la simulation MUSCL. Ce coût est acceptable dans les cas 2D mais devient critique pour les configurations 3D. Par conséquent, un développement ultérieur important consiste à examiner les stratégies potentielles pour réduire ce coût de CPU.

Chapitre 6. Maillage non homogene

Le coût de calcul élevé des problèmes actuellement considérés, dû à la combinaison de la nécessité d'un grand nombre de points par diamètre de bulle et de la taille du stencil de calcul, conduit à envisager des stratégies possibles pour réduire soit le nombre de points, soit le CPU, soit les deux avec une perte de précision minimale. La réduction de l'unité centrale peut être obtenue en utilisant diverses techniques de parallélisation. Cependant, afin de réaliser des calculs 3D de haute fidélité qui nécessitent des grilles très fines, le coût de calcul devient prohibitif même avec des solveurs parallèles. Par conséquent, la réduction des points de maillage est nécessaire.

L'une des solutions possibles à ce problème est l'introduction d'un maillage non uniforme. On peut observer que la bulle n'occupe pas la totalité du domaine de calcul et, selon le problème considéré, la zone du maillage uniforme peut être définie autour de l'emplacement de la bulle. En d'autres termes, le nombre de points par diamètre de bulle sera identique à celui du problème initialement résolu, tandis qu'en dehors de cette zone, la taille des cellules sera progressivement augmentée jusqu'à la limite du domaine.

La deuxième solution, qui est quelque peu liée à la première, consiste en une augmentation continue de la taille des cellules à partir d'un point arbitraire donné à l'intérieur du domaine de calcul, le milieu de la bulle, par exemple.

L'hypothèse testée ici est de déterminer si oui ou non le coût du CPU peut être réduit en gardant constant le nombre de points par diamètre de bulle et en réduisant le nombre de points à

l'extérieur de la bulle sans réduction conséquente de la précision.

L'émergence des grilles non-uniformes peut être liée principalement à la nécessité de résoudre les équations aux dérivées partielles sur une géométrie arbitraire des domaines de calcul. Il s'agit d'une exigence particulière pour le problème de la dynamique des fluides computationnelle, d'où proviennent la plupart des développements de ce domaine de recherche. Généralement, ces grilles sont explorées dans les problèmes où les systèmes de coordonnées curvilignes sont nécessaires. Ces problèmes avec introduction de grilles non uniformes ont fait l'objet de nombreuses recherches, en particulier dans le cadre de l'ordre de précision formel de la solution dans le cas de grilles non uniformes. Par exemple, Thompson *et al.* (1985) a réalisé une étude analytique approfondie sur les variations de précision en utilisant deux stratégies différentes de grille non-uniforme : fonction de distribution fixe et nombre de points fixe. De plus, l'évaluation des fonctions de distribution a été effectuée, le résultat pouvant être étendu à d'autres systèmes où les mailles non-uniformes pourraient être utilisées. Dix fonctions de distribution ont été considérées, dont la fonction exponentielle, le sinus hyperbolique et la tangente, etc. Les conclusions concernant la fonction de distribution la plus appropriée pour des problèmes particuliers ont été tirées.

Une stratégie alternative pour la génération de maillage non-uniforme est l'introduction du maillage adaptatif où le groupe de points est généré dans certaines zones critiques de la solution. Cette méthode est divisée en deux classes principales. La première classe de raffinement est la redistribution adaptative du maillage ou ce qu'on appelle le p-refinement Chung (2002). L'idée du p-refinement est de repositionner continuellement un nombre fixe de cellules pour améliorer localement la précision de la solution. Bien que ce type de raffinement soit assez facile à mettre en œuvre, il n'y a aucune possibilité de modifier la topologie dans le cas de discontinuités. Cela peut conduire à une distorsion de la grille. La deuxième classe de raffinement adaptatif est le h-refinement ou communément appelé AMR Berger & Joseph (1984), où les groupes de points sont continuellement modifiés par l'ajout et la suppression de cellules. L'avantage de cette méthode est la possibilité de l'utiliser dans de nombreux problèmes où les grands gradients localisés sont présents, par exemple les problèmes avec des discontinuités, des chocs et des changements de phase. Cependant, cette méthode est considérablement plus complexe en termes d'implémentation et de parallélisation. Certaines des difficultés potentielles dans la programmation séquentielle de cette méthode incluent la définition du critère de raffinement, les contraintes de raffinement et son ordre.

Les grilles structurées non uniformes plus simples peuvent être mises en œuvre pour les problèmes dont les solutions présentent une zone de variation localisée. Les fonctions appropriées pour générer de telles grilles ont été analysées en termes d'erreur de troncature par Vinokur (1980). Ces fonctions sont destinées à être utilisées lorsque la réduction des points avec une précision conservée de la solution est requise et appliquée de manière à ce que les points se regroupent autour des régions où la solution varie le plus. En réalité, ces régions sont souvent inconnues et complexes. De plus, certains problèmes peuvent avoir une solution avec plusieurs régions de ce type qui changent avec les itérations temporelles. Ainsi, le système de génération de grille parfait est un système adaptatif, qui régénère la grille aussi souvent que nécessaire en fonction de la physique du problème considéré. Ce type de grilles a été considéré dans le contexte des méthodes de différences finies avec des problèmes unidimensionnels, par exemple dans Pierson & Kutler (1980) et Gough *et al.* (1975). Cependant, pour utiliser ces grilles dans un espace multidimensionnel, des développements supplémentaires sont nécessaires en raison de la géométrie généralement difficile des régions groupées.

Dans la pratique, certains problèmes peuvent être évalués à l'avance en termes de régions où le clustering est nécessaire. En particulier, cette estimation peut être basée sur la topologie bien prévisible du problème, des configurations simples de l'onde de choc, etc. Souvent, de tels problèmes sont basés sur le problème des valeurs limites elliptiques et l'étude du clustering pour ce type de cas a été étudiée dans Middlecoff & Thomas (1979) et Thompson *et al.* (1977). Le regroupement aux frontières peut être établi en utilisant des systèmes algébriques avec des fonctions unidimensionnelles, normalement appelées fonctions d'étirement. De tels systèmes algébriques sont discutés en détail dans Thompson (1983) et Thompson *et al.* (1985). En supposant une géométrie simple, le regroupement peut être obtenu en utilisant uniquement des systèmes algébriques avec une fonction d'étirement unidimensionnelle.

Plusieurs types de fonctions d'étirement sont disponibles pour travailler avec des problèmes où la géométrie de la zone à solution très variable peut être prédéfinie. La fonction d'étirement

unidimensionnelle la plus simple n'implique que deux paramètres. Par exemple, une fonction d'étirement intérieur nécessiterait le point de localisation dans le domaine de calcul, où la fonction est initialisée, et la valeur de l'espacement qui est prise comme première valeur minimale pour la pente. D'autre part, pour une fonction d'étirement bilatérale, ces deux paramètres sont les valeurs de la pente aux deux extrémités de la distribution. Une autre fonction d'étirement peut avoir une nature asymétrique, où les pentes aux deux extrémités sont égales et construite en utilisant deux fonctions d'étirement unilatérales. De plus, la fonction d'étirement intérieur peut être utilisée pour construire une fonction unilatérale où le regroupement est défini à l'une ou l'autre des extrémités.

Différentes distributions sont utilisées pour construire ces fonctions d'étirement. L'étude de Thompson (1972) a exploré la fonction de distribution sinus hyperbolique inverse pour les calculs numériques dans le cadre d'un écoulement supersonique inviscide sur une aile delta émoussée. Les points ont été regroupés sur le corps de l'aile en employant la fonction unilatérale. La fonction logarithmique de classe antisymétrique à deux côtés est utilisée dans l'étude de Roberts (1971) pour le type de limite du problème. Cependant, comme indiqué dans Vinokur (1983), la dérivation d'une telle fonction ignorait les erreurs de troncature et, même si une telle fonction pouvait être utilisée dans certains problèmes d'écoulement, il y a une forte motivation pour développer une fonction d'étirement bilatérale qui permettrait un étirement arbitraire à l'une ou l'autre des extrémités de la fonction indépendamment l'une de l'autre.

Ce chapitre explore les deux classes de fonctions d'étirement. La première est une fonction d'étirement unilatérale basée sur des distributions de sinus ou de tangente hyperboliques. La seconde est une fonction d'étirement intérieur basée sur le sinus hyperbolique. La discussion des raisons de ces deux fonctions est proposée et la construction de ces fonctions est discutée. En outre, la dérivation des schémas numériques d'ordre supérieur tels que PPM, WENO5 et WENO3 pour le maillage non uniforme est discutée. Enfin, la validation de ces techniques est effectuée sur le problème de bulle de choc air-hélium et l'implémentation est ensuite étendue à l'effondrement de la bulle avec et sans paroi. Les stratégies de clustering pour chaque problème considéré sont proposées.

Les fonctions d'étirement utilisées pour la génération de maillage non-uniforme peuvent être basées sur une variété de distributions. Une évaluation des fonctions de distribution a été présentée par Thompson *et al.* (1985) sur la base des mesures de l'ordre. Les fonctions de distribution qui conviennent à un très petit espacement ont été déterminées.

Les conclusions suivantes ont été tirées sur la base de l'analyse présentée par les auteurs:

1. Même si la fonction exponentielle est proche de la fonction tangente hyperbolique en termes de régularité, la conclusion finale est que la fonction exponentielle n'est pas aussi bonne. Par conséquent, la fonction hyperbolique est préférable.

2. La comparaison entre la tangente hyperbolique et le sinus hyperbolique a montré que le sinus hyperbolique convient mieux aux frontières où l'espacement initial est spécifié. Cependant, en considérant les autres critères, la tangente hyperbolique est globalement meilleure.

3. considérant l'adéquation des fonctions à l'intérieur et à l'extérieur des couches limites, l'erreur et la tangente hyperbolique sont les plus appropriées. La fonction tangente hyperbolique est meilleure à l'intérieur et la fonction erreur est meilleure à l'extérieur de la couche limite.

4. les autres fonctions, c'est-à-dire le sinus, la tangente, l'arc-tangente, la tangente hyperbolique inverse et les fonctions sinus, quadratique et logarithme ne sont pas adaptées à la grille d'étirement.

Chapitre 7. Calculs en 2D sur un maillage non homogene

Le problème de l'étirement des mailles n'est pas arbitraire. Si le choix de la fonction d'étirement est une étape importante, la décision d'application d'une telle fonction est cruciale. Par exemple, la fonction d'étirement bilatéral permet de concentrer davantage de points du maillage sur les limites du domaine, tandis que la fonction d'étirement à partir d'un point intérieur localise un plus grand nombre de points autour de l'emplacement initial de la fonction. Ces deux exemples peuvent

être appliqués à des problèmes différents : le premier convient aux problèmes de frontières, par exemple, tandis que le second fonctionnerait pour les problèmes où la zone d'intérêt se trouve à l'intérieur du domaine de calcul.

Ce deuxième exemple d'utilisation de la fonction d'étirement du maillage peut également être résolu par la fonction d'étirement unilatéral en définissant la zone d'intérêt comme un bloc de maillage uniforme. Dans ce cas, deux fonctions unilatérales doivent être utilisées, en supposant que le bloc de maillage uniforme est situé dans une zone interne arbitraire du domaine de calcul. Autrement dit, une fonction est générée pour s'étirer à gauche du bloc de maillage uniforme et une autre à droite. Cette stratégie est une alternative à l'utilisation de la fonction partant du point intérieur et pourrait améliorer la précision à l'intérieur de la zone d'intérêt, puisque cette zone est uniformément maillée. Cette façon d'introduire l'étirement du maillage pourrait être intéressante pour les problèmes où la zone d'intérêt est relativement petite par rapport à l'ensemble du domaine de calcul.

Ces deux points de considération lors de la mise en œuvre du domaine de calcul avec étirement du maillage doivent être combinés et la décision dépend fortement du problème. L'une des questions initiales évidentes est de savoir comment choisir un emplacement approprié du bloc de maillage uniforme ou du point intérieur à partir duquel la fonction d'étirement sera appliquée. La stratégie où deux fonctions unilatérales sont utilisées est relativement simple si la zone d'intérêt a un emplacement constant dans le temps. Cependant, si le problème consiste en un objet en mouvement, on est confronté à plusieurs choix quant à l'endroit et à la manière de générer les mailles uniformes et non uniformes. Considérons deux cas. Le premier est celui où un certain objet est défini comme zone d'intérêt, situé quelque part à l'intérieur du domaine de calcul (et suffisamment loin des limites) et où il a soit un emplacement et une taille constants, soit se déplace et change très peu de taille. Un tel problème peut être résolu numériquement sur un maillage étiré et la zone où se trouve l'objet est maillée uniformément, tandis que deux fonctions d'étirement unilatéral sont utilisées des deux côtés de la boîte de maillage uniforme. Une autre solution consiste à appliquer une fonction d'étirement bilatérale à partir d'un point intérieur, par exemple un point interne de l'objet. Bien que l'application d'une telle fonction entraîne une perte de précision de la reconstruction de l'objet en raison du changement continu de dx, si le facteur d'étirement est suffisamment petit, l'erreur numérique peut être acceptable.

Considérons maintenant le problème où l'objet se déplace dans le temps et change de taille ou de forme. Plusieurs questions doivent être abordées. En supposant que le maillage étiré est défini uniquement à la première itération, comment la zone d'intérêt doit-elle être traitée? Doit-elle être uniquement la position initiale de l'objet? Doit-elle être la trajectoire complète du déplacement de l'objet ? Cette dernière solution pourrait conduire à une zone uniforme si grande que la signification du maillage étiré s'en trouverait diminuée. Cependant, si seule la position initiale de l'objet est uniformément maillée, certaines informations de reconstruction ne seront-elles pas perdues au moment final de la solution? D'autre part, si le maillage est redéfini avec une certaine fréquence au fur et à mesure que l'objet se déplace dans le temps, cela nécessiterait une méthode supplémentaire de définition de l'interface de l'objet et un coût de calcul supplémentaire dû au nombre plus élevé d'opérations.

Ce chapitre examine trois problèmes d'interaction choc-bulle avec application de l'étirement de maille. Le premier cas, la bulle d'hélium, sert de problème de validation pour appliquer et tester plusieurs fonctions d'étirement de maille. La fonction unilatérale est utilisée des deux côtés de la boîte de maillage uniforme dans la direction X et une autre fonction unilatérale est générée de gauche à droite dans la direction Y. Des tests alternatifs sont effectués avec une fonction d'étirement des points intérieurs dans la direction X. Le deuxième cas, l'effondrement d'une bulle induite par un choc en champ libre, est un exemple parfait lorsque l'objet d'intérêt occupe une grande partie du domaine de calcul, et la fonction d'étirement intérieur est testée plus avant en utilisant ce problème. Enfin, les calculs de l'effondrement d'une bulle induit par un choc à proximité d'un mur sont effectués. La stratégie particulière d'étirement du maillage pour ce cas est discutée et les résultats sont présentés. Enfin, le plan pour les calculs 3D avec étirement du maillage pour le problème précédent est dessiné. Sauf indication contraire, le solveur de Riemann HLLC avec reconstruction WENO5-IS et la méthode de Hancock sont utilisés dans tous les calculs. Ceci est dû à la similarité de l'effet de l'étirement du maillage couplé à différents schémas numériques.

Les stratégies de localisation des fonctions d'étirement ont été discutées et celles adaptées à chaque problème ont été définies. L'analyse du coût du CPU a été proposée.

Finalement, un maillage non-uniforme approprié a été introduit pour le problème de l'effondrement de bulles induit par un choc à proximité d'un mur. Nous avons défini un endroit approprié du domaine où la solution varie le plus et avons utilisé un espacement uniforme fin dans cette région. Cet espacement de maillage a ensuite été utilisé comme valeur initiale pour créer un maillage continu s'étendant en dehors de la zone de variation de la solution. Nous avons déterminé le degré d'étirement qui est nécessaire pour atteindre le coût CPU requis. En outre, les méthodes hybrides ont été mises en œuvre et testées comme moyen de réduire davantage le temps de calcul. Dans l'ensemble, la réduction du CPU est proportionnelle à la réduction du nombre de points dans le domaine de calcul et nous avons réussi à accélérer les calculs de cinq fois pour le problème de l'effondrement d'une bulle induit par un choc près d'un mur.

Cependant, la question du coût de la communication se pose lors de l'extension de ces méthodes aux calculs en 3D, où des techniques de parallélisation sont nécessaires. Il faut alors trouver un compromis entre la plus grande précision de la méthode et un temps de calcul acceptable. Par exemple, la différence de CPU entre la méthode de WENO3 et WENO5 est considérable même en 2D, alors que la différence de résultats n'est probablement pas énorme. C'est le cas au moins pour un nombre donné de points dans le domaine de calcul, ce que nos ressources informatiques nous permettent de faire. Par conséquent, il faut se demander si la méthode d'ordre 3 n'est pas plus appropriée en termes de complexité qu'une méthode d'ordre 5. Une évaluation similaire doit être faite concernant l'approche hybride dont la complexité est également augmentée par l'introduction de deux méthodes ensemble. Ces questions seront partiellement clarifiées dans le prochain chapitre.

Chapitre 8. Calculs 3D sur maillage non homogene

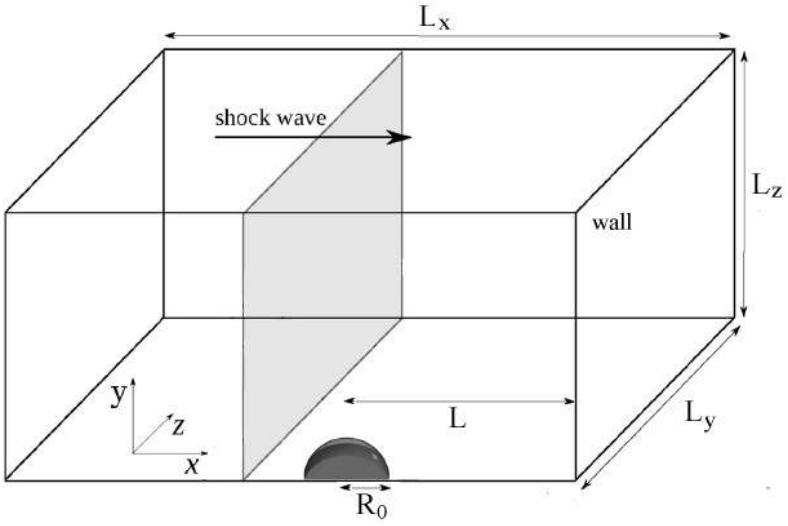

Figure 9: Configuration au condition initiale, P_{sh}=1200 bar

Ce chapitre traite de l'extension aux calculs 3D des méthodes numériques d'ordre élevé et des techniques d'étirement de maillage examinées précédemment. En raison de la complexité de la mise en œuvre des méthodes d'ordre élevé sur un maillage non uniforme, seule la méthode WENO3-Z est considérée pour le moment. Deux cas d'essai sont présentés.

Le premier problème est une extension directe de l'effondrement d'une bulle de choc à proximité d'une paroi, détaillé au chapitre 7. En raison des limites des ressources de calcul, les solutions sont obtenues en utilisant le maillage étiré et comparées aux résultats de Goncalves & Parnaudeau (2021) et Dubois *et al.* (2021). La stratégie d'étirement du maillage doit être modifiée pour inclure l'emplacement de l'onde de choc.

Le second problème considère un autre effondrement de bulle induit par un choc près d'un mur avec une valeur plus faible pour P_{sh} pour lequel le calcul haute-fidélité a été effectué Wermelinger

et al. (2018). Les calculs sont effectués sur un maillage uniforme et étiré en utilisant les méthodes MUSCL et WENO. La dépendance de la pression maximale près de la paroi par rapport à la distance d'éloignement de la bulle est proposée. Toutes les solutions présentées ici sont obtenues à partir de calculs dans le solveur parallèle SCB sur le supercalculateur Jean Zay JeanZay (2019).

SCB solveur est un solveur multiphase parallèle simple et efficace développé pour simuler divers écoulements multiphases compressibles, en particulier l'effondrement de bulles. La parallélisation du solveur est basée sur une approche hybride utilisant les bibliothèques OpenMP et MPI. Récemment, la stratégie de parallélisation combinant MPI et OpenACC a été mise en œuvre en raison du développement important des superordinateurs basés sur les CPU et les GPU (voir Dubois *et al.* (2021)).

La parallélisation de la mémoire distribuée est basée sur la bibliothèque MPI. Le stencil de calcul de SCB est basé sur cinq points par direction, ce qui implique que chaque inconnue est calculée en utilisant 13 voisins. Le solveur de Riemann de HLLC est parallélisé en utilisant la distribution de tableaux globaux entre les processus. Un partitionnement par blocs 3D de la matrice est utilisé afin d'effectuer une décomposition. Cette technique est basée sur l'introduction de cellules "fantômes" dans chaque sous-domaine et sur la communication de données entre les cellules voisines d'un sous-domaine. Une topologie de processeur cartésien est utilisée pour organiser les sous-domaines et les calculs sont couplés en utilisant deux couches de cellules auxiliaires définies aux limites de chaque sous-domaine. Les performances sont meilleures si les sous-domaines ont une taille égale et une topologie carrée.

Modèle de parallélisation de l'accélérateur est basé sur la bibliothèque OpenMP. Trois principes principaux ont été utilisés pour distribuer les boucles entre les threads (c'est-à-dire une programmation à grain fin). Le premier principe est une estimation de la taille du problème qui permet d'éviter le partage de données non pertinentes si la taille du problème devient trop petite. Le second principe est le choix d'un ordonnancement approprié. La meilleure charge autour des threads peut être obtenue en basculant entre quatre types différents d'ordonnancement de boucle OpenMP. Il s'agit de *static, dynamic, guided* et *runtime*. Le premier est destiné à basculer entre les trois types précédents lorsqu'une exécution qui utilise un environnement système variable est exécutée. Le dernier principe concerne la fusion des boucles internes, *COLLAPSE*, qui conduit à un élargissement de l'espace d'itération et, par conséquent, à une meilleure distribution des itérations. Un exemple simplifié avec une implémentation OpenMP dans SCB est donné en annexe B.

Le maillage non uniforme est généré par un programme développé séparément, qui prend comme entrées l'emplacement initial et la taille des pas spatiaux dx, dy et dz. Comme l'étirement du maillage dépend du problème, chaque stratégie doit être mise en œuvre en fonction du cas d'essai considéré. Tous les problèmes et stratégies d'étirement de maillage discutés dans cette thèse sont inclus dans ce logiciel. Le maillage non-uniforme est généré et écrit dans le fichier de données, qui est ensuite utilisé par SCB. La distribution des valeurs des coordonnées de la grille est nécessaire pour les calculs parallèles.

L'introduction des schémas d'ordre élevé dans SCB nécessite une communication de voisins supplémentaires par inconnue. C'est particulièrement le cas pour les schémas d'ordre 5 où le coût élevé de communication est discutable en termes de proportionnalité avec l'amélioration de la solution. À ce stade, la méthode WENO3-Z avec maillage uniforme et non uniforme a été introduite dans le cadre d'OpenMP et de MPI. L'implémentation de la méthode sur le maillage uniforme ne nécessite pas un agrandissement du stencil existant. Cependant, une nouvelle communication est nécessaire pour le maillage non-uniforme, où nous devons partager les valeurs des coefficients du maillage non-uniforme requis pour le schéma. Si cela n'augmente pas le nombre de voisins pour la méthode MUSCL, c'est certainement le cas pour la méthode WENO3 reformulée pour la grille non uniforme, où deux nœuds supplémentaires doivent être définis à la première itération temporelle pour calculer les coefficients. Cela peut augmenter le coût de communication. Pour éviter cela, nous notons que, grâce à la fonction d'étirement du maillage lisse utilisée dans cette étude, la variation des valeurs des coefficients nécessaires pour le maillage non uniforme est très faible. Ainsi, les derniers coefficients calculés pour WENO3 aux limites du domaine sont égaux à son voisin. Un exemple de cette mise en œuvre dans la direction x est présenté dans l'annexe C. Une méthode similaire est utilisée pour toutes les directions.

Nous considérons un effondrement de bulle sphérique avec une distance d'éloignement du mur

L/R_0=2. Le cas d'essai est similaire à l'effondrement de bulles près d'un mur présenté dans le chapitre précédent avec une extension à la 3D. En exploitant la symétrie du problème, seul un quart de la bulle est calculé. La configuration au temps initial est présentée sur la Figure Finit.

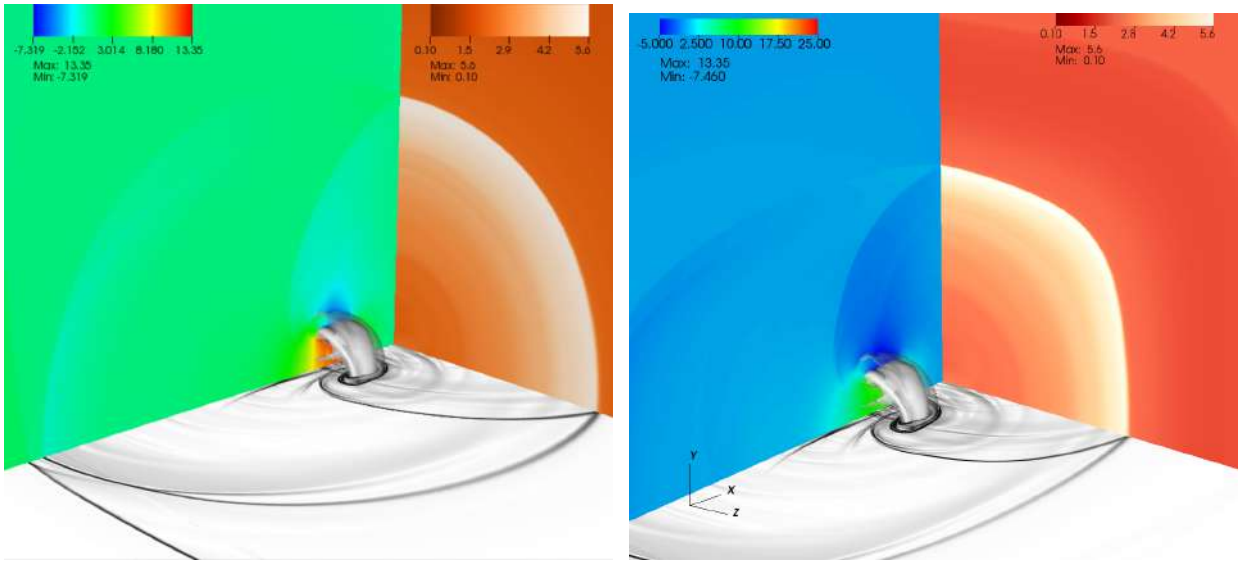

(a) t = 0.25 μs, 1050×1780×1780 (b) t = 0.25 μs, 1050×850×850

Figure 10: Visualisation de l'effondrement de bulles en 3D à différents moments pour une distance de séparation $L/R_0 = 2$. Composante de vitesse longitudinale sans dimension u/u_{sh}, pression de paroi sans dimension P/P_{sh}, représentation de type Schlieren et isosurface du α. WENO3-Z. Comparaison du facteur de maillage non homogene. $P_{sh} = 1200$ bar

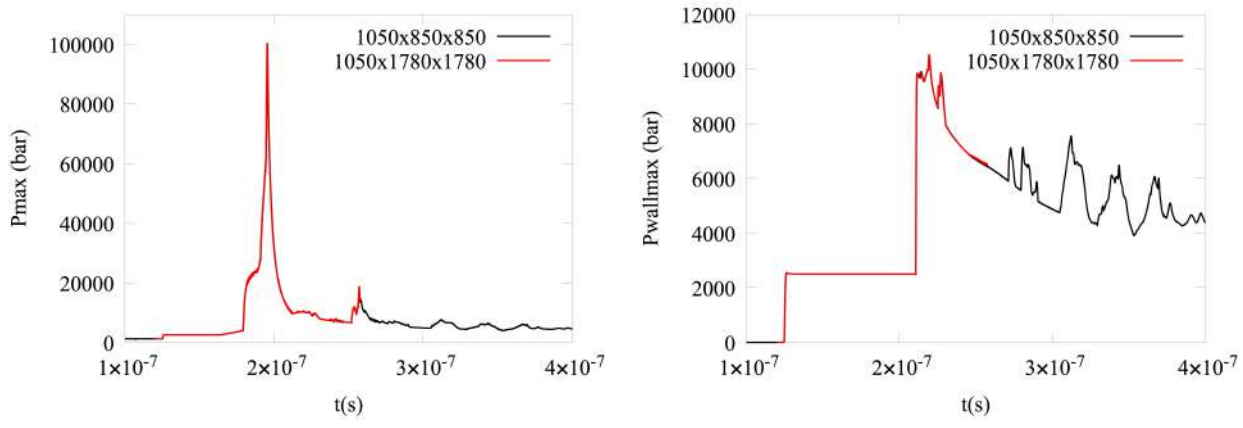

(a) P_{max} (b) $P_{wallmax}$

Une illustration de l'évolution de l'effondrement des bulles est proposée sur la figure 8.10. Nous présentons la vitesse longitudinale normalisée de $u_{sh} = 75.07$ m/s sur le plan de symétrie vertical, la pression normalisée de $P_{sh} = 1.2 \times 10^8$ Pa sur la paroi, le gradient de densité sur le plan de symétrie horizontal et le taux de vide à l'intérieur du volume. L'onde de choc incidente atteint la paroi et une onde réfléchie est générée. Au temps $t = 0.15\mu$s, l'onde de réflexion est localisée près de la bulle. On note la déformation de la bulle par rapport à sa forme sphérique initiale à $t = 0,12\mu$s. Cela se produit en raison de la différence de pression entre les deux côtés. Le jet d'eau pénétrant dans la bulle lui donne une forme toroïdale à $t = 0,18\mu$s et l'onde de choc réfléchie a atteint l'interface de la bulle. L'onde de choc sphérique intense est générée au moment $t = 0,20\mu$s lorsque le jet d'eau frappe le côté opposé de l'interface de la bulle. Les valeurs de vitesse élevées sont générées et atteignent 1500 m/s. L'apparition d'un fort pic de pression causé par l'onde de souffle atteignant la paroi est observée à $t = 0,23\mu$s. L'onde réfléchie se propage en direction de la bulle toroïdale. Enfin, l'impact de cette onde sur la bulle entraîne sa recollapse à $t = 0,25\mu$s.

Par conséquent, un autre pic de pression est généré, comme on peut l'observer sur la figure 8.12.

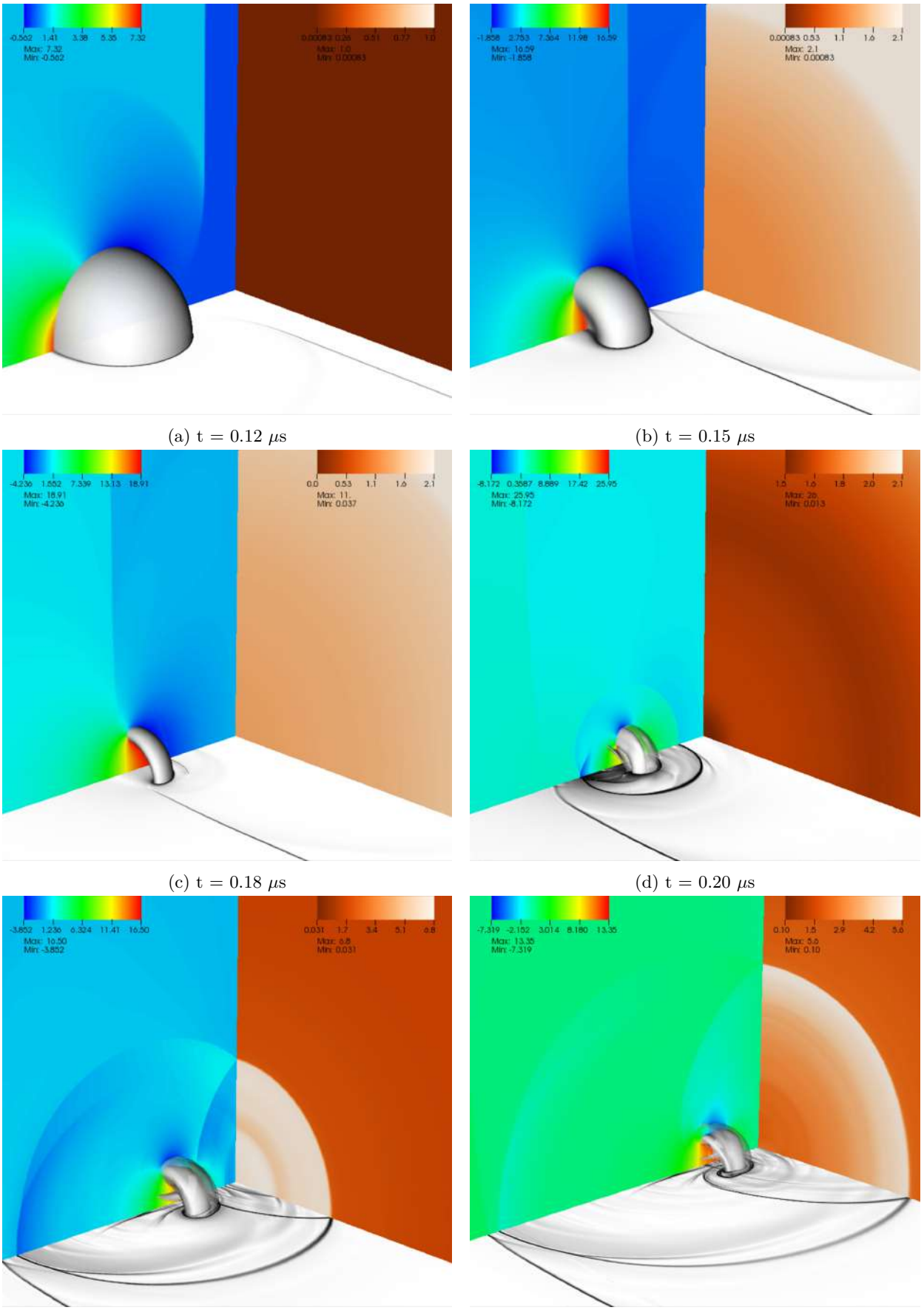

(a) t = 0.12 μs

(b) t = 0.15 μs

(c) t = 0.18 μs

(d) t = 0.20 μs

(e) t = 0.23 μs

(f) t = 0.25 μs

Figure 12: Visualisation de l'effondrement de bulles en 3D à différents moments pour une distance de séparation $L/R_0 = 2$. Composante de vitesse longitudinale sans dimension u/u_{sh}, pression de paroi sans dimension P/P_{sh}, représentation de type Schlieren et isosurface du α. WENO3-Z, maillage non homogene: 1050×1780×1780. $P_{sh} = 1200$ bar

L'étape suivante a été définie pour appliquer un facteur d'étirement plus fort. La figure 8.8 présente une comparaison côte à côte de la visualisation 3D au moment du rétrécissement de la bulle sous l'incidence de l'onde de réflexion. On note une reconstruction en forme de carré du profil de pression à l'écart de la bulle. Elle est certainement due à l'étirement du maillage puisque les calculs sur un maillage uniforme et sur un maillage étiré avec un facteur plus faible ne la présentent pas. Bien que l'effet d'un étirement aussi fort ait également été observé dans les calculs en 2D, il n'a pas affecté la région de pression autour de la bulle. De même, en 3D, le profil de pression à proximité de la bulle a une forme correcte et commence à être plus carré en s'éloignant de la bulle lorsque l'espacement de la grille continue d'augmenter. Cela peut être corrigé en utilisant un facteur d'étirement plus faible ou une plus grande surface de maille uniforme. La manière de déterminer ce facteur dépendrait du coût final du processeur que l'on peut acquérir et de la taille initiale de dy et dz.

La comparaison de la pression maximale à l'intérieur du fluide et à côté d'une paroi est proposée en utilisant une configuration similaire de maillage étiré sur la figure 8.8. Les pics de pression les plus élevés et les plus critiques n'ont pas été affectés par un degré d'étirement plus fort.

Le coût du CPU pour le présent problème (Tableau 8.1) est de 6 heures pour le maillage étiré de 1050×850×850 et de 34 heures pour le maillage étiré de 1050×1780×1780 en utilisant 4 000 processeurs. En comparaison, le temps de calcul d'un problème similaire en 3D avec un espacement uniforme plus grossier de 750×1250×1250 et une valeur dt deux fois plus élevée, est seulement 0,7 h de moins. Nous pensons qu'étant donné le coût de calcul et la précision de la solution dans la zone critique des phénomènes physiques, un étirement plus fort du maillage (c'est-à-dire un maillage étiré de 1050×850×850) peut être utilisé pour récupérer les caractéristiques clés du processus d'effondrement des bulles.

Dans ce chapitre, nous avons effectué des calculs 3D basés sur les méthodes numériques d'ordre élevé validées et les techniques de maillage étiré. La complexité des méthodes numériques d'ordre élevé dans l'implémentation parallèle a limité notre considération à la méthode WENO3-Z d'ordre 3 pour le moment. L'implémentation de la méthode est faite dans le cadre parallèle d'OpenMP et MPI. Le maillage non-uniforme a été introduit dans le solveur au moyen d'un logiciel d'étirement de maillage créé séparément. La stratégie de parallélisation des coefficients de maillage requis pour le schéma reformulé WENO a été proposée. Deux problèmes d'effondrement de bulles induit par un choc près d'un mur avec différentes conditions post-choc ont été étudiés.

Le premier problème est une extension de l'effondrement de bulles sous l'effet d'un choc en 2D à proximité d'un mur. Les tests préliminaires effectués ont permis d'établir la configuration principale de la stratégie d'étirement du maillage adaptée à ce problème. Précisément, un emplacement approprié de la zone de maillage uniforme est proposé et différents degrés d'étirement sont compris ainsi que leur effet sur la précision de la solution. Il a été observé que le rapport entre dy_{max} et dy_{min} et dz_{max} et dz_{min} a un effet sur la solution aux points éloignés de la zone de maillage uniforme. Cependant, cela n'a pas entraîné la détérioration de la solution aux points critiques. Les principaux phénomènes physiques sont reconstitués avec précision par rapport à des études similaires. Les solutions 2D et 3D ont été comparées et l'effondrement plus rapide et plus intense des bulles sphériques est confirmé dans notre étude. Nous pensons que la stratégie de la maille étirée est généralement une idée réussie, même si la divergence dans la formation du profil de pression loin de la zone de maille uniforme est détectée. Cela peut être corrigé en utilisant un facteur plus faible pour l'étirement.

Le deuxième problème présente une valeur inférieure pour la condition de choc. La stratégie d'étirement du maillage basée sur une taille de domaine différente est introduite. Les résultats sont validés en utilisant un maillage uniforme avec les méthodes MUSCL et weno3-Z. Nous avons constaté que les solutions sont relativement similaires. La méthode WENO3-Z est ensuite utilisée dans le cadre de l'étirement du maillage. L'effet du maillage non-uniforme est faible. De même, les principaux phénomènes physiques sont reconstruits avec précision par rapport aux calculs de référence effectués dans Goncalves & Parnaudeau (2021). Nous proposons une comparaison de la pression maximale de la paroi en fonction de la distance de la bulle par rapport à la paroi. On note l'augmentation rapide de l'intensité du pic maximal lorsque la distance à la paroi se réduit. En effet, un schéma similaire a été observé dans les cas où la valeur de P_{sh} est plus élevée (voir Johnsen & Colonius (2009) et Goncalves & Parnaudeau (2021), par exemple).

Ces calculs ont illustré une vitesse de calcul d'un facteur cinq. Par conséquent, nous pensons que la stratégie non-uniforme présentée est un sujet prometteur pour des développements futurs.

Chapitre 9. Conclusion générale et perspectives

L'effondrement des bulles induit par un choc est un problème important, qui fait partie du processus d'érosion par cavitation. Les applications industrielles nécessitent des études approfondies de ce phénomène en raison de l'endommagement des parois dû à l'effondrement des bulles à proximité des parois solides, ce qui peut provoquer une érosion. La dynamique physique impliquée dans ce processus est caractérisée par des vitesses élevées et de très petites échelles spatio-temporelles. Ainsi, la reconstruction numérique de tels phénomènes nécessite un maillage très fin, qui est de l'ordre de 10^6 pour les calculs en 2D et de 10^9 en 3D ou plus. La taille du problème peut être réduite en utilisant les méthodes numériques d'ordre élevé appropriées, ce qui peut entraîner une convergence plus rapide et, par conséquent, une réduction du nombre de points nécessaires pour obtenir une reconstruction précise. Ceci a été défini comme l'une des principales préoccupations de cette thèse.

Modèle mathématique et discrétisation de base utilisés dans cette étude ont été discutés dans le chapitre 2. Un modèle à quatre équations basé sur l'approche du mélange d'un seul fluide est utilisé. La discrétisation de base est effectuée en utilisant les formulations HLLC ou KNP pour le flux et la méthode MUSCL-Hancock pour la résolution spatio-temporelle du second ordre. Le schéma prédicteur-correcteur de Hancock s'est avéré robuste dans notre étude et nous pensons que ce schéma est une bonne alternative aux autres méthodes numériques temporelles, où le temps de calcul augmente en même temps que la précision de la méthode. Ceci est particulièrement important pour les calculs en 3D.

Les méthodes numériques d'ordre elevé qui peuvent être utilisées afin d'améliorer la résolution spatiale dans l'algorithme MUSCL-Hancock ont été discutées au chapitre 3. Nous nous sommes particulièrement intéressés à la classe de schémas WENO en raison de sa grande disponibilité et des études approfondies dont elle fait l'objet dans la littérature. Plusieurs variations récentes ont été proposées dans ce chapitre. D'autres schémas moins populaires, à savoir PPM et MP5, ont été présentés. En particulier, la méthode PPM a été examinée du point de vue de sa formulation améliorée pour l'EOS du gaz raidi.

La méthodologie de validation a été définie au chapitre 4. Nous notons que les problèmes qui nous intéressent n'ont pas de solutions analytiques et présentent des discontinuités. Ainsi, une validation numérique classique du solveur n'est pas possible. Le processus de validation qui a été présenté dans le chapitre est basé sur le calcul d'une solution de référence approximative qui est ensuite utilisée pour calculer l'ordre de précision relatif. Cette méthodologie est ensuite appliquée à trois problèmes 1D, testés par ordre hiérarchique en termes de rigidité et de complexité. Le problème 2D de la bulle de choc air-hélium a conclu la validation.

Calculs de l'effondrement d'une bulle induite par un choc en 2D sont présentés au chapitre 5. Nous avons considéré deux problèmes : le premier est une bulle d'eau-gaz immergée en champ libre et le second, une bulle d'eau-gaz située à proximité d'une paroi. Ces calculs avaient pour but de déterminer l'effet des schémas numériques d'ordre élevé sur la précision de la reconstruction des phénomènes physiques.

Les techniques de maillage non uniforme ont été abordées dans le chapitre 6 où nous avons présenté le cadre de maillage étiré. La dérivation des fonctions d'étirement de maillage jugées intéressantes pour notre étude a été proposée. Le besoin de versions reformulées de certaines méthodes numériques d'ordre élevé a été souligné et ces dérivations sont développées pour les méthodes WENO.

Les résultats des calculs 2D sur maillage non-uniforme ont été proposés au chapitre 7, où trois problèmes ont été considérés. Nous avons discuté et validé les stratégies d'étirement de maillage en utilisant la bulle de choc air-hélium, qui est un problème approprié pour tester diverses techniques d'étirement de maillage en raison de la topologie du problème. Ce faisant, nous avons défini les fonctions d'étirement pour la génération de maillage non uniforme pour les problèmes d'effondrement de bulles induit par un choc. Dans les sections suivantes du chapitre, nous avons développé les méthodes d'étirement de maillage spécifiques à ces problèmes et montré les résultats.

De plus, nous avons proposé une approche de méthodes hybrides où deux schémas numériques peuvent être utilisés sur le maillage non-uniforme. Ces techniques sont développées dans le but de réduire les coûts de calcul.

Les résultats des calculs 3D sur maillage non uniforme ont été présentés au chapitre 8. Le problème de l'effondrement d'une bulle induit par un choc à proximité d'une paroi a été étendu à la 3D et calculé sur un maillage non uniforme avec la méthode WENO3-Z. La stratégie d'étirement du maillage est généralement restée inchangée par rapport à la reconstruction des bulles. Les principaux phénomènes physiques du problème ont été décrits et une comparaison avec les résultats 2D correspondants a été montrée. Enfin, un problème similaire avec une valeur inférieure pour la condition post-choc a été calculé sur un maillage uniforme et non-uniforme en utilisant les méthodes MUSCL et WENO3-Z. L'effet du schéma numérique d'ordre élevé dans le calcul 3D a été vérifié sur un maillage uniforme. Le faible impact du maillage non-uniforme sur la précision de la solution a également été illustré. Nous avons montré la dépendance de l'intensité de la pression par rapport à la position de la bulle par rapport à la paroi.

Ces développements nous ont permis de dresser un tableau plus large de l'approche numérique générale de la résolution d'un problème d'effondrement de bulles induit par un choc. En partant d'une discrétisation de base du modèle mathématique, nous avons constaté que le solveur de Riemann HLLC est plus performant lorsque la complexité du problème augmente et que des chocs et des discontinuités plus importants sont impliqués. Une conclusion similaire a été faite en ce qui concerne certains des schémas numériques d'ordre élevé. En général, la classe des schémas WENO, et en particulier ses formulations les plus récentes, se sont avérées les plus précises et les plus robustes lors de nos tests. La méthode PPM, qui comprend plusieurs algorithmes pour traiter les zones de discontinuité de la solution, s'est avérée fonctionner relativement bien. Cependant, dans le problème de l'effondrement d'une bulle de choc dans un champ libre, elle a conduit à des variations de la solution qui n'étaient pas présentes en utilisant d'autres schémas. La méthode MP5, la moins populaire parmi les méthodes envisagées, s'est révélée oscillante dès les problèmes de validation et a donc été écartée de la suite de l'analyse.

Une perspective de choix d'un schéma numérique d'ordre élevé approprié dans le cadre de calculs très intensifs a été envisagée. Compte tenu du coût de calcul du plus grand stencil, généralement impliqué dans les schémas numériques d'ordre élevé, il faut décider de la relation entre la quantification de la reconstruction améliorée et l'augmentation du CPU. C'est ce qui nous a préoccupé dans le cas des schémas d'ordre 3 et 5. Alors qu'une amélioration a été clairement observée entre la solution calculée avec MUSCL et WENO3, la même chose n'est pas exactement évidente entre cette dernière et WENO5. Les résultats que nous avons analysés dans cette thèse n'ont pas démontré une amélioration significative entre les deux et, par conséquent, la méthode WENO3 a été étendue aux calculs 3D.

Cependant, même un stencil de calcul plus court nécessite une puissance de calcul importante, que l'on pensait pouvoir réduire en utilisant le solveur SCB entièrement parallélisé et en introduisant des techniques d'étirement de maillage. Nous avons constaté que l'approche d'étirement du maillage la plus appropriée est celle basée sur l'introduction d'une zone de maillage uniforme dans le domaine où se trouve la zone de forte variation de la solution. Dans notre cas, il s'agit de la zone de la bulle et de son interaction avec l'onde de choc et la paroi. La fonction d'étirement basée sur la tangente hyperbolique est déterminée comme étant la plus appropriée dans nos calculs. Cependant, le choix entre la tangente hyperbolique et le sinus peut être plus problématique.

Les méthodes d'étirement du maillage nous ont permis de réduire de cinq fois le coût des calculs en 2D pour le problème de l'effondrement des bulles induit par un choc. Par conséquent, son extension a été appliquée avec succès aux calculs en 3D. De plus, le schéma WENO3-Z a conduit à la reconstruction précise des phénomènes physiques dans des problèmes 3D avec des conditions post-chocs supérieures et inférieures où un gain de CPU similaire a été observé. Nous pensons que cette méthode est un choix approprié pour obtenir une reconstruction de haute précision pour les calculs difficiles de l'effondrement des bulles induit par un choc.

La présente thèse a développé les méthodes qui ont permis d'atteindre une meilleure précision de la solution sans rencontrer un coût de calcul élevé. Cependant, ces travaux pourraient être poursuivis et améliorés dans une ou plusieurs directions.

Le premier domaine immédiat d'investigation est le modèle mathématique sous-jacent qui pour-

rait être modifié afin d'examiner son effet sur la solution. Par exemple, Goncalves & Parnaudeau (2020) a réalisé une étude approfondie de plusieurs modèles en 2D et cette étude pourrait être étendue à 3D avec une réduction des coûts de calcul au moyen d'un maillage non uniforme. En outre, les effets visqueux peuvent être étudiés dans le même cadre.

Sans aucun doute, le domaine des schémas hautement numériques peut être étendu presque à l'infini. Les variations d'autres formulations des méthodes WENO et de ses dérivés continuent d'apparaître. Ainsi, cette partie peut être étendue à d'autres développements en utilisant spécifiquement la classe WENO. La publication la plus récente à cet égard est, par exemple, Luo & Wu (2021). En outre, les méthodes supérieures de WENO peuvent être examinées, mais avec précaution.

Une autre grande partie de l'amélioration du présent travail concerne l'introduction de maillages non-uniformes. Cette thèse n'a présenté que des techniques d'étirement de maillage arbitraire liées au problème, qui sont initialisées une fois lors de la première itération. Le processus de recherche d'une stratégie appropriée a été basé sur des tests. Ceci pourrait être tourné dans une direction différente et aborder un problème de méthodes de maillage adaptatif. Par exemple, l'étirement du maillage pourrait être redéfini à certains moments où la bulle modifie le plus sa topologie et son emplacement ou lorsque la plus forte variation de solution est détectée. Cependant, l'étirement adaptatif du maillage peut être une tâche difficile et très coûteuse en termes de calcul. En tant que tel, le coût de sa mise en œuvre dans des cadres séquentiels et parallèles, les reformulations des schémas numériques et les dérivations analytiques supplémentaires doivent être soigneusement examinés.

Enfin, et ce n'est pas le moins important, une étude du couplage solide-fluide dans le contexte de l'endommagement de la paroi causé par l'effondrement des bulles peut être réalisée. L'analyse de la charge de pression de la paroi basée sur la distance de séparation entre la bulle et la paroi est un bon point de départ pour ce type d'étude. Par exemple, elle a déjà été examinée dans Johnsen & Colonius (2009) et Goncalves & Parnaudeau (2021) dans des calculs 2D et 3D. Ces études peuvent être poursuivies en testant différentes configurations de l'effondrement de la bulle pour confirmer les lois de charge de pression suggérées par les auteurs. La partie de cette analyse pour différentes configurations de test est présentée dans cette thèse.

D'une manière générale, le domaine de recherche concernant l'effondrement des bulles induit par un choc est vaste et de nombreuses améliorations numériques peuvent être et seront apportées à l'avenir car nous observons une croissance technologique constante. Cela permettra de résoudre des problèmes encore plus lourds en termes de calcul sur des mailles extrêmement fines. Nous espérons que cette étude constitue un pas en avant dans ces persuasions.

Contents

Chapter 1

Introduction and Background

1.1 The context of a shock-induced bubble collapse

Cavitation erosion is an important problem which has to be tackled in many domains, such as hydraulic and marine applications. This process occurs as a result of bubble collapse near the solid walls causing the material damage. The physical process of such phenomena has been studied in many experimental and numerical investigations. For instance Haas & Sturtevant (1987) has performed an experimental study where the gas bubble has been affected by the plane weak shock wave. Authors presented the geometry of the bubble deformation which made it possible the validation of many numerical studies using this configuration. On the other hand, Johnsen & Colonius (2009) performed a numerical simulations of a gas-bubble collapse immersed in a free field and in a proximity to a wall, comparing the obtained results to available experimental data. This study has been a first one where the validation of the numerical solution has been done quantitatively against those obtained by experiments. The response of the solid material caused by such a bubble collapse has been numerically investigated in Gong & Klaseboer (2016), where authors performed a coupling of the methods to study the bubble evolution with methods to analyse quantitatively the effect of the impulsive pressure, caused by bubble collapse, to the solid material. From numerical computations point of view, the cavitation phenomena requires a compressible two-phase flow modelling. The contribution to this need is done in Goncalves & Zeidan (2018) where a compressible multiphase solver has been implemented to study liquid-gas type of flows with presence of shock and expansion waves which cause the cavitation process. However, this type of computations is still a challenge for the applied mathematics and numerical methods, even though the industrial demand of such a modelling is high. This complexity is due to high variations of thermodynamic properties, strong pressure waves and their interaction with interfaces and the involved fast dynamics.

1.2 Basic numerical methods

There are several widely used strategies for such two-phase problems. One of the often used is a method based on an average approach. This method led to the development of the variety of different perspectives based on the physical assumptions for the slip condition between phases and mechanical and thermodynamic equilibrium. The most complete modelling approach is known to be the two-fluid model Baer & Nunziato (1986), which has a high computational complexity since it consists of seven equations. An alternative method, which is more suitable for practical applications, is a reduced five-equation model with the underlying assumption of pressure and velocity equilibrium between phases Kapila *et al.* (2001); Saurel *et al.* (2008). Furthermore, this model can be reduced by using the assumption of thermal equilibrium. Such a model consists of

three equations for conservation laws and a fourth one for the void ratio Goncalves & Parnaudeau (2020).

One of the important and difficult domains of studying the two-phase compressible flows is the suitable numerical methods. One challenge comes from the characteristic waves structure of the hyperbolic system describing this physical phenomena, which yields to the unstable simulations. Moreover, the problem of discontinuities of thermodynamic variables and equations of state occurring due to the material interfaces causes difficulties in the derivation of Riemann solvers. The speed of sound component is also a challenge. Due to the large differences between its values in mixture and liquid phases, some large variations are present and cause the non smooth behaviour and inaccuracies in the solution. Thus, nonphysical oscillations can appear in the solution of the whole wave structure Abgrall (1996). The numerical dissipation of the numerical schemes which is required to follow the thermodynamic law is also a result of these inaccuracies of the modelling. Generally, the full process of establishing the numerical model can be divided into three parts. The first one, is a basic discretization, where the global framework of spatial and temporal discretization is defined. The second part is an improvement of these global methods in order to achieve higher accuracy of reconstruction in smooth parts of the solution. The final part is related to the observation of computational cost which generally becomes quickly prohibitive as the order of accuracy and required fine grid of the problem increases. Hence, additional methods of decreasing the time of computations are required.

In terms of basic numerical discretization, three underlying methods are mainly used: those based on Lagrangian, arbitrary Lagrangian-Eulerian (ALE) and Eulerian meshes. The first two methods are using the tracking of material interface by using the moving mesh. The disadvantage of such an approach lies in the high computational complexity and difficult implementation due to the requirement of frequent reinitialisation of the mesh to accommodate its deformation as the flow moves. The Eulerian method, on the other hand, uses the Lagrangian markers to track the material interface and captures this interface by using an additional scalar along with required advection term. The introduction of the scalar itself is further divided into two subcategories of methods: sharp-interface and diffuse-interface methods.

Additional part of basic discretization is a choice of the solver to use for the finite volume methods. One of the usual formulation is Harten-Lax-van Leer-Contact (HLLC) initially introduced in Toro *et al.* (1994). It has been used in numerous studies where the high-order reconstruction is successfully achieved, e.g. Johnsen & Colonius (2006, 2009); Wang *et al.* (2018) among many others. Another popular choice is upwind schemes, where the Riemann solver and characteristic decomposition are the underlying techniques. The inspiration for these methods is Godunov schemes and yet again, they are not easy to implement in the framework of multiphase flows. Yet, another type of the methods is central schemes which are advantageous due to its independence of the eigenstructure of the considered problem. Some examples of such schemes are Lax–Friedrichs scheme Lax (2005) and the Nessyahu–Tadmor scheme Nessyahu & Tadmor (1990). The combination of both, the upwind and central schemes is a method discussed in Spina & Vitturi (2012), which is addressed as KNP formulation. This method takes an advantage point from both sides, the independence of characteristic decomposition and retained upwind nature due to the one-sided type computation of eigenvalues required in formulation.

1.3 High-order numerical methods

The complexity of physical phenomena of cavitation requires an improvement of the order of accuracy of finite-volume solvers, i.e. high-order reconstruction methods have to be used. While numerous amount of such schemes exist, the choice is not straightforward. The methods used to improve the accuracy of solution must satisfy several requirements: stability in non-smooth regions of solution, sharp reconstruction of discontinuity regions and non-oscillatory behaviour. According to Johnsen & Colonius (2006), the numerical instabilities due to the material interface, for instance, can be improved by using the primitive variables reconstruction in contrast to conservative variables which are normally default reconstruction values in finite volume methods. The authors successfully applied Weighted Essentially Non-Oscillatory (WENO) for gas-gas two-phase problems. However, this strategy is not as suitable when a large density ratio between phases is

present leading to high gradients in the flow. Indeed, it has been shown that high-order schemes can lead to spurious oscillations when applied to stiff compressible two-phase flows. Two methods have been suggested to tackle this issue in Coralic & Colonius (2014). One of them, the hybrid construction of the scheme, where the fifth order WENO is locally reduced to the second order reconstruction near the interface. Another method is a smoothing the material interface as a part of initial condition. However, there are disadvantages in both strategies. The first method is problem-dependent, since the interface condition is different based on the physical phenomena involved. On the other hand, the second method has a problem of thickening the interface artificially, which can cause further numerical instabilities. In order to avoid these problems, an alternative method have been suggested by Wang et al. Wang *et al.* (2018), where an incremental 2- and 3-point stencil is used to obtain a fifth order WENO scheme. This choice between the smaller and larger stencil is conditioned based on the discontinuity criteria.

The above mentioned WENO class of the methods is one of the mostly used in modern research in the context of variety of the compressible two-phase flow. Initially introduced by Liu *et al.* (1994), where the essentially non-oscillatory scheme for shock capturing has been proposed based on the convex combination of interpolating polynomial candidates, this method has been a topic of many studies. The preliminary numerical results demonstrated promising tendency on variety problems, including the problem of shock-tube. The earliest biggest improvement of this method has been suggested in Jiang & Shu (1996*a*). The new method of measuring the solution smoothness has been derived, which led to one additional order of accuracy and resulted in fifth-order scheme. The main characteristic of this new scheme is its efficiency, since an improved order of scheme is derived as such that it is twice faster than its earlier counterpart. This version of WENO has been tested in many numerical frameworks, including a shock entropy wave interaction problem in 2D. The authors demonstrated that the new smoothness measure is a capable tool of solving the complex shocks. Many more improvements of WENO of fifth and third order followed. Along with already mentioned improvement in Wang *et al.* (2018), there have been Henrick *et al.* (2005) with observation that the convergence of the scheme is not satisfactory near the critical points and suggestion to improve this drawback with a special mapping technique to keep the nonlinear weights in agreement with linear ones everywhere where the discontinuity is detected. An inspiration from this idea has been taken by Borges *et al.* (2008) and yet another version of the scheme has been introduced with superior smoothness indicator measure which led to the superior results with similar computational cost. Moreover, the arbitrary formulation suitable for all odd orders of accuracy has been derived in Castro *et al.* (2011). An improved design and redesign of smoothness indicator function of WENO has been mainly focused around the method accuracy at critical points and is based on the assignment of larger weights to the less smooth stencils with preservation of essentially non-oscillatory property (ENO). This type of methods has been proven to be efficient in solving problems with strong shocks and discontinuities.

While the WENO methods are extremely popular, some other methods occasionally get an attention in the literature. Somewhat related method is proposed in Suresh & Huynh (1997) which developed a monotonicity preserving scheme, where the high-order polynomial reconstruction is limited based on the discontinuity detection. Authors provided the validation based on the linear advection equation that the method is monotonicity-preserving and maintains the high order uniformly. A much less available in the context of compressible two-phase flows and different class of high-order numerical reconstruction is a Piecewise Parabolic Method (PPM). This scheme has been initially discussed in Colella & Woodward (1984) and designed for single-phase ideal gas problems. This scheme has been extended and successfully applied in Zheng & Lee (2013) in the framework of inviscid system of equations with a suitable contact discontinuity detection for stiffened EOS and a simplified flattening algorithm. The modified version has provided the method with capability of solving problems with strong discontinuities and better resolved sharp gradients. The PPM strategy has been also redefined in the context of extremum-preserving limiters in Colella & Sekora (2008), where authors suggested a modification leading to the smooth extrema accuracy preservation. This modified method has been designed yet again for the gas-dynamics type of problems.

1.4 Stretched mesh and numerical methods

Although high-order numerical methods improve the solution of complex physical phenomena, there is still a need of highly fine meshes. Thus, along with larger computational stencil normally required for achieving higher order of accuracy, the computational complexity is also increasing due to the number of points in computational domain. While the problems with smooth solutions can be optimised by using high-order numerical schemes with less number of points, the cases involving strong shocks and discontinuities do not necessarily follow this rule. The need for the strategies where the computational cost can be decreased while preserving the accuracy of the solution arises. One of them is an introduction of non-uniform meshes.

Several mesh reduction methods exist. The adaptive mesh refinement (AMR), one of the most often used in recent literature, is a method where the solution accuracy is adapted based on the location of certain critical solution components. The main underlying idea of this method is to apply higher numerical precision by means of finer mesh in the zones of computational domain where the high gradients are detected and reduction of this precision otherwise. The original AMR algorithm had been presented in Berger & Joseph (1984) and Berger & Colella (1989) where authors presented a dynamic gridding or local adaptive mesh refinement. An alternative non-uniform mesh method is a mesh stretching. The mesh stretching can be achieved by introduction of any function to distribute the points non-uniformly. The easiest function can be based on the geometrical progression and more complex one is on smoother functions, such as sine, tan etc. The analytical studies of these functions suitable for the grid generation have been studied in Thompson *et al.* (1985); Vinokur (1983); Pierson & Kutler (1980); Gough *et al.* (1975).

While both mesh reduction techniques have been successfully used to introduce non-uniform mesh, some difficulties may arise. Namely, the suitability of the numerical schemes for such meshes can be questioned, since majority of the schemes are derived for the uniform meshes. The modified derivation of the high-order reconstruction is required should it be used with not equal grid spacing. Interestingly, the PPM method has been presented in Colella & Woodward (1984) with the account for the non-uniform grid, which significantly facilitates its use on the non-homogeneous mesh. On the other hand, WENO methods have been addressed in the framework of non-uniform grid in Wang *et al.* (2008).

1.5 Objectives and outline of the thesis

In regard to the above overview, the present thesis focus is on high-order numerical methods suitable to solve with high accuracy the problem of a water-air shock-induced bubble collapse next to a wall. The method of modelling such a problem is based on the four-equation model presented in Goncalves & Charriere (2014). A gas bubble immersed in water and collapsing under the incidence of shock wave either in a free field Nourgaliev *et al.* (2006) or in the vicinity of a wall is considered. The second problem is particularly important for the investigation of material damage leading to the erosion and is based on the study of Paquette *et al.* (2018).

The following objectives have been established for this study and can be divided into three parts.

- **The basic discretization and high-order numerical schemes.** This part is meant to study the underlying mathematical model and basic numerical discretization. Specifically, the appropriate methods for the problems which involve strong shocks and discontinuities have to be reviewed with the focus on the techniques which have been validated in the context of compressible two-phase flows. Particular attention has to be paid to the existence of a source term in the underlying mathematical model. In addition to the spatial basic discretization, the temporal integration has to be chosen with preserving the features of other chosen numerical methods. Finally, high-order numerical methods have to be examined in the framework of the problem in consideration. The appropriate techniques have to be validated on the problems which can demonstrate the schemes compatibility of the involved phenomena.

- **Non-uniform mesh.** This part of the thesis is dealing with the techniques of reducing the computational cost by means of the mesh stretching techniques. The mesh stretching methods have to reviewed and appropriate methods have to be implemented and tested. The problem-dependent strategies of mesh stretching have to be proposed, tested and validated. The final mesh stretching framework has to be established.

- **3D computations.** The final objective of this thesis is an extension of the proposed numerical methods computed on the non-homogeneous mesh with the necessary resolution to the problem of shock-bubble collapse in vicinity to the wall in 3D. The high computational cost of such computations requires an introduction of fully parallelized solver and efficient parallel implementation of high-order numerical schemes. Additional attention has to be paid to the implementation of the non-uniform mesh in the framework of parallelized computational environment. The final appropriate strategy in terms of the high-order numerical method and non-uniform mesh has to be suggested.

This thesis addresses the above objectives in the following outline. The Chapter 2 presents the underlying mathematical model used in this study and develops the basic numerical discretization. Chapter 3 addresses an extension of basic discretization to the high-order numerical schemes and reviews the key numerical methods available. These methods are then validated in Chapter 4, where three 1D problems are used in hierarchical order in terms of its stiffness. The validation is finalised by using selected schemes in the 2D problem of air-helium shock-bubble interaction. The Chapter 5 presents an extension of these methods to the problems of shock-induced bubble collapse in a free field and near a wall. We improve these methods in terms of the computational cost reduction by introducing a non-uniform mesh and these techniques are discussed in Chapter 6 and validated for 2D computations in Chapter 7. Finally we present 3D computations by using appropriate schemes and non-uniform mesh in Chapter 8. The general summary of this work and its perspectives are given in Chapter 9.

Chapter 2

Mathematical model and basic discretization

The Chapter is organised as following. The Section 1 reviews the mathematical model itself with the governing equations and equations of states (EOS). The Section 2 proposes two global methods for the basic spatial discretization and methods for the temporal integration. The treatment of boundary conditions is presented in Section 3. The summary of the discussed methods concludes this Chapter.

In this study we focus on a four-equation model which is the first part of work of establishing the numerical scheme effect on the basis of inviscid simulations. The 4-equation system includes three conservation laws for mixture quantities and a supplementary transport equation for the void fraction. The solver is based on the explicit finite volume methods using two different flux approximates (HLLC and KNP) with different resolution approaches in time and limiting techniques in space.

We start by presenting the mathematical problem and governing equations followed by the description of numerical approximation schemes implemented and tested.

2.1 Mathematical model

This Section discusses the mathematical model and basic discretization, which are used throughout this thesis. It is employed based on the one-fluid mixture approach with following assumptions:

- strong coupling of phases with the same velocity
- thermal and mechanical equilibrium between the phases
- saturation state of liquid
- viscous effects and surface tension are neglected

The model uses a four-equation system where three equations consist of conservation laws for mixture quantities and the fourth one of the void ratio transport equation Goncalves & Zeidan (2018). The basic discretization is performed by using the finite volume method with explicit time integration. Using the conservative variables representation, i.e. $w = (\rho, \rho\overrightarrow{V}, \rho E)$ and the volume fraction of gas α), the 2D inviscid system can be written as,

$$\begin{aligned} \frac{\partial \rho}{\partial t} + \mathrm{div}(\rho \overrightarrow{V}) &= 0 \\ \frac{\partial(\rho \overrightarrow{V})}{\partial t} + \mathrm{div}(\rho \overrightarrow{V} \otimes \overrightarrow{V} + PId) &= 0 \\ \frac{\partial(\rho E)}{\partial t} + \mathrm{div}(\rho \overrightarrow{V} H) &= 0 \\ \frac{\partial \alpha}{\partial t} + \overrightarrow{V}.\mathrm{grad}(\alpha) &= \mathrm{Kdiv}(\overrightarrow{V}) \end{aligned} \tag{2.1}$$

where $\overrightarrow{V} = (u, v)$ denotes the centre of mass velocity, $E = e + V^2/2$ is the total energy of mixture and $H = h + V^2/2$ is the enthalpy of this mixture. The reflection of the change in each phase volume and speed of sound of pure phases c_k are included into the term K, which is derived according to the following formulation,

$$K = \frac{\rho_l c_l^2 - \rho_v c_v^2}{\frac{\rho_l c_l^2}{1-\alpha} + \frac{\rho_v c_v^2}{\alpha}}$$

where index g stands for the gas phase and l for the liquid one. Several studies by Wermelinger *et al.* (2018) and Schidmayer *et al.* (2020) demonstrated an effect of this term in the framework of studying the five-equation model with and without K-term. It has been established that this term is improving the accuracy of thermodynamic behaviour in mixture.

An equation of state (EOS) for the mixture is required to close the system. The formulation is deduced from convex stiffened gas EOS LeMétayer *et al.* (2004) for both phases and obtained from the thermal and mechanical equilibrium assumption. The equations for the pressure and temperature are,

$$P(\rho, e, \alpha, Y) = (\gamma(\alpha) - 1)\rho(e - q(Y)) - \gamma(\alpha)P_\infty(\alpha) \tag{2.2}$$

$$T(\rho, h, Y) = \frac{h - q(Y)}{C_p(Y)} \tag{2.3}$$

with

$$\begin{aligned} \frac{1}{\gamma(\alpha) - 1} &= \frac{\alpha}{\gamma_v - 1} + \frac{1 - \alpha}{\gamma_l - 1} \\ q(Y) &= Y q_v + (1 - Y) q_l \\ C_p(Y) &= Y C_{p_v} + (1 - Y) C_{p_l} \end{aligned} \tag{2.4}$$

$$P_\infty(\alpha) = \frac{\gamma(\alpha) - 1}{\gamma(\alpha)} \Big[\alpha \frac{\gamma_v}{\gamma_v - 1} P_\infty^v + (1 - \alpha) \frac{\gamma_l}{\gamma_l - 1} P_\infty^l \Big] \tag{2.5}$$

where C_p and C_v are thermal capacities, q is the energy of formation, $\Gamma = C_p/C_v$ is the heat capacity ratio and $Y = \alpha\rho_v/\rho$ is the mass fraction of gas. The quantity P_∞ denotes a constant reference pressure.

The present system is hyperbolic and the eigenvalues are $\lambda_1 = u - c_{wallis}$, $\lambda_{2,3,4} = u$, $\lambda_5 = u + c_{wallis}$, where c_{wallis} corresponds to the propagation of the acoustic waves without mass and heat transfer and has the following formulation,

$$\frac{1}{\rho c_{wallis}^2} = \frac{\alpha}{\rho_v c_v^2} + \frac{1 - \alpha}{\rho_l c_l^2} \tag{2.6}$$

where c_v and c_l is the speed of sound of vapour and liquid phases, respectively.

2.2 Basic discretization

This section presents the key basic discretization techniques in space and time which are used throughout present study. The choice of the discussed methods are due to their suitability for the problems where strong shock waves and discontinuities are present. In order to apply the discretization, the system 2.1 has to be rewritten in 1D form as following,

$$\frac{\partial U}{\partial t} + \frac{\partial G(U)}{\partial x} + B(U)\frac{\partial u}{\partial x} = 0 \tag{2.7}$$

where $U = \begin{pmatrix} \mathbf{w} \\ \alpha \end{pmatrix}$, $G(U) = \begin{pmatrix} F(\mathbf{w}) \\ \alpha u \end{pmatrix}$, $B(U) = \begin{pmatrix} 0 \\ -K - \alpha \end{pmatrix}$, and F denotes the convective flux.

This 1D new formulation can then be used for the directional splitting when solving problems in several dimensions. The computational spatial and temporal domains are divided into regular meshes of the uniform length Δx and uniform intervals Δt, respectively. The reformulated discrete form of (2.1) is obtained by using the finite-volume method. The system can be expressed as,

$$\Delta x \frac{U_i^{n+1} - U_i^n}{\Delta t} + G_{i+1/2}^n - G_{i-1/2}^n + \int_{x_{i-1/2}}^{x_{i+1/2}} B(U)\frac{\partial u}{\partial x} = 0 \tag{2.8}$$

The discretization of the non-conservative term is discussed below. The discretization is meant to approximate the numerical flux $G_{i+1/2}^n$, $G_{i-1/2}^n$ using the solution to Riemann problem or any other numerical technique. While many formulations are available for the estimation of the numerical flux, such as Roe-type Gallouet *et al.* (2002), AUSM-type Kitamura *et al.* (2014), Jameson-Schmidt-Turkel Jameson *et al.* (1981), two formulations are considered in this paper: HLLC Toro *et al.* (1994) and KNP Spina & Vitturi (2012). The HLLC scheme has been widely used in most of the recent literature and has been demonstrated to be suitable for the problems involving strong shocks. The KNP formulation, on the other hand, more specifically central unpwind formulation, has been implemented in the Hancock predictor-corrector scheme and tested for compressible flows, which is indeed the problem considered in present thesis.

2.2.1 Harten-Lax-van Leer-Contact Riemann solver

The first flux approximation, HLLC approximate Riemann solver, has been chosen due to its stability, availability of contact discontinuity resolution and accurate shock capturing. This method uses two intermediate states, w_L^* and w_R^*, which are separated by the speed contact wave S_M. The conservative part of the equation (2.7) is discretized according to the classical HLLC formulation Toro *et al.* (1994).

$$F_{i+1/2} = \begin{cases} F(w_L), & \text{if } S_L > 0 \\ F(w_L^*), & \text{if } S_L \leq 0 < S_M \\ F(w_R^*), & \text{if } S_M \leq 0 \leq S_R \\ F(w_R), & \text{if } S_R < 0 \end{cases} \tag{2.9}$$

where S_L and S_R are the smallest and largest speed waves, respectively, inside the given cell. The fluxes and, both, left and right states can be defined according to,

$$w_K^* = \begin{pmatrix} \rho_K^* \\ (\rho u)_K^* \\ (\rho E)_K^* \\ \alpha_K^* \end{pmatrix} = \frac{1}{S_K - S_M} \begin{pmatrix} \rho_K (S_K - u_K) \\ (\rho u)_K (S_K - u_K) + P^* - P_K \\ (\rho E)_K (S_K - u_K) + P^* S_M - P_K u_K \\ \alpha_K (S_K - u_K) \end{pmatrix}$$

$$F(w_K^*) = \begin{pmatrix} \rho_K^* S_M \\ (\rho u)_K^* S_M + P^* \\ (\rho E)_K^* S_M + P^* S_M \\ \alpha_K^* S_M \end{pmatrix}$$

where pressure is

$$P^* = P_L + \rho_L(u_L - S_L)(u_L - S_M) = P_R + \rho_R(u_R - S_R)(u_R - S_M)$$

and contact wave speed is

$$S_M = \frac{P_R - P_L + \rho_L u_L(S_L - u_L) - \rho_R u_R(S_R - u_R)}{\rho_L(S_L - u_L) - \rho_R(S_R - uR)}$$

while the speed estimation of the left and right waves speed for Riemann problem is

$$S_L = min(u_L - c_L, u_R - c_R)$$

$$S_R = max(u_L + c_L, u_R + c_R)$$

The discretization of the non-conservative part, on the other hand, is based on the approach proposed in Daude *et al.* (2014). The $B(U)$ term is formulated as,

$$\int_{x_{i-1/2}}^{x_{i+1/2}} B(U)\frac{\partial u}{\partial x} \simeq B(U_i)(u_{i+1/2} - u_{i-1/2}) \tag{2.10}$$

and the interface cell value is then derived,

$$u_{i+1/2} = \begin{cases} u_L & \text{if } S_L > 0 \\ \frac{S_L - u_L}{S_L - SM} S_M & \text{if } S_L \leq 0 < S_M \\ \frac{S_R - u_R}{S_R - SM} S_M & \text{if } S_M \leq 0 \leq S_R \\ u_R & \text{if } S_R < 0 \end{cases} \tag{2.11}$$

2.2.2 Kurganov, Noelle, Petrova upwind-central scheme

Another flux approximate used in present work is Kurganov, Noelle, Petrova scheme Spina & Vitturi (2012). This scheme approximates the numerical flux using the calculation of positive and negative local speeds at each interface. Let $\lambda_{i+\frac{1}{2},R}$ and $\lambda_{i+\frac{1}{2},L}$ be the maximum eigenvalue of the Jacobian and $\mu_{i+\frac{1}{2},R}$ and $\mu_{i+\frac{1}{2},L}$ be the negative eigenvalue of the same Jacobian. We define the positive and negative local speeds as,

$$a^+_{i+\frac{1}{2}} = max(\lambda_{i+\frac{1}{2},R}, \lambda_{i+\frac{1}{2},L}, 0)$$

$$a^-_{i+\frac{1}{2}} = max(\mu_{i+\frac{1}{2},R}, \mu_{i+\frac{1}{2},L}, 0)$$

Numerical fluxes are then derived as,

$$F_{i+\frac{1}{2}} = \frac{a^+_{i+\frac{1}{2}}\mathbf{F}(\mathbf{U}_{i+\frac{1}{2},L}) - a^-_{i+\frac{1}{2}}\mathbf{F}(\mathbf{U}_{i+\frac{1}{2},R})}{a^+_{i+\frac{1}{2}} - a^-_{i+\frac{1}{2}}} + \frac{a^+_{i+\frac{1}{2}}a^-_{i+\frac{1}{2}}}{a^+_{i+\frac{1}{2}} - a^-_{i+\frac{1}{2}}}(\mathbf{U}_{i+\frac{1}{2},R} - \mathbf{U}_{i+\frac{1}{2},L}) \tag{2.12}$$

Both numerical fluxes, HLLC and KNP, lead to the first order scheme in space. However, the spatial order can be straight forwardly increased by using MUSCL extrapolation technique with TVD slopes limiters to avoid unnatural oscillations or more sophisticated high order numerical methods. In terms of the time integration, the solver is based on the explicit approach with either simple Euler or Runge-Kutta time stepping or an alternative predictor-corrector scheme, referred as the Hancock's method van Leer (2003), which is discussed in detail in the next subsection.

The non-conservative term in present model can pose several difficulties. Generally, the obtained solution has to satisfy the conservation properties of the system. Moreover, the discontinuities of the solution should be reconstructed as such that they reflect the real physics of phenomena. While these two conditions are satisfied in fully conservative formulations, it is not necessarily the

case for its non-conservative counterparts. One has to tackle the following difficulties related to the non-conservative term: sharp capturing of the gradients without non-physical oscillations, accurate reconstruction in smooth regions of the solution and approximating smooth nontrivial solutions to avoid these non-physical solutions near equlibria.

2.2.3 MUSCL and TVD limiters

One of the simplest numerical methods for space resolution is the MUSCL reconstruction (Monotonic Upstream-centered Scheme for Conservation Law) which has been initially presented by Van Leer in 1977 van Leer (1977). The underlying assumption of this method is existence of linear variation inside the cell. Consequently, the main idea follows that the discrete average values at the cell borders are used to reconstruct the average interface values. In order to do so, the second order expansion is employed to obtain the slope of the reconstructed variables. Generally, two types of approximation are used:

- one-sided approximation

$$\begin{aligned} w^L_{j+\frac{1}{2}} &= w_j + \frac{w_j - w_{j-1}}{2} \\ w^R_{j+\frac{1}{2}} &= w_j - \frac{w_{j+2} - w_{j+1}}{2} \end{aligned} \tag{2.13}$$

- centered approximation

$$\begin{aligned} w^L_{j+\frac{1}{2}} &= w_j + \frac{w_{j+1} - w_j}{2} \\ w^R_{j+\frac{1}{2}} &= w_{j+1} - \frac{w_{j+1} - w_j}{2} \end{aligned} \tag{2.14}$$

These two formulations can be combined in general from by using the parameter ϕ. That is,

$$w^L_{\frac{1}{2}} = w_j + \frac{1-\phi}{4}(w_j - w_{j-1}) + \frac{1+\phi}{4}(w_{j+1} - w_j) \tag{2.15}$$

where setting $\phi = -1, 1, 1/3$ leads to the one-sided, centered or third order approximations, respectively.

The MUSCL method stand alone had been known to lead to the oscillations around strong shocks and discontinuities. The methods to tackle this problem which are known as TVD (Total Variation Diminishing) methods have been introduced in Harten (1983). The solution obtained by the numerical scheme is considered to be TVD if it satisfies the following condition,

$$TV[w^{n+1}] \leq TV[w^n] \tag{2.16}$$

This method can then be included into the general MUSCL formulation by introducing yet another parameter Ψ,

$$\begin{aligned} w^L_{\frac{1}{2}} &= w_j + \frac{1-\phi}{4}\Psi(r^L)(w_j - w_{j-1}) + \frac{1+\phi}{4}\Psi(\frac{1}{r^L})(w_{j+1} - w_j) \text{ with} \\ & \qquad r^L = \frac{w_{i+1} - w_i}{w_i - w_{i-1}} \\ w^R_{\frac{1}{2}} &= w_i - \frac{1+\phi}{4}\Psi(r^R)(w_{j+1} - w_j) + \frac{1-\phi}{4}\Psi(\frac{1}{r^R})(w_{j+1} - w_j) \text{ with} \\ & \qquad r^R = \frac{w_{j+1} - w_j}{w_{j+2} - w_{j+1}} \end{aligned} \tag{2.17}$$

Some mostly used TVD slope limiters are, for instance,

$$\begin{aligned} \text{van Albada } \Psi(r) &= \max(0, \frac{r+r^2}{1+r^2}) \\ \text{minmod } \Psi(r) &= \max(0, \min(1, r)) \\ \text{superbee } \Psi(r) &= \max(0, \min(1, 2r), \min(2, r)) \end{aligned} \tag{2.18}$$

2.2.4 MUSCL-Hancock predictor-corrector

The main interest of MUSCL-Hancock method lies in its remarkable robustness and the ability to carry out stable computations of complex problems involving discontinuities and shocks. The method has been found by Steve Hancock in 1980, where the original MUSCL technique has been simplified van Leer (1984). The more recent version is presented in van Leer (2006). The stability of the method has been proven in Berthon (2005) and Berthon (2006).

The method can be sketched by using the following steps:

1. denoting the set of variables $\mathbf{W}$, perform the reconstruction on linear subcell distribution over the whole chosen set. In general, the choice of variables does not alter structure of algorithm. We define,

$$\delta W_j = \text{limiter } (W_j - W_{j-1}, W_{j+1} - W_j) \tag{2.19}$$

2. perform the advancement of solution by half time step using the following form of equations,

$$\mathbf{W}_t + (\mathbf{A}_{W_j})_j \mathbf{W}_x = 0 \tag{2.20}$$

where $\mathbf{A}_W$ is a matrix which depends on the variables choice for the reconstruction. For the primitive variables, this matrix $\mathbf{A}_W$ in direction x is

$$A_x = \begin{pmatrix} u & \rho & 0 & 0 & 0 \\ 0 & u & 0 & \frac{1}{\rho} & 0 \\ 0 & 0 & u & 0 & 0 \\ 0 & \rho c^2 & 0 & u & 0 \\ 0 & -K & 0 & 0 & u \end{pmatrix}$$

Note, that the source term S is included to this matrix A. The predictor step is then computed as,

$$\tilde{\mathbf{W}}_j = \mathbf{W}_j - \frac{\Delta t}{2\Delta x} \mathbf{A}_W \delta \mathbf{W}_j \tag{2.21}$$

3. using previously computed gradients, solve for the time-centered interface values,

$$\begin{aligned} \tilde{\mathbf{W}}_{j-\frac{1}{2}R} &= \tilde{\mathbf{W}}_j - \frac{1}{2}\delta \mathbf{W}_j \\ \tilde{\mathbf{W}}_{j+\frac{1}{2}R} &= \tilde{\mathbf{W}}_j + \frac{1}{2}\delta \mathbf{W}_j \end{aligned} \tag{2.22}$$

4. perform the computation for time-centered interface fluxes using the chosen numerical approximation flux scheme (e.g. HLLC), i.e.

$$\tilde{\mathbf{F}}_{j+\frac{1}{2}} = \mathbf{F}(\tilde{\mathbf{W}}_{j+\frac{1}{2}L}, \tilde{\mathbf{W}}_{j+\frac{1}{2}R}) \tag{2.23}$$

5. advance the solution over the full time-step

$$\mathbf{U}_j^{n+1} = \mathbf{U}_j - \frac{\Delta t}{\Delta x}(\tilde{\mathbf{F}}_{j+\frac{1}{2}} - \tilde{\mathbf{F}}_{j-\frac{1}{2}}) - \frac{\Delta t}{\Delta x} B(U_j)(u_{j+1/2} - u_{j-1/2}) \tag{2.24}$$

The reconstruction step can be applied to either the primitive or characteristic variables. Some authors note the latter choice leads to more robust solutions. The main focus of the analysis in this thesis is based on the choice of the primitive variables, but the characteristic reconstruction is studied for completeness. The case of the characteristic reconstruction in the limiting step (2.19) is replaced by the following transformation step

$$\delta W_j = R(\mathbf{W}_j)\text{limiter } (\Delta_j - \Delta_{j-1}, \Delta_{j+1} - \Delta_j) \tag{2.25}$$

where $\Delta_i^j = L(W_{j+1} - W_j)$, L is the matrix of left eigenvectors arranged as rows, and R is the matrix of right eigenvectors arranged as columns. Since both Jacobian matrix and primitive coefficient matrix relates to the same transformation, the left and right eigenvectors associated with primitive variables can be straightforwardly derived. For instance, the following associated matrices have been derived for the direction x,

$$R_x = \begin{bmatrix} 1 & 0 & 0 & -\frac{\rho}{c} & \frac{\rho}{c} \\ 0 & 0 & 0 & 1 & 1 \\ 0 & 1 & 0 & 0 & 0 \\ 0 & 0 & 0 & -\rho c & \rho c \\ 0 & 0 & 1 & \frac{K}{c} & -\frac{K}{c} \end{bmatrix} \quad L_x = \begin{bmatrix} 1 & 0 & 0 & 0 & \frac{\rho}{K} \\ 0 & 0 & 1 & 0 & 0 \\ 0 & 0 & 0 & 1 & \frac{\rho c^2}{K} \\ 0 & 1 & 0 & -\frac{1}{\rho c} & 0 \\ 0 & 1 & 0 & \frac{1}{\rho c} & 0 \end{bmatrix} \tag{2.26}$$

The limiting formulation (2.19) can be performed by simple MUSCL TVD techniques Harten (1983), as in original presentation of the method. However, in this study we replace this step by high-order reconstruction methods in the framework of predictor-corrector Hancock method. These high order methods are discussed in the next Chapter.

2.3 Inlet and outlet boundary conditions

The characteristic relations of Euler equations are used to impose boundary conditions as described in Goncalves & Zeidan (2018). The positive characteristics directed into the domain of interest define the variables which are set at boundaries.

The following notations are used: the superscript c stands for the variables imposed at the boundaries, s is for those which are computed by using the numerical scheme, V_t and V_n are the tangential and normal components of the mean velocity, respectively. The mathematical model which is based on 4-equations systems in present study leads to the following characteristic relations in two-dimensional flow,

$$-c^2(\rho^c - \rho^s) + (P^c - P^s) = 0 \tag{2.27}$$

$$V_t^c - V_t^s = 0 \tag{2.28}$$

$$\rho(\alpha^c - \alpha^s) - K(\rho^c - \rho^s) = 0 \tag{2.29}$$

$$(P^c - P^s) + \rho c(V_n^c - V_n^s) = 0 \tag{2.30}$$

$$(P^c - P^s) - \rho c(V_n^c - V_n^s) = 0 \tag{2.31}$$

The inlet boundaries have the values of α, densities of pure phases and velocity imposed. All variables can be evaluated at the boundaries by using the derivation of pressure from equation 2.31.

The outlet boundaries have the static pressure imposed and the variables are computed by using equations 2.27-2.30.

2.4 Synthesis

This Chapter reviewed the mathematical model of four equations which is an underlying of all computations to follow. The EOS for stiffened gas have been stated. Next, two formulations for the basic spatial discretization have been proposed. One of them, HLLC, is based on the Riemann solver and it is one of the mostly used formulation for problems where shock and discontinuities are present. The second method is KNP, which has been successfully applied in the context of compressible two-phase flow with the presence of the source term and has been particularly tested in the framework of MUSCL-Hancock predictor-corrector scheme. Consequently, the MUSCL-Hancock scheme has been described step by step with the description of the source treatment. The choice of the reconstruction variables has been discussed and the transformation step between primitive and characteristic variables was stated. The MUSCL and TVD limiters techniques which can be used as a first step of improving the spatial order are reviewed and key derivations are presented. The treatment of the boundary conditions is discussed.

Chapter 3

High-order numerical methods

The basic discretization based on the finite volume solver with predictor-corrector MUSCL-Hancock scheme generally leads to the second order of accuracy in space and time. However, it should be noted that the non-conservative part in 2.24 is always reconstructed with first order in time. In order to achieve the detailed reconstruction of complex physical phenomena, such numerical approach would require extremely fine grid, which might be unrealistic for computations in 3D. Similar accuracy with less points in computational domain can be achieved by using higher order numerical schemes, due to their formal faster convergence properties.

The higher order of accuracy can be obtained by two means: MUSCL TVD techniques as discussed in Section 2.2 to obtain second or third order convergence in space and more advanced numerical methods, addressed here as high-order numerical methods. The first choice, i.e. MUSCL TVD requires additional limiting procedures, such as slope limiters which are meant to reduce the nonphysical oscillations and, consequently, might lead to the diffusive solution around discontinuity regions. The second choice, on the other hand, the high-order numerical schemes, have more complex techniques of defining the areas of the solution where special treatment required and can change the order of the solution in these areas to lead to the monotonic, non-oscillating results. However, these methods can have a disadvantage of high computational complexity, difficult implementation methods and the treatment of critical regions which can be either too diffusive or too oscillating. Thus, the choice of the high-order methods which is a main concern of present Chapter, is based on these criteria. Particularly, the methods in consideration have to lead to the formal uniform order of accuracy higher than 2, the monotonicity properties have to be preserved and non-oscillating algorithms have to be thought. Moreover, the schemes have to be capable of working with problems with strong shocks and discontinuities and have the stability properties on the mesh with small value of the space step dx.

This Chapter organised as following. Firstly, a brief schemes overview is proposed. Secondly, the piecewise parabolic method (PPM) is presented with discussion of additional algorithms which can improve the monotonicity and reduce oscillations. More recent developments of the method are reviewed in the framework of the problems other than single-phase perfect gas, which has been originally a main topic of concern of PPM scheme. This class of the methods is followed by monotonicity preserving scheme (MP5) which has been designed particularly for the uniform high-order of the solution. Finally, the Chapter is concluded by the discussion of the weighted essentially non-oscillating WENO methods of third and fifth order, which are most widely used in the recent computational fluid dynamics computations.

3.1 High-order numerical methods overview

The computational fluid dynamics domain of research often characterised by the problems where the uniform solution is disturbed by discontinuities. This leads to a challenge of finding the high-

order schemes with preserving the sharp non-oscillatory reconstruction around discontinuities along with accuracy in smooth regions. One of the very first attempts to tackle this problem was Colella & Woodward (1984), where authors presented piecewise parabolic method using the four-point centered stencil for the interface value derivation. This method then uses limiting procedures to reduce the oscillations in regions of discontinuities. Some additional higher-order techniques coupled with limiting algorithms were introduced by, for example, Leonard (1991). However, this class of methods has a disadvantage of reducing the local scheme order near the extrema.

An alternative approach to the reducing local order limiting technique is an adaptive stencil techniques first introduced by Harten *et al.* (1987) inside his essentially non-oscillatory schemes ENO framework, where the 'smoothest' data is used to avoid interpolations in discontinuous regions. This method, however, does not use all available data in comparison with weighted ENO scheme by Liu *et al.* (1994) and Jiang & Shu (1996*b*), where authors derive the interface value using the weighted average of the interface values from all available stencils. The idea behind this method is to use the weighted average of all stencils around smooth areas of solution and only the 'smoothest' stencil in discontinuous regions. Nevertheless, earlier versions of ENO and WENO schemes are considered to be diffusive schemes and, thus, these schemes tend to smear the discontinuous regions.

Another technique is introduced by Suresh & Huynh (1997), where the limiting approach mentioned above is used. The base of the scheme is five-point stencil reconstruction. The advantage of this numerical technique is a larger stencil (in comparison with PPM) which leads to the less staircasing due to the dissipating nature of the scheme. According to the authors of the method, this scheme has several principal differences compared to those mentioned above: monotonicity and accuracy is preserved, specific design for Runge-Kutta time stepping and low computational complexity due to the simpler limiting procedures.

The high-order numerical methods are introduced in the framework of either HLLC Hancock Riemann solver or KNP Hancock solver. This is achieved by changing the calculation of the slope limiter $\delta\mathbf{W}_j$ in Hancock algorithm.

3.2 Piecewise parabolic method

This section proposes the derivation and discussion of the piecewise parabolic reconstruction strategy (PPM). The classic scheme which is presented in the form of accounting for the non-uniform meshes has been suggested in Colella & Woodward (1984).

The first step in reconstruction under the PPM strategy is based on building the parabolic distribution for the reconstructed variables by using its cell averages. We denote w the reconstructing variable and w_j^n the cell average of numerical solution $w(x,t^n)$ in the cell j, i.e. $(x_{j-\frac{1}{2}}, x_{j+\frac{1}{2}})$ at time t^n and where $x_{j+\frac{1}{2}}$, $x_{j-\frac{1}{2}}$ are the boundaries between the cells j and $j+1$, and j and $j-1$, respectively. The cell average w_j^n is defined according to the following formulation,

$$w_j^n = \frac{1}{\Delta x_j}\int_{x_{j-\frac{1}{2}}}^{x_{j+\frac{1}{2}}} w(x,t^n)dx, \tag{3.1}$$

where $\Delta x = x_{j+\frac{1}{2}} - x_{j-\frac{1}{2}}$ is the grid spacing of jth cell. The computational stencil w_j^n is formed by using this average w_j^n and other averages computed from the cells neighbouring to the cell j. This stencil is then used to construct the interpolation polynomial which is following the integration relation,

$$w_j^n = \frac{1}{\Delta x_j}\int_{x_{j-\frac{1}{2}}}^{x_{j+\frac{1}{2}}} w(x)dx \tag{3.2}$$

The parabolic interpolation function suggested in Colella & Woodward (1984) satisfies,

$$\begin{aligned} w(x) =& w_{L,j} + \epsilon(\Delta w_j + w_{6,j}(1-\epsilon)), \text{ where} \\ \epsilon =& \frac{x - x_{j-\frac{1}{2}}}{\Delta x_j},\ x_{j-\frac{1}{2}} \le x \le x_{j+\frac{1}{2}} \end{aligned} \tag{3.3}$$

with following interpolation coefficients,

$$\lim_{x\to x^+_{j-\frac{1}{2}}} w(x) = w_{L,j}, \quad \lim_{x\to x^-_{j+\frac{1}{2}}} w(x) = w_{R,j}$$

In order to define a unique polynomial, the coefficients must satisfy,

$$w_{L,j+1} = w_{R,j} = w^n_{j+\frac{1}{2}}, \tag{3.4}$$

where we denote $w^n_{j+\frac{1}{2}}$ to be an approximation to the numerical solution $w(x,t^n)$ at the border between cell j and $j+1$, i.e. the interface $x_{j+\frac{1}{2}}$. The evaluation of this quantity is performed as,

$$\begin{aligned} w^n_{j+\frac{1}{2}} =& w^n_j + \frac{\Delta x}{\Delta x_j + \Delta x_{j+1}}(w^n_{j+1} - w^n_j)\frac{1}{\sum_{k=-1}^{2}\Delta x_{j+k}} \\ &\times \Big(\frac{2\Delta x_{j+1}\Delta x_j}{\Delta x_j + \Delta x_{j+1}}\Big(\frac{\Delta x_{j-1} + \Delta x_j}{2\Delta x_j + \Delta x_{j+1}} - \frac{\Delta x_{j+2} + \Delta x_{j+1}}{2\Delta x_{j+1} + \Delta x_j}\Big)(w^n_{j+1} - w^n_j) \\ &- \Delta x_j \frac{\Delta x_{j-1} + \Delta x_j}{2\Delta x_j + \Delta x_{j+1}}\delta w_{j+1} - \Delta x_{j+1}\frac{\Delta x_{j+1} + \Delta x_{j+2}}{\Delta x_j + 2\Delta x_{j+1}}\delta w_j\Big) \end{aligned} \tag{3.5}$$

The slope δw_j can be set as a simple average slope by using the cell average quantities. For instance, for w^n_j it states,

$$\begin{aligned} \delta w_j =& \frac{\Delta x_j}{\Delta x_{j-1} + \Delta x_j + \Delta x_{j+1}} \times \\ & \left(\frac{2\Delta x_{j-1} + \Delta x_j}{\Delta x_j + \Delta x_{j+1}}(w^n_{j+1} - w^n_j) + \frac{\Delta x_j + 2\Delta x_{j+1}}{\Delta x_{j-1} + \Delta x_j}(w^n_j - w^n_{j-1})\right) \end{aligned} \tag{3.6}$$

The alternative slope should be used in order to ensure that the value $w_{j+\frac{1}{2}}$ is located between the averages of the two neighbouring cells. Moreover, this slope leads to the sharper representation of discontinuities compared with the average slope. The modified formulation is,

$$\delta_m w_j = \begin{cases} \min(|\delta w_j|, 2|w^n_j - w^n_{j-1}|, 2|w^n_{j+1} - w^n_j|)\mathrm{sgn}(\delta w_j), \\ \text{if } (w^n_{j+1} - w^n_j)(w^n_j - w^n_{j-1}) > 0 \\ 0, \text{ otherwise} \end{cases} \tag{3.7}$$

Assuming the solution is smooth, the values defined in 3.4 are applied. Otherwise, several modifications are proposed in order to obtain better results in more complicated problems.

3.2.1 Monotonocity algorithm

The oscillation-free reconstruction of the variables is conditioned by maintained monotonic distribution in each cell. This is achieved by the following algorithm. Firstly, should w^n_j be determined to be local minimum or maximum, the $w(x)$ is set constant. Saying that we have,

$$w_{L,j} \to w^n_j, w_{R,j} \to w^n_j, \text{ if } (w_{R,j} - w^n_j)(w^n_j - w_{L,j}) \le 0 \tag{3.8}$$

Secondly, the case when the value of w^n_j is close enough to $w_{R,j}$ or $w_{L,j}$, the value of interpolation function might fall outside the defined range. Should this be the case, the interface quantities are reset as,

$$\begin{aligned} &w_{L,j} \to 3w^n_j - 2w_{R,j} \text{ if } (w_{R,j} - w_{L,j})(w^n_j - \frac{1}{2}(w_{L,j} + w_{R,j})) > \frac{(w_{R,j} - w_{L,j})^2}{6} \\ &w_{R,j} \to 3w^n_j - 2w_{L,j} \text{ if } -\frac{(w_{R,j} - w_{L,j})^2}{6} > (w_{R,j} - w_{L,j})(w^n_j - \frac{1}{2}(w_{L,j} + w_{R,j})) \end{aligned} \tag{3.9}$$

3.2.2 Contact discontinuity detection

There are cases where the interface values should be adjusted if the cell is defined to be within contact discontinuity. One would search for a method to reproduce a sharper profile if contact discontinuity is detected by modifying the interpolation polynomial. Such a cell can be identified by using several conditions. Firstly, the third derivative of the density should be large enough along with the second derivative changing its sign across the cell. Secondly, the first and third derivatives should have opposite signs. Lastly, we should determine weather or not the density change is sufficiently large. In the following, the sketched framework of using the contact discontinuity detection is presented.

The modified left and right interface values in case of contact discontinuity detection are,

$$\begin{aligned} w_{L,j} &\rightarrow w^d_{L,j} = w^n_{j-1} + \frac{1}{2}\delta_m w_{j-1} \\ w_{R,j} &\rightarrow w^d_{R,j} = w^n_{j+1} - \frac{1}{2}\delta_m w_{j+1} \end{aligned} \tag{3.10}$$

In order to define the switching rule between 3.4 and 3.10, the generalisation of the expressions for interface values follow,

$$\begin{aligned} w_{L,j} &\rightarrow w_{L,j}(1-\nu_j) + w^d_{L,j}\nu_j \\ w_{R,j} &\rightarrow w_{R,j}(1-\nu_j) + w^d_{R,j}\nu_j \end{aligned} \tag{3.11}$$

with switching coefficient ν_j defined as,

$$\nu_j = \max(0, \min(\nu^1(\tilde{\nu}_j - \nu^2), 1)) \tag{3.12}$$

where

$$\tilde{\nu}_j = \begin{cases} -\left(\frac{\delta^2\rho^n_{j+1} - \delta^2\rho^n_{j-1}}{x_{j+1}-x_{j-1}}\right)\left(\frac{(x_j - x_{j-1})^3 + (x_{j+1}-x_j)^3}{\rho^n_{j+1}-\rho^n_{j-1}}\right) \\ \text{if } -\delta^2\rho^n_{j+1}\delta^2\rho^n_{j-1} > 0, \\ |\rho^n_{j+1} - \rho^n_{j-1}| - \min(|\rho^n_{j+1}|, |\rho^n_{j-1}|) > 0 \\ 0 \qquad\qquad\qquad\qquad\qquad\qquad \text{otherwise} \end{cases} \tag{3.13}$$

and

$$\delta^2\rho^n_j = \frac{1}{\Delta x_{j-1} + \Delta x_j + \Delta x_{j+1}} \left| \frac{\rho^n_{j+1} - \rho^n_j}{\Delta x_{j+1} + \Delta x_j} - \frac{\rho^n_j - \rho^n_{j-1}}{\Delta x_j + \Delta x_{j-1}} \right| \tag{3.14}$$

The constants ν^1 and ν^2 are meant to switch between 3.4 and 3.10, while the parameter is set to determine how big the change in the cell solution should be that it is considered to be a contact discontinuity. Here, we propose these parameters based on the approach presented in Zheng & Lee (2013), i.e. $\nu^1 = 18$, $\nu^2 = 0.05$ and $\epsilon = 0.05$. These parameters have been tested by authors in the framework of multi-phase problems with EOS of stiffened gas.

Finally, the condition for the cell to be determined as a contact discontinuity is,

$$\gamma_j K_0 \frac{|\rho_{j+1} - \rho_{j-1}|}{\min(\rho_{j+1}, \rho_{j-1})} \geq \frac{|p_{j+1} - p_{j-1}|}{\min(p_{j+1} + \gamma_{j+1}\pi_{j+1}, p_{j-1} + \gamma_{j-1}\pi_{j-1})}, \tag{3.15}$$

where $K_0 = 0.15$. This condition allows not only to switch between the formulations with and without contact discontinuity adjustment, but also to determine the degree to which we would like to impose the contact discontinuity detection. For instance, to determine how large the density gradient and shock should be for it being considered as contact discontinuity.

3.2.3 Flattening method

The PPM method assumes to tackle the post-shock oscillations issues in the situations where the characteristic speed of the post-shock is higher than shock speed. The original presentation of the method by Colella & Woodward (1984) suggests several methods to reduce these oscillations by adding the dissipation. These methods have been designed by authors to work with problems where the perfect gas EOS are employed and, what is more, with problems of single-phase flows. Here, we review the adjusted approach by Zheng & Lee (2013), where authors suggest less complex modification of original 'flattening' method, which is essentially an order reduction of the interpolation function around strong shocks.

We define the weighted coefficient $f_j \in [0,0.5]$ which goes to zero as we move further away from the shock,

$$\begin{aligned} f_j =& \max(0, \min(0.5, \bar{f}_j)), \text{ with } \bar{f}_j = \max(\tilde{f}_{j-1}, \tilde{f}_j, \tilde{f}_{j+1}) \\ & \text{and} \\ \tilde{f}_j =& \omega_j \times \max\Big(0, (\frac{p_{j+1} - p_{j-1}}{p_{j+2} - p_{j-2}} - \omega^{(1)})\omega^{(2)}\Big) \end{aligned} \tag{3.16}$$

where $\omega^{(1)}$=0.75, $\omega^{(2)}$=5. The value of ω_j is computed as,

$$w_j = \begin{cases} 1 & \text{if} \frac{(p_{j+1}-p_{j-1})}{\min(p_{j+1},p_{j-1})} \text{ and } u_{j-1} - u_{j+1} > 0 \\ 0 & \text{otherwise} \end{cases} \tag{3.17}$$

where ϵ=0.33.

The present approach is different from the one in Colella & Woodward (1984) by maximum value of weighted coefficient f_j where it can be set equal to 1 if we would like to lower the order of the scheme in case of smaller shocks. Moreover, the value $\tilde{f}_j$ could be computed based on the choice of two stencils depending on the direction of the shock propagation.

3.2.4 Extrema preservation

An additional technique of improving the PPM method has been suggested more recently by Colella & Sekora (2008), where authors emphasise on the drawback of the classical strategy to reduce the local order of the scheme around the discontinuities, i.e. the reduction to the 1st order at all extrema. Their improved approach of extrema preservation is based on the modifying the original framework at only extrema points by introducing the non-linear combinations of the second derivatives approximations. This idea is meant to keep the overall accuracy of the method while providing the reconstruction at extrema points without clipping.

The method includes the initialisation of the interface value to be of higher, sixth order,

$$w_{j+\frac{1}{2}} = \frac{37}{60}(w_j^n + w_{j+1}^n) - \frac{2}{15}(w_{j-1}^n + w_{j+2}^n) + \frac{1}{60}(w_{j-2}^n + w_{j+3}^n) \tag{3.18}$$

This value is then constrained in the areas where the condition in 3.7 does not hold. The constraints are based on the evaluations of the second order derivative approximations, which are,

$$\begin{aligned} (D^2w)_{j+\frac{1}{2}} &= \frac{3}{\Delta x^2}(w_j^n - 2w_{j+\frac{1}{2}}^n + w_{j+\frac{1}{2}}^n)(D^2w)_{j+\frac{1}{2},L} \\ &= \frac{1}{\Delta x^2}(w_{j-1}^n - 2w_j^n + w_{j+1}^n)(D^2w)_{j+\frac{1}{2},R} \\ &= \frac{1}{\Delta x^2}(w_j^n - 2w_{j+1}^n + w_{j+2}^n) \end{aligned}$$

Should the signs of the above computed derivatives, $(D^2w)_{j+\frac{1}{2},L}$, $(D^2w)_{j+\frac{1}{2},R}$ and $(D^2w)_{j+\frac{1}{2}}$, be the same, the following quantity is computed,

$$(D^2w)_{j+\frac{1}{2},lim} = s\min(C(|D^2w)_{j+\frac{1}{2},L}|, C|(D^2w)_{j+\frac{1}{2},R}|, |(D^2w)_{j+\frac{1}{2}}|), \tag{3.19}$$

where $s = \text{sgn}((D^2w)_{j+\frac{1}{2}})$. Otherwise, we set $(D^2w)_{j+\frac{1}{2},lim} = 0$. Using these evaluations we modify the interface value as,

$$w^n_{j+\frac{1}{2}} = \frac{1}{2}(w^n_j + w^n_{j+1}) - \frac{\Delta x^2}{3}(D^2w)_{j+\frac{1}{2},lim}), \text{where } C > 1 \text{ is a constant} \tag{3.20}$$

We then define the condition for the location at local extrema. If the following inequality

$$\begin{aligned}(w^n_{j+\frac{1}{2}} - w^n_j)(-w^n_{j-\frac{1}{2}} + w^n_j) \leq 0 \text{or} \\ (w^n_{j-1} - w^n_j)(-w^n_{j+1} + w^n_j) \leq 0\end{aligned} \tag{3.21}$$

holds true, then we are at local extrema and the following constraints to the interface value are defined,

$$\begin{aligned}(D^2w)_j &= \frac{2w_{6,j}}{\Delta x^2} \\ (D^2w)_{j,L} &= \frac{1}{\Delta x^2}(w^n_{j-2} - 2w^n_{j-1} + w^n_{j+1}) \\ (D^2w)_{j,R} &= \frac{1}{\Delta x^2}(w^n_j - 2w^n_{j+1} + w^n_{j+2}) \\ (D^2w)_{j,C} &= \frac{1}{\Delta x^2}(w^n_{j-1} - 2w^n_j + w^n_{j+1})\end{aligned} \tag{3.22}$$

As before, if the above four quantities have the same sign, then

$$\begin{aligned}(D^2w)_{j,lim} = s^{'}\min(C(|D^2w)_{j,L}|, C|(D^2w)_{j,R}|, C|(D^2w)_{j,C}|, |(D^2w)_j|) \\ \text{with } s^{'} = \text{sgn}((D^2w)_j)\end{aligned} \tag{3.23}$$

and $(D^2w)_{j,lim} = 0$ otherwise. The interface value follows,

$$\begin{aligned}w^n_{j+\frac{1}{2}} &= w^n_j + (w^n_{j+\frac{1}{2}} - w^n_j)\frac{(D^2w)_{j,lim}}{(D^2w)_j} \\ w^n_{j-\frac{1}{2}} &= w^n_j + (w^n_{j-\frac{1}{2}} - w^n_j)\frac{(D^2w)_{j,lim}}{(D^2w)_j}\end{aligned} \tag{3.24}$$

The second part of the expression is set to be equal to zero if the denominator diminishes. On the other hand, if the condition of the local extrema is not satisfied, we continue with monotonicity constraints described in the subsection above. However, the authors in Colella & Sekora (2008) note that the original monotonicity constraints are being too restrictive and suggest simpler approach. In particular we are looking for the interpolation function to satisfy the following van Leer-like condition,

$$\begin{aligned}&s^{''}w^n_{j-1} \leq s^{''}I_{j,-}(\sigma) \leq s^{''}w^n_j \leq s^{''}I_{j,+}(\sigma) \leq s^{''}w^n_{j+1} \\ &s^{''} = \text{sgn}(w^n_{j+1} - w^n_{j-1})\end{aligned} \tag{3.25}$$

where σ is CFL number.

For simplicity we define, $w_{j,\frac{+}{-}} = w_{j,\frac{+}{-}\frac{1}{2}} - w^n_j$. Should any of the two $|w_{j,\frac{+}{-}}| \geq 2|w_{j,\frac{-}{+}}|$ hold, we compute the following slopes,

$$\delta I_{ext} = \frac{-w^2_{j,\frac{+}{-}}}{4(w^+_j - w^-_j)}, \ \delta w = w^n_{j_-+1} - w^n_j \tag{3.26}$$

Finally, if $s^{'}\delta I_{ext} \geq s^{'}\delta w$, the interface values are computed as,

$$\begin{aligned}w^n_{j+\frac{1}{2}} &= w^n_j - (2\delta w + 2s((\delta w)^2 - \delta w w_{j,-})^{\frac{1}{2}}) \\ w^n_{j-\frac{1}{2}} &= w^n_j - (2\delta w + 2s((\delta w)^2 - \delta w w_{j,+})^{\frac{1}{2}})\end{aligned} \tag{3.27}$$

The PPM method leads to the third order method for the smooth problems (e.g. linear advection) and fourth order in the limit of vanishing CFL. The strategy described here can be easily applied to the primitive, conservative or characteristic variables, where the latter one needs the derivation of the left and right eigenvectors (see Section 2 for more details). Moreover, the derivation of PPM is ready to be used on non-uniform mesh. This method provides some choices: for the problems involving contact discontinuity (water-gas shock tube problems, for instance), the contact discontinuity detection procedure can be enabled, and disabled otherwise. Moreover, depending on the degree of the involved shock, more dissipation can be added in order to avoid oscillations. Finally, where the extrema clipping is observed, an application of extrema preserving technique can be switched. While complex, the PPM method, nevertheless, provides plenty of possibilities to resolve different kind of problems.

3.3 Monotonicity preserving method

This section details the MP5 numerical framework which includes two principal steps according to Suresh & Huynh (1997): the computation of *original* value and *modified* or *final* value. To start with, a fourth-degree polynomial is formulated at $x_{j+1/2}$ as fifth-order in space interface value,

$$w^L_{j+1/2} = (2w_{j-2} - 13w_{j-1} + 47w_j + 27w_{j+1} - 3w_{j+2})/60 \tag{3.28}$$

The 3.28 can be modified to become fourth-order formulation with low phase error,

$$w^L_{j+1/2} = (9w_{j-2} - 56w_{j-1} + 194w_j + 104w_{j+1} - 11w_{j+2})/240 \tag{3.29}$$

The interface values defined by 3.28 and 3.29 might lead to the non-physical oscillations near the regions of discontinuity as noted by authors in Suresh & Huynh (1997), which are eliminated by using the limiting procedure to obtain *final* interface value. In order to preserve monotonicity it is proposed to use an assumption that at interface $j - 1/2$, the value $w^L_{j-1/2}$ belongs to the following interval,

$$w^L_{j-1/2} \in I[w_{j-1}, w_j]$$

while the upper limit (UL) value for the interface $j + 1/2$ is,

$$w^{UL} = w_j + \alpha(w_j - w_{j-1}),$$

where $\alpha \geq 2$ and

$$w^L_{j+1/2} \in I[w_j, w^{UL}]$$

Then, the obtained solution belongs to the interval between w_{j-1} and w_j, which is a consequent result of the condition $w^{UL} - w_{j-1} \leq (\alpha + 1)(w_j - w_{j-1})$.

The choice of the specific values for α depends on the time stepping scheme one can choose to work with. However, according to Suresh & Huynh (1997), $\alpha = 4$ works better for Runge-Kutta type of methods compared to $\alpha = 2$ which leads to the staircasing. These values are not discussed in the framework of other temporal resolutions.

Assuming that the above interval conditions hold for all j, we rewrite,

$$w^L_{j+1/2} \in I[w_j, w_{j+1}]$$

These interval conditions imply that the value $w^L_{j+1/2}$ belongs to the intersection of $I[w_j, w_{j+1}]$ and $I[w_j, w^{UL}]$. We note that one end of this intersection is w_j and the other one is set to be the monotonicity preserving (MP) median function, w^{MP} of w_j, w_{j+1}, w^{UL}, which can be expressed using the minmod function,

$$\omega^{MP} = w_j + \mathbf{minmod}[w_{j+1} - w_j, \alpha(w_j - w_{j-1})] \tag{3.30}$$

Hence, this results in,

$$w^L_{j+1/2} \in I[w_j, w^{MP}]$$

The median function can be employed to satisfy the above condition. That is,

$$w^L_{j+1/2} \leftarrow \textbf{median}(w^L_{j+1/2}, w_j, w^{MP}) \tag{3.31}$$

This condition has a disadvantage of local accuracy decrease near the discontinuity. In order to fix thus issue, Suresh & Huynh (1997) suggests the technique where the constraint 3.31 is coupled with additional accuracy preserving constraint. This is achieved by enlarging the intervals using the adjoining median value and extrapolating interface values linearly. This means,

$$w^{FL} = w_j + \frac{1}{2}(w_j - w_{j-1}); w^{FR} = w_{j+1} + \frac{1}{2}(w_{j+1} - w_{j+2}); w^{AV} = \frac{1}{2}(w_j + w_{j+1}) \tag{3.32}$$

Setting the median value, $w^{MD} = \textbf{median}(w^{AV}, w^{FL}, w^{FR})$, the constraint is relaxed to,

$$w^L_{j+1/2} \in I[w_j, w_{j+1}, w^{MD}] \tag{3.33}$$

It is important to note, that this monotonicity constraints were initially derived for solving simple linear advection equation, where the scheme demonstrated the characteristics of monotonicity and uniformly high-order of accuracy. However, in practice, these expectations are not necessarily satisfied in the non-linear solutions.

3.4 Weighted essentially non-oscillatory method

This section presents weighted essentially non-oscillatory (WENO) scheme, which is an extension of essentially non-oscillatory method (ENO), and had been first introduced by Liu *et al.* (1994). The main difference between ENO and WENO is the underlying method of reconstruction to achieve high-order accurate approximation result. In contrast to the ENO, where adaptive-stencil method had been used, WENO strategy is based on convex combination. This convex counterpart to the adaptive-stencil uses all respective stencils assigned to each cell. It is also coupled with convex combination of all respective reconstructing stencil polynomials derived as an approximating polynomial. The former is achieved by the derivation of appropriate convex combination weights. Among the advantages of WENO method comparing with non-weighted counterpart, the key ones rely in smoother data dependence, which is expected to result in less oscillations but, at the same time, sharper representation. In order to describe general idea behind the WENO reconstruction, we consider the general extrapolation problem. The fifth order strategy is proposed as an example.

Given the uniform mesh $x_i = i\Delta x$ with corresponding points in the middle, that is, $x_{i+\frac{1}{2}} = \frac{1}{2}(x_i + x_{i+1})$ and the interval $I_i = (x_{i-\frac{1}{2}}, x_{i+\frac{1}{2}})$, cell average values of arbitrary function $w(x)$ are computed,

$$\tilde{w}_i = \frac{1}{\Delta x}\int_{x-\frac{1}{2}}^{x+\frac{1}{2}} w(x)dx$$

We are looking for approximating values of the function u_x at the interface nodes, $x_{i+\frac{1}{2}}$. Defining some primitive function with lower limit given by any arbitrary fixed point,

$$W(x) = \int_{x_{-\frac{1}{2}}}^{x} w(\epsilon)d\epsilon$$

This results in,

$$W(x_{i+\frac{1}{2}}) = \int_{x_{-\frac{1}{2}}}^{x+\frac{1}{2}} w(\epsilon)d\epsilon = \sum_{l=0}^{i}\int_{x_{l-\frac{1}{2}}}^{x_{l+\frac{1}{2}}} w(\epsilon)d\epsilon = \sum_{l=0}^{i}\Delta x\tilde{w}_l$$

(3.34)

This means that the values of all half nodes are known, $W(x_{i+\frac{1}{2}})$, given the cell averages $\bar{w}_l$. Hence, the computation of the interpolation polynomial for the primitive function $W(x)$ is possible, which will be used as an approximation to $w(x) = W'(x)$.

For the general understanding purposes, let $P_1(x)$ be the polynomial of the highest degree of three to interpolate given function $W(x)$ at four points, $x_{j+\frac{1}{2}}, j = i-3, i-2, i-1, i$, and set $p_1(x) = P_1'(x)$, where it can be proven that $p_1(x)$ is a unique polynomial with a highest degree of two and which reconstructs $w(x)$ over the stencil $S_1 = I_{i-2}, I_{i-1}, I_i$. That is,

$$(\bar{p}_1)_j = \frac{1}{\Delta x}\int_{x_{j-\frac{1}{2}}}^{x_{j+\frac{1}{2}}} p_1(x)dx = \bar{u}_j,\ \ j = i-2, i-1, i \tag{3.35}$$

Assuming the smoothness of the function $w(x)$ in the stencil S_1, the approximation to the value $w(x_{i+\frac{1}{2}})$ is $w^{(1)}_{i+\frac{1}{2}} \equiv p_1(x_{i+\frac{1}{2}})$ or explicitly,

$$w^{(1)}_{j+\frac{1}{2}} = \frac{1}{3}\bar{w}_{j-2} - \frac{7}{6}\bar{w}_{j-1} + \frac{11}{6}\bar{w}_j$$

which is third order accurate, i.e. $w_{i+\frac{1}{2}^{(1)}} - w(x_{i+\frac{1}{2}}) = \mathcal{O}(\Delta x^3)$ by using the relationship $p_1 = P_1'(x)$. In similar manner two more stencils can be considered, $S_2 = I_{i-1}, I_i, I_{i+1}$ and $S_3 = I_i, I_{i+1}, I_{i+2}$, which lead to two other polynomials, $(\bar{p}_2)_j = \bar{w}_j$ for $j = i-1, i, i+1$ and $(\bar{p}_3)_j = w_j$ for $j = i, i+1, i+2$, respectively. Explicit approximation is then given by,

$$w^{(2)}_{j+\frac{1}{2}} \equiv p_2(x_{j+\frac{1}{2}}) = -\frac{1}{6}\bar{w}_{j-1} + \frac{5}{6}\bar{w}_j + \frac{1}{3}\bar{w}_{j+1}$$

$$w^{(3)}_{j+\frac{1}{2}} \equiv p_3(x_{j+\frac{1}{2}}) = \frac{1}{3}\bar{w}_j + \frac{5}{6}\bar{w}_{j+1} - \frac{1}{6}\bar{w}_{j+2}$$

which is yet again a third order accurate, given the function is smooth enough in the stencils S_2 and S_3.

To sum up, assuming that the function is globally smooth, we can expect third order accurate approximations across whole considered domain and we can choose any of the obtained approximations based on other reasoning, e.g. stability or local error estimates.

On the other hand, there is an interest to work with a union of these three stencils. That is, our larger stencil is $S = I_{i-2}, I_{i-1}, I_i, I_{i+1}, I_{i+2}$, which allows to obtain the polynomial $p(x)$ of degree four at most which satisfies $\bar{p}_j = \bar{w}_j$, where $j = i-2, i-1, i, i+1, i+2$ and which leads to explicitly expressed approximation,

$$w_{j+\frac{1}{2}} \equiv (x_{j+\frac{1}{2}}) = \frac{1}{30}\bar{w}_{j-2} - \frac{13}{60}\bar{w}_{j-1} + \frac{47}{60}\bar{w}_j + \frac{9}{20}\bar{w}_{j+1} - \frac{1}{20}\bar{w}_{j+2}$$

with fifth order of accuracy, $w_{j+\frac{1}{2}} - w(x_{j+\frac{1}{2}}) = \mathcal{O}(\Delta x^5)$, if the function $w(x)$ is globally smooth in our new large stencil S.

The core point of WENO method is an observation that, in fact, we can rewrite in this particular case the fifth order formulation, using the large stencil, as a linear convex combination using previously derived third-order approximations, $w^{(1)}_{j+\frac{1}{2}}$, $w^{(2)}_{j+\frac{1}{2}}$, $w^{(3)}_{j+\frac{1}{2}}$. Saying that, we have

$$w_{j+\frac{1}{2}} = \gamma_1 w^{(1)}_{j+\frac{1}{2}} + \gamma_2 w^{(2)}_{j+\frac{1}{2}} + \gamma_3 w^{(3)}_{j+\frac{1}{2}} \tag{3.36}$$

where $\gamma_1 = \frac{1}{10}$, $\gamma_2 = \frac{3}{5}$ and $\gamma_3 = \frac{3}{10}$ are constants satisfying the condition $\sum_i \gamma_i = 1$.

Special attention deserves the case when the function $w(x)$ has a discontinuity in $[x_{i-2}, x_{i+2}]$, and which means that not all three approximations $w^{(1)}_{j+\frac{1}{2}}$, $w^{(2)}_{j+\frac{1}{2}}$, $w^{(3)}_{j+\frac{1}{2}}$ are equally good. To obtain the guaranteed third order accuracy and essentially non-oscillatory behaviour Harten *et al.* (1987), suggest to use one of these three approximations based on the strategy of finding local smoothness of given data w_j for $i-2 \leq j \leq i+2$ derived from divided differences. This would work well

should $w(x)$ be smooth in at least one of the stencils discussed above. On the contrary, WENO method suggests to derive the approximation using the convex combination of three third-order approximations, hence,

$$w_{j+\frac{1}{2}} = \omega_1 w^{(1)}_{j+\frac{1}{2}} + \omega_2 w^{(2)}_{j+\frac{1}{2}} + \omega_3 w^{(3)}_{j+\frac{1}{2}}, \tag{3.37}$$

where $\sum_i \omega_i = 1$ and $\omega_j \geq 0$. The new weights are not linear and will be approximately equal to γ_j if the function $w(x)$ is smooth in the stencil S and zero if the discontinuity had been detected in any of the stencils S_j. However, in the later case we assume that $w(x)$ is smooth in at least one of the other two stencils. Otherwise, the oscillations near discontinuities can occur. Thus, a particular design of nonlinear weights is required. The WENO class of the schemes uses the following idea to compute these nonlinear weights.

Let the nonlinear weight ω_j be close to the linear weight γ_j if the function $w(x)$ is smooth in each of the substencils of S and close to zero near discontinuities. This allows to retain the improved accuracy in smooth regions and reduce the oscillations in discontinuities area. Define the smoothness indicator β_j as,

$$\beta_j = \sum_{r=1}^{2} \Delta x_j 2r - 1 \int_{x_{j+1/2}}^{x_{j+1/2}} \Big(\frac{d^r}{dx^r} p^{(j)}(x)\Big)^2 dx, \tag{3.38}$$

where $\Delta x_j 2r - 1$ is a scaling factor. The above formulation can be seen as a scaled square sum of the L^2 derivatives norms of the reconstruction polynomial $p^{(j)}(x)$ over the subinterval I.

This section discusses two types on WENO schemes, i.e. of third, WENO3, and fifth WENO5 order of accuracy. Each of them has different variations of formulations to achieve better convergence while reducing the oscillations. One of the main ideas of the research around the improvement of this class of schemes has been around the calculation of the smoothness indicator β_j, which is used in order to calculate the nonlinear weights ω_j and determines whether or not the function $w(x)$ is smooth in the stencil S_j. Another popular topic is the small number ϵ which was originally meant to make the denominator to be non zero. However, later it has been established that this number makes the scheme being bias towards upwind- or central-like scheme. It is, thus, important to determine which strategy is the best for the problem one solves. The focus of the following subsections is on the third order and fifth order method and mostly different strategies to tackle the question of smoothness indicator formulations and appropriate ϵ number.

3.4.1 WENO of third order

The originally presented WENO of third order in Jiang & Shu (1996*b*) is based on the convex combination of the second-order approximations in each of the two candidate stencils, S_0 and S_1, that is

$$w_{j+\frac{1}{2}} = \omega_0 w_{0,j+\frac{1}{2}} + \omega_1 w_{1,j+\frac{1}{2}} \tag{3.39}$$

with

$$w_{0,j+\frac{1}{2}} = -\frac{1}{2} w_{j-1} + \frac{3}{2} w_j, \;\; w_{1,j+\frac{1}{2}} = \frac{1}{2} w_j + \frac{1}{2} w_{j+1} \tag{3.40}$$

Jiang & Shu (1996*b*) suggested the following non-linear weight function,

$$\omega_k = \frac{\alpha_k}{\sum_{s=0}^{1} \alpha_s}, \;\; \alpha_k = \frac{d_k}{(\epsilon + \beta_k)^2}, \;\; k = 0, 1, \tag{3.41}$$

where ϵ is introduced to avoid zero in denominator and d_k is the optimal weights choice which leads to the third-order upwind scheme with the following values,

$$d_0 = \frac{1}{3}, \;\; d_1 = \frac{2}{3} \tag{3.42}$$

and β_k is the smoothness indicator computed as,

$$\beta_0 = (w_{j-1} - wj)^2,\ \beta_1 = (w_j - w_{j+1})^2 \tag{3.43}$$

The above formulation has been widely used particularly due to the calculation of nonlinear weights as per 3.41. However, this procedure has been later proven to fail to achieve the desired order of convergence at critical points and to lead to the oscillations around discontinuities and shocks. This drawback has been successfully improved by Borges *et al.* (2008). In particular, the non-linear weights are modified and are computed in order to lead to faster achievement of the WENO weights towards the optimal weights. These new nonlinear weights computed as,

$$\begin{gathered}\omega_k = \frac{\alpha_k}{\sum_{s=0}^{1}} = \frac{d_k(1+\frac{\tau}{\beta_k})}{\sum_{s=0}^{1} d_s(1+\frac{\tau}{\beta_s})} = d_k(1+\frac{\tau}{\beta_k}), \\ \text{where } \alpha_k = d_k(1+\frac{\tau}{\beta_k+\epsilon}),\ k=0,1,\ \text{and } \tau = |\beta_0 - \beta_1|\end{gathered} \tag{3.44}$$

The above modification has been popular to particularly resolve the discontinuities. However, originally proposed ϵ number for WENO methods failed to achieve the same speed of convergence for the third order.

The alternative improvement has been suggested by Wu & Zhao (2013) where authors attempt to compute the so-called reference indicator which satisfies the sufficient condition to achieve the third order scheme. The new smoothness indicator covering the complete stencil is formulated as,

$$\beta_3 = \frac{13}{12}(w_{j-1} - 2w_i + w_{j+1})^2 + \frac{1}{4}(w_{j-1} - w_{j+1})^2 \tag{3.45}$$

and the new reference smoothness indicator replaces τ_Z and has the form,

$$\tau_N = |\frac{\beta_0 + \beta_1}{2} - \beta_3| \tag{3.46}$$

or alternative one as have been proposed in Xu & Wu (2017);

$$\tau_P = |\frac{\beta_0 + \beta_1}{2} - \frac{1}{4}(w_{j-1} - w_{j+1})^2| \tag{3.47}$$

Nevertheless, while these methods address the problem of the right order at critical points, it had been pointed out in Baeza *et al.* (2013), that these modifications involve an additional exponent and, thus, depend on the data scaling. This issue has been tried to be resolved by adjusting the ϵ number to keep the accuracy, where the proper scaling would be required.

Thus, an optimized WENO scheme, proposed by Baeza *et al.* (2013), involves an additional node to the original two-node stencil. Authors argue that by using the conventional stencil in the framework of third order WENO scheme, it is not possible to achieve the following properties at the same time:

- discontinuities and critical points detection in the given data
- independence of the weights formulation from data scaling
- avoidance of the ϵ-parameter tuning

Hence, the new modified procedure is suggested to satisfy all the above points at once by introducing one additional node. While the original stencil of two nodes had been defined as $S = (w_{j-1}, w_j, w_{j+1})$, the new extension of this stencil is $S_e = (w_{j-1}, f_j, f_{j+1}), f_{j+2})$.

We start by defining the interpolating polynomials which correspond to two stencils, i.e. $S_0 = (w_{j-1}, w_j)$ and $S_1 = (w_j, w_{j+1})$ for which the smoothness indicators remain unchanged and are computed as in Jiang & Shu (1996*b*). As for the additional node, new associated smoothness indicator is computed as $\beta_{oweno3} = (w_{j+2} - w_{j+1})^2$. The weights are then computed with ϵ being the same small quantity to avoid zero in denominator,

$$\begin{aligned} \tilde{\omega}_0 &= \frac{\beta_1 + \epsilon}{\beta_0 + \beta_1 + 2 * \epsilon} \\ \tilde{\omega}_1 &= \frac{\beta_0 + \epsilon}{\beta_0 + \beta_1 + 2 * \epsilon} = 1 - \omega_0 \end{aligned} \tag{3.48}$$

The corrector weight is proposed and computed as following,

$$\omega = \frac{J}{J + \tau + \epsilon} \text{ with } J = \beta_0(\beta_1 + \beta_2) + (\beta_0 + \beta_1)\beta_2 \tag{3.49}$$

and the quantity τ involves the extended stencil and is defined as,

$$\tau = dI,\ d = (-w_{j-1} + 3w_j - 3w_{j+1} + w_{j+2})^2,\ \beta = \beta_0 + \beta_1 + \beta 2 \tag{3.50}$$

The new corrector weight is then computed with $c_0 = \frac{1}{3}$ and $c_1 = \frac{2}{3}$,

$$\begin{aligned} \omega_0 &= \omega c_0 + (1 - \omega)\tilde{\omega}_0 \\ \omega_1 &= \omega c_1 + (1 - \omega)\tilde{\omega}_1 \end{aligned} \tag{3.51}$$

Finally the reconstruction of the interface values is,

$$w_{j+\frac{1}{2}} = \omega_0 w_{0,j+\frac{1}{2}} + \omega_1 w_{1,j+\frac{1}{2}} \tag{3.52}$$

3.4.2 WENO of fifth order

The fifth order WENO scheme has been extremely popular and the initial idea of the smoothness indicator formulation appears in Jiang & Shu (1996*b*), where the scaled sum of the square L^2 norms of all the derivatives of corresponding reconstruction polynomial $p_j(x)$ in the respective interval $[x_{i-\frac{1}{2}}, x_{i+\frac{1}{2}}]$ is used,

$$\beta_j = \sum_{l=1}^{k} = \Delta x^{2l-1} \int_{x-\frac{1}{2}}^{i+\frac{1}{2}} \left(\frac{d^l}{dx^l} p_j(x) \right)^2 dx \tag{3.53}$$

with k standing for the degree of polynomial $p_j(x)$. For instance, if we choose $k = 2$, the explicit formulations for left (β_0), central (β_1) and right (β_2) smoothness indicators are,

$$\beta_0 = \frac{13}{12} (w_{j-2} - 2w_{j-1} + w_j)^2 + \frac{1}{4} (w_{j-2} - 4w_{j-1} + 3w_j)^2 \tag{3.54}$$

$$\beta_1 = \frac{13}{12} (w_{j-1} - 2w_j + w_{j+1})^2 + \frac{1}{4} (w_{j-1} - w_{j+1})^2 \tag{3.55}$$

$$\beta_2 = \frac{13}{12} (w_j - 2w_{j+1} + w_{j+2})^2 + \frac{1}{4} (3u_j - 4w_{j+1} + w_{j+2})^2 \tag{3.56}$$

Using these calculations, we define the non-linear weights according to the formulation,

$$\omega_j = \frac{\tilde{\omega_j}}{\tilde{\omega_1} + \tilde{\omega_2}\tilde{\omega_3}}, \tag{3.57}$$

where

$$\tilde{\omega_j} = \frac{\gamma_j}{(\epsilon + \beta_j)^2}$$

Number ϵ is a small number which allows us to avoid zero in denominator.

Over the years there have been several developments around main WENO, which were meant to improve or adapt this method for different problems. Among those are the development of smoothness indicator calculations, different derivation of non-linear weights, algorithms for scheme order adaption depending on the discontinuities and the small number ϵ.

For example, Henrick *et al.* (2005) and Borges *et al.* (2008) demonstrated the strong sensitivity of the scheme order to the number ϵ, that is, they observed the ENO nature mitigation if the value for ϵ has been chosen too large. In order to tackle this problem, Borges *et al.* (2008) derived alternative set of non-linear weights which would ensure the fifth-order convergence,

$$\omega_k^{+,-} - \gamma_k = \mathcal{O}(\Delta x^3) \tag{3.58}$$

using new smoothness indicator definition,

$$\beta_j^z = \frac{\beta_k + \epsilon}{\beta_k + \tau_5 + \epsilon}, \ k = 0, 1, 2 \tag{3.59}$$

with $\tau_5 = |\beta_0 - \beta_2|$.

Furthermore, in practical applications, as noted by Shen (2009), there exists the non-uniformity in the flow solution or finite grid size. This fact might lead to the variation between β_k and β_k^z, which can result in deviation between non-linear and linear weights. Thus, Shen (2009) proposed yet another formulation for smoothness indicator,

$$\beta_k^{'} = R_0 A \min(\beta_0, \ldots, \beta_{r-1}) + \beta_k \tag{3.60}$$

where $R_0 = \frac{min(\beta_0,\ldots,\beta r-1)}{max(\beta_0,\ldots,\beta_{r-1})+\epsilon'}$, with $\epsilon' = 10^{-10}$ set to avoid zero in denominator. Based on this new derivation, we define a new weight function as,

$$\omega_j = \frac{\tilde{\omega_j}}{\tilde{\omega_1} + \tilde{\omega_2} + \tilde{\omega_3}} \tag{3.61}$$

where

$$\tilde{\omega_j} = \frac{\gamma_j}{(\epsilon + \beta_j^{'})^2}$$

The parameter ϵ is based on the chosen underlying smoothness indicator, β_k or β_k^z. Precisely, $\epsilon = 10^{-6}$ is used for β_k, and $\epsilon = 10^{-20}$ for β_k^z. The number A=10 in this study.

Furthermore, Peer *et al.* (2009) suggested an alternative strategy of improving the WENO method around discontinuities by introducing an algorithm of adapted ϵ number which had been observed to add some bias approach either to upwind or central-like scheme, and, manage oscillations at critical points. Their idea is based on the definition of whether or not stencil contains discontinuity, that is, stencil S defined to have discontinuity if $\beta_0 > \frac{1}{dx}\beta_2$. More precisely, authors suggest to switch to ENO3 scheme if this condition satisfies. Otherwise, the classical WENO is used with ϵ computed as following,

$$\epsilon = 10^{-6}\min\Big(1, \frac{\min(\beta_k)}{\max\beta_k - \min\beta_k + 10^{-99}}\Big) + 10^{-99} \tag{3.62}$$

Yet, another improvement of WENO5 method is presented in Wang *et al.* (2018) where authors propose an incremental stencil approach. This method is using the incremental stencil of 2- and 3-points with the underlying idea that the reconstruction should be reduced to the second order where closely located discontinuities are detected. The upwind-like stencil is used as in Jiang & Shu (1996*b*) with, however, splitted 3-points stencil into two 2-points stencils. Such splitting allows to switch between these two 2-points stencils where all originally formulated stencils have been crossed by discontinuity. The new smoothness indicator reference formulated in this strategy is,

$$\tau_5 = \frac{1}{4}(w_{j+2} - 2w_{j+1} + 2w_{j-1} - w_{j-2})^2 + \frac{13}{12}(w_{j+2} - 4w_{j+1} + 6w_j - 4w_{j-1} + w_{j-2}) \tag{3.63}$$

while the smoothness indicators defined as,

$$\begin{aligned}
\beta_0 &= (w_{j+1} - w_j)^2 \\
\beta_1 &= (w_j - w_{j-1})^2 \\
\beta_2 &= \frac{13}{12}\left(w_j - 2w_{j+1} + w_{j+2}\right)^2 + \frac{1}{4}\left(3w_j - 4w_{j+1} + w_{j+2}\right)^2 \\
\beta_3 &= \frac{13}{12}\left(w_{j-2} - 2w_{j-1} + w_j\right)^2 + \frac{1}{4}\left(3w_{j-2} - 4w_{j-1} + 3w_j\right)^2
\end{aligned} \tag{3.64}$$

The issue arises when the values of β_0 and β_1 calculated from the first derivatives are much smaller than the value of β_2 and β_3, which are obtained from first and second derivatives. This can happen near the critical points and lead to the assignment of the considerably larger weight to the two-points stencil and, as a result, eventual reduction of accuracy order. This can be avoided by slight weight modification, i.e.

$$\begin{aligned}
\alpha_1 &= d_1(1 + \frac{\tau_5}{\beta_0 + \epsilon} \times \frac{\tau_5}{\beta_{01} + \epsilon}) \\
\alpha_2 &= d_2(1 + \frac{\tau_5}{\beta_1 + \epsilon} \times \frac{\tau_5}{\beta_{01} + \epsilon})
\end{aligned} \tag{3.65}$$

where β_{01} is the smoothness indicator in stencil S_{01} computed according to,

$$\beta_{01} = \frac{13}{12}\left(w_{j-1} - 2w_j + w_{j+1}\right)^2 + \frac{1}{4}\left(w_{j-1} - w_{j+1}\right)^2\Big) \tag{3.66}$$

The general WENO approach is, thus, one of the most studied numerical methods to solve the problems with shocks and discontinuities. This scheme has been a subject of continuous improvements depending on the problem one solves. While there is no WENO solution for arbitrary problem, since the discontinuity can be defined differently in some problems, this class of the methods can be capable to solve many practical problems in computational fluid dynamics by providing smooth high-order result.

3.5 Synthesis

This Chapter has defined the motivation for high-order numerical schemes and requirements which these methods have to satisfy. These are: monotonicity preservation, uniformy high order, stability on fine meshes, non-oscillating behaviour amongst others. The brief overview of such schemes in Section 1 has followed by detailed presentations of numerical techniques formally and sometimes practically satisfying these requirements. These schemes are PPM, MP5 and WENO.

The Section 2 proposed PPM scheme derivation with several recent developments available. The monotonocity algorithm, flattening technique and discontinuity detection are integrated into the scheme. The extrema preserving technique is proposed. The PPM method is suitable for the non-uniform mesh. The accuracy of formal fourth order in smooth solutions can be obtained by using this strategy.

The Section 3 presents MP5 technique. This method has been validated on linear advection equation and led to the high-order uniform solutions. The TVD limiting technique is used in the underlying of the method. The MP5 method yields to formal fifth order of accuracy.

Lastly, Section 4 is dedicated to WENO class of the methods. These are discussed in the context of third and fifth order of accuracy. Some recent improvements of these schemes are proposed. This type of the methods is the most promising compared with PPM and MP5 counterparts due to the huge amount of research focused on this kind of technique and its application to many problems of compressible two-phase flow problems. In order to differentiate between the variety of methods discussed, the following notations will be used throughout the thesis.

- WENO3-JS and WENO5-JS are the methods of third and fifth order of accuracy, respectively, based on the studies by Liu *et al.* (1994) and Jiang & Shu (1996*b*)
- WENO3-Z and WENO5-Z are modifications proposed by Borges *et al.* (2008)

- WENO3-P is third order accuracy method suggested in Xu & Wu (2017)
- OWENO3 is an improvement discussed in Baeza *et al.* (2013)
- WENO5-SZ is a fifth order accuracy improved method presented by Shen (2009)
- WENO5-IS is yet another fifth order modified version proposed in Wang *et al.* (2018)
- *c* stands for characteristic variables reconstruction

The methods discussed in this Chapter will undergo the numerical validation procedure in order to confirm their formal compatibility of solving the problems with strong shocks and discontinuities.

Chapter 4

Numerical validation

The formal order of numerical schemes can be derived analytically for some easy problems. However, such derivation is nearly impossible for majority of practical cases involved into computational fluid dynamics. While all numerical methods presented in this thesis underwent the formal order of accuracy validation in different studies, the real order heavily depends on the problem which is being solved. Some factors which can reduce the accuracy of the scheme are presence of discontinuities, shocks. Thus, even though the considered numerical schemes are of high-order, e.g. third, fourth or fifth order, it does not necessarily mean that when it is applied to the problem of shock-bubble interaction, the analytical order of accuracy is retained. Variety of authors observed that once the problem has a presence of discontinuities, the numerical order of accuracy of majority of schemes deteriorates due to the well known Gibbs phenomenon. It has been shown Majda & Osher (1977); Lax & Mock (1978); Toro (1999) that approximating discontinuous solutions by high-order methods yield, in general, only first-order accuracy, because information passing through the shock along characteristics is degraded.

This Chapter addresses the validation of the numerical schemes reviewed in Chapter 3. The Section 1 revises the overall methodology of the validation process. An approximate derivation of numerical error and order of convergence are presented in the framework of HLLC Riemann solver. The applied validation methodology to 1D shock-tube problem is presented in Section 2. Two problems of expansion tube with initial low and high velocities are used to test the numerical schemes further in Sections 3 and 4, respectively. The validation is closed by applying the numerical schemes to the 2D problem of air-helium shock-bubble interaction. It should be mentioned, that the ideal starting point of such a validation procedure is a problem with analytical solution or exact approximate solution. However, such problems are not accurately representing schemes performance for the final shock-bubble collapse case. Indeed, the problems chosen for validation, are meant to demonstrate the numerical methods behaviour for the strong shocks and discontinuities.

4.1 Methodology

The validation of theoretical order of accuracy for a real computational dynamics problem can be a difficult task. While the schemes are normally presented with accuracy derivation based on 'toy' problems, the real order of accuracy can be demonstrated numerically by using a simple problem with available analytical solution. These test cases are normally based on the derivative approximation and linear advection equation. However, this task becomes a challenge when more difficult problems are being solved and where the analytical solutions are either difficult to obtain or unknown. Moreover, the order of accuracy for the simple test case of derivative approximation is not necessarily an exact prediction for the solutions involved to compressible two-phase flows. Thus, alternative validation methods are required in order to get an idea of the schemes performance.

The classical procedure of analysis for numerical method performance relies on the error calculation between the numerical and analytical solutions and demonstration of how fast this error decreases along with an increase of number of points in computational domain. However, what if the analytical solution is not available?

The inspiration for such a case is presented by Spina & Vitturi (2012). The work of these authors demonstrates the numerical validation based on the computed reference numerical solution. This reference solution is obtained by computations on considerably finer mesh than the compared numerical solutions. The error estimation E_{est} and convergence rate R are computed in following manner,

$$E_{est}(sol_N, sol_{ref}) = \frac{\sum_j (sol_N(x_j) - sol_{ref}(x_j))^2}{\sum_j (sol_{ref}(x_j))^2} \tag{4.1}$$

$$R(sol_N, sol_{2N}, sol_{ref}) = \frac{\sum_j |(sol_N(x_j) - sol_{ref}(x_j))|}{\sum_j |(sol_{ref}(x_j))|} \tag{4.2}$$

where sol_{ref} is a reference solution computed on the fine mesh and sol_N denotes the solution computed on the mesh with N number of points.

The error and convergence rate are estimated for the problem of shock-tube. The particular interest of the shock-tube problem is due to the several types of physical phenomena involved, i.e. expansion wave, shock and contact discontinuity. Hence, the behaviour of the schemes can be properly evaluated for each of these physical processes. The reference solution is computed on 128,000 nodes in the framework of HLLC Hancock solver with WENO5-IS reconstruction.

The schemes are then tested for the problems of expansion tube with low and high velocities. The stronger discontinuities involved into the problem allow to access the performance of numerical schemes. The solutions are compared qualitatively.

The validation is concluded by 2D air-helium case. This problem is chosen as a good starting point for accessing the performance of the schemes in 2D and availability of experimental data. The validation based on this problem is performed by analysing the convergence of the maximum pressure component of the solution P_{max} converging to the value obtained on the finest mesh. The qualitative assessment of the density gradient contour is used to draw a conclusion of a degree of detailed reconstruction of bubble deformation.

Unless stated otherwise, the reconstruction is performed on primitive variables and HLLC Hancock solver is used by default.

4.2 1D shock-tube problem

The first case in consideration has been introduced in Murrone & Guillard (2005) and is a one-meter long shock tube with discontinuity in volume fraction, with right side ($x > 0.7$) filled with air and left side with high pressure liquid water. The volume fractions are 0.8 and 0.2, for $x > 0.7$ and $x > 0.7$, respectively. Both fluids are initially at rest and described by the stiffened gas equation of state (EOS). The air filled part is at low pressure $10^5 Pa$, while water part is at high pressure $10^9 Pa$. The EOS parameters for this test are,

$$\begin{pmatrix} \Gamma \\ P_\infty \\ \rho \end{pmatrix}_{Water} = \begin{pmatrix} 4.4 \\ 6 \times 10^8 \text{ Pa} \\ 1000 \text{ kg/m}^3 \end{pmatrix} \text{ and } \begin{pmatrix} \Gamma \\ P_\infty \\ \rho \end{pmatrix}_{Air} = \begin{pmatrix} 1.4 \\ 0 \text{ Pa} \\ 1 \text{ kg/m}^3 \end{pmatrix}$$

The computations have been performed on the mesh of 1000 cells with fixed time step dt=10^{-7} s. We compare the results at final time $t_{final} = 0.2$ μ s. The computed results are obtained by either HLLC Hancock or KNP Hancock based solver. While our main concern is high-order schemes, second order MUSCL TVD method is used for comparison purposes. Unless stated otherwise, van Albada slope limiter is used in MUSCL TVD framework.

The comparison of the solutions obtained with different solver, i.e. KNP and HLLC, is presented combined with the WENO5 reconstruction on Figure 4.1. The solutions for all components are in good agreement with reference solution and are very similar. The variations in the critical

zones of expansion wave and post-shock area are not observed. Similar results are obtained for other reconstruction techniques. In what is to follow, HLLC solver with Hancock approach is used by default unless stated otherwise.

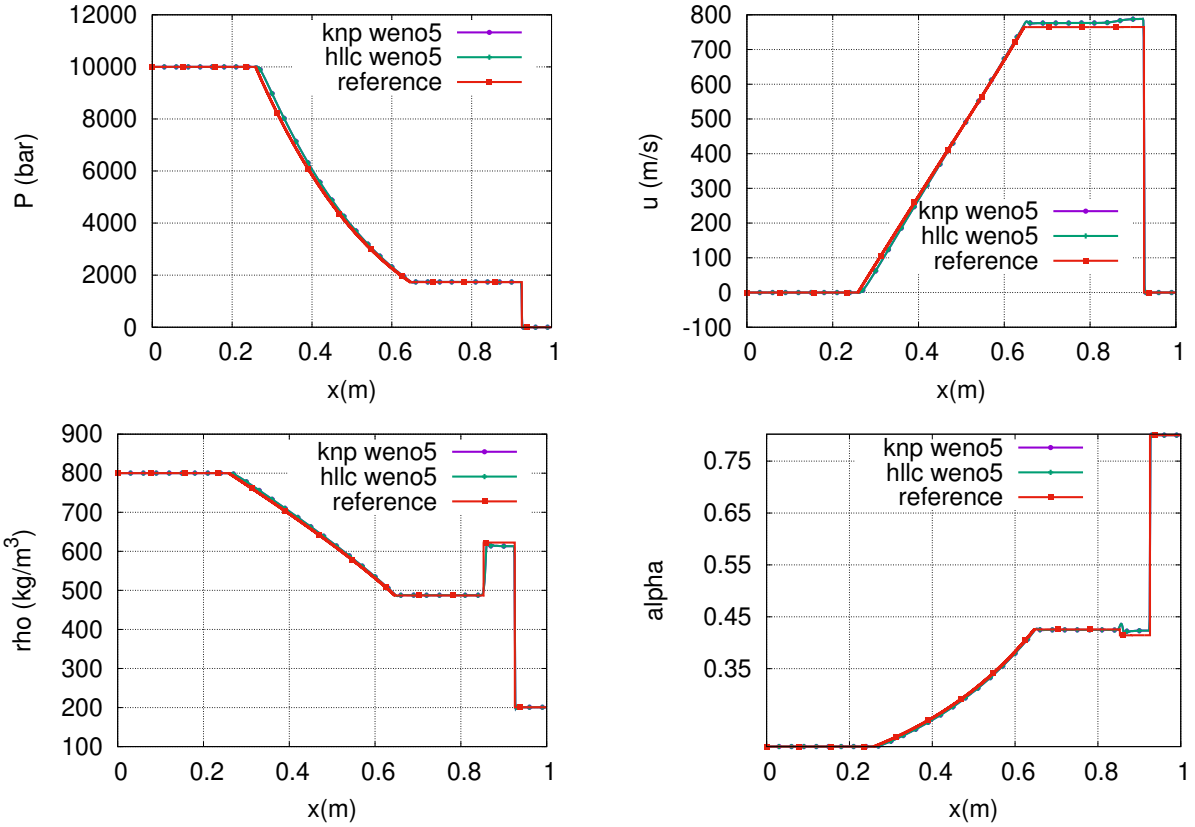

Figure 4.1: Water-gas shock-tube problem, HLLC Hancock WENO5 and KNP Hancock WENO5 solver comparison, mesh 1000 cells, t_{final}=0.2 μs. Pressure and velocity (top), mixture density and void ratio (bottom) profiles along the tube.

The results obtained with WENO5 methods illustrate relatively similar reconstruction and are in good agreement with reference solution. Figure 4.2 shows the pressure, density, velocity and alpha profiles. The slight oscillation along the expansion wave in the interval 0.2-0.4 m is observed in the pressure solution by WENO5-JS. However, the post-shock area is well resolved by all schemes. The velocity profile is equally well solved by all schemes. This observation includes the shock zone. On the other hand, the density and alpha profiles demonstrate the differences in the solution. Figure 4.3 presents the enlargement of the density and void ratio solutions at the post-shock area, 0.6-1 m. The oscillations in density and void fraction solutions around contact discontinuity are the highest by using the WENO5-SZ, WENO5-Z and WENO5-JS. However, these peaks are reduced by applying the reconstruction on the characteristic variables (WENO5-SZ, for instance on 4.4). Notably, the application of WENO5-IS method to both, primitive and characteristic variables, led to the good resolution of the contact discontinuities.

The solutions for pressure, velocity, mixture density and void ratio obtained by WENO3 methods are proposed on Figures 4.5 and 4.6. We note relatively similar reconstruction by all WENO3 methods. Slight oscillation is noted for the mixture density near the post-shock area produced by OWENO3 method. An undershoot of the mixture density solution by WENO3-JS is observed in the same region. Otherwise, WENO3 methods provided accurate smooth solutions.

Some variations have been noticed in the solution profiles by using different formulations for PPM method. Figures 4.7 and 4.8 present the solutions of pressure, velocity, mixture density and void ratio along the tube obtained by PPM method. The enlargement of every component solution in the post-shock area is proposed on the left hand side. The following notations are used:

- 'PPM CW' stands for the PPM method originally presented by Colella & Woodward (1984),
- 'PPM c CW' is similar method with its application to characteristic variables,
- 'PPM CD' is for the modified contact discontinuity formulation by Zheng & Lee (2013),
- 'PPM EP' denotes the extrema preservation modification as per Colella & Sekora (2008).

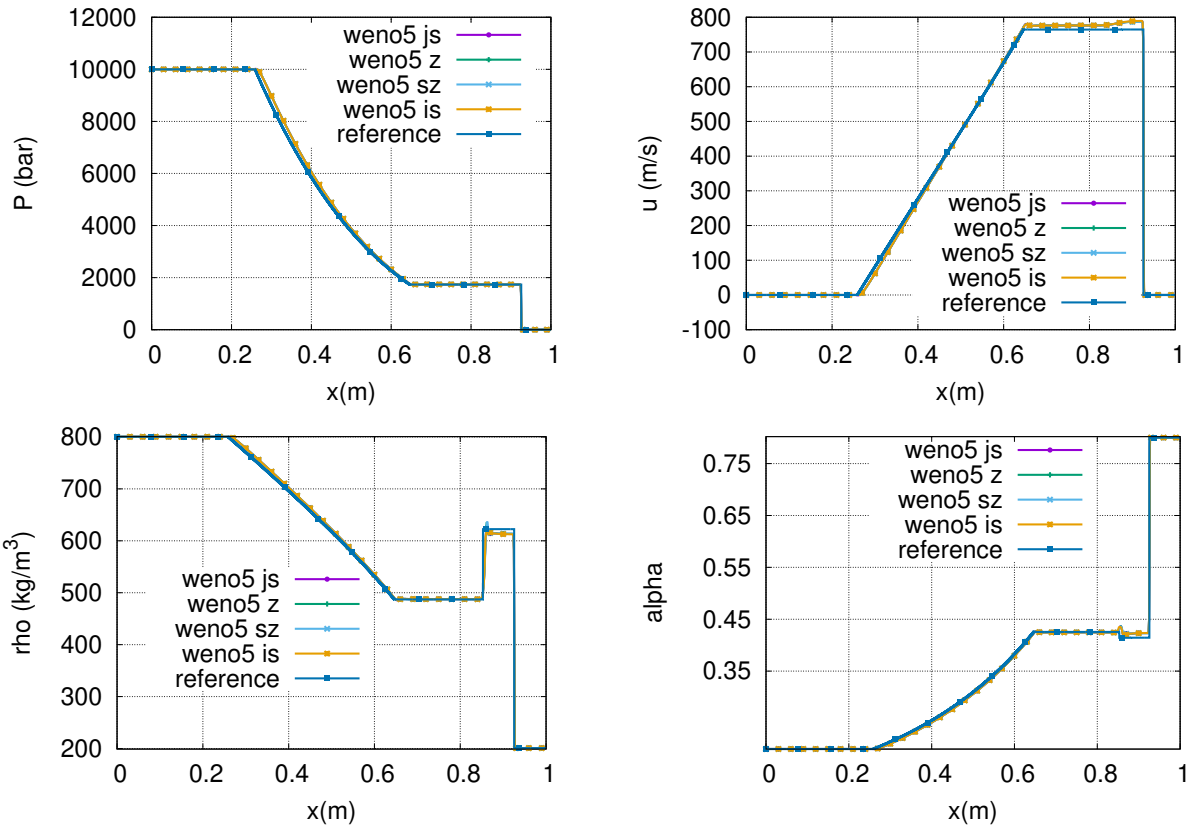

Figure 4.2: Water-gas shock-tube problem, WENO5 reconstructions comparison, mesh 1000 cells, t_{final}=0.2 μs. Pressure and velocity (top), mixture density and void ratio (bottom) profiles along the tube.

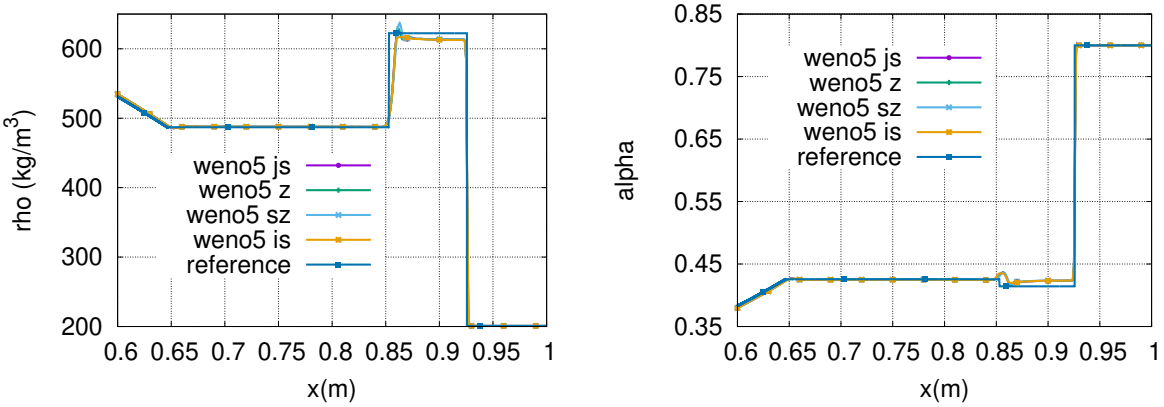

Figure 4.3: Water-gas shock-tube problem, WENO5 reconstructions comparison, mesh 1000 cells, t_{final}=0.2 μs. Enlargement of post-shock area of mixture density (left) and void ratio (right) profiles

Overall, all solutions computed with PPM methods are in close agreement with reference solution. The classical PPM-CW method led to oscillations around discontinuity zone in the post-shock area for all components of the solution. However, these oscillations are reduced by application of similar formulation to the characteristic variables.

The extrema preservation modification led to a slight variation in the solution for the void ratio around the coordinate x=0.85 in the post-shock area compared with solution obtained by methods with special treatment for contact discontinuity and classical formulation with characteristic variables. This modification has also led to oscillation in discontinuity zone for the void ratio.

The solutions with modified contact discontinuity algorithm and classical formulation of PPM are in close agreement with reference solution.

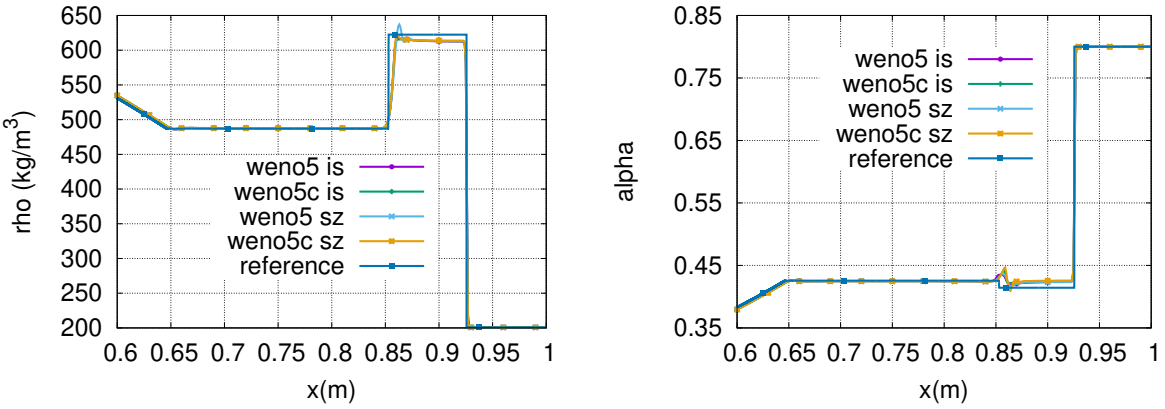

Figure 4.4: Water-gas shock-tube problem, WENO5 reconstructions comparison, characteristic variables, mesh 1000 cells, t_{final}=0.2 μs. Enlargement of post-shock area of mixture density (left) and void ratio (right) profiles

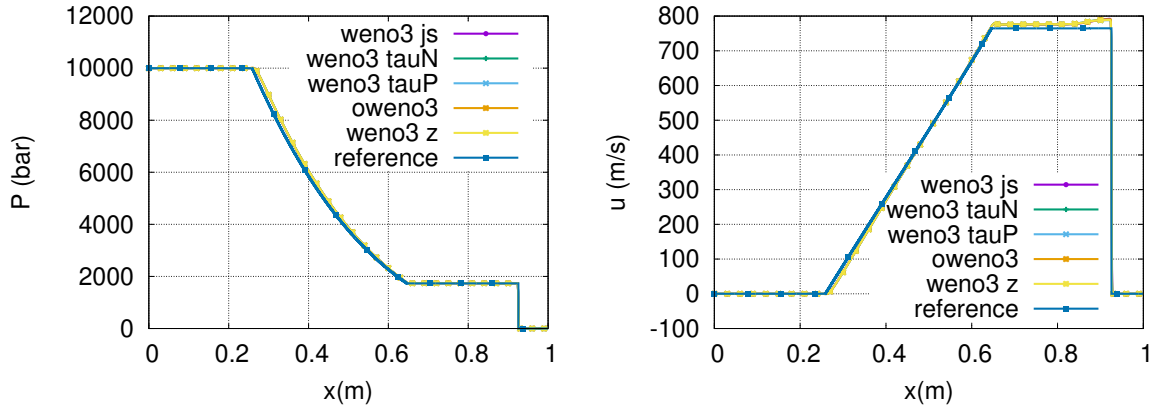

Figure 4.5: Water-gas shock-tube problem, WENO3 reconstructions comparison, mesh 1000 cells, t_{final}=0.2 μs. Pressure (left) and velocity (right) profiles along the tube.

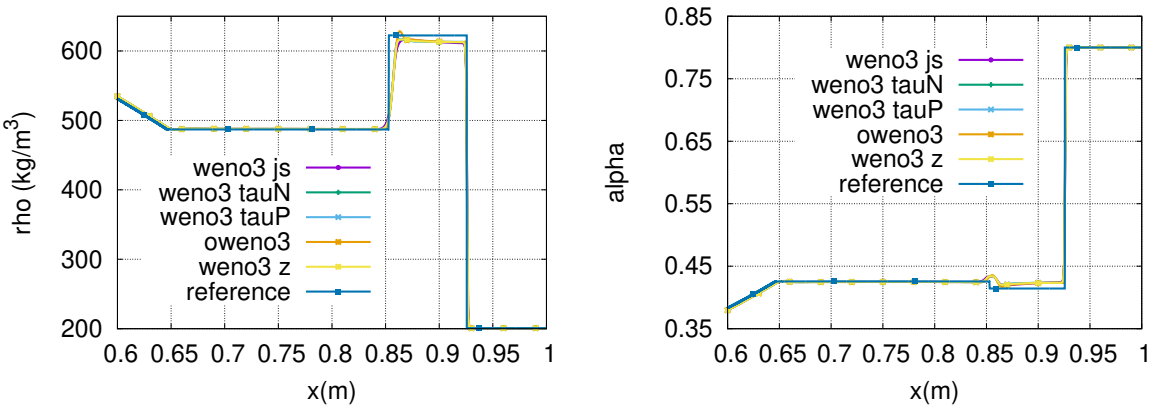

Figure 4.6: Water-gas shock-tube problem, WENO3 reconstructions comparison, mesh 1000 cells, t_{final}=0.2 μs. Enlargement of post-shock area of mixture density (left) and void ratio (right) profiles along the tube.

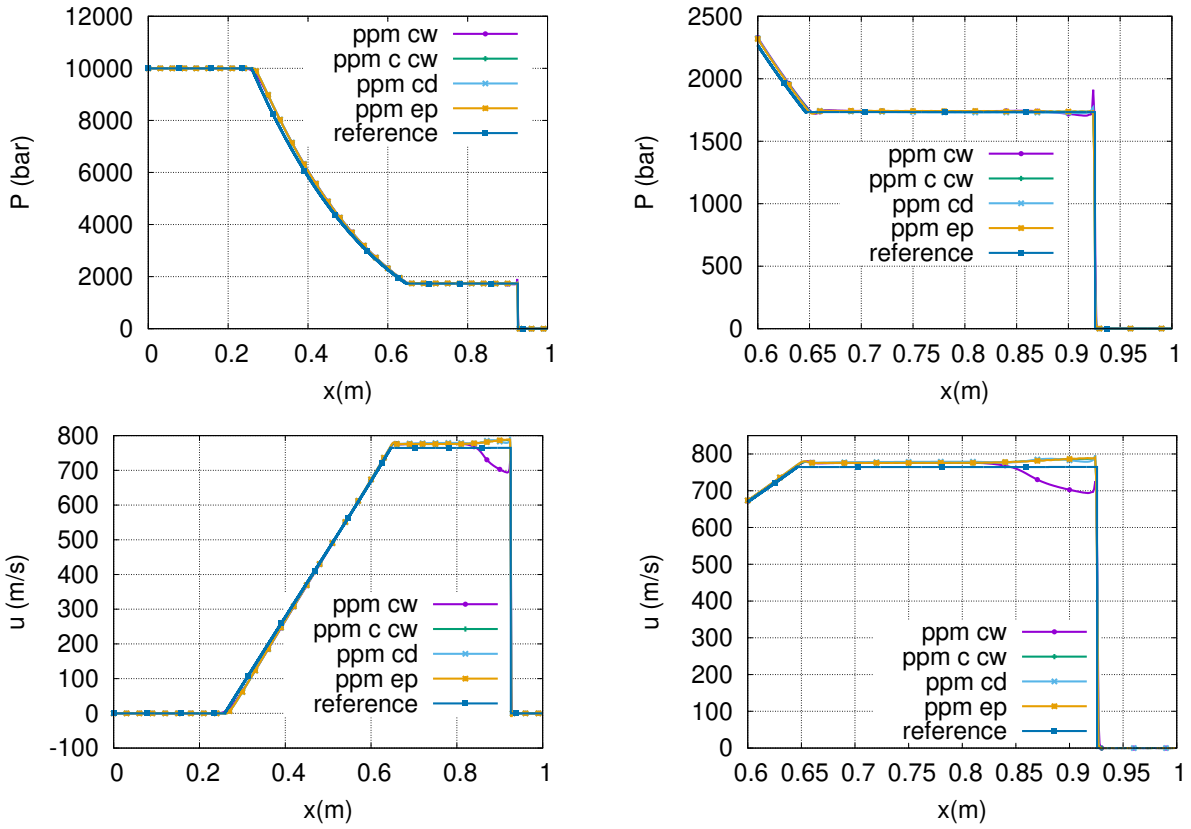

Figure 4.7: Water-gas shock-tube problem, PPM methods comparison, mesh 1000 cells, t_{final}=0.2 μs. Pressure and velocity profiles along the tube (left), enlargement of post-shock area (right).

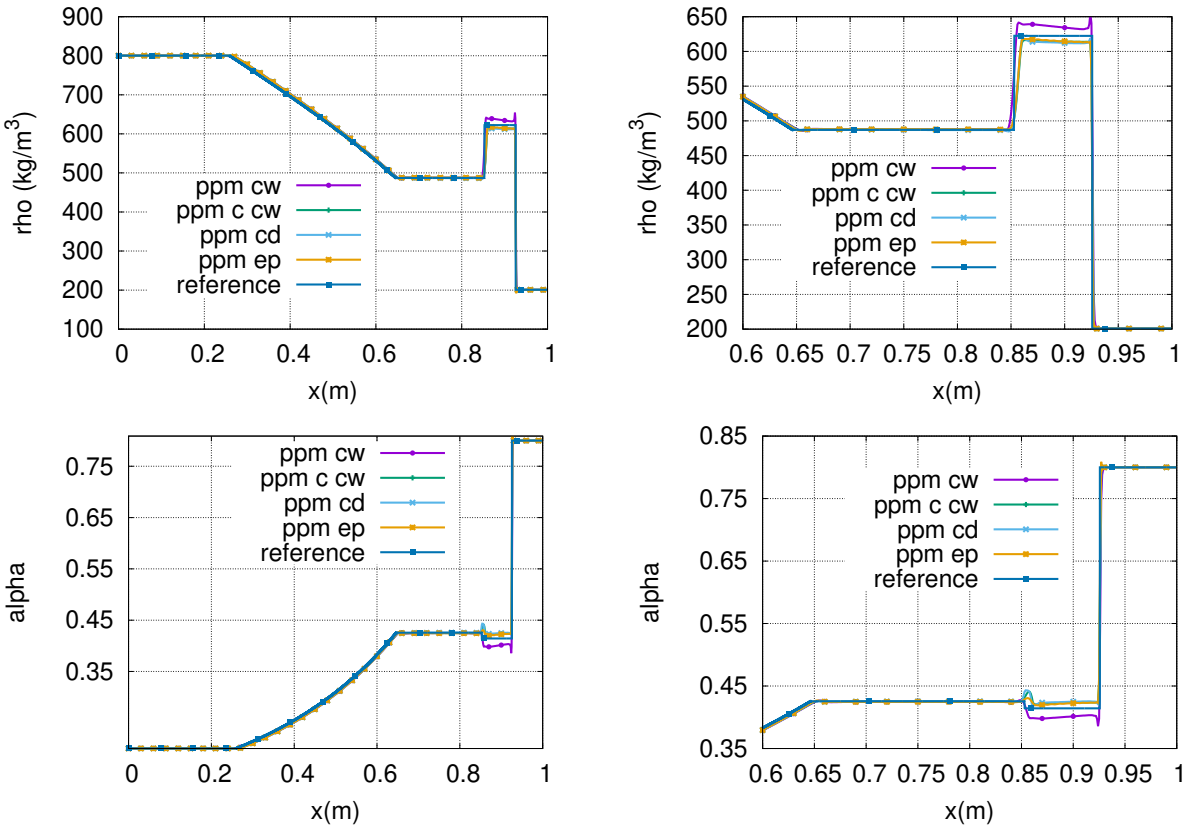

Figure 4.8: Water-gas shock-tube problem, PPM methods comparison, mesh 1000 cells, t_{final}=0.2 μs. Mixture density and void ratio profiles along the tube (left), enlargement of post-shock area (right).

Table 4.1 presents the error and convergence estimations with fixed CFL=0.4. The error estimation E_{est} demonstrated that the higher order schemes, e.g. WENO5 and PPM, do indeed lead to the more accurate solution. In general, it has been found that the error is lower for the higher order schemes and is reduced as the mesh is refined. The convergence rate R calculated by using (4.2) is estimated by refining the mesh starting from 1,000 nodes and up to 8,000 nodes with the step 1,000. All schemes yielded to approximately second order of convergence in contrast to the higher theoretical accuracy. However, should the classical formulations of order derivation be used (i.e. a norm difference), the first order of convergence is observed across all schemes due to the present discontinuities in the solution. Indeed, the order of accuracy of high-order methods decreases for the problems where a strong discontinuity is present (see Toro (1999); Schidmayer *et al.* (2020)).

Table 4.1: Shock-tube problem: relative error (left) and convergence rate (right).

Relative error				Convergence rate		
N	WENO5SZ	WENO5IS	PPM	WENO5SZ	WENO5IS	PPM
8000	3.9×10^{-6}	4.5×10^{-6}	5.3×10^{-6}	2.3	2.3	2.2
4000	1.9×10^{-5}	1.9×10^{-5}	2.4×10^{-5}	2.1	2.1	2.1
2000	9.3×10^{-5}	9.2×10^{-5}	1.0×10^{-4}	2.1	2.1	2.1
1000	3.9×10^{-4}	3.9×10^{-4}	4.2×10^{-4}	-	-	-
N	WENO3JS	WENO3Z	WENO3P	WENO3JS	WENO3Z	WENO3P
8000	4.4×10^{-6}	4.4×10^{-6}	4.3×10^{-6}	2.3	2.3	2.3
4000	1.8×10^{-5}	1.9×10^{-5}	1.9×10^{-5}	2.2	2.1	2.1
2000	8.4×10^{-5}	9.2×10^{-5}	9.2×10^{-4}	2.1	2.1	2.1
1000	3.5×10^{-4}	3.9×10^{-4}	3.9×10^{-4}	-	-	-

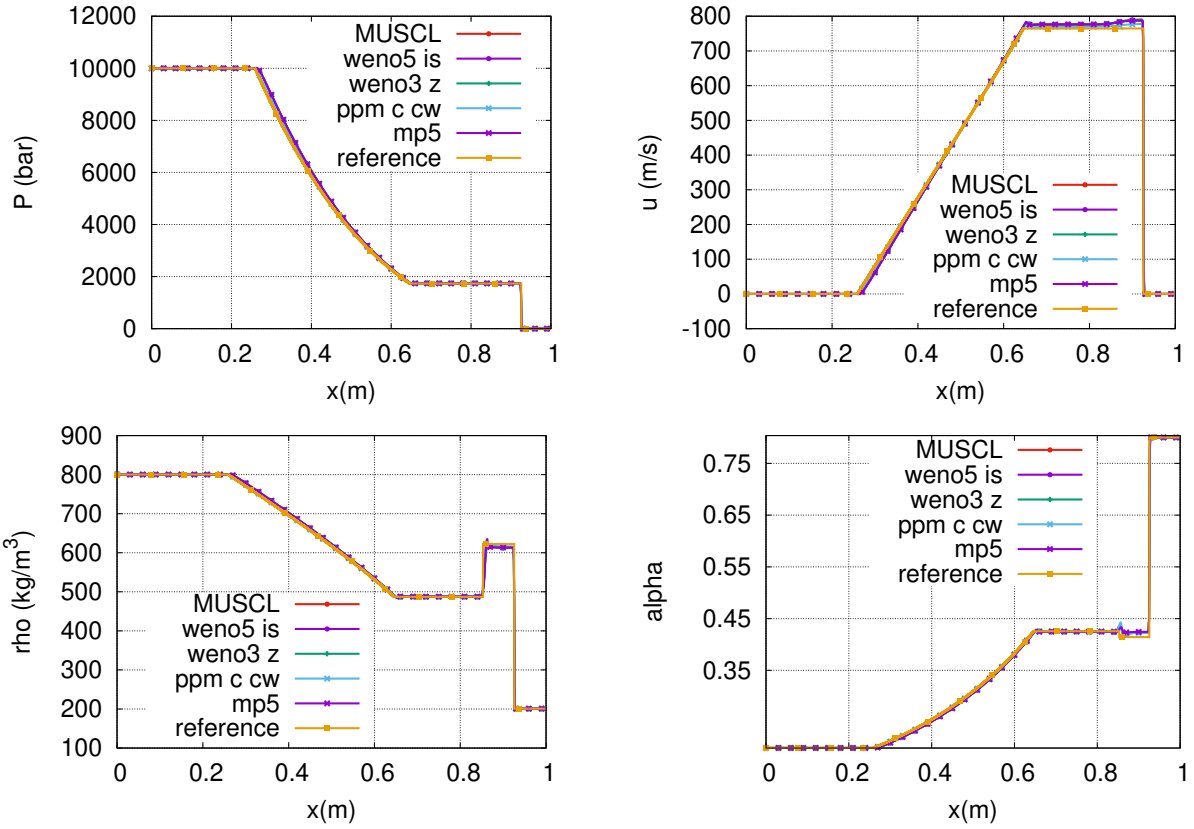

Figure 4.9: Water-gas shock-tube problem, numerical schemes comparison, mesh 1000 cells, t_{final}=0.2 μs. Pressure and velocity (top), mixture density and void ratio (bottom) profiles along the tube.

Finally, the comparison of solutions between the key numerical schemes is proposed on Figure

4.9 where the results obtained by using MUSCL, PPM, MP5, WENO3-Z and WENO5-IS are presented. PPM scheme led to slight variation near the contact discontinuity for the void ratio profile. Method MP5 has the oscillating result for the mixture density in the post-shock area. Otherwise, all schemes led to accurate solution in close agreement with reference solution.

The water-gas shock-tube problem is a starting point for the validation process. The performance of the schemes is estimated. Most of schemes led to the accurate solution with exception of WENO5-JS, MP5 and PPM-CW where oscillations are observed in post-shock area.

4.3 1D Expansion tube with initial velocity $|u_0|$=2 m/s

The second considered case is the double rarefaction problem. It consists in a one meter long tube where the velocity set with discontinuity located in the middle. The tube is filled with liquid water with density ρ_l=1150 kg/m^3, atmospheric pressure and a small fraction of vapour α =0.01. The initial velocity is set to be -2 m/s on the left and 2 m/s on the right. The fluids are described by EOS with the following parameters,

$$\begin{pmatrix} \Gamma \\ P_\infty \\ q \\ \rho \\ C_\rho \end{pmatrix}_{Water} = \begin{pmatrix} 2.35 \\ 10^9 \text{ Pa} \\ -0.1167 \times 10^7 \text{ J/kg} \\ 1150 \text{ kg/m}^3 \\ 4267 \text{ J/K.kg} \end{pmatrix} \text{ and } \begin{pmatrix} \Gamma \\ P_\infty \\ q \\ \rho \\ C_\rho \end{pmatrix}_{Gas} = \begin{pmatrix} 1.43 \\ 0 \text{ Pa} \\ 0.2030 \times 10^7 \text{ J/kg} \\ 1 \text{ kg/m}^3 \\ 1487 \text{ J/K.kg} \end{pmatrix}$$

For this case, the pressure remains positive since gas is present initially and an increase in gas volume fraction is observed due to the gas mechanical expansion. The obtained numerical solution presents two expansion waves. The computations have been done by using 1000 cells at time step $dt = 10^{-7}$ s. We compare the results at final time $t_{\text{final}} = 3.2$ ms.

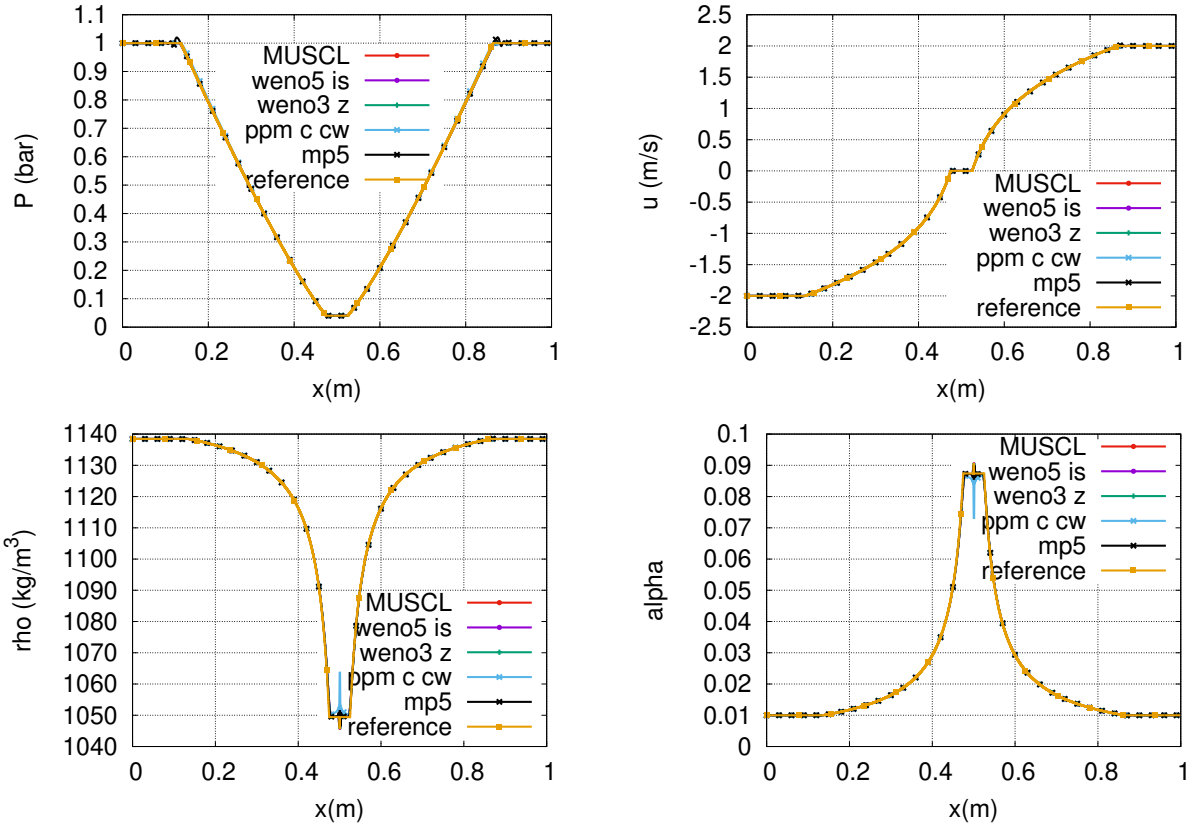

Figure 4.10: Water-gas double rarefaction $|u_0|$=2 m/s, reconstruction methods comparison, mesh 1000 cells, $t = 3.2$ ms. Pressure, velocity, mixture density and void ratio profiles

We first consider the solution for pressure, velocity, mixture density and void ratio obtained by using key high-order numerical schemes, i.e. MUSCL (for comparison purposes), WENO5-IS, WENO3-Z and PPM-CW with characteristic reconstruction. The results of computations are proposed on 4.10. The solutions for the pressure and velocity components are in close agreement with reference solution. The variation in the mixture density and void ratio is noted by using PPM scheme, where a strong oscillation around the region of initial discontinuity is observed. However, the solution recovers as the expansion wave progresses and we obtain a smooth reconstruction. Oscillations along the expansion waves are noticed by using MP5 method for the pressure profile.

The deviation between results of using different variations of WENO5 and PPM are present for the pressure component, where oscillations along the expansion waves appear (on the interval x=[0,0.2] and x=[0.8,1]). The solution for pressure obtained by using several modifications of WENO5, WENO3 and PPM are presented on Figure 4.11. We observe two symmetrical oscillations by using WENO5-JS scheme. These oscillations are eliminated with later modifications of the schemes (e.g. WENO5-Z, WENO5-IS etc). On the other hand, all WENO schemes of third order accuracy have smooth reconstruction in similar area and in agreement with reference solution with only a slight undershoot provided by WENO3-JS in the angle of expansion waves. The PPM method variations led to relatively similar results. However, an unsymmetrical oscillation is present on the left expansion wave by using primitive variable reconstruction.

Finally, the solution discrepancy in the pressure profile is obtained from computations with KNP solver (see Figure 4.11 bottom right). The unsymmetrical oscillations are noticed along the expansion waves propagation on the interval $x = [0, 0.2]$m and $x = [0.8, 1]$m.

The characteristic variables reconstruction does not have any effect on present computations except for the PPM method.

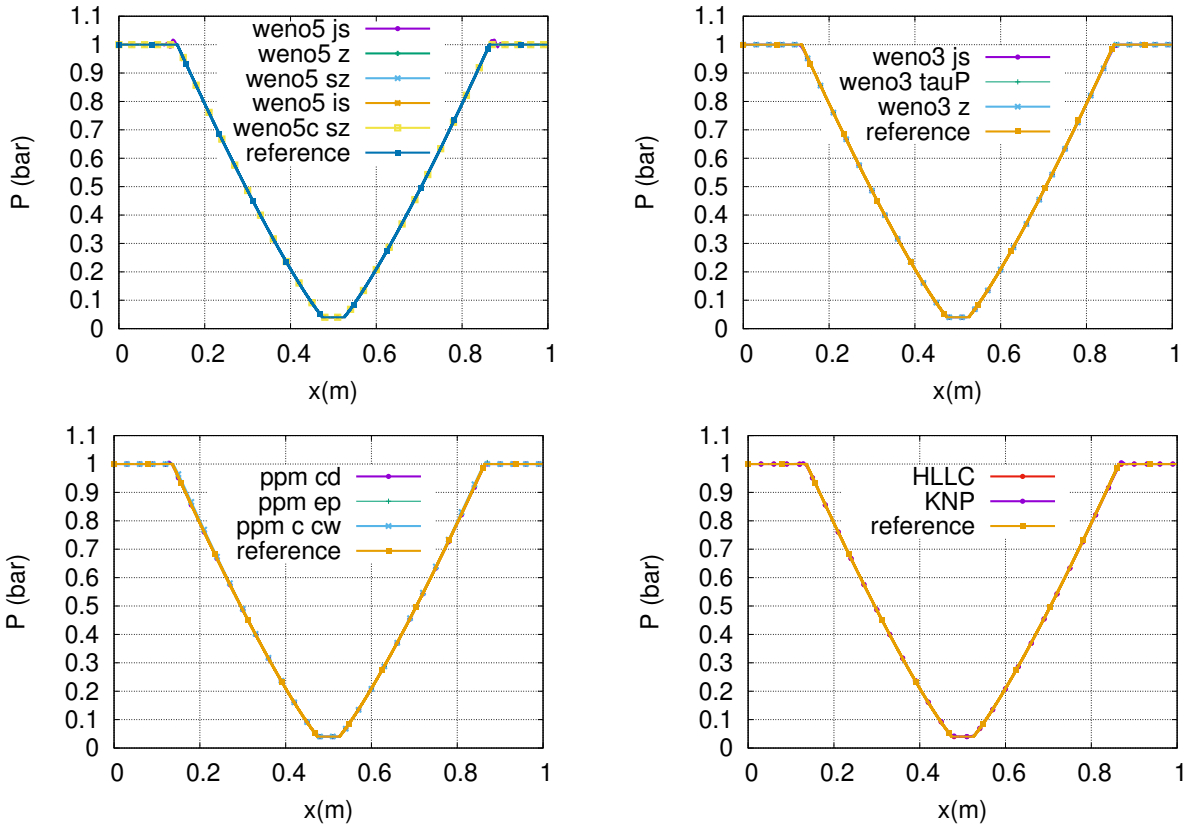

Figure 4.11: Water-gas double rarefaction $|u_0|$=2 m/s, numerical schemes comparison: WENO5, WENO3, PPM, HLLC and KNP, mesh 1000 cells, $t = 3.2$ ms. Pressure profile

4.4 1D Expansion tube with initial velocity $|u_0|$=100 m/s

We consider a similar test to the previous one, except for the initial velocity value increased to 100 m/s, which leads to stiff and challenging numerical problem. EOS are unchanged. As before, we set the time step $dt = 10^{-7}$ s and perform the computations on the domain with 1000 cells. The solutions have been compared at final time $t_{\text{final}} = 1.5$ ms. For this test the reference solution has been obtained by using MUSCL reconstruction on 128,000 nodes due to the strong oscillation at initial discontinuity region produced by high-order schemes by using this mesh refinement.

The solutions obtained by using different key numerical schemes are presented on Figure 4.12. In agreement with previous test, PPM method led to the oscillations in mixture density and void ratio components around the zone of initial discontinuity. All other schemes provided accurate smooth solutions around the initial discontinuity and along the expansion waves. We did not obtain any solution for this problem by using MP5 method.

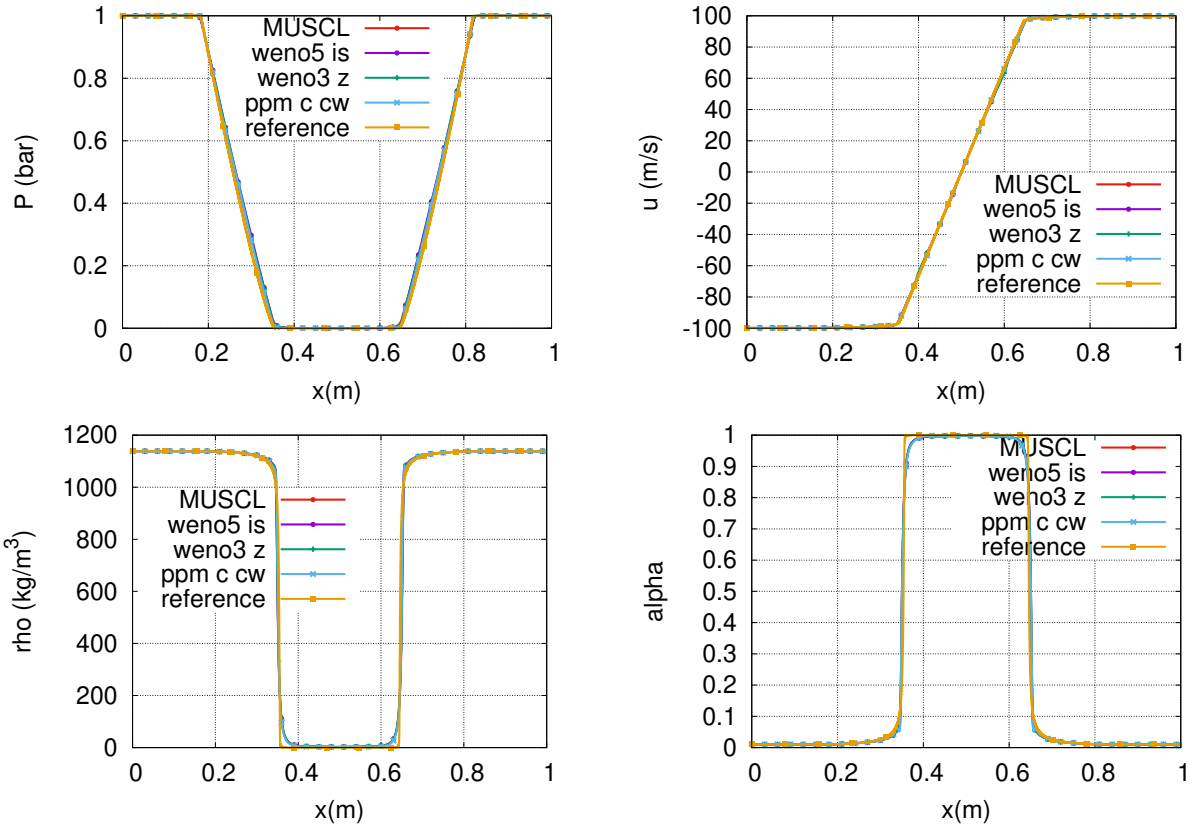

Figure 4.12: Water-gas double rarefaction $|u_0|$=100 m/s, numerical schemes comparison, mesh 1000 cells, t=1.5 ms. Pressure, velocity, mixture density and void ratio profiles

Large discrepancies are marked for the pressure profile by testing variations of schemes. The solution for the pressure evolution is proposed on Figure 4.13. Similarly to the previous test, WENO5-JS formulation (top left) provides the solution with badly reconstructed rarefaction waves where the symmetrical oscillations are present on the interval $x = [0, 0.2]$m and $x = [0.8, 1]$m. However, other methods of this class allowed to obtain an accurate solution in close agreement with the reference computations.

Unlike the expansion tube with lower velocity, the variation in the solution for pressure variable is noted between the schemes WENO3-τ_N and WENO3-τ_P (Figure 4.13, top right). The modification in the reference smoothness indicator as per equations 3.46 and 3.47 led to the difference in the reconstruction of the rarefaction waves. Particularly, the solution where 3.47 has been applied, symmetrical oscillations are observed along the wave expansion on the interval $x = [0, 0.2]$m and $x = [0.8, 1]$m.

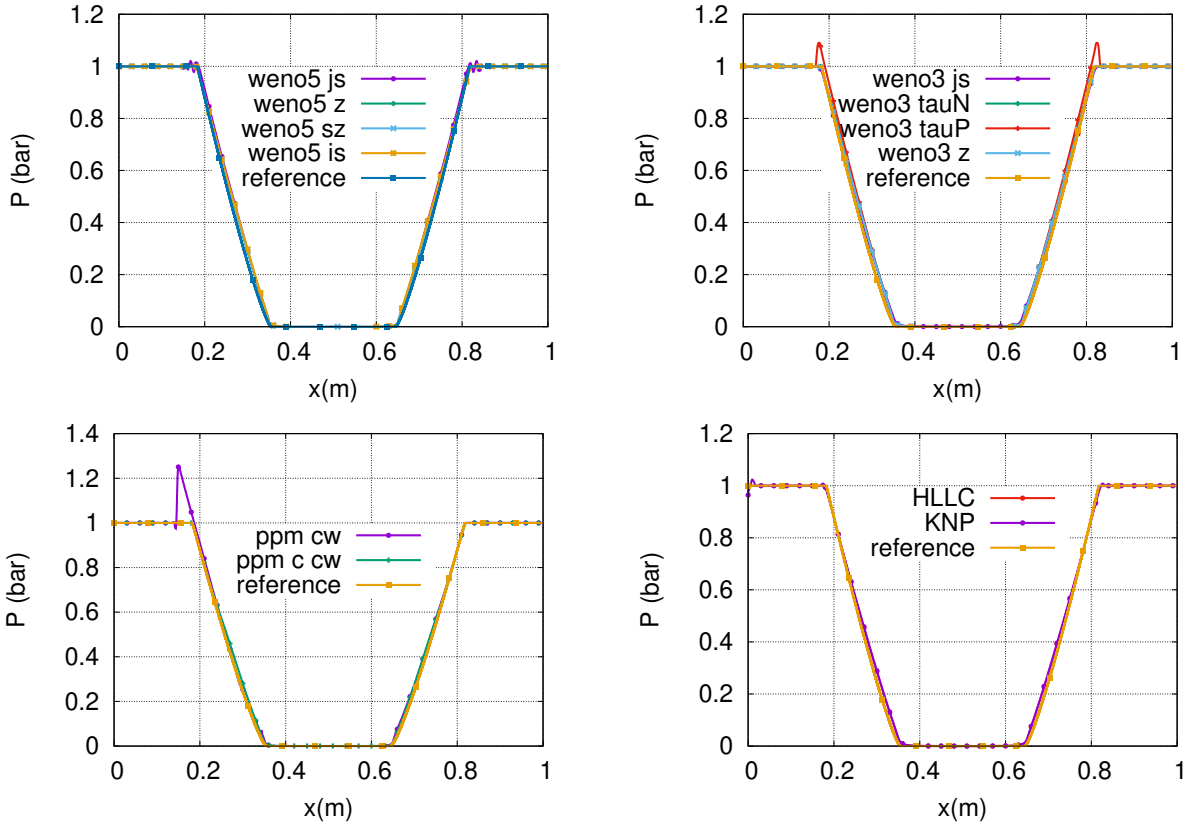

Figure 4.13: Water-gas double rarefaction $|u_0|$=100 m/s, numerical schemes comparison: WENO5, WENO3, PPM, HLLC and KNP, mesh 1000 cells, t=1.5 ms. Pressure profile

The pressure solution computed by using PPM methods (Figure 4.13 bottom left) illustrates the discrepancy in the reconstruction of left rarefaction wave by using primitive variables. The oscillation appears only on the left wave, while the right part of the wave has an accurate result. This problem is fixed by using characteristic variables reconstruction.

Finally, the KNP solver (Figure 4.13, bottom right) result demonstrates the problem on the left boundary, where the oscillation is present. Moreover, symmetrical discrepancies of the solution along the angle of rarefaction waves are noted on the interval x=[0,0.2] and x=[0.8,1]. These problems do not appear in the solution obtained by using HLLC solver.

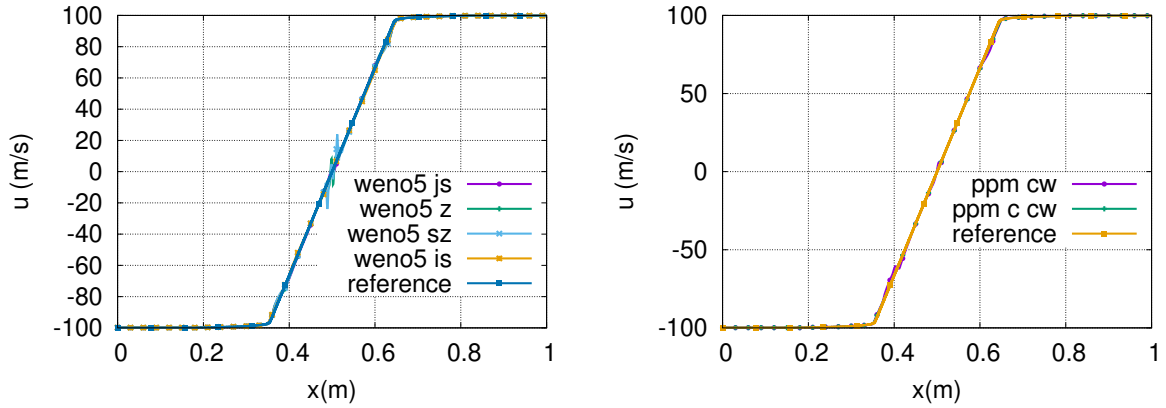

Figure 4.14: Water-gas double rarefaction $|u_0|$=100 m/s, numerical schemes comparison: WENO5, and PPM, mesh 1000 cells, t=1.5 ms. Velocity profile

The velocity component of the solution has a variation in the solution by using modified versions of WENO5 formulations. Figure 4.14 (left) illustrates strong oscillations around initial

discontinuity zone resulted by WENO5-Z and WENO5-SZ. The solutions are recovered smoothly at other regions of the domain.

The PPM method with primitive variables reconstruction Figure 4.14 (left) has similarly led to a slight oscillation around initial discontinuity for the velocity solution. Moreover, further discrepancies appear at x=0.4 and x=0.6 which are not present in reference computations. This problem disappears by using characteristic variables.

Other schemes do not have effect of characteristic variables reconstruction in present computations.

4.5 Synthesis

The first part of the validation process of the numerical schemes used in this study has started by doing 1D computations for the tests of water-gas shock-tube and expansion tube with low and high initial velocities.

Firstly, the computations of the shock-tube problem show that most of the reconstruction techniques provide results in good agreement with the reference solution. However, some discrepancies have been found. For instance, WENO5-SZ scheme has an oscillation for the mixture density around the discontinuity zone, which is not observed neither in other WENO5 methods, nor in reference solution. This oscillation has been eliminated by using characteristic variables reconstruction. On the other hand, WENO3 schemes led to the accurate and smooth reconstruction of all variables with one exception of OWENO formulation, where slight discrepancy is noted for the mixture density in the discontinuity zone. Moreover, PPM method produces oscillations of the solution in the post-shock zone by using primitive variables reconstruction (PPM CW). This problem is fixed by using characteristic variables. This test did not demonstrate any difference between HLLC and KNP solvers. The numerical analysis by using reference solution computed on the fine grid has been performed and an approximate second order of convergence is obtained by using all schemes.

Secondly, two expansion tube tests have been performed. Here, the initial velocity set up with low and high values allows to examine the scheme behaviour where stronger waves are involved. Indeed, more variations of the numerical solution have been illustrated. For instance, the WENO5-JS scheme led to symmetrical oscillations along the expansion waves in both tests for the pressure. Unlike the shock-tube problem, these tests have also shown a difference in the pressure evolution by using WENO3-τ_N and WENO3-τ_P, where the former one led to the inaccurate rarefaction wave reconstruction for the case with stronger initial velocity. Furthermore, all PPM methods produce oscillations for the mixture density and void ratio profiles even with characteristic reconstruction, either at mid-tube for the low initial velocity case or along the expansion waves for the high velocity case. Moreover, the PPM method with primitive reconstruction presents a big unsymmetrical oscillation in the rarefaction zone for the case with high initial velocity, which is not present in similar computations with characteristic reconstruction. Finally, these tests presented the discrepancies in the solution for the pressure variable by using KNP solver.

These first results give an indication of the schemes behaviour when strong shocks or expansion waves are involved. We can preliminary conclude that PPM method provides more accurate solution when applied to the characteristic variables, since most of the issues are eliminated in comparison to the primitive variables reconstruction. Furthermore, WENO5-JS formulation becomes oscillating if strong shock is involved and, hence, probably should not be used in such problems. On the other hand, WENO5-IS scheme demonstrated accurate results in all tests. Similarly, the tendency of solution deterioration is noted for some WENO3 schemes, i.e. OWENO3 method is oscillating even for the shock-tube case and WENO3-τ_P is not accurate for the problems involving a strong expansion wave. Finally, we note deteriorating nature of the solution of KNP solver, while HLLC formulation is preliminary preferred choice for the computations of such cases.

4.6 2D air-helium shock-bubble interaction

The second part of validation is a 2D shock-bubble interaction: a helium bubble immersed in air is impacted and accelerated by a shock wave. This particular problem has been chosen due to the existence of experimental studies by Haas & Sturtevant (1987) and more recently by Layes *et al.* (2009). It implies that the experimental data visualisations can be used for qualitative assessment.

The helium bubble has an initial diameter of 4 cm and is impacted by a normal shock wave moving at the Mach number 1.175. The EOS and post-shock parameters are given in Table 4.2. The volume fraction α represents here the ratio of the lighter gas to the carrier gas.

Table 4.2: Air-Helium EOS parameters and post-shock condition

	γ	P_∞	ρ
air	1.4	0 Pa	1.163 kg/m^3
helium	1.648	0 Pa	0.16 kg/m^3
	P	ρ	u
post-shock	1.444 10^5 Pa	1.51 kg/m^3	93.65 m/s

The computations are performed on a half-domain due to the symmetry of the problem. Unless stated otherwise, the results have been obtained by using a uniform mesh discretization of 4000 $\times$ 400 cells, the time step of 2.5×10^{-9} s and the HLLC flux formulation. The PPM method in present computations is used with characteristic variables with contact discontinuity detection. The notation WENO3-P denotes the formulation with reference smoothness indicator as per 3.46, which is not oscillating in the problem of expansion tube with high initial velocity.

Firstly, the density gradient evolution compared to the experimental visualisations is shown in Figures 4.15 and 4.16 for simulations performed by using the WENO5-IS reconstruction. The numerical and experimental solutions are compared at approximately similar times. The bubble deformation starts by its flattening in the direction of the shock wave and eventually takes the shape of the kidney as a result of the high speed air jet formation located at the upstream interface. On the other hand, the downstream interface jet leads to the appearance of the counter-rotating vortices which cause the bubble elongation. The computations obtained with all schemes are able to reproduce the main elements of the bubble shape evolution compared to the experimental data.

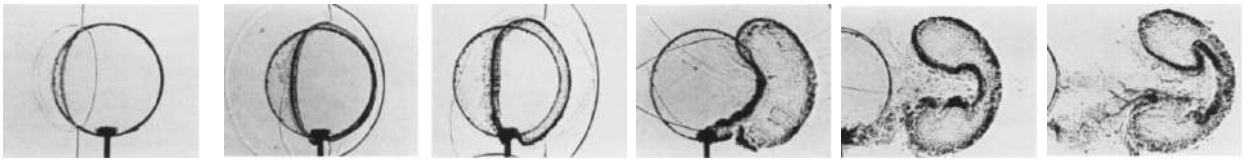

Figure 4.15: Experimental visualisation by Haas and Sturtevant, extracted from Haas & Sturtevant (1987).

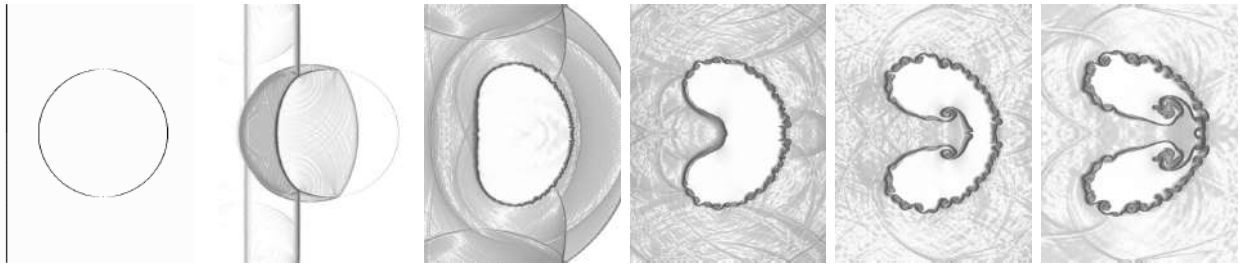

Figure 4.16: Numerical results computed on 4000$\times$400 nodes, dt=2.5×10^{-9} s, HLLC Hancock WENO5-IS

The comparison of the numerical schemes performance is now proposed. Firstly, the deviation in the solution obtained by using different formulations of WENO3 scheme is discussed. The WENO3-JS method solution is presented in Figure 4.17 left. Although the bubble interface has

been reconstructed accurately, overall the bubble interface is smeared with little reconstruction of vortices. On the other hand, the improved extensions, i.e. WENO3-Z and WENO3-P (Figure 4.17 middle and right, respectively) demonstrate considerably better reconstruction without noticeable oscillations inside or outside the bubble. The vortices on the bubble interface are reconstructed fairly well but with less details compared to the higher order PPM and WENO5 schemes. The two core vortices are diffused but still improved in WENO3-Z and WENO3-P compared with the originally formulated WENO3-JS.

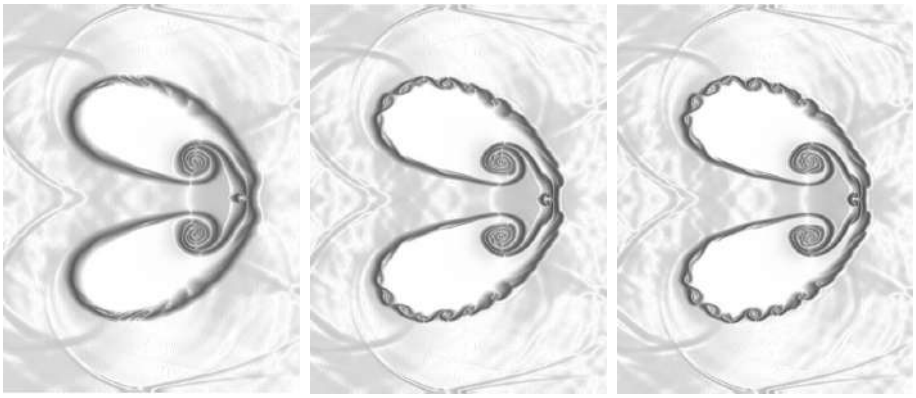

Figure 4.17: Air-helium shock-bubble interaction, comparison of the numerical schemes. Mesh: 4000×400, dt=2.5 × 10^{-9} s, t_{final}=0.05 ms, left to right: WENO3-JS, WENO3-Z, WENO3-P.

Similarly, an improvement is illustrated with higher order WENO5 schemes in Figure 4.18. The WENO5-JS has fairly well reconstructed bubble interface and the vortex-like structure including the core vortices. However, the oscillations can be noticed in the direction of the wave propagation (inside the bubble on the left and outside the bubble on the right part of the plot). The inside oscillations have been eliminated almost completely by using improved versions of the method (Z, IS and SZ). All three schemes led to the accurate bubble structure reconstruction with slight deviations inside the vortices. We notice that WENO5-Z and WENO5-SZ produce more structure inside the vortices on the bubble interface, while these structures have been diffused in the case of WENO5-IS. On the other hand, the two vortices inside the bubble have been reconstructed well by all three schemes with, however, again, more diffusion by WENO5-IS. Interestingly, small oscillations outside the bubble are observed by WENO5-Z and WENO5-SZ, while WENO5-IS eliminates these oscillations and instead has fluctuations in the solution around two core vortices.

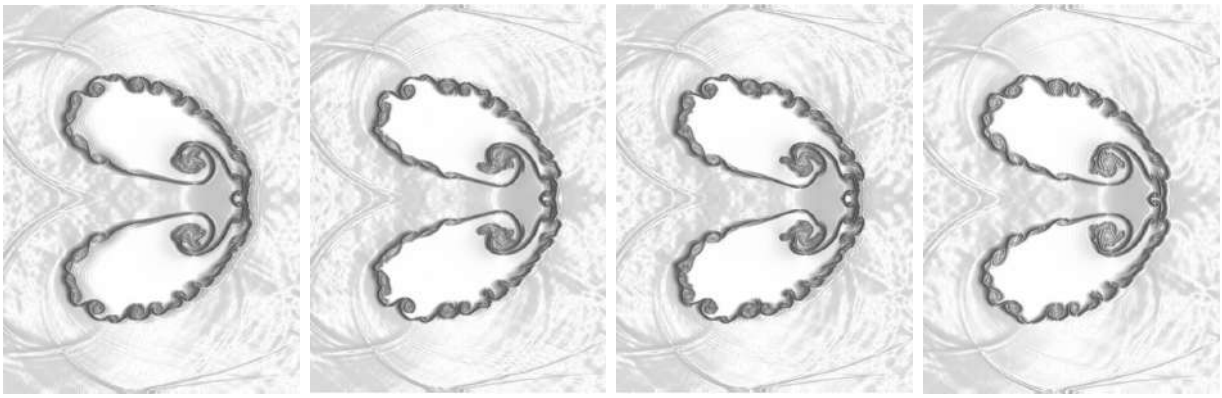

Figure 4.18: Air-helium shock-bubble interaction, comparison of WENO5 class methods, mesh: 4000×400, dt=2.5 × 10^{-9}, t_{final}=0.05 ms, left to right: WENO5-JS, WENO5-Z, WENO5-SZ, WENO5-IS.

Furthermore, the impact of the numerical flux formulation (HLLC versus KNP) is presented in Figure 4.19. We notice a strong diffusivity in the case of both, second-order MUSCL and fifth order WENO5-SZ method. The KNP flux formulation is proved to be very diffusive in the present study.

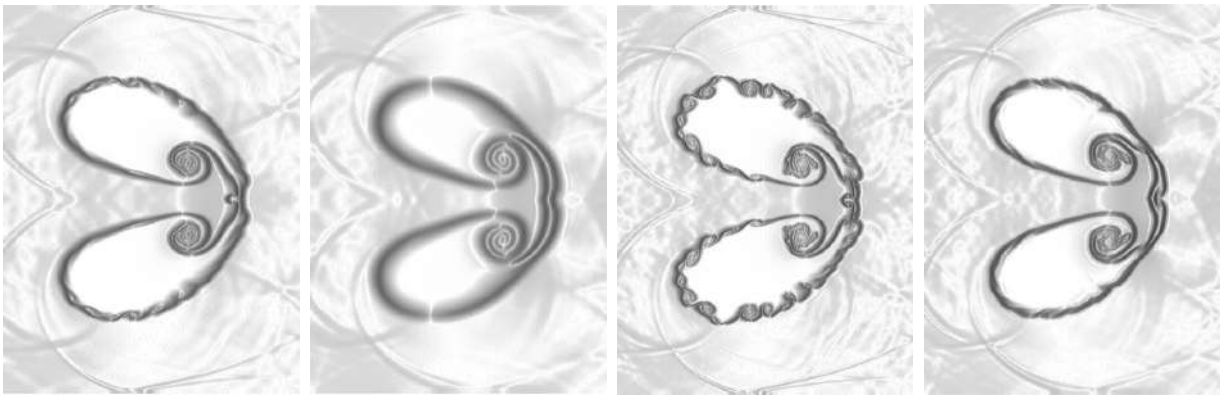

Figure 4.19: Air-helium shock-bubble interaction, comparison of the numerical flux formulations, mesh: 4000×400, dt=2.5 × 10^{-9} s, t_{final}=0.05 ms, left to right: HLLC Hancock-MUSCL, KNP Hancock-MUSCL, HLLC Hancock-WENO5-IS, KNP Hancock-WENO5-IS

Lastly, the effect of the characteristic variables reconstruction has been analysed. No strong discrepancy for the results by using characteristic or primitive variables have been observed.

The study of the mesh convergence of the schemes have been performed on the maximum pressure component computed at the final time t_{final}=0.05 μs with CFL=0.3 by using MUSCL, WENO3-Z, PPM and WENO5-IS reconstruction methods. The evolution of the maximum pressure reached during the process is plotted in Figure 4.20 (left part). The solution of the maximum pressure has three main peaks. The first one of the approximate value 1.8 bar occurs at time 0.3 μs. All schemes led to the similar pressure values. The second and highest peak of 2.2 bar happens at time 1.2 μs, which has been correctly reconstructed by all schemes with HLLC formulation and has been delayed and smoothed by using KNP formulation. Finally, the third peak of 1.9 bar with two parts occurring at times between 2.9-3.5 μs has been slightly decreased in intensity by using PPM reconstruction with HLLC formulation and shifted in time and lacking the accurate intensity by using KNP formulation.

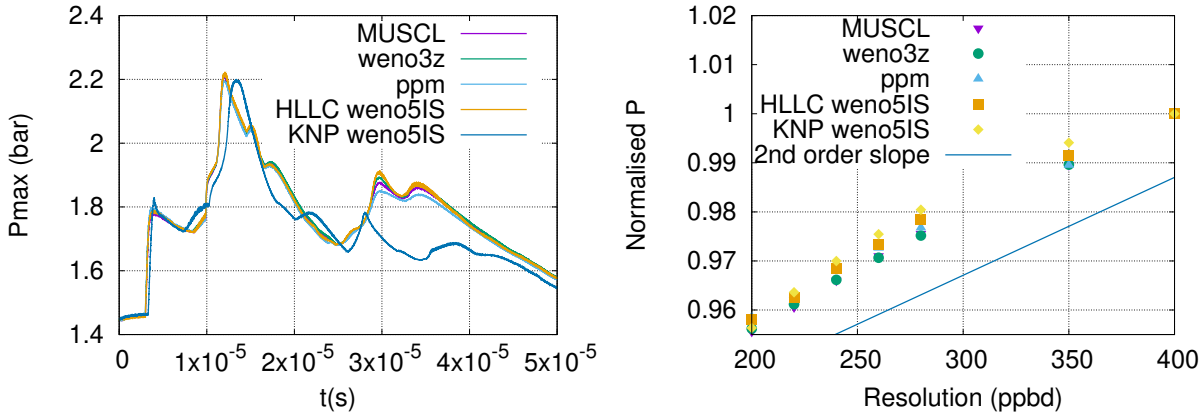

Figure 4.20: Air-helium shock-bubble interaction, maximum pressure comparison, mesh: 4000×400 (left), convergence of the maximum pressure (right). CFL=0.3

The normalized pressure value of the highest peak (estimated by using the solution computed on the finest mesh 4000×400 nodes with the WENO5-IS formulation) is shown in Figure 4.20 (right part) against the gradually increased mesh resolution indicated by the number of points per bubble diameter (ppbd). The convergence of approximate second order is verified by computing the approximate error related to the finest mesh pressure value. This confirms the numerical accuracy of the schemes achieved in previously discussed 1D tests of shock-tube.

The validation study in 2D highlighted a fairly good performance of all numerical schemes. The HLLC solver is shown to be more suitable for present computations, while KNP flux formu-

lation is diffusive. The effect of high order reconstruction compared to the second order MUSCL reconstruction is illustrated. The standard formulations of WENO3-JS and WENO5-JS are more diffusive compared to its modified counterparts, e.g. WENO3-Z and WENO5-SZ,IS. The variation between the primitive and characteristic reconstruction is negligible, hence, the primitive reconstruction is preferred due to its simpler derivation and implementation.

4.7 Conclusion

The objective of validation process has been set up to define the schemes performance based on different problems. Three problems in 1D (shock-tube and two expansion tube problems) and one problem in 2D (air-helium shock-bubble interaction) have been defined as suitable tests to examine the response of the numerical schemes to phenomena of shocks, contact discontinuities and expansions waves. The problems have been tested in hierarchical order from easiest to the most difficult in 1D: shock-tube, expansion tube with low velocity, expansion tube with high velocity. The following conclusion can be draw:

- **Order of accuracy.** While the numerical schemes presented in this thesis have a high formal order of accuracy, this order cannot be achieved where discontinuities in the solution are present. The average second order of accuracy is estimated for all the considered schemes.
- **Flux formulation.** The choice of the flux formulation was crucial as we computed more complicated cases. As such, while shock-tube problem did not illustrate differences in the solution, discrepancies appear in the pressure profile for the expansion tube. Moreover, the solution obtained with the KNP scheme for the 2D shock-bubble interaction is strongly diffusive. Hence, we believe that in this regard, HLLC solver is preferred.
- **Reconstruction variables.** The effect of reconstruction variables has not been shown to be important. While several schemes are responding better to characteristic variables (PPM in particular), we have noted that generally stable schemes, such as WENO5-IS, WENO3-Z, WENO3-P have similar solution with primitive and characteristic variables. Overall, the primitive variables reconstruction is simpler in terms of analytical derivation and implementation. Hence, it makes sense of choosing the schemes where the choice of variables is not crucial. Nevertheless, PPM method should be used with characteristic variables based on our tests.
- **High-order reconstruction.** We have tested variety of high-order numerical schemes and several methods have demonstrated better overall results in all the considered problems. These schemes are: WENO5-IS, WENO3-Z, WENO3-P. The PPM method is working well with characteristic reconstruction and can be used in this way. MP5 method is oscillating in all problems. MUSCL scheme is always stable but has considerably less detail in reconstruction as per our qualitative assessment.

Chapter 5

2D Shock-induced bubble collapse

This Chapter addresses the problem of a liquid-gas shock-induced bubble collapse. Two problems are proposed: firstly, the bubble collapse in a free-field and, secondly, the similar problem in the vicinity of a wall (which can lead to the erosion of the solid material).

The objective of this Chapter is to establish the high-order numerical schemes effect on the solution reconstruction. Precisely, the solutions of maximum pressure inside the fluid P_{max} in the case of bubble collapse in a free field and, additionally, maximum pressure next to the wall $Pwall_{max}$ in the case of bubble collapse close to a wall are examined on the point of accurate overall reconstruction and, more importantly, accurate recovery of pressure peaks. The study for the convergence of pressure intensity peaks is presented. The qualitative examination of the contours of the density gradients is proposed. We aim to quantify the numerical schemes impact on the solutions and draw a preliminary conclusion for further 3D computations.

5.1 Bubble collapse in a free-field

The present test is based on the one presented in Bourne & Field (1992) and computed by various authors (for example Nourgaliev *et al.* (2006)). An air bubble with diameter 6 mm, immersed in water at rest, is impacted by a normal shock wave for which the Mach number M_{sh}=1.7. The physical conditions are initialised as following: $P = 10^5$ Pa, $\rho_{air} = 1$ kg/m^3 and ρ_{water} 1000 kg/m^3. Only a half of the bubble is considered due to the symmetry of the problem. The domain has top and bottom boundaries set as slip walls, left and right boundaries have imposed non-reflective conditions. The computations are made with spatial discretization of 2000×1000 nodes using either a fixed time step $dt = 10^{-9}$ s or a fixed CFL number. The EOS parameters and post-shock condition are stated in Table 5.1.

Table 5.1: Water-air EOS parameters and post-shock condition

	γ	P_∞	C_p
air	1.4	0 Pa	4180 J/K.kg
water	4.4	6×10^8 Pa	1487 J/K.kg
	P	ρ	u
post-shock	1.9×10^9 Pa	1323.65 kg/m^3	681.58 m/s

Firstly, a description of the main physical phenomena is proposed in Figure 5.1 where the density gradient modulus (the top of the plot) and the pressure field (the bottom of the plot) obtained by using WENO5-IS scheme are plotted. The collision of the shock with the bubble causes a strong rarefaction wave to be reflected in the backward direction and a weak shock wave

to penetrate the bubble (at time t=2 μs). The pressure difference leads to the bubble deformation which becomes kidney shaped (at time t=3 μs). This particular shape is a result of the vorticity occurred at the bubble edge due to the water jet caused by the passing shock wave. The high pressure zone is generated once this water jet hits the standing still water in front of the bubble causing the emission of a strong blast wave (time $t = 4$ μs). Moreover, further propagation of the water jet and its high speed makes the blast front expand asymmetrically. Finally, a high pressure area is generated at time t=4.8 μs due to the recollapse of the bubble pieces by the leftward front of the blast wave. While the blast wave continues to expand, the cavity shrinks and the low pressure fields are observed at the vortices core.

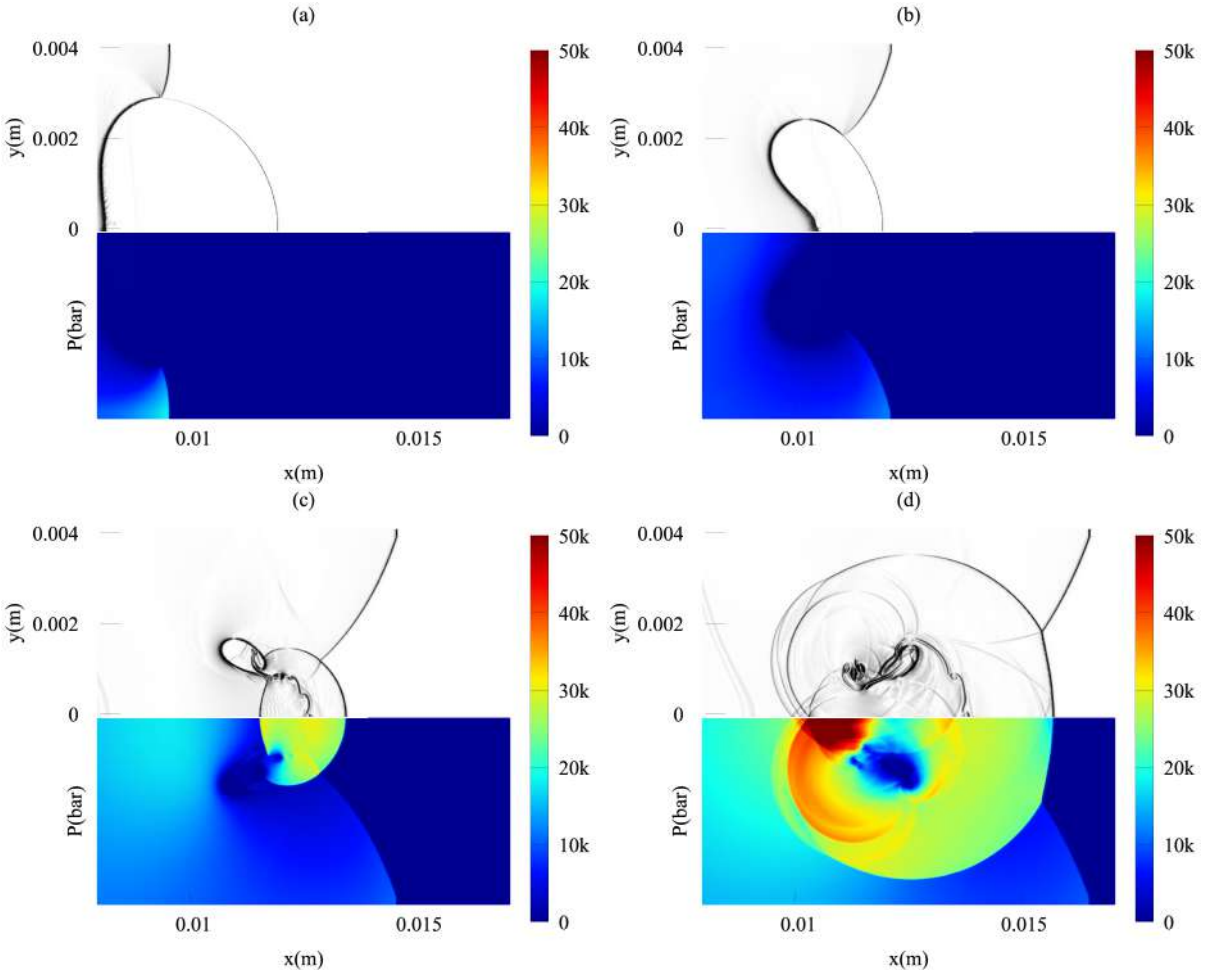

Figure 5.1: Bubble collapse time evolution, (a) 2 μs, (b) 3 μs, (c) 4 μs, (d) 4.8 μs, HLLC Hancock WENO5-IS, mesh 2000 $\times$ 1000, CFL=0.3.

The time and the intensity of the maximum pressure peaks reached during the collapse are analysed. The mesh convergence is attested through the evolution of the highest pressure peak. Figure 5.2 (left) presents the evolution of the maximum pressure where three main peaks are observed (see Table 5.2). The first peak occurs at approximately 3.6 μs due to the generation of the blast wave and highest values are obtained by using WENO3-Z and WENO5-IS, i.e. 50,600 bar and 50,700, respectively. The second peak happens at approximate time 4.4 μs due to the generation of another strong shock wave in the liquid when the expelled-gas shock focuses on the bubble's most upstream point. Finally, the third and strongest peak is observed at approximate time 4.7-4.8 μs due to the recollapse of the bubble fragments. This peak has the most deviations in solution. The PPM method results in the strongest peak intensity, around 98,000 bar, which is almost 10% higher than the two other schemes. The difference between pressure intensities obtained by WENO3-Z and WENO5-IS at this peak is approximately 3,000 bar with higher value computed by using WENO5-IS. This corresponds to approximately 3% difference. Similar solution variation has been noted by using MUSCL method which led to the lower intensity of pressure by

around 3%.

Table 5.2: Shock-induced bubble collapse, comparison of the maximum pressure peaks P_{max}.

Water-air shock-bubble, Pmax (bar)						
Scheme	t1	P1	t2	P2	t3	P3
MUSCL	3.6μs	49,900	4.4μs	58,100	4.8μs	86,600
WENO3-Z	3.6μs	50,600	4.4μs	59,600	4.8μs	86,300
PPM	3.7μs	51,506	4.39μs	65,950	4.7μs	97,930
WENO5-IS	3.6μs	50,700	4.4μs	67,300	4.8μs	89,300

The convergence of the schemes is studied by refining the mesh and examining the third peak pressure intensity. Figure 5.2 (right) presents the convergence by using the second order MUSCL reconstruction and higher order methods, WENO3-Z and WENO5-IS. The values have been normalised by the pressure value obtained on the finest mesh, i.e. 2000×1000 nodes. The computations have been performed by using fixed CFL=0.1 which has been chosen based on the preliminary studies of CFL effect. The oscillating nature of the solution is noted across all schemes which makes it problematic to perform the numerical convergence study. This is especially the case for the PPM scheme which led to the most oscillating result. Thus, in order to perform approximate convergence study, the Savitsky-Golay filter of fourth order with 100 points is used to smooth the data Savitzky & Golay (1964). The PPM reconstruction is not included to this analysis due to the strong oscillations. The better convergence of high-order WENO3-Z and WENO5-IS is noted compared with second-order MUSCL scheme, where slight discrepancy is observed. The mesh independent solution is achieved at around 500 points per bubble diameter, which corresponds to the mesh 2000×1000 nodes.

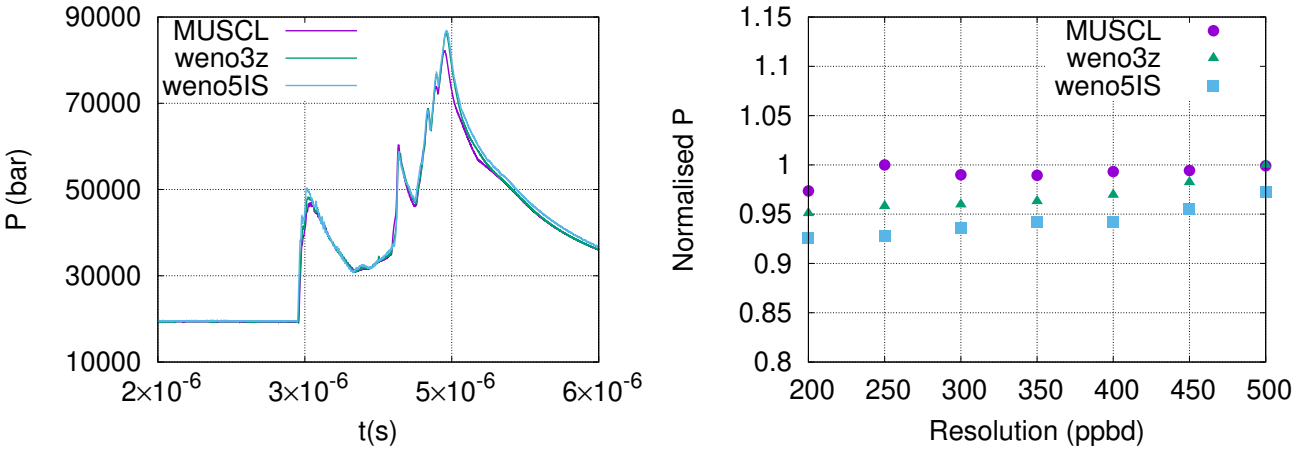

Figure 5.2: Shock-induced bubble collapse, maximum pressure filtered with Savitsky-Golay method, mesh 2000 × 1000 (left), convergence of the third pressure peak (right), CFL=0.1.

The density gradient along with the pressure profile evolution at the time of the third pressure peak t_3 is proposed in Figures 5.3-5.4. The presented results have been computed on the mesh 2000×1000 with CFL=0.3. The variation in the solution obtained by using different order schemes is noticed. The most detailed solution is obtained by using WENO5-IS scheme where all the details of the bubble core structure can be distinguished. The PPM method, on the other hand, has a structure which is smeared, the internal structure lines are thicker. However, the least amount of details is produced by the second order MUSCL approach, which is a consistent result based on the theoretical order of accuracy of these schemes. The pressure profiles are illustrated at the bottom of the plots. The highest values are observed in the solution computed with PPM as has been noticed with the maximum pressure analysis. The low pressure area inside the vortices is present on the plots of all three schemes.

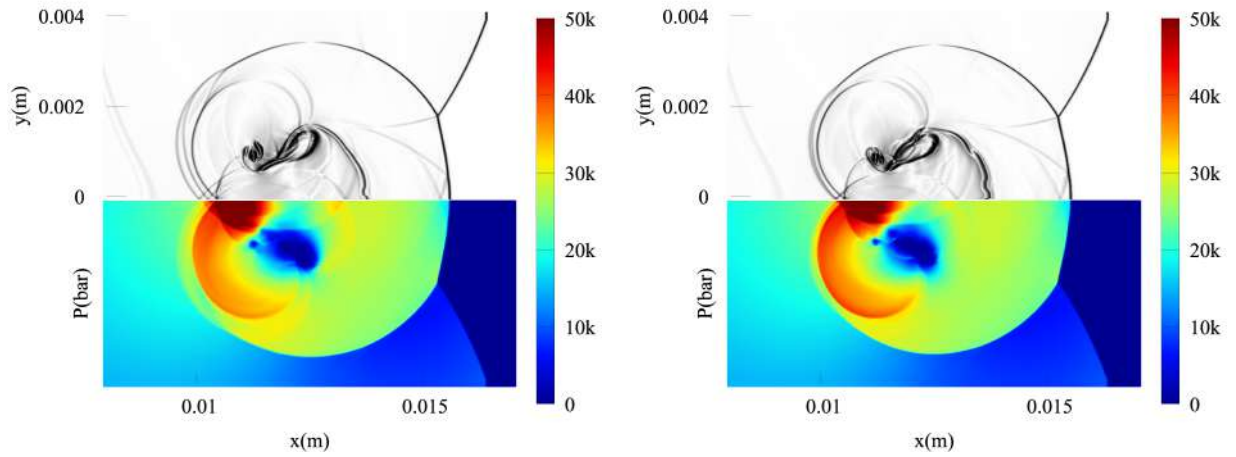

Figure 5.3: Shock-induced bubble collapse, contour of density gradient (top) and pressure field (bottom), MUSCL (left), PPM (right). Mesh 2000 × 1000 nodes, CFL=0.3, time t=4.8μs.

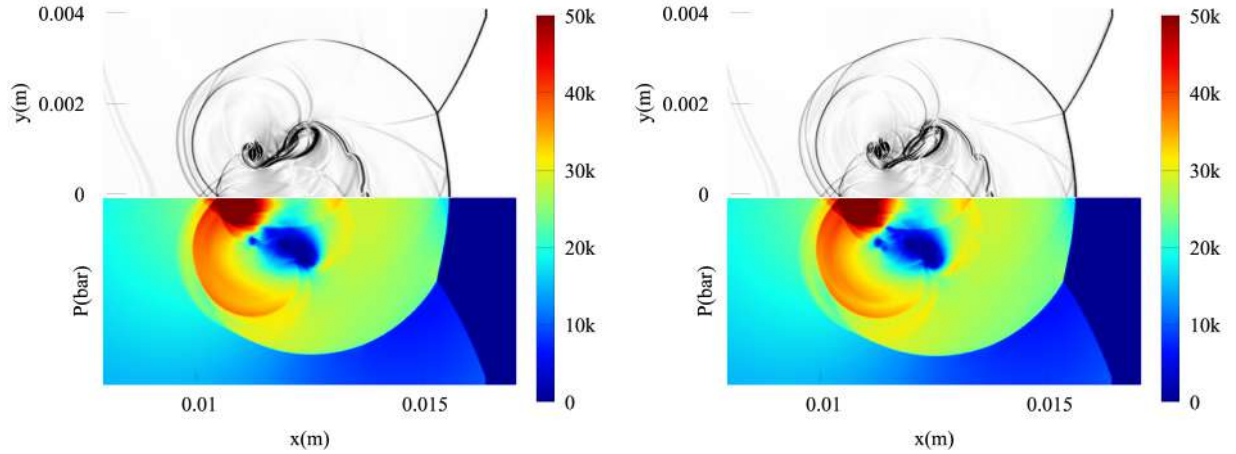

Figure 5.4: Water-air shock-bubble collapse, contour of density gradient (top) and pressure field (bottom), WENO3-Z (left), WENO5-IS (right). Mesh 2000 × 1000 nodes, CFL=0.3, time t=4.8μs.

The problem of the shock-bubble collapse in a free field is characterised by large pressure jump at the time of the recollapse of the bubble fragments. It is expected that the high-order numerical schemes are able to recover the value of such a pressure intensity with more accuracy than MUSCL methods. Moreover, the complexity of the physical phenomena involved into this problem can be reconstructed only by using very fine mesh during the computations. The results presented in this Section illustrated an effect of high-order reconstruction. Indeed, the solutions obtained by using WENO3-Z and WENO5-IS have better accuracy compared with MUSCL scheme by using the same mesh. PPM method has a variation which is not observed with other schemes. The highest pressure peak and its intensity might be a result of the oscillating nature of the method.

5.2 Bubble collapse near a wall

The present test has been proposed by Paquette Paquette *et al.* (2018) to study the potential wall damage due to the bubble collapse. A wall is placed behind the bubble. A normal shock wave initially located at 0.1 mm is moving with a Mach number M_{sh}=1.09 causing the bubble collapse. The EOS parameters stay the same and the post shock conditions are given below:

$$\begin{pmatrix} P \\ \rho \\ u \end{pmatrix}_{post-shock} = \begin{pmatrix} 1.2 \times 10^8 \text{ Pa} \\ 1049 \text{ kg/m}^3 \\ 75 \text{ m/s} \end{pmatrix} \tag{5.1}$$

The computational domain is of a size 0.3×0.5 mm and the initial bubble diameter is 0.1 mm with its initial location at (0.2,0) mm. The ratio L/R_0 between the position of the bubble center to the wall and the initial bubble radius is a major parameter that governs the bubble collapse dynamics. As suggested in the study of Johnsen and Colonius Johnsen & Colonius (2009), the bubble initially located at a distance lower than $L/R_0 = 2$ presents a high potential to cause damage. We consider in this section only the case where the ratio $L/R_0 = 2$.

The computations are made with fixed CFL=0.1 and 650 points per bubble diameter, which corresponds to a spatial discretization of 1908×3180 nodes. The solutions are obtained by using MUSCL, WENO3-Z, WENO3-P, PPM and WENO5-IS.

The mesh convergence is verified on the evolution of the maximum pressure peaks based on the solutions obtained with MUSCL, WENO3-Z and WENO5-IS. The mesh is ranged between 750×1250 and 1908×3180 (250 to 650 points per bubble diameter). Three main peaks in the pressure solution are observed. The first one, with the lowest intensity, occurs at around time 0.13 μs and is due to the impact of the incident shock wave on the wall. The second one is observed at time 0.28 μs and is a result of the impact of the generated blast wave on the wall. The third one, at time 0.36 μs, is caused by the impact of a secondary wave emitted by the recollapse of the bubble. All numerical schemes lead to approximately similar time for these peaks. The intensity of the peak depending on the employed numerical scheme is presented in Table 5.3. The tests have shown the convergence of all schemes with a mesh independent solution achieved using 500 points per bubble diameter. However, the strong dependency of the third pressure peak on the CFL number has been established. The first and second pressure peaks converge faster even with higher CFL numbers.

Table 5.3: Bubble collapse near a wall, comparison of the maximum pressure peaks P_{max}.

Water-air shock-bubble with a wall, maximum pressure P_{max} (bar)						
Scheme	t_1	P_1	t_2	P_2	t_3	P_3
MUSCL	0.13μs	2,573	0.28μs	9,444	0.36μs	8,829
weno3-Z	0.13μs	2,565	0.28μs	9,453	0.36μs	8,938
weno3-P	0.13μs	2,565	0.28μs	9,440	0.36μs	9,158
PPM	0.13μs	2,553	0.28μs	9,449	0.36μs	9,070
weno5-IS	0.13μs	2,563	0.28μs	9,456	0.35μs	9,138

The highest third pressure peak has been obtained by computing the solution with the schemes of higher order, i.e. WENO5-IS, PPM and WENO3-P, while the first and second pressure peaks have only slight difference caused by the numerical scheme. Figures 5.5 and 5.6 present the mesh convergence of the MUSCL, WENO3-Z and WENO5-IS schemes.

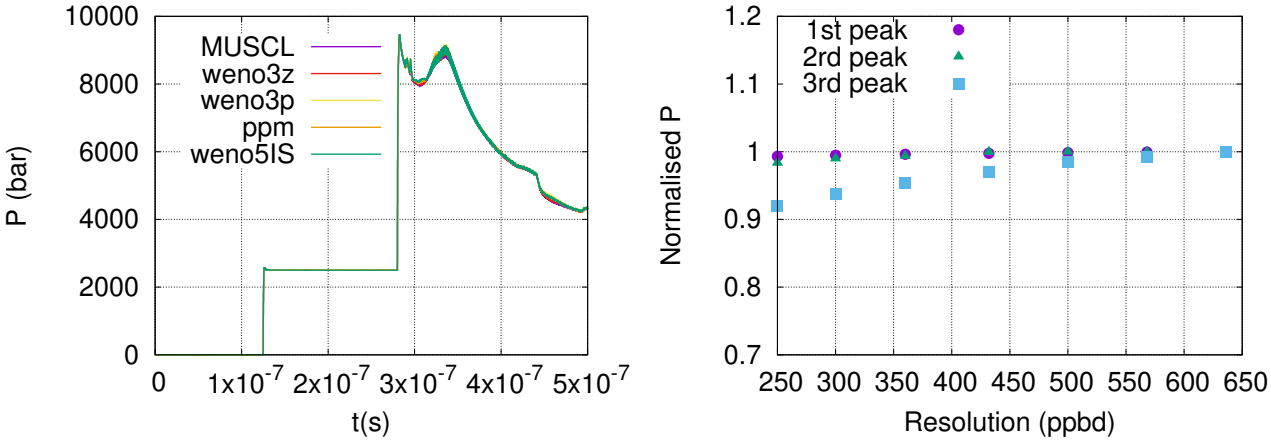

Figure 5.5: Bubble collapse next to a wall, maximum wall pressure obtained with the mesh 1908 × 3180 nodes, CFL=0.1 (left), convergence of the maximum pressure peaks P_{max} obtained with MUSCL, CFL=0.1 (right).

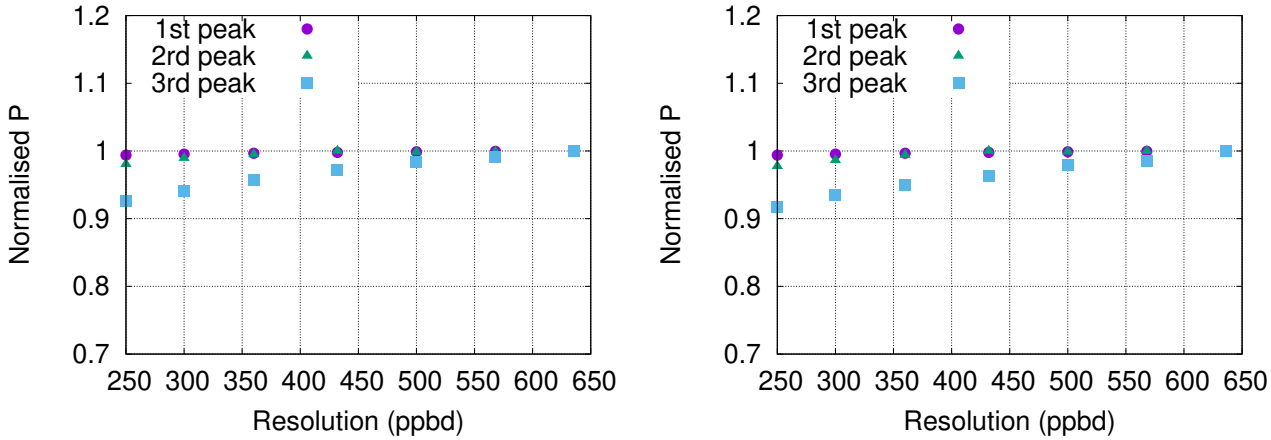

Figure 5.6: Bubble collapse next to a wall, convergence of the maximum pressure peaks P_{max}, CFL=0.1, WENO3-Z (left), WENO5-IS (right).

The solution improvement based on the enlargement of the density gradient is illustrated. The gradient of the density with corresponded pressure profile at the time of the third pressure peak is proposed in Figure 5.7. For comparison purposes, five main elements are distinguished in the bubble vortices curvature, c_1, c_2, c_3, c_4 and c_5. These elements are noted on the plot with WENO5-IS solution since this scheme led to overall most accurate results. In the discussion to follow, the comparisons of the solutions will be relative to this method.

We note that the numerical solution computed with MUSCL does not reconstruct the vortices accurately. All the elements of curvature have been smoothed out and, moreover, the element c_4 does not have the complete shape. The pressure profile has also considerably less area of high pressure values. On the other hand, WENO3-P and WENO3-Z led to the reconstruction of better accuracy. The element c_5 is best resolved by WENO3-P, where internal space of the vortex has the curved structure as we indeed also observe in the solution by WENO5-IS. The shape of the element c_4 is computed with the most amount of details by 3-P and also WENO3-Z. The c_2 element is reconstructed accurately by all schemes of this class with slightly more concave structure produced by WENO3-P. The element c_1 is smoothed out considerably by using the schemes WENO3-P and WENO3-Z. Finally, the comparison with PPM solution is proposed. This solution is the most close to the solution produced by WENO5-IS. The main deviations are in the curvature of the element c_2, where WENO5-IS has more concave structure. The c_3 element is not reconstructed sufficiently by PPM and only the top part is present. The inside vortex elements, c_4 and c_5, are solved accurately with again less detailed resolution of the element c_5. Precisely, the inside structure is more smeared and lacks some details in the PPM solution.

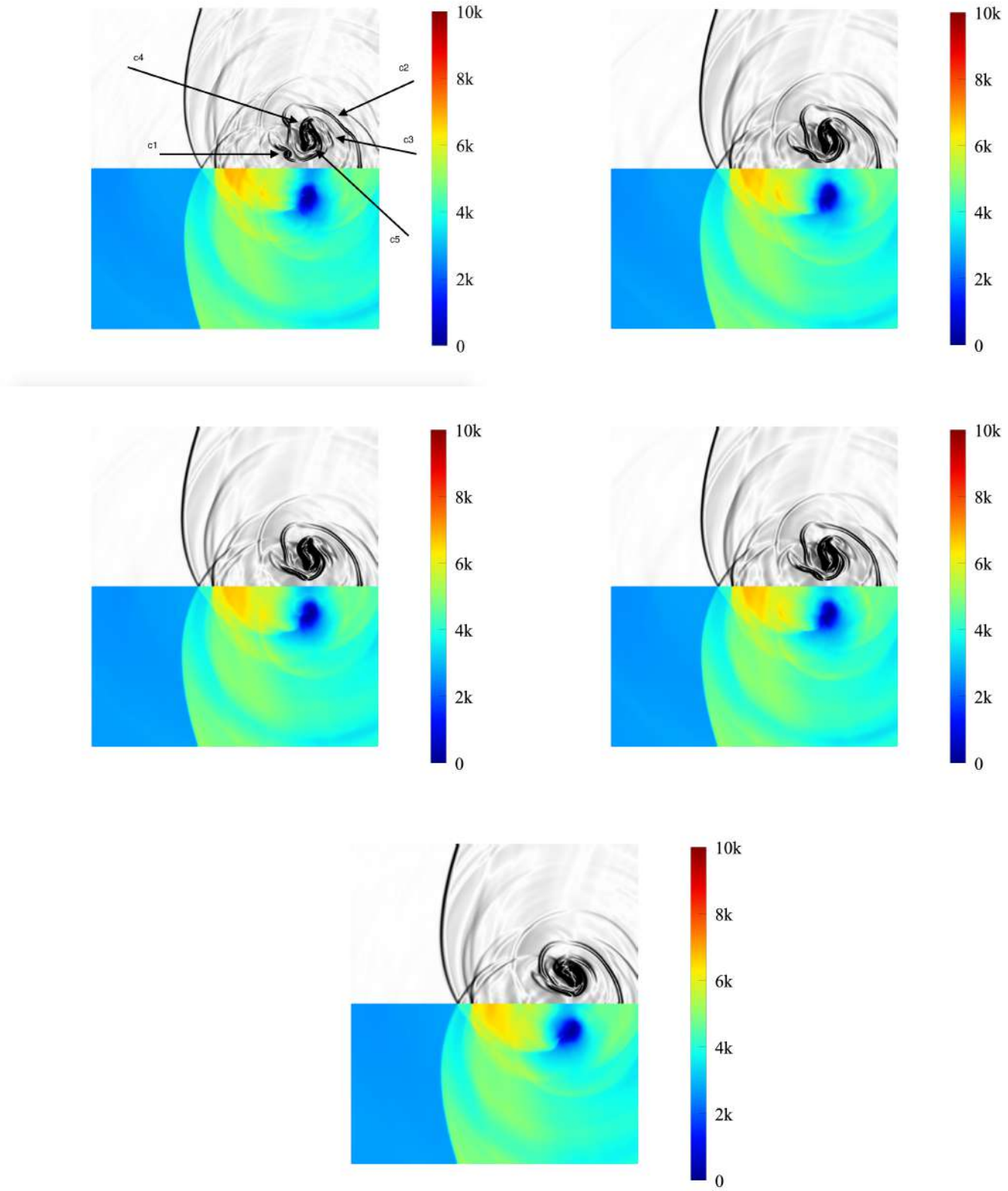

Figure 5.7: Bubble collapse next to a wall, comparison of the reconstruction method, contour of density gradient (top), pressure field (bottom), mesh: 1908×3180, CFL=0.1, left to right: WENO5-IS, PPM, WENO3-z, WENO3-P, MUSCL

The computational time of the solutions obtained by using the key numerical schemes (i.e. MUSCL, WENO3-Z, WENO5-IS) is given in Table 5.4. The cost has been increased by 40% between MUSCL and WENO5-IS schemes. This cost of computations is critical for higher resolution computations and, particularly, for 3D problems.

Table 5.4: CPU cost, bubble collapse near a wall. Mesh: 1908×3180. CFL=0.1.

Scheme	CPU (h)	ratio
MUSCL	94.7	1
WENO3-Z	121.6	1.28
WENO5-IS	133.7	1.41

5.3 Synthesis

The objective of this Chapter has been set to define the effect of high-order numerical schemes and to map a strategy of further 3D computations. Two tests have been performed: shock-bubble collapse in a free field and in vicinity to a wall.

The numerical schemes response to the large pressure jump generated by bubble's fragments recollapse in the first case has been observed. Indeed, superior reconstruction of the pressure intensity has been observed by using WENO5-IS and WENO3-Z schemes compared with second order MUSCL reconstruction. Furthermore, the qualitative examination of the density gradient highlighted more detailed solution. The PPM method, while led to the highest pressure intensity value, is thought to be less accurate and these values are accounted to the oscillating nature.

The results obtained from the computations of the bubble-collapse next to a wall showed similar tendency. The most accurate results were achieved by using WENO5-IS scheme. The solution has been considerably improved in comparison to the second order MUSCL technique.

The part of the objective of this Chapter, however, was a quantification of the high-order numerical schemes results. The computations of a reference solution being not feasible, this quantification is based only on two components: the magnitude of pressure peaks and the computational cost.

Interestingly, by only looking at the maximum pressure components of the solution (maximum pressure next to a wall in the case of bubble collapse in vicinity to a wall), we do not observe a huge difference. Particularly, an improvement of only 3% is noted by using WENO5-IS for the first problem. On the other hand, bubble collapse next to a wall illustrated very similar pressure intensities values by all methods. Hence, most of the conclusions can be drawn by qualitative observations.

While these observations indeed lead to the conclusion of better results obtained with WENO5-IS and WENO3-Z schemes, the numerical solution assessment is not complete without the comparison of the CPU cost. Indeed, an increase of the CPU cost is present as the order of the method improves, in particular due to the increase of the computational stencil size. The cost has been increased by 40% using WENO5-IS scheme in comparison with the MUSCL simulation. This cost is acceptable in 2D cases but becomes critical for 3D configurations. Thus, an important further development is to examine potential strategies to reduce this CPU cost.

Chapter 6

Mesh stretching

The high computational cost of presently considered problems due to the combination of necessity of the large number of points per bubble diameter and the size of computational stencil, leads to the consideration of possible strategies to reduce either number of points or CPU or both with minimum accuracy loss. The CPU reduction stand-alone can be achieved by employing various parallelization techniques. However, in order to achieve high-fidelity 3D computations which require very fine grids, the computational cost becomes prohibitive even with parallel solvers. Hence, the mesh points reduction is required.

One of the possible solutions to this problem is an introduction of a non-uniform mesh. One can observe that the bubble does not occupy the whole computational domain and depending on the considered problem the area of the uniform mesh can be defined around the bubble location. That is, the number of the points per bubble diameter will be the same as the originally solved problem, while outside this area, the cell size will be gradually increased up to the boundary of the domain.

The second solution, which is somewhat related to the first one, is continuous increase of the cell size from a given arbitrary point inside the computational domain, the middle of the bubble, for instance.

The hypothesis tested here is to determine whether or not the CPU cost can be reduced by keeping constant the number of points per bubble diameter and reducing the number of points outside the bubble without consequential reduction of the accuracy.

6.1 Non-uniform mesh overview

The emergence of the non-uniform grids can be related mainly to the need of solving the partial differential equations on arbitrary geometry of the computational domains. This is especially a requirement for the computational fluid dynamics problem, from where most developments of this research domain originated. Generally, these grids are explored in the problems where the curvilinear coordinate systems are required. These problems with an introduction of non-uniform grids became a focus of many researches, in particular in the framework of formal accuracy order of the solution in the case of non-uniform grids. For instance, Thompson *et al.* (1985) performed an extensive analytical study about the accuracy variations by using two different non-uniform grid strategies: fixed distribution function and fixed number of points. Moreover, the evaluation of the distribution functions has been performed, the result of which can be extended to other systems where the non-uniform meshes might be used. Ten distribution functions have been considered, including the exponential function, hyperbolic sine and tangent etc. The conclusions about which distribution function is the most suitable for particular problems have been drawn.

An alternative strategy for non-uniform mesh generation is an introduction of the adaptive mesh where the cluster of points is generated in certain critical areas of the solution. This method

is divided into two main classes. The first class of refinement is adaptive mesh redistribution or so-called p-refinement Chung (2002). The idea of p-refinement is to continuously reposition a fixed number of cells to locally improve the solution accuracy. While this type of refinement is fairly easy to implement, there is no possibility to change the topology in the case of discontinuities. This may lead to the grid distortion. The second class of adaptive refinement is h-refinement or commonly called AMR Berger & Joseph (1984), where the point clusters are continuously changing by adding and removing cells. The advantage of this method is the possibility to use it in many problems where the localised large-gradients are present, e.g. the problems with discontinuities, shocks and phase changes. However, this method is considerably more complex in terms of its implementation and parallelization. Some of the potential difficulties in sequential programming of this method include the definition of refinement criterion, the refinement constraints and its order.

The simpler non-uniform structured grids can be implemented for the problems where the solutions have the localised variation area. The functions suitable to generate such grids have been analysed in terms of the truncation error by Vinokur (1980). These functions are meant to be used when the reduction of the points with retained accuracy of the solution is required and applied in a way of the points clustering around the regions where the solution varies the most. Realistically, these regions are often unknown and complex. Moreover, some problems might have the solution with several such regions which are changing with the time iterations. Thus, the perfect grid generating system is an adaptive system, which regenerates the grid as often as needed according to the physics of the problem in consideration. This type of grids have been considered in the context of the finite difference methods with one-dimensional problems, for instance in Pierson & Kutler (1980) and Gough *et al.* (1975). However, in order to use these grids in multi-dimensional space, further developments are required due to the usually difficult geometry of the clustered regions.

Some problems in practice can be evaluated beforehand in terms of the regions where the clustering is needed. Particularly, this estimation can be based on the well predictable topology of the problem, simple configurations of the shock wave etc. Often, such problems are based on the elliptic boundary-value problem and clustering study for these type of cases have been studied in Middlecoff & Thomas (1979) and Thompson *et al.* (1977). The clustering at the boundaries can be set by using the algebraic systems with one-dimensional functions, normally addressed as stretching functions. Such algebraic systems are discussed in some details in Thompson (1983) and Thompson *et al.* (1985). Assuming a simple geometry, the clustering can be obtained by using only algebraic systems with one-dimensional stretching function.

Several types of stretching functions are available to work with problems where the geometry of the area with highly varied solution can be predefined. The most straightforward one-dimensional stretching function involves only two parameters. For instance, an interior stretching function would require the location point in the computational domain, where the function is initialised, and the value of spacing which is taken as the first and minimal value for the slope. On the other hand, for two-sided stretching function these two parameters are the slope values at both ends of the distribution. Yet another stretching function can have the asymmetrical nature, where the slopes at both ends are equal and constructed by using two one-sided stretching functions. Moreover, the interior stretching function can be used to construct one-sided function where the clustering is defined at either of the ends.

Different distributions are used two construct these stretching functions. The study of Thompson (1972) explored the inverse hyperbolic sine distribution function for the numerical computations in the framework of inviscid supersonic flow over the blunt delta wing. The points have been clustered on the body of the wing by employing the one-sided function. The logarithmic function of two-sided anti-symmetrical class is used in the study of Roberts (1971) for the boundary-type of the problem. However, as noted in Vinokur (1983), the derivation of such a function ignored the truncation errors and, even though, such a function could be used in some flow problems, there is a strong motivation for developing two-sided stretching function which would allow arbitrary stretching at either of the ends of the function independently from each other.

This Chapter explores the two classes of stretching functions. The first one is a one-sided stretching function based on either hyperbolic sine or tangent distributions. The second one is

interior stretching function based on the hyperbolic sine. The discussion of reasons for these two functions is proposed and the construction of these functions is discussed. Moreover, the derivation of the high-order numerical schemes such as PPM, WENO5 and WENO3 for the non-uniform mesh is discussed. Finally, the validation of these techniques is performed on the air-helium shock-bubble problem and the implementation is then extended to the bubble collapse with and without a wall. The strategies of the clustering for every considered problems are proposed.

6.2 Evaluation of distribution functions

The stretching functions used for the non-uniform mesh generation can be based on variety of distributions. An evaluation of the distribution functions has been presented by Thompson *et al.* (1985) based on the measures of the order. The distribution functions which are suitable for a very small spacing were determined.

The following conclusions were drawn based on the analysis presented by authors:

1. even though exponential function is close to the hyperbolic tangent function in terms of the smoothness, the final conclusion is that the exponential function is not as good. Hence, the hyperbolic function is preferable

2. the comparison between hyperbolic tangent and hyperbolic sine demonstrated a better suitability of the hyperbolic sine for the boundaries where the initial spacing is specified. However, considering other criteria, the hyperbolic tangent is better overall

3. considering the suitability of the functions in terms of within and outside the boundary layers, the error and hyperbolic tangent are the most suitable. The hyperbolic tangent function is better within and the error function is better outside the boundary layer.

4. the other functions, i.e. the sine, tangent, arc-tangent, inverse hyperbolic tangent and sine, quadratic and logarithm functions are not suitable for the stretching grid

In what is to follow, the hyperbolic tangent and sine functions will be considered and the construction of the functions to set up the grid stretching will be discussed.

6.3 Construction of one-dimensional stretching functions

This Section's concern is a one-dimensional stretching function. A particular interest for this function is due to its suitability for present study since the directional splitting is used for multi-dimensional problems and its simplicity since it can be constructed by using only two parameters. These two parameters involved into the stretching function are the arbitrary internal point in the domain and the initial size of the spacing. The objective of this section is to draw the conditions which such a stretching function should satisfy and present its derivation.

6.3.1 A general two-sided stretching function

The derivation of general two-sided stretching function was presented in Vinokur (1983). The following notations are used. The function is denoted by ε and its general form is $\varepsilon(t; s_0, s_1)$, where ε is a coordinate and t is a smoothly varied parameter which are normalised and defined as,

$$t = \frac{\bar{t} - \bar{t}_A}{\bar{t}_B - \bar{t}_A} \qquad \text{and} \qquad \varepsilon = \frac{\bar{\varepsilon} - \bar{\varepsilon}_A}{\bar{\varepsilon}_B - \bar{\varepsilon}_A} \tag{6.1}$$

The variables A and B denote the either ends of the curve. The parameters s_0 and s_1 stand for the dimensionless slopes at the points A and B and formulated as,

$$s_0 = \frac{d\varepsilon}{dt}(0) \qquad \text{and} \qquad s_1 = \frac{d\varepsilon}{dt}(1) \tag{6.2}$$

The criteria for the stretching function is based on the fractional truncation error analysis for the specific situation when the solution has a localised region of rapid variation. It has two points:

1. the order of all inverse scales of the t-variation with respect to ε should not be higher than one

2. the order of the slope $dt/d\varepsilon$ must be equal to the order of minimum length scale of function of unknowns ϕ or vector function r-variations with respect to t in the region where a rapid variation is located

These conditions should be satisfied for all s_0 and s_1. Additionally, the function should be monotonic and preferably simple, easily invertible and continuous for all s_0, s_1. Moreover, the stretching function is required to be constructed as such that $\bar{\varepsilon}(\bar{t})$ is independent of the choice of either ends of the curve, A and B, when not normalised.

Consider some universal function $\theta(z)$ and its scaled portion for defined values of s_0 and s_1 by using the corresponding points z_0 and z_1. These observations lead to the condition that the considered universal function θ is, in fact, odd. That is, the following is satisfied,

$$\theta(-z) = -\theta(z) \tag{6.3}$$

The two immediate candidates of the function described above, which are monotonic and invertible, are $sin(z)$ and $tan(z)$ which have the related hyperbolic functions if z is complex. The inverse function can be formulated by association of z with either ε or t. One can observe that the most conservative case is when the antisymmetric function is constructed by setting $s_0 = s_1$, which means that z_0=-z_1.

A case when $s_0 = s_1 > 1$ for $\sin(z)$ and $\tan(z)$ has been analysed in Vinokur (1980) where author demonstrated that only $\theta = tan(z)$ satisfies all the requirements to obtain the suitable stretching function. It is, thus, the function in consideration in present study. This function is constructed as follows. Defining the z ranges as $\Delta z = z_1 - z_0$ and θ ranges as $\Delta\theta = \tan(z_1) - \tan(z_0)$ for arbitrary s_0 and s_1, the normalized variables are defined,

$$\varepsilon = \frac{z - z_0}{\Delta z} \qquad \text{and} \qquad t = \frac{\tan(z) - \tan(z_0)}{\Delta\theta} \tag{6.4}$$

The slope of the stretching function is computed by taking the partial derivative of the coordinate ε with respect to the variable t,

$$\frac{d\varepsilon}{dt} = \frac{\Delta\theta}{\Delta z} cos^2(z) \tag{6.5}$$

In order to compute parameters s_0 and s_1, the trigonometric identity is used to rearrange equation (6.5),

$$\tan(z_1) - \tan(z_0) = \frac{\sin(z_1 - z_0)}{\cos(z_1)\cos(z_0)} \tag{6.6}$$

The equations for s_0 and s_1 follow,

$$s_0 = \frac{\sin(\Delta z)\cos(z_0)}{\Delta z \cos(z_1)} \qquad \text{and} \qquad s_1 = \frac{\sin(\Delta z)\cos(z_1)}{\Delta z \cos(z_0)} \tag{6.7}$$

The relation between the ends of the curve A and B with z_0 and z_1 are established by introducing the following,

$$A = \sqrt{\frac{s_0}{s_1}} \qquad \text{and} \qquad B = \sqrt{s_0 s_1} \tag{6.8}$$

Then, we have,

$$A = \frac{\cos(z_0)}{\cos(z_1)} \qquad \text{and} \qquad B = \frac{\sin(\Delta z)}{\Delta z} \tag{6.9}$$

The rearrangement by using the cosine sum identity leads the 6.9 to be rewritten as,

$$A = \cos(\Delta z) + \tan(z_1)\sin(\Delta z) \qquad \text{and} \qquad \frac{1}{A} = \cos(\Delta z) + \tan(z_0)\sin(\Delta z) \tag{6.10}$$

The setting arbitrary value for B and solving equation (6.9) for Δz, the value z_0 is then obtained from equation (6.10) with arbitrary value A. Finally, these developments and right equation in (6.4) lead to the following expression for the stretching function,

$$t = \frac{\tan(\varepsilon\Delta z + z_0) - \tan(z_0)}{\Delta\theta} \tag{6.11}$$

This expression, however, requires one more step to be used in the computations. One should notice that depending on the set value B, the ranges Δz and $\Delta\theta$ can be of imaginary type and, moreover, depending on the values for both, A and B, z_0 can be complex. The latter can be avoided by using the tangent sum identity to rewrite 6.11,

$$t = \frac{\tan(\varepsilon\Delta z)}{A\sin(\Delta z) + (1 - \cos(\Delta z))\tan(\varepsilon\Delta z)} \tag{6.12}$$

Furthermore, to find an antisymmetric solution which corresponds to $A = 1$ in order to simplify the above expression, the tangent sum identity is used once more to obtain the solution $u(\varepsilon)$,

$$u = \frac{1}{2} + \frac{\tan(\Delta z(\varepsilon - 0.5))}{2tan(0.5\Delta z)} \tag{6.13}$$

which is invertible. Hence, in order to obtain the slopes s_0 and s_1, only antisymmetric stretching function result is required. Furthermore, the desired stretching function is obtained by taking a square root of the ratio s_0/s_1.

The choice of the tangent function is also predetermined by noticing that the tangent of the sum is a rational function of each of the tangent components. The same argument, however, demonstrates an unsuitability of similar derivations by using sine function, since by definition the sine of the sum cannot be expressed as a rational function of individual sines, but, instead involves individual cosines along with individual sines.

The value for B is required in order to compute the antisymmetric function. Here, the type of z depends on B and three cases are present. Firstly, if $B > 1$, then z takes the form of imaginary type and the following expressions are obtained,

$$B = \frac{\sinh(\Delta y)}{\Delta y} \qquad \text{and} \qquad u = \frac{1}{2} + \frac{\tanh(\Delta y(\varepsilon - 0.5))}{2\tanh(0.5\Delta y)} \tag{6.14}$$

with the inverted formulation,

$$\varepsilon = \frac{1}{2} + \frac{\tanh^{-1}((2u - 1)\tanh(0.5\Delta y))}{2\Delta y} \tag{6.15}$$

Both formulations of hyperbolic tangent and its inverted counterpart can be expressed in terms of exponential and logarithmic functions.

Secondly, if $B < 1$, then Δz takes a real form and the following is valid,

$$B = \frac{\sin(\Delta x)}{\Delta x} \qquad \text{and} \qquad u = \frac{1}{2} + \frac{\tan(\Delta x(\varepsilon - 0.5))}{2\tan(0.5\Delta x)} \tag{6.16}$$

with the inverted formulation,

$$\varepsilon = \frac{1}{2} + \frac{\tan^{-1}((2u - 1)\tanh(0.5\Delta x))}{2\Delta x} \tag{6.17}$$

Finally, if the value of B is close to 1, the observation that both, Δx and Δy converge to zero and, thus, both previous formulations do not work. Hence, equations (6.16) and (6.17) have to be expanded in powers of Δx. That is, in $B - 1$ the first order expression is,

$$u \asymp \varepsilon(1 + 2(B - 1)(\varepsilon - 0.5)(1 - \varepsilon)) \tag{6.18}$$

and

$$\varepsilon \asymp u(1 - 2(B - 1)(u - 0.5)(1 - u)) \tag{6.19}$$

The one-sided stretching function with zero slope at $t = 1$ and given initial slope at $t = 0$ can be derived by scaling the half of the functions defined above. There are three cases which have to be taken into account. Firstly, if $s_0 > 1$ we have,

$$s_0 = \frac{\sinh(2\Delta y)}{2\Delta y} \qquad \text{and} \qquad t = 1 + \frac{\tanh(\Delta y(\varepsilon - 1))}{\tanh(\Delta y)} \tag{6.20}$$

with the inverted equation as,

$$\varepsilon = 1 + \frac{\tanh^{-1}((t-1)\tanh(\Delta y))}{\Delta y} \tag{6.21}$$

Secondly, if $s_0 < 1$ we have,

$$s_0 = \frac{\sin(2\Delta x)}{2\Delta x} \qquad \text{and} \qquad t = 1 + \frac{\tan(\Delta x(\varepsilon - 1))}{\tan(\Delta x)} \tag{6.22}$$

with the inverted equation as,

$$\varepsilon = 1 + \frac{\tan^{-1}((t-1)\tan(\Delta x))}{\Delta x} \tag{6.23}$$

Finally, if $s_0 \asymp 0$, the following is an approximate formulations for t and its inversion,

$$t = \varepsilon(1 - 0.5(s_0 - 1)(1 - \varepsilon)(2 - \varepsilon)) \tag{6.24}$$

and

$$\varepsilon = t(1 + 0.5(s_0 - 1)(1 - t)(2 - t)) \tag{6.25}$$

In order to incorporate the above developments, the solution of the non-linear equation has to be computed $y = sinh(x)/x$ for the case when $B > 1$ and $s_0 > 1$ for two-sided and one-sided stretching functions, respectively. This solution can be obtained by either solving this equation with one of the available iterative methods or by using approximate analytical formulation.

The solution to this implicit equation by using iterative method requires the following rearrangement,

- rearrange: $\sinh(x) = yx$
- apply inverse hyperbolic sine to both sides: $\operatorname{arcsinh}(\sinh(x)) = \operatorname{arcsinh}(yx)$
- result: $x = \operatorname{arcsinh}(yx)$

The last expression is then used as $f'(x)$ for the fixed point or Newton iterative methods.

However, in order to avoid the iterative methods, an approximate analytical expression is presented in Vinokur (1983). This analytical solution leads to a negligible error and, thus, the resulting mesh discontinuity does not have an effect on the final solution. These approximate analytical expressions are presented in Appendix A.

6.3.2 A general interior point stretching function

Another stretching function is an interior stretching function which equally requires two parameters: a slope, which is independent from the dimension s_i, and infliction point t_i, where the initial spacing is specified. The general interior stretching function is denoted as $\varepsilon(t, s_i, t_i)$ and the initial slope at the arbitrary interior point is then formulated,

$$s_i = \frac{d\varepsilon}{dt}(t_i) \tag{6.26}$$

The curvature of this slope is defined as,

$$\frac{d^2\varepsilon}{dt^2}(t_i) = 0, \text{ for } 0 \leq t_i \leq 1 \tag{6.27}$$

It appears that the only case which is practical is when $s_i > 1$. Similarly as for the two-sided stretching function, the odd universal function $\theta(z)$ is scaled and its portion is considered. While author in Vinokur (1980) analyses both, $\sin(z)$ and $\tan(z)$, the main conclusion is drawn that $\sin(z)$ satisfies the requirements of the desired stretching function based on the antisymmetric case when $t_i = 0.5$ and s_i takes a large value. Thus, a scaled portion of the inverse hyperbolic sine results in another stretching function $\varepsilon(t)$.

In order to construct an interior stretching function, let us consider $z = iy$ and the universal function $\theta = sin(z)$. Then, for the arbitrary t_i and the range $\Delta(y) = y_1 - y_0$ we write,

$$t = t_i\Big(1 + \frac{\sinh(\Delta y(\varepsilon - \varepsilon_i))}{\sinh\varepsilon_i \Delta y}\Big), \tag{6.28}$$

with its inverse formulation

$$\varepsilon = \varepsilon_i + \frac{1}{\Delta y}\sinh^{-1}((\frac{t}{t_i} - 1)\sinh\varepsilon_i\Delta y) \tag{6.29}$$

It has been suggested in Thompson (1972) to set $t = \varepsilon = 1$ and, given a value for Δy, we can write the relation between t_i and ε_i,

$$\frac{1}{t_i} = 1 - \cosh(\Delta y) + \sinh(\Delta y)\coth(\varepsilon_i\Delta y) \tag{6.30}$$

The inverse formulation is obtained by replacing the hyperbolic cotangent by its logarithmic formulation. Then

$$\varepsilon_i = \frac{1}{2\Delta y}\log(\frac{1 + t_i(\exp^{\Delta y} - 1)}{1 - t_i(1 - \exp^{-\Delta y})}) \tag{6.31}$$

Solving the equations for the value Δy requires to provide parameters s_i and t_i. In order to compute Δy, the equation 6.28 is differentiated with respect to t and used on the right hand side in equation 6.26. Finally, 6.30 is used to find an expression for ε_i and the result is the following expression,

$$\frac{1}{(s_i t_i \Delta y_i)^2} = (\frac{cosh(\Delta y) - 1 + 1/t_i}{sinh(\Delta y)})^2 - 1 \tag{6.32}$$

This equation can be simplified if the interior point, where the initial spacing has been specified, is not given as a values close to either end of the computational domain and the given initial spacing s_i is large enough. Then, by using the assumption that $\exp -2\Delta y << 1$, the simplification of (6.32) is,

$$2s_i\sqrt{t_i(1 - t_i)} \approx \frac{\sinh(0.5\Delta y)}{0.5\Delta y} \tag{6.33}$$

We note, that the above equation is implicit for Δy and the right hand side is similar to the equation from previous Section. Hence, the previously defined approximate analytical expressions can be used to solve it (see Appendix 1).

Lastly, a special case when $t_i = \varepsilon_i = 0.5$ leads to the antisymmetric case. The corresponding solution is,

$$t = 0.5(1 + \frac{\sinh(\Delta y(\varepsilon - 0.5))}{\sinh(0.5\Delta y)}) \tag{6.34}$$

The inversed formulation is,

$$\varepsilon = 0.5 + \frac{1}{\Delta y}sinh^{-1}((2t - 1)\sinh(\Delta y/2)), \text{ where } s_i = s_0 = \frac{sinh(\Delta y/2)}{\Delta y/2} \tag{6.35}$$

On the other hand, if $t_i = \varepsilon_i = 0$, one-sided function is defined as,

$$t = \frac{\sinh(\varepsilon\Delta y)}{\sinh\Delta y} \tag{6.36}$$

The inversed formulation is,

$$\varepsilon = \frac{1}{\Delta y}\sinh^{-1}(t\sinh\Delta y), \text{ where } s_i = s_0 = \frac{\sinh(\Delta y)}{\Delta y} \tag{6.37}$$

The presented here stretching functions require a setting the slopes of one or two location of the domain. These two parameters is not an arbitrary choice, however and strongly problem dependent. One of the logical way of defining it, is knowing where the solution has a strongly localised region of rapid variation and set the function as such as to cluster more points around this region. Thus, a successful application of mesh stretching is not only finding an appropriate stretching function, but also defining a suitable problem dependent stretching strategy. This discussion is developed further in the next Chapter.

6.4 WENO formulation for non-uniform mesh

The high-order numerical reconstruction presented in Chapter 3 have to be reformulated in order to account for the non-uniform mesh spacing. The PPM method is originally formulated for the non-uniform mesh and presented in Colella & Woodward (1984). The complete formulations suitable for the most variations of WENO3 and WENO5 are presented in this section. Here we follow the developments of Wang *et al.* (2007).

Spacial stencil In order to reformulate the key formulations of WENO class of schemes, the formal formulation for the quadratic polynomial is recalled from Jiang & Shu (1996*b*),

$$p_r(x) = \sum_{j=0}^{2} C_{rj}(x)\bar{u}_{i-r+j}, \text{ with } r = 0, 1, 2, \tag{6.38}$$

where

$$C_{rj}(x) = B_{rj}(x)h_{3-r+j}, \text{ where } h_m = \Delta x_{i-3+m},\ m = 1, \ldots, 5 \tag{6.39}$$

$$B_{rj}(x) = \sum_{m=j+1}^{3} \frac{\sum_{l=0,l\neq m}^{3}(\prod_{q=0,q\neq m,l}^{3}(x - x_{i-r+q-\frac{1}{2}}))}{\prod_{l=0,l\neq m}^{3}(x_{i-r+m-\frac{1}{2}} - x_{i-r+l-\frac{1}{2}})} \tag{6.40}$$

where $r, j = 0, 1, 2$.

Now, by defining $\hat{c}_{rj} = C_{rj}(x_{j+\frac{1}{2}})$ and $\hat{b}_{rj} = B_{rj}(x_{j+\frac{1}{2}})$ and recalling that WENO reconstruction is

$$w^{+}_{i+1/2} = \sum_{r=0}^{2} \omega_r^{i+1} p_r^{i+1}(x_{i+1/2}) \qquad \text{and} \qquad w^{-}_{i+1/2} = \sum_{r=0}^{2} \omega_r^{i} p_r^{i}(x_{i+1/2}) \tag{6.41}$$

we can compute $P_r(x_{i+\frac{1}{2}})$,

$$P_r(x_{i+\frac{1}{2}}) = \sum_{j=0}^{2} \hat{c}_{rj}\bar{u}_{i-r+j}, \text{ where } \hat{c}_{rj} = \hat{b}_{rj}h_{3-r+j} \tag{6.42}$$

and

$$\hat{b}_{rj} = \sum_{m=j+1}^{3} \frac{\sum_{l=0,l\neq m}^{3}(\prod_{q=0,q\neq m,l}^{3}(x_{i+\frac{1}{2}} - x_{i-r+q-\frac{1}{2}}))}{\prod_{l=0,l\neq m}^{3}(x_{i-r+m-\frac{1}{2}} - x_{i-r+l-\frac{1}{2}})} \tag{6.43}$$

Here we provide the explicit formulations for the spacing $h_m = \Delta x_{i-3+m}$ with $m = 1, \ldots 5$, the explicit formulations for $\hat{b}_{rj}$ are

$$\hat{b}_{22} = \frac{1}{h_1+h_2+h_3} + \frac{1}{h_2+h_3} + \frac{1}{h_3} \quad ; \quad \hat{b}_{21} = \hat{b}_{22} - \frac{(h_1+h_2+h_3)(h_2+h_3)}{(h_1+h_2)h_3h_2} \tag{6.44}$$

$$\hat{b}_{20} = \hat{b}_{21} + \frac{(h_1+h_2+h_3)h_3}{(h_2+h_3)h_2h_1} \quad ; \quad \hat{b}_{12} = \frac{(h_2+h_3)h_3}{(h_2+h_3+h_4)(h_3+h_4)h_4} \tag{6.45}$$

$$\hat{b}_{11} = \hat{b}_{12} - \frac{1}{h_2+h_3} + \frac{1}{h_3} - \frac{1}{h_4} \quad ; \quad \hat{b}_{10} = \hat{b}_{11} - \frac{(h_2+h_3)h_4}{(h_3+h_4)h_2h_3} \tag{6.46}$$

$$\hat{b}_{02} = -\frac{h_4h_3}{(h_3+h_4+h_5)(h_4+h_5)h_5} \quad ; \quad \hat{b}_{01} = \hat{b}_{02} + \frac{h_3(h_4+h_5)}{(h_3+h_4)h_4h_5} \tag{6.47}$$

$$\hat{b}_{00} = \hat{b}_{01} - \frac{1}{h_3} - \frac{1}{h_4} - \frac{1}{h_4+h_5} \tag{6.48}$$

Similarly, we can define $p_r(x_{i-\frac{1}{2}}) = \sum_{j=0}^{2} c_{rj}\bar{u}_{i-r+j}$ with $\hat{c}_{rj} = C_{rj}(x_{j-\frac{1}{2}}) = \hat{b}_{rj}h_{3-r+j}$ and

$$\hat{b}_{rj} = B_{rj}(x-j-\frac{1}{2}) = \sum_{m=j+1}^{3} \frac{\sum_{l=0,l\neq m}^{3}(\prod_{q=0,q\neq m,l}^{3}(x_{i-\frac{1}{2}} - x_{i-r+q-\frac{1}{2}}))}{\prod_{l=0,l\neq m}^{3}(x_{i-r+m-\frac{1}{2}} - x_{i-r+l-\frac{1}{2}})} \tag{6.49}$$

We can demonstrate that $b_{rj} = \hat{b}_{r-1,j}$ while $j = 0,1,2$ and $r = 1,2$. Then the only coefficients to be computed are when $r = 0$ and $j = 0,1,2$. These coefficients, $b_{0,j}$ are,

$$\hat{b}_{02} = \frac{h_3(h_4+h_3}{(h_3+h_4+h_5)(h_4+h_5)h_5} \quad ; \quad \hat{b}_{01} = \hat{b}_{02} - \frac{h_3(h_3+h_4+h_5)}{(h_3+h_4)h_4h_5} \tag{6.50}$$

$$\hat{b}_{00} = \hat{b}_{01} + \frac{(h_3+h_4)(h_3+h_4+h_5)}{h_3h_4(h_4+h_5)} \tag{6.51}$$

Thus, we have explicit formulations for the approximate solution at the cell boundaries $x_{i-1/2}$ and $x_{i+1/2}$, $p_r(x_{i-\frac{1}{2}})$ and $p_r(x_{i+\frac{1}{2}})$, respectively with spacial stencils formulations needed to account for the non-uniform mesh. The coefficients c_{rj} and $\hat{c}_{rj}$ have to be computed only once since they depend only on the spacial spacing h_m.

Smoothness measure We recall that the smoothness indicator function are introduced in WENO class of the methods in order to improve the solution on the border between the areas with discontinuities and area where the solution is smooth. This function is formulated in classical WENO as,

$$\beta_r = \int_{x-1/2}^{x+1/2} h_3(p_r^{'}(x))^2dx + \int_{i-1/2}^{i+1/2}(h_3)^3(P_r^{''}(x))^2dx \tag{6.52}$$

Note, that when the above expression satisfies the condition that the approximate solution p_r is smooth in I_r, that is, the computational stencil S_r is smooth, we have,

$$\beta_r = (p_r^{'}(x_i)h_3)^2(1+\mathcal{O}((h_3)^2)) \tag{6.53}$$

If, however, the stencil S_r is not smooth, the following is satisfied,

$$\beta_r = \mathcal{O}(1) \tag{6.54}$$

By using the fact that $p_r(x)$ is a quadratic polynomial, it follows that $p_r^{'}(x)$ and $p_r^{''}$ are linear and constant, respectively. The latter one is derived as,

$$p_r^{''} = \sum_{j=0}^{2} C_{rj}^{''}\bar{u}_{i-r+j} = \sum_{j=0}^{2} B_{rj}^{''}h_{3-r+j}\bar{u}_{i-r+j} \tag{6.55}$$

The argument x has been dropped since $C_{rj}^{"}(x)$ and $B_{rj}^{"}$ are constants. We now can have the expressions for the $B_{rj}^{"}$,

$$B^{"}_{r2} = \frac{6}{(h_{3-r} + h_{4-r} + h_{5-r})(h_{4-r} + h_{5-r})h_{5-r}} \tag{6.56}$$

$$B^{"}_{r1} = B^{"}_{r2} - \frac{6}{(h_{3-r} + h_{4-r})h_{4-r}h_{5-r}} \quad ; \quad B^{"}_{r0} = B^{"}_{r1} + \frac{6}{(h_{4-r} + h_{5-r})h_{3-r}h_{4-r}} \tag{6.57}$$

By substituting these coefficients into 6.52, the second integral of the equation can be rewritten,

$$\int_{x_{i-1/2}}^{x_{i+1/2}} h_3(p^{"}_r(x))^2 dx = (h_3)^4 (\sum_{j=0}^{2} B^{"}_{rj}(x) h_{3-r+j} \bar{u}_{i-r+j})^2 \tag{6.58}$$

The first integral can be reformulated by using the property that if the first derivative $p^{'}_r(x)$ is linear in x, then $(p^{"}_r(x))^2$ is quadratic in x. That leads to the way to compute the exact value for the first integral in 6.52 by applying the Simpson's quadrature rule,

$$\int_{x_{i-1/2}}^{x_{i+1/2}} h_3(p^{'}_r(x))^2 dx = (h_3)^2((p^{'}_r(x-1/2))^2 + 4(p^{'}_r(x_i))^2 + (p^{'}_r(x_{i+1/2}))^2) \tag{6.59}$$

It follows from 6.38, that the values for $p^{'}_r(x_{i-1/2})$, $p^{'}_r(x)$, $p^{'}_r(x_{i+1/2})$ are,

$$p^{'}_r(x) = \frac{1}{6}\sum_{j=0}^{2} C^{'}_{rj}(x)\bar{u}_{i-r+j} = \frac{1}{6}\sum_{j=0}^{2} B^{'}_{rj}(x) h_{3-r+j}\bar{u}_{i-r+j} \tag{6.60}$$

The formulations for the coefficients $B^{'}_{rj}$ are obtained from 6.40. We have,

$$\begin{aligned}
B^{'}_{22}(x_{i-\frac{1}{2}}) &= \frac{2(h_1+2h_2)}{(h_1+h_2+h_3)(h_2+h_3)h_3} \quad ; \quad B^{'}_{21}(x_{i-\frac{1}{2}}) = B^{'}_{22}(x_{i-\frac{1}{2}}) - \frac{2(h_1+2h_2-h_3)}{(h_1+h_2)h_2h_3} \\
B^{'}_{20}(x_{i-\frac{1}{2}}) &= B^{'}_{21}(x_{i-\frac{1}{2}}) + \frac{2(h_1+2h_2-h_3)}{(h_2+h_3)h_1h_2} \quad ; \quad B^{'}_{12}(x_{i-\frac{1}{2}}) = \frac{2(h_2-h_3)}{(h_2+h_3+h_4)(h_3+h_4)h_4} \\
B^{'}_{11}(x_{i-\frac{1}{2}}) &= B^{'}_{12}(x_{i-\frac{1}{2}}) - \frac{2(h_2-h_3-h_4)}{(h_2+h_3)h_3h_4} \quad ; \quad B^{'}_{10}(x_{i-\frac{1}{2}}) = B^{'}_{11}(x_{i-\frac{1}{2}}) + \frac{2(h_2-2h_3-h_4)}{(h_3+h_4)h_2h_3} \\
B^{'}_{02}(x_{i-\frac{1}{2}}) &= -\frac{4(h_3+h_4)}{(h_3+h_4+h_5)(h_4+h_5)h_5} \quad ; \quad B^{'}_{01}(x_{i-\frac{1}{2}}) = B^{'}_{02}(x_{i-\frac{1}{2}}) + \frac{2(2h_3+h_4+h_5)}{(h_3+h_4)h_4h_5} \\
B^{'}_{00}(x_{i-\frac{1}{2}}) &= B^{'}_{01}(x_{i-\frac{1}{2}}) - \frac{2(2h_3-2h_4-h_5)}{(h_4+h_5)h_3h_4}
\end{aligned} \tag{6.61}$$

Similarly,

$$B^{'}_{r2}(x_i) = B^{'}_{r2}(x_{i-\frac{1}{2}}) + \frac{1}{2}h_3 B^{"}_{r2} \quad ; \quad B^{'}_{r2}(x_{i+\frac{1}{2}}) = B^{'}_{r2}(x_{i-\frac{1}{2}}) + h_3 B^{"}_{r2} \tag{6.62}$$

$$B^{'}_{r1}(x_i) = B^{'}_{r1}(x_{i-\frac{1}{2}}) + \frac{1}{2}h_3 B^{"}_{r1} \quad ; \quad B^{'}_{r1}(x_i) = B^{'}_{r1}(x_{i-\frac{1}{2}}) + h_3 B^{"}_{r1} \tag{6.63}$$

$$B^{'}_{r0}(x_i) = B^{'}_{r0}(x_{i-\frac{1}{2}}) + \frac{1}{2}h_3 B^{"}_{r0} \quad ; \quad B^{'}_{r0}(x_i) = B^{'}_{r0}(x_{i-\frac{1}{2}}) + h_3 B^{"}_{r0} \tag{6.64}$$

Weights coefficients. We recall that the fifth order approximation to the solution $u(x, t_n)$ is unique and, thus the weights can be derived from following relations,

$$\tilde{p}(x_{i-\frac{1}{2}}) = \sum_{r=0}^{2} d_r P_r(x_{i-\frac{1}{2}}) \qquad \text{and} \qquad \tilde{p}(x_{i+\frac{1}{2}}) = \sum_{r=0}^{2} \hat{d}_r P_r(x_{i+\frac{1}{2}}) \tag{6.65}$$

The explicit formulations for the constants d_r and $\hat{d}_r$ are,

$$d_2 = \frac{(h_3+h_4)(h_3+h_4+h_5)}{(h_1+h_2+h_3+h_4)(h_1+h_2+h_3+h_4+h_5)} \tag{6.66}$$

$$d_1 = \frac{(h_1+h_2)(h_3+h_4+h_5)(h_1+2h_2+2h_3+2h_4+h_5)}{(h_1+h_2+h_3+h_4)(h_2+h_3+h_4+h_5)(h_1+h_2+h_3+h_4+h_5)} \tag{6.67}$$

$$d_0 = \frac{(h_1+h_2)h_2}{(h_2+h_3+h_4+h_5)(h_1+h_2+h_3+h_4+h_5)} \tag{6.68}$$

$$\hat{d}_2 = \frac{(h_4+h_5)h_4}{(h_1+h_2+h_3+h_4)(h_1+h_2+h_3+h_4+h_5)} \tag{6.69}$$

$$\hat{d}_1 = \frac{(h_1+h_2+h_3)(h_4+h_5)(h_1+2h_2+2h_3+2h_4+h_5)}{(h_1+h_2+h_3+h_4)(h_2+h_3+h_4+h_5)(h_1+h_2+h_3+h_4+h_5)} \tag{6.70}$$

$$\hat{d}_0 = \frac{(h_2+h_3)(h_1+h_2+h_3)}{(h_2+h_3+h_4+h_5)(h_1+h_2+h_3+h_4+h_5)} \tag{6.71}$$

These derivations can be used to obtain full formulations of WENO schemes to account for the non-uniform mesh.

Chapter 7

2D computations on non-uniform mesh

The mesh stretching problem is not an arbitrary one. While the choice of stretching function is an important step, a decision of application of such a function is crucial. For instance, two-sided stretching function allows to concentrate more points of the mesh on the boundaries of the domain, while the stretching function from interior point locates higher number of points around the initial location of the function. These two examples could be applied to different problems: the first one is suitable for the boundary problems, for instance, while the second one would work for the problems where the area of interest is inside of the computational domain.

This second example of using the mesh stretching function can be also resolved by one-sided stretching function by defining the area of the interest as a block of uniform mesh. In this case, two one-sided functions have to be used, assuming the uniform mesh block is located in some arbitrary internal area of computational domain. That is, one function is generated to stretch to the left of the uniform mesh block and one to the right. Such strategy is an alternative to using the function starting from the interior point and could improve the accuracy inside the zone of the interest, since this zone is uniformly meshed. This way of introducing the mesh stretching could be interesting for the problems where the interest zone is relatively small in comparison to the whole computational domain.

These two points of consideration when implementing the computational domain with mesh stretching have to be combined and the decision is strongly problem-dependent. One of the obvious initial questions is how to choose an appropriate location of the uniform mesh block or interior point from which the stretching function will be applied. The strategy where two one-sided functions are used is relatively simple should the area of the interest has a constant location in time. However, if the problem consists of a moving object, one faces several choices of where and how generate the uniform and non-uniform meshes. Consider two cases. The first one, is where a certain object is defined as area of the interest, located somewhere inside the computational domain (and far enough from the boundaries) and it either has a constant location and size or moves and changes the size very little. Such a problem could be numerically resolved on stretched mesh and the area where the object is located is uniformly meshed, while two one-sided stretching functions are used on the both sides of the uniform mesh box. Alternatively, two-sided stretching function from interior point can be applied from, for instance, internal point of the object. While applying such a function leads to the loss of accuracy of the object reconstruction due to the continuous change of dx, assuming the small enough stretching factor, the numerical error can be acceptable.

Now, let us consider the problem where the object moves in time and changes it size or shape. Several question have to be addressed. Assuming that the stretched mesh is defined only at the first iteration, how the zone of the interest should be addressed? Should it be only initial location of the object? Should it be the whole path of the object move? The latter one might lead to the

uniform area so big that the meaning of the stretching mesh is getting diminished. However, if only initial location of the object is uniformly meshed, then will some reconstruction information be lost at the final time of the solution? On the other hand, if the mesh is redefined with certain frequency as object moves in time, this would require the additional method of definition of the object interface and added computational cost due to the higher number of operations.

The present chapter considers three problems of shock-bubble interaction with application of the mesh stretching. The first case, the helium bubble, stands as a validation problem for applying and testing several mesh stretching functions. The one-sided function is used on both sides of the uniform mesh box in X direction and another one-sided function is generated from left to right in Y direction. Alternative tests are performed with an interior point stretching function in X direction. The second case, shock-induced bubble collapsing in free field, is a perfect example when the object of interest occupies a big part of the computational domain, and interior stretching function is tested further by using this problem. Finally, the shock-induced bubble collapse in vicinity to a wall computations are performed. The particular mesh stretching strategy for this case is discussed and results are presented. Finally, the plan for 3D computations with mesh stretching for the former problem is drawn. Unless stated otherwise, the HLLC Riemann solver with WENO5-IS reconstruction and Hancock method are used in all computations. This is due to the similarity of the effect of the mesh stretching coupled with different numerical schemes.

7.1 Air-helium shock-bubble interaction

Following the numerical schemes validation, the air-helium shock-bubble is used in this Section to validate several mesh stretching strategies. The initial condition of the bubble and its location at final time of the solution $t_{final} = 0.05\mu$s are presented on Figure 7.12. The centre of the bubble moves along the x-coordinate from 0.006 to 0.011. The shock wave is initially located at $x = 0.003$. Here, the bubble is considered as a zone of interest and the goal is to apply the mesh stretching in a way, that the accuracy of the bubble reconstruction is similar to the solution obtained on the uniform mesh.

The process of defining the area of uniform mesh and its consequent stretching has to take into account the following peculiarities of the present problem:

- the initial location of the bubble takes a relatively small part of the computational domain
- the bubble moves along x-direction and changes the overall shape
- the presence of the shock wave and its effect of the bubble has to be considered
- only half of the bubble computed; that is, the bubble size in y-direction takes approximately half of the computational domain

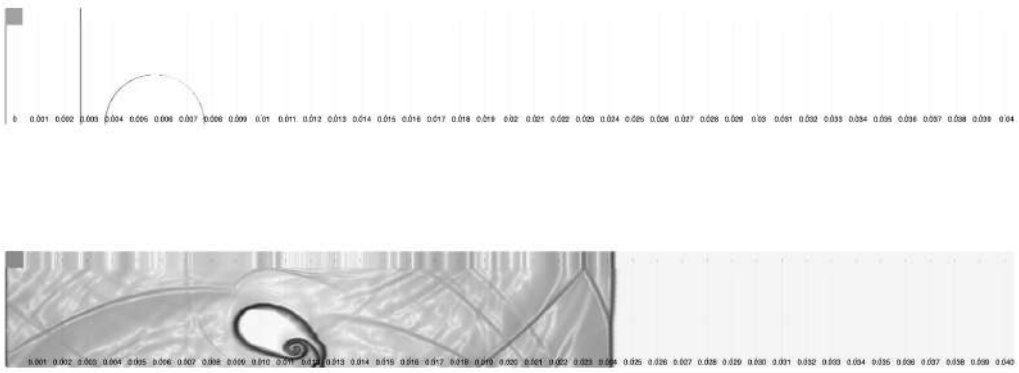

Figure 7.1: Air-helium shock-bubble, initial condition (top), final time location (bottom)

Based on these points two strategies are applied in x-direction. The first one has a uniform mesh box located around the bubble and includes the shock wave location taking into account the final location of the bubble. That is, the uniform mesh area is set on 0.003-0.019 interval. This interval allows to have the uniform mesh along the whole trajectory of the bubble in x-direction. Next, two one-sided stretching functions on each of the sides of the uniform mesh block are set by using different arbitrary stretching factors. The second strategy defines the interior point of the domain based on the approximate center of the bubble at its final location and applies the two-sided stretching function from this point. In the first case, more points are located on and around the uniform mesh box, while in the second case, more points are concentrated around the center of the bubble at the final time of the solution. The strategy for mesh stretching in y-direction is based on one-sided stretching function due to the computations of only half of the bubble.

The validation process based on air-helium shock-bubble means to answer the following questions:

- considering two stretching functions based on *sinh* and *tanh*, which function leads to higher accuracy of the method?
- what is the loss of accuracy by using the interior point stretching function in comparison to the uniform mesh block method?
- what is the effect of the mesh stretching applied only in x, y and both directions?
- what is the CPU decrease by using different mesh stretching strategies?

The cost of analytical derivation of reformulated numerical schemes is considered to be negligible.

The comparison of the obtained solutions is done at the final time $t_{final} = 0.05\mu$s and uses the solution obtained on the uniform mesh 4000×400 as a reference. The computations are performed by fixing CFL=0.3. The values of space steps dx and dy in obtained solutions always correspond to the spacing of the mesh 4000×400. The stretching factor of the mesh, β, is set arbitrary and the system of equations to generate the mesh is always solved for number of points rather than the stretching factor.

The first step in present analysis is a comparison of the non-uniform mesh distribution in terms of the size of dx and dy. Let us consider, firstly, the x-direction and the uniform mesh block located around the bubble and shock wave location, and the mesh stretching on either of its sides. The minimal dx in this case is set similar to the size of the spacing in the uniform mesh, i.e. $dx = Lx/(4000) = 1 \times 10^{-5}$ m. Figure 7.2 shows the mesh distribution by using two hyperbolic stretching functions, *tanh* on the left and *sinh* on the right. The faster increase of dx values is noticed by using the *sinh*-function. Precisely, by applying the highest degree of stretching, corresponding to β=3 and $imax$=2320, the maximum values for dx are 5.5×10^{-5} m and 9.4×10^{-5} m by using *tanh* and *sinh*, respectively. This means that by using the same number of points in x direction, the accuracy of the method away from the uniform mesh zone is different since the values of dx are higher, i.e. theoretically, the solution by using *tanh* is better than one achieved by using *sinh*.

Similar argumentation is used for the stretching function applied to y-direction. Figure 7.3 presents the mesh distribution in y-direction by using *tanh* (left) and *sinh* (right) stretching functions. Similarly, the higher value of dy is obtained by using *sinh* function, i.e. $dy_{max} = 9.8 \times 10^{-5}$ m while *tanh* led to the smaller value, $dy_{max} = 5.5 \times 10^{-5}$ m.

In order to confirm this theoretical loss of accuracy by simply using different stretching functions, the solutions of the maximum pressure are compared. Figures 7.4-7.5 present the maximum pressure solution by applying different factors of stretching and using either *tanh* or *sinh* stretching functions. Both functions led to the overall accurate reconstruction of P_{max} curve. The slight decrease of the intensity of the peaks at times 1.2μs and 3μs by using the highest stretching factor $\beta = 3$ is observed and its similar to both, *tanh* and *sinh* functions. The time of occurrence the pressure jumps stays similar in comparison to the uniform mesh solution.

While the deterioration of the solutions obtained by using stretching mesh in x-direction is very small, the error increases when the stretching is applied in y-direction. Generally, the decrease

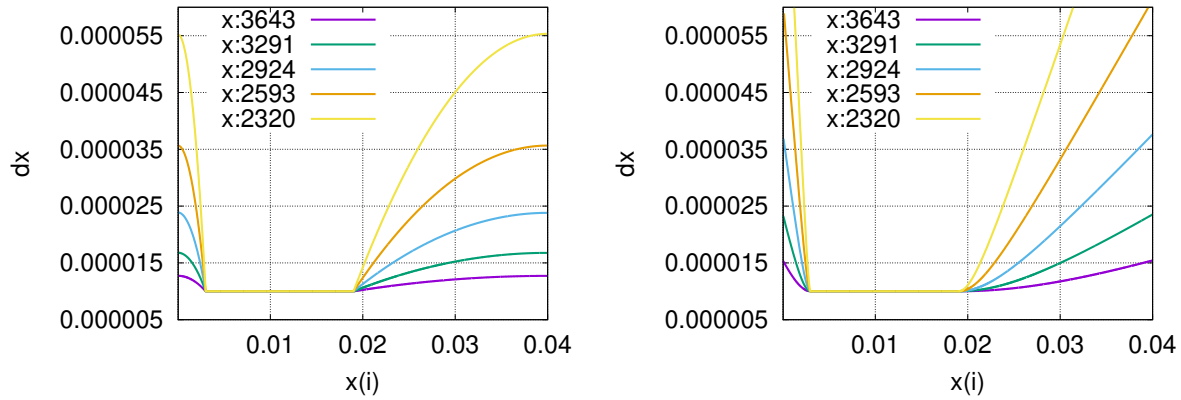

Figure 7.2: Air-helium shock-bubble interaction, mesh stretching comparison, hyperbolic **tan** (left), **sin** (right, zoom of y-abscissa from 5×10^{-6} m to 6×10^{-5} m)

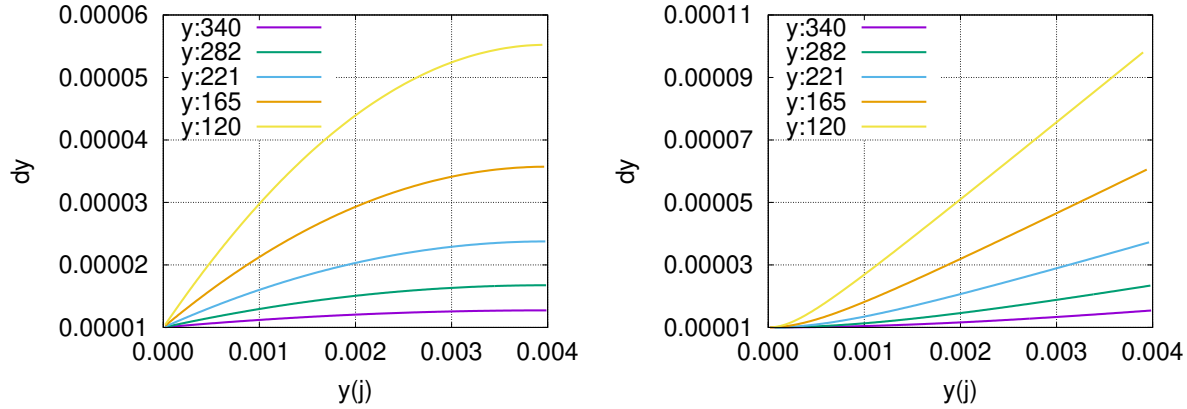

Figure 7.3: Air-helium shock-bubble interaction, mesh stretching comparison, hyperbolic **tan** (left), **sin** (right)

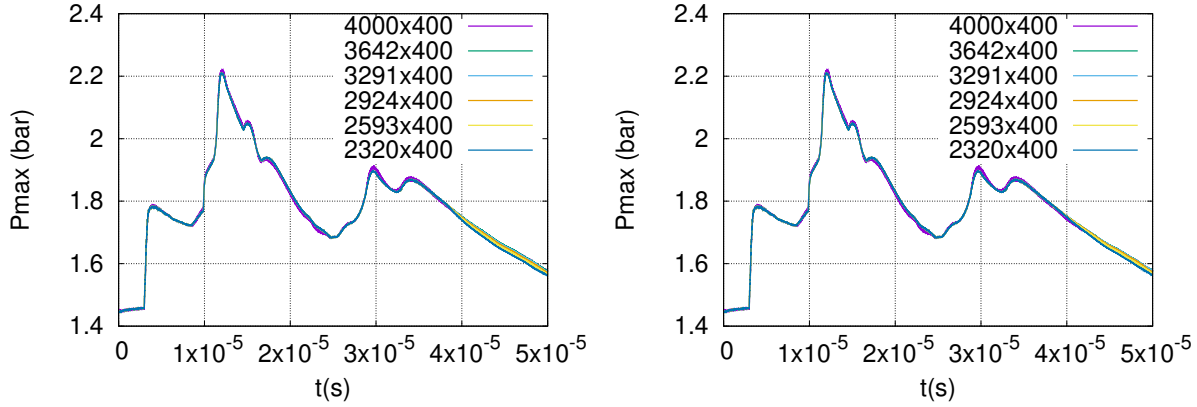

Figure 7.4: Air-helium shock-bubble interaction, Pmax (bar) solution comparison with mesh stretching, hyperbolic **tan** (left), **sin** (right), WENO5-IS

of the pressure intensity and the delay of its occurrence is noted. For instance, a decrease of approximately 7% of the highest peak at $t = 1.2\mu$s and delay of about 0.03μs for *tanh* function with highest stretching factor is present. In comparison, *sinh* function with similar factor of stretching led to 9% decrease and delay of 0.07μs. This demonstrates the lower accuracy of the solution by using the *sinh* function in comparison to *tanh* with similar stretching factor.

The second strategy of mesh stretching applied to this validation problem, is interior point *sinh* function applied in x-direction. The interior point of stretching is an arbitrary and problem-related choice, and has been set to $x = 0.011$ m, which corresponds to the approximate center of the bubble at the considered final time of the computation. The stretching in y-direction stays

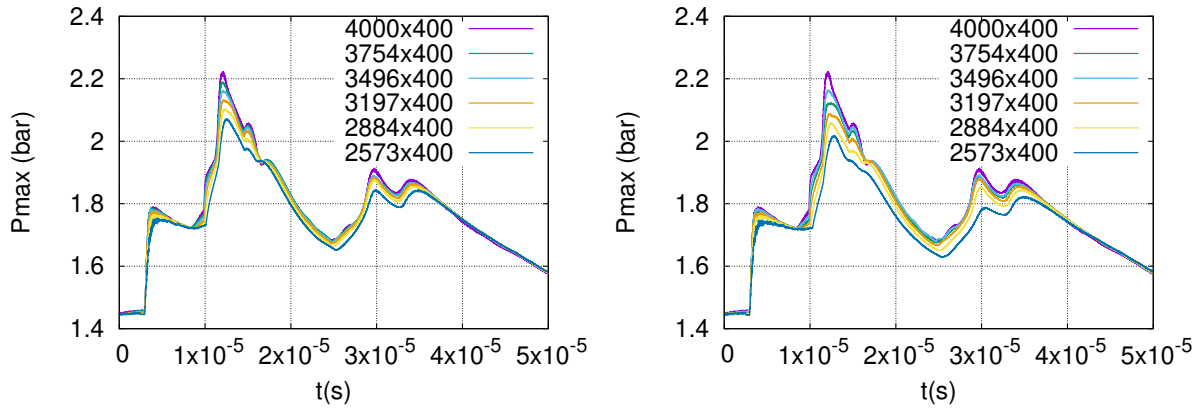

Figure 7.5: Air-helium shock-bubble interaction, Pmax (bar) solution comparison with mesh stretching, hyperbolic **tan** (left), hyperbolic **sin** in y-direction (right), WENO5-IS

similar to the first strategy. Figure 7.6 shows the mesh distribution is x and y directions. Here, the maximum stretching in x-direction corresponds to 2573 points and $dx_{max} = 3.5 \times 10^{-5}$m.

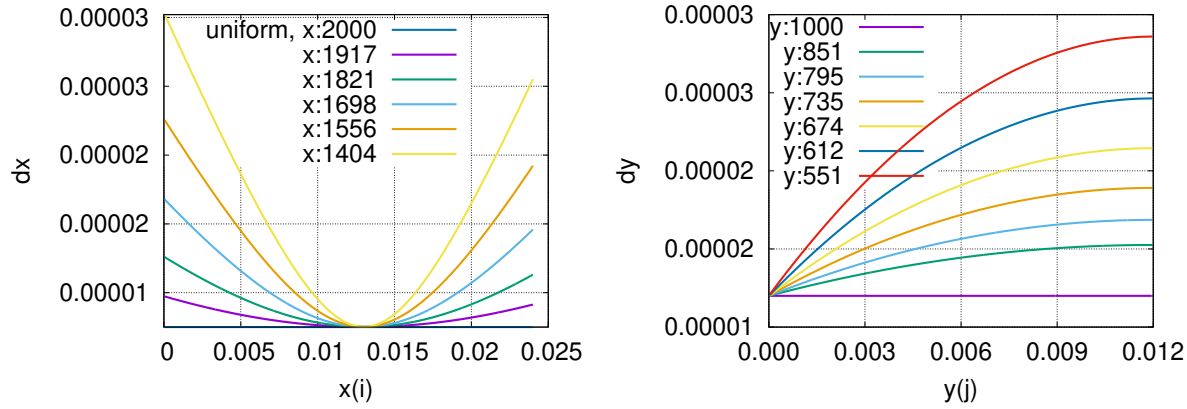

Figure 7.6: Air-helium shock-bubble interaction, mesh stretching comparison, hyperbolic sin function from interior point, x-direction (left), hyperbolic tangent function y-direction (right)

The solutions of maximum pressure are compared by using two-sided *sinh*-function from the interior point in x-direction by applying different stretching factor β. Figure 7.7 illustrates that while the curve of P_{max} is generally correctly reconstructed, a slight deterioration of the pressure intensity is present. For instance, the decrease of P_{max} value at time of the peak, $t = 3.4\mu$s is around 2% with stretching applied only in x-direction.

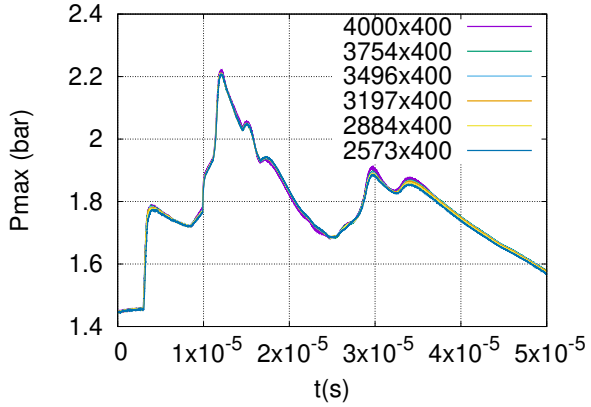

Figure 7.7: Air-helium shock-bubble interaction, Pmax (bar) solution comparison with mesh stretching, hyperbolic **sin** from interior point in x-direction, WENO5-IS

In order to finalize the examination of mesh stretching in either x or y-directions, the assessment of the contour of the density gradient is performed. Figure 7.8 illustrates the difference of the density gradient reconstruction between the uniform mesh (left), *tanh* from the uniform mesh block (middle) and *sinh* from interior point (right). The final shape of the bubble has been correctly reconstructed in both cases. The internal structure of the bubble is slightly changed in case of the mesh stretched from the internal point, due to the continuously changing of dx value. However, the solution around the bubble obtained by using the stretching mesh from uniform mesh block with *tanh* function is almost identical to the one computed on uniform mesh.

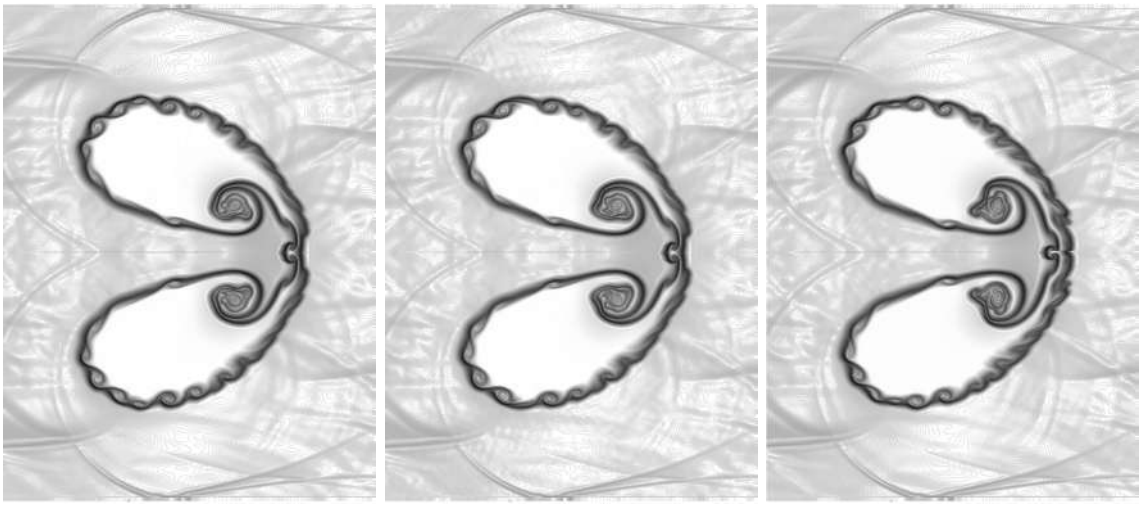

Figure 7.8: Air-helium shock-bubble interaction, HLLC Hancock WENO5-IS scheme, gradient of the density, comparison of mesh stretching strategies in X direction: uniform mesh (left), **tanh** from the uniform mesh block (middle), **sinh** from interior point (right)

While the little difference in the solution is noticed as a result of the mesh stretching in x-direction, the deterioration is more critical when non-uniform mesh in both directions is used. The gradients of density computed on non-uniform mesh with *tanh* and *sinh* function applied from bottom to top are shown on Figure 7.9. The diffusion of the solution with $\beta = 3$ is noticed. Although the general shape of the bubble is correct, the interface vortices are lacking as well as the internal structure of the bubble is diffused by using both stretching functions. However, the *sinh* function led to the higher error on the top boundary.

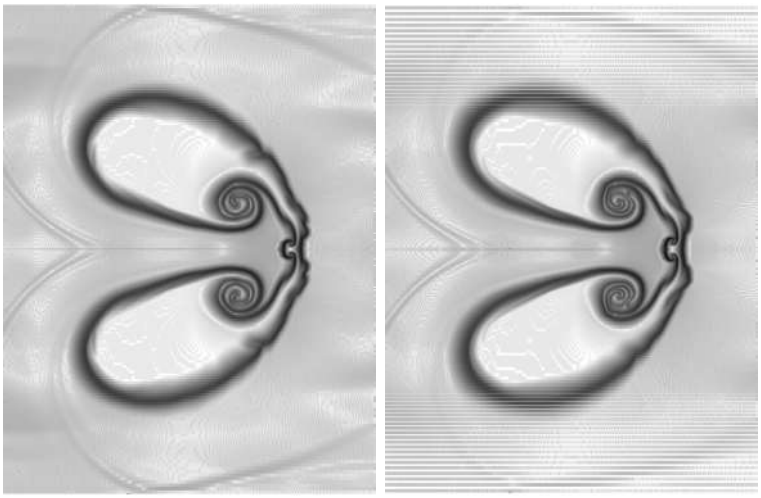

Figure 7.9: Air-helium shock-bubble interaction, HLLC Hancock WENO5-IS scheme, gradient of the density, comparison of mesh stretching strategies in Y direction: **tanh** (left), **sinh** (right)

The reason why the effect of the solution by stretching mesh in y-direction is stronger compared with stretched mesh applied to direction x is due to the relatively short length of y-direction and,

consequently, smaller number of points. Indeed, the factor of stretching have to be reduced when the number of points is not big enough to avoid the over stretching of the values of spacing.

The following conclusions can be drawn based on these results. An application of the mesh stretching in both direction has to take into account of the results of isolated results in either direction x or y. For instance, in terms of one-sided function, the better solution is obtained by using *tanh* function for same number of points due to the smaller increase of spacing values compared with *sinh* function. On the other hand, two-sided *sinh* stretching function from interior point, leads to slightly less accurate solution due to the constant change of dx. This function can be useful for the problems where the object occupies a large part of the computational domain. The result of these observations is the following idea for the appropriate mesh stretching in both directions: one-sided *tanh* from uniform mesh area or two-sided *sinh* from interior point of domain in x-direction and one-sided *tanh* function in y-direction. The solutions of P_{max} obtained by using these two strategies are presented on Figure 7.10. The mesh stretching in y-direction is moderate due to the strong deterioration of the result by using mesh stretching. The higher decrease in pressure intensity at peak times is noticed by using the *sinh* from interior point along with *tanh* in y-direction. However, the unphysical and abrupt drop of maximum pressure at the end of the computations is noted by using *tanh* in both directions (from uniform mesh block in x-direction) which is not present by using *sinh* from interior point in x-direction. This drop might be an indication of too high stretching factor, which led to high final dx value. On the other hand, all peaks of the maximum pressure solution have been captured accurately by using *tanh* function in both directions, while the second strategy, where *sinh* function from interior point has been used, yields to around 3-4% pressure intensity loss (see Tables 7.1 and 7.2).

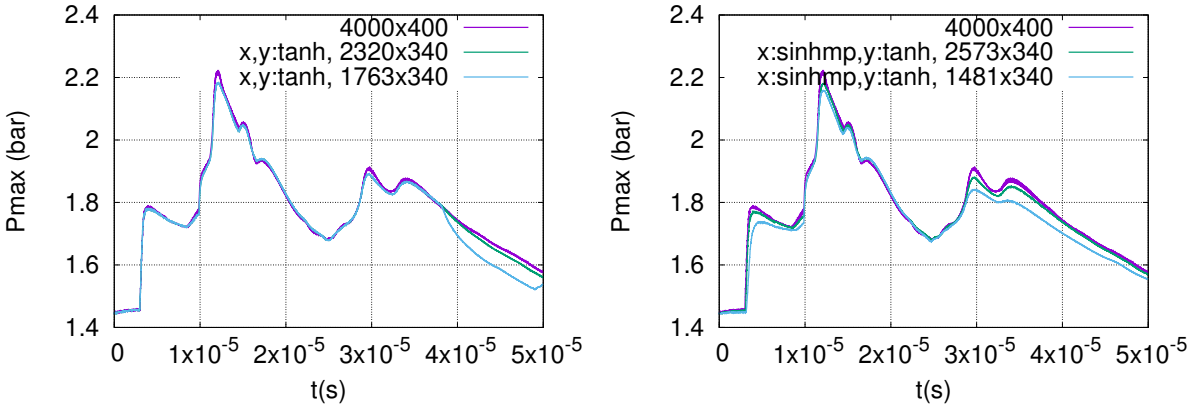

Figure 7.10: Air-helium shock-bubble interaction, mesh stretching in both directions. x-direction: hyperbolic **tan** from uniform mesh block (left), **sin** from interior point (right). y-direction: *tanh* from top to bottom

Lastly, the gradients of the density are presented on Figure 7.11. The solution obtained by using *tanh* function from uniform mesh area in x direction (with $\beta = 5$ and $imax = 1763$) and *tanh* function in y direction (with $\beta = 1$ and $jmax = 340$) presents an accurate bubble reconstruction with vortices on the bubble interface. Moreover, the internal vortex has similar shape compared to the solution computed on uniform mesh. On the other hand, the gradient computed by using the mesh generated by using *sinh* from the interior point similarly has correct general shape and the interface vortices, while the vortex in the bubble center has deformed shape. Furthermore, the area around the bubble is diffused which is a result of continuous change of dx-value and, consequently, the accuracy reduction.

The concluding part of the mesh stretching validation is an examination of CPU cost. The objective of this part is to define the theoretical computational cost and compare it to the factual one. Assuming that such an estimation is a consistent one, the interval of accepted CPU can be established and, hence, the maximum number of points used to compute the solution can be derived. For instance, if the goal is to compute the given problem in 2 hours and the actual time of computation by using uniform mesh is 5 hours, the degree of mesh stretching can be defined as such to achieve 3h of computational time gain.

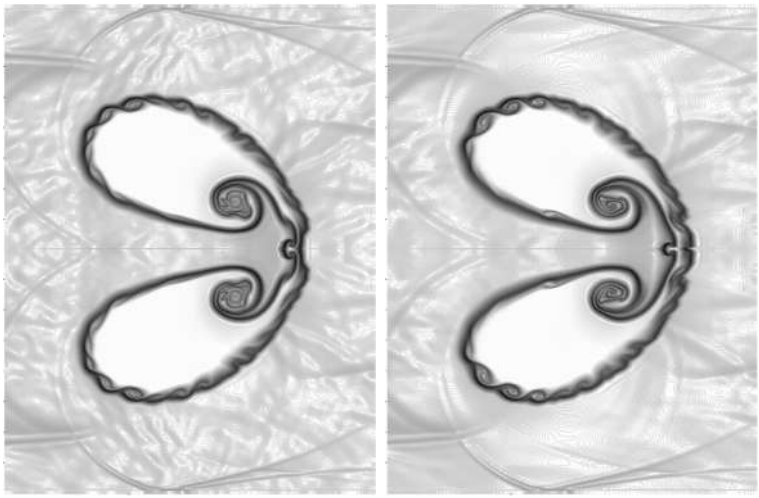

Figure 7.11: Air-helium shock-bubble interaction, HLLC Hancock WENO5-IS scheme, gradient of the density, comparison of mesh stretching strategies in Y direction: **tanh** (left), **sinh** (right)

Table 7.1: Air-helium shock-bubble interaction, comparison of mesh stretching strategies. X: *tanh* from uniform mesh block, Y: *tanh* from top to bottom. P_{max} peaks (bar) and CPU time. WENO5-IS

nbp	$P1_{max}$	$P2_{max}$	$P3_{max}$	CPU (h)	CPU ratio
4000×400	1.79	2.22	1.91	19.8	2.5
2320×340	1.78	2.18	1.89	11.1	1.4
1763×340	1.78	2.18	1.89	8.0	1

Table 7.2: Air-helium shock-bubble interaction, comparison of mesh stretching strategies. X: *sinh* from interior point, Y: *tanh* from top to bottom. P_{max} peaks (bar) and CPU time. WENO5-IS

nbp	$P1_{max}$	$P2_{max}$	$P3_{max}$	CPU (h)	CPU ratio
4000×400	1.79	2.22	1.91	19.8	3.2
1573×340	1.77	2.18	1.88	11.5	1.9
1481×340	1.74	2.16	1.84	6.1	1

While the mesh stretching is a possible mean of reducing the CPU cost, it has its own contribution to increasing the final computational time. This increase arises from the fact that the numerical schemes have to be reformulated in order to account for the non-uniform mesh. Although part of these reformulations can be computed only at first iteration, the algebraic operations have to be included into the numerical scheme derivation and, thus, have to be used at every time the solution advances in time. By saying that, these fraction of CPU has to be estimated and included into the theoretical estimation.

The theoretical estimation of the computational cost is computed by taking the CPU cost value while using the uniform mesh and adding the CPU cost of the stretching mesh generation (e.g. the computation of the coefficients and its introduction to the numerical scheme in the means of algebraic operations) and finally adding the percentage multiplier proportional to the grid nodes reduction. The final formulation is then a difference between the CPU of the problem computed on the uniform mesh and a sum of CPU time of the uniform mesh with new reformulated numerical scheme and number of the nodes reduction factor,

$$T_{theoretical} = t_f - (m * t_f) + t_{mr}, \tag{7.1}$$

where t_f is CPU time to finish the computation on the uniform mesh, t_{mr} is the CPU time to compute the same test with the scheme reformulation to account different mesh size and m is mesh reduction number computed as,

$$m = \left(1 - \left(\frac{(imax_{new} * jmax_{new})}{(imax * jmax)}\right)\right) \tag{7.2}$$

The CPU gains by using the stretched mesh techniques are estimated from the computational time presented in Tables 7.1-7.2. The computational gains are in line with or above our estimations.

7.2 Bubble collapse in a free-field

The problem of water-air shock-induced bubble collapse has a different topology than the air-helium case. Figure 7.12 shows the initial condition, the final location and the size of the bubble. Firstly, the expansion of the bubble is of considerate size. Secondly, the size and location of the bubble at final time of the solution occupies a large part of the computational domain. Hence, mesh stretching in a framework of setting the uniform mesh area is not suitable for this problem since the reduction of point number is not high unless a strong stretching factor applied. On the other hand, two-sided *sinh* function from the interior point in x-direction with moderate stretching degree seems to be an appropriate way of reducing number of points. However, since the bubble computations are performed only for half of the bubble, the strategy in y-direction can be similar to one of air-helium problem, i.e. *tanh*-function applied from bottom to top part of the whole domain.

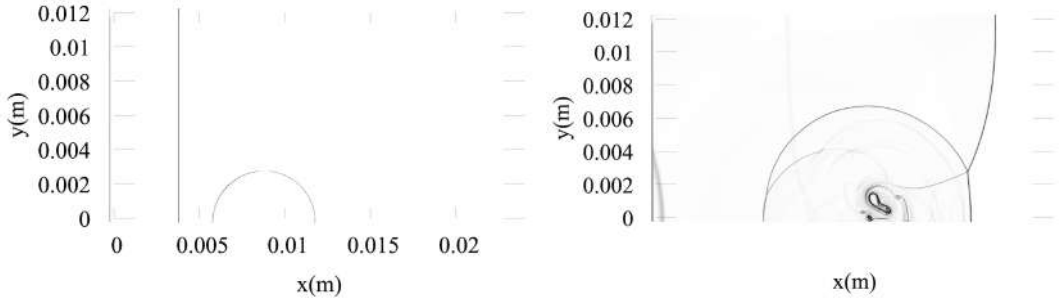

Figure 7.12: Bubble collapse in a free-field, initial condition (left), final location of the bubble(right)

The effect of the mesh stretching applied in either x- or y-direction is first demonstrated. The mesh distribution used in this testing is presented in Figure 7.13. The interior point for the initialisation of stretching function is set to be approximatevely at the bubble center at its final location, i.e. at position $x = 0.013$ m. The minimal value of dx and dy are corresponding to the uniform mesh 2000×1000, which is also used as a discretization for the reference solution computed on the uniform mesh. The size of spacing in x-direction varies from 1.2×10^{-5} to 3×10^{-5} with maximum stretching factor $\beta_x = 3$ for x-direction and from 1.2×10^{-5} to 2.5×10^{-5} with maximum stretching factor $\beta_x = 2$ for y-direction.

The solutions for P_{max} computed with these mesh configurations and compared with corresponding solution obtained by using the uniform mesh are presented in Figure 7.14. The overall correct curve reconstruction is observed by using the mesh stretching, including maximum degree of stretching. The highest discrepancy of the pressure intensity is noticed at the time of the first pressure peak, at time t=3.6μs, and at the time of the highest pressure peak, t=4.8μs. Precisely, the first pressure peak has been reduced by approximately 7% by using stretching factor β_x=3, which corresponds to the maximum stretching tested in x-direction and number of points equal to 1404, which is almost 30% reduction. On the other hand, the same peak has been decreased by approximately 5% when using the stretched mesh with β_y=2 which results in almost 50% decrease in number of points in y-direction. The highest pressure peak occurring at t=4.8μs has a reduction of around 3% with maximum stretching in direction x and approximately 7% in direction y.

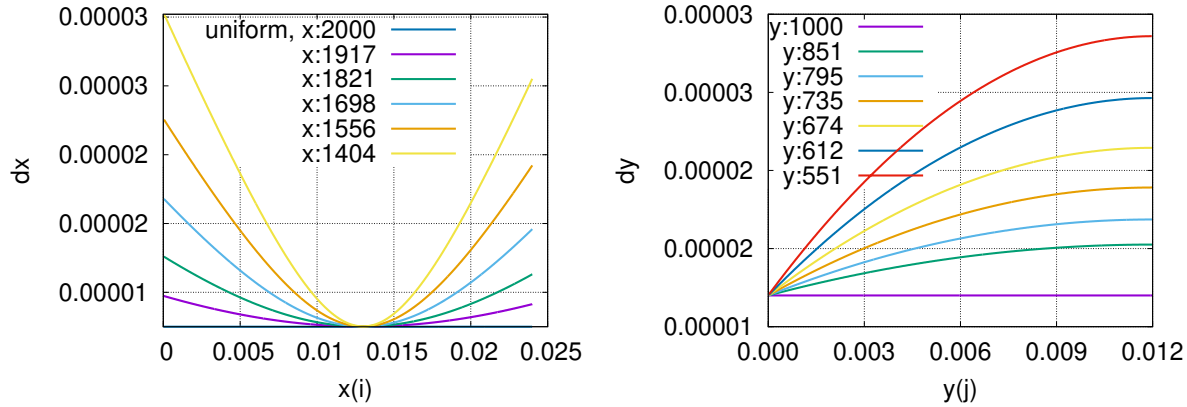

Figure 7.13: Water-air shock-bubble collapse, mesh stretching comparison, hyperbolic **tan** (left), **sin** (right)

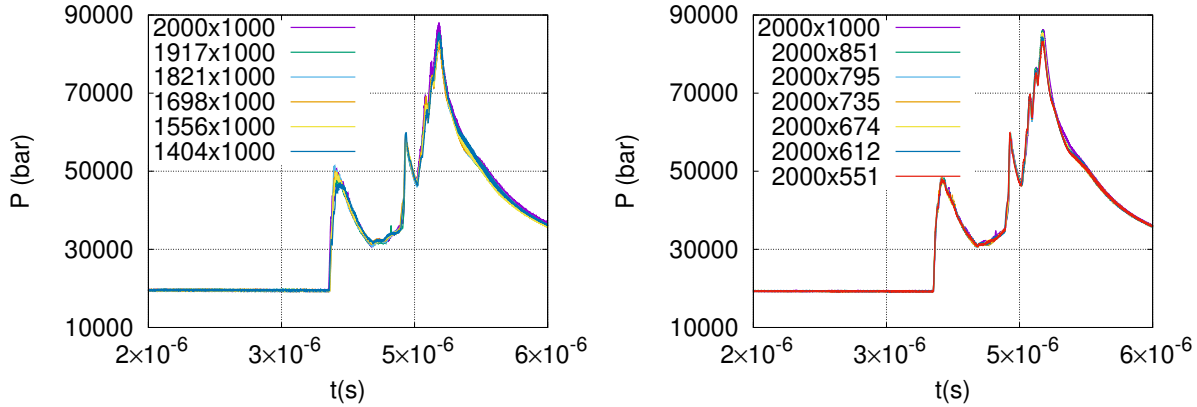

Figure 7.14: Water-air shock-bubble collapse, P_{max} (bar) solution, mesh stretching effect, **sinh** from a point in x-direction (left), **tanh** from bottom to top in y-direction (right)

The mesh stretching applied simultaneously in both directions by using the strategy described above is performed by using two combinations with $\beta_{x,y} = 3,1$ and $\beta_{x,y} = 3,2$. The P_{max} solution is shown on Figure 7.15. Similarly to the stretched mesh used on either of directions, the highest loss of pressure intensity is observed at times of the first and third (highest) pressure jumps. The decrease of 2% and 4% for the highest pressure jump is noted by using $\beta_{x,y} = 3,1$ and $\beta_{x,y} = 3,2$, respectively. However, the consistency of such a decrease may vary due to the highly oscillating solution of P_{max} as previously noted in the numerical methods chapter.

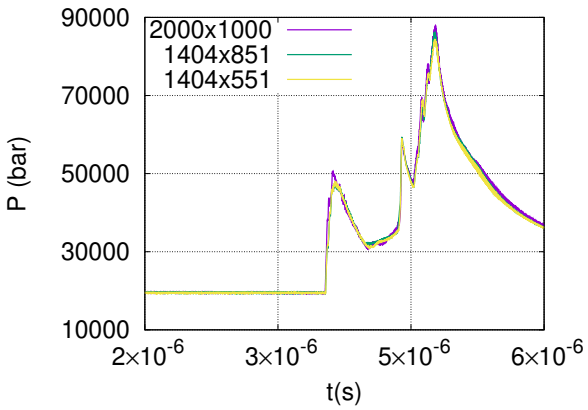

Figure 7.15: Water-air shock-bubble collapse, P_{max} (bar) solution, mesh stretching effect, **sinh** from a point in x-direction, **tanh** from bottom to top in y-direction

The qualitative examination of the effect of mesh stretching in both directions is proposed. The contours of the density gradients and pressure profiles corresponding to times t=3.6μs (the

Table 7.3: Water-air shock-bubble collapse, comparison of the maximum pressure occurrence times and intensity (bar) depending on the mesh stretching level using *sinh* function from interior point in x-direction. WENO5-IS, CFL=0.1

mesh	β_x,β_y	$T_{P1_{\max}}$, μs	$P1_{\max}$	$T_{P3_{\max}}$	$P3_{\max}$
2000×1000	n/a	3.62	50,640	4.78	87,882
1404×851	3,1	3.64	47,600	4.77	86,254
1404×551	3,2	3.64	48,030	4.77	84,488

first pressure peak), t=4.8μs (the third pressure peak) and t=6μs (the final time of the solution) are presented on Figures 7.16, 7.17 and 7.18, respectively. The shape of the bubble has been reconstructed accurately by using both mesh strategy combinations. The pressure profile at t=3.6μs has changed the maximum values distribution (red area on the plot) by being slightly diffused when mesh stretching is used. Similarly, the bubble interface has the slight smearing due to the continuous spacing change in both directions. The internal structure has been slightly deformed comparing to the solution obtained on the uniform mesh.

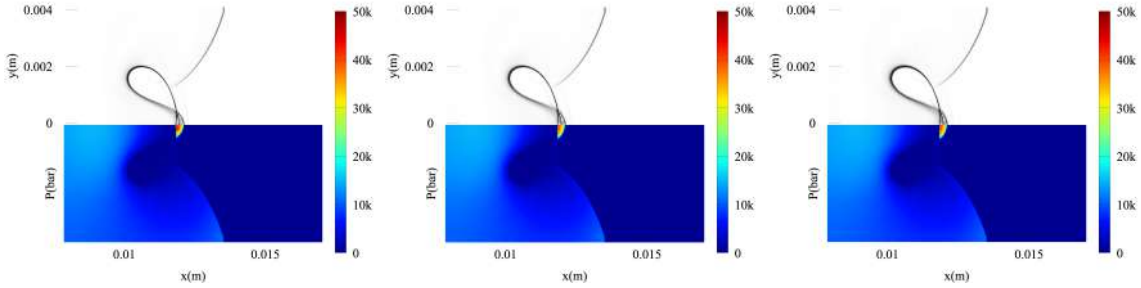

Figure 7.16: Water-air shock-bubble collapse, gradient of the density (top), pressure (bottom) at time t=3.6μs, comparison of mesh stretching strategies (from left to right): uniform mesh, hyperbolic **sin** from a point in x-direction, hyperbolic **tan** in y-direction, stretching in both directions

The pressure profile at the time of the highest pressure peak, t=4.8μs, has similar slight deterioration, i.e. the values of around 40,000 bar are more diffused when using the mesh stretching. The gradient of the density has very similar shape compared to the uniform mesh solution. However, the bubble interface is rather smeared and well distinguished internal vortex is diffused and lacks the clarity of small details.

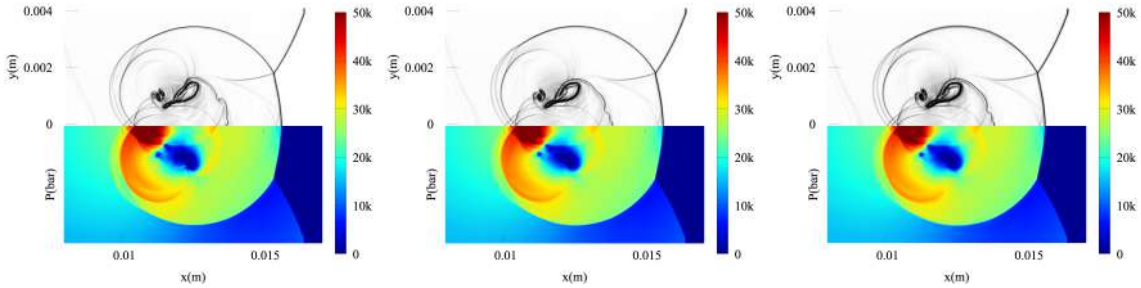

Figure 7.17: Water-air shock-bubble collapse, gradient of the density (top), pressure (bottom) at time t=4.8μs, comparison of mesh stretching strategies (from left to right): uniform mesh, hyperbolic **sin** from a point in x-direction, hyperbolic **tan** in y-direction, stretching in both directions

At the final time of the simulation, t=6μs, a similar lack of clarity of the internal vortex and smearing of the bubble interface is illustrated. Moreover, the left boundary where the highest dx value is recorded due to the mesh stretching and location of the final location of the bubble lacks completely the wave reflection which is noted on the left boundary of the density gradient contour

obtained by using the uniform mesh. The distribution of the pressure values is accurate by using both mesh stretching configurations.

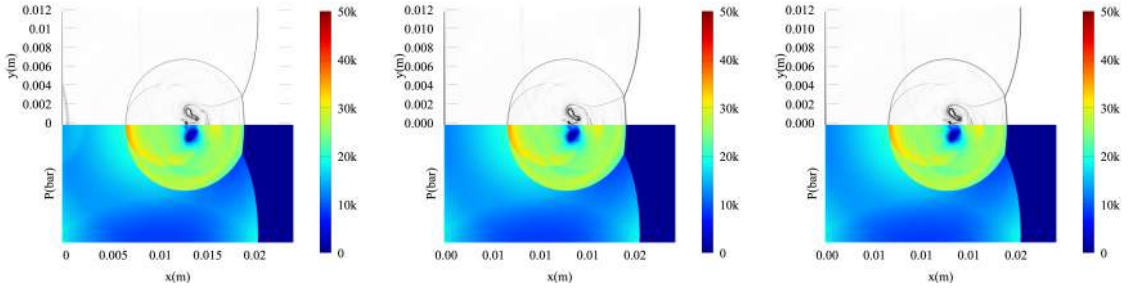

Figure 7.18: Water-air shock-bubble collapse, gradient of the density (top), pressure (bottom) at time t=6μs, comparison of mesh stretching strategies (from left to right): uniform mesh, hyperbolic **sin** from a point in x-direction, hyperbolic **tan** in y-direction, stretching in both directions

Finally, the CPU values recorded by using non-uniform mesh are presented in Table 7.4. The overall number of points reduction in both directions is approximately 40% and 60% by using $\beta_{x,y} = 3, 1$ and $\beta_{x,y} = 3, 2$, respectively. The corresponding CPU decrease is around 45% and 60%. Thus, the reduction in computational time is consistent with number of points decrease.

Table 7.4: Water-air bubble collapse, *sinh* stretching function from interior point x-direction, *tanh* stretching from bottom top in y-direction. CPU (h), fixed CFL=0.1. WENO5-IS

mesh	CPU (h)	ratio
2000×1000	13.5	2.7
1404×851	7.5	1.5
1404×551	4.9	1

7.3 Bubble collapse near a wall

The final and concluding problem of the mesh stretching study is the bubble collapse near a wall. Once again, the topology of this present problem is somewhat different from the previous case. Two main variations of this problem compared with similar bubble collapse considered in the previous Section is the existence of the wall defined at x-axis, where the main phenomena of the accurate reconstruction occurs and the geometry of the computational domain, which is 1.7 times longer in y-direction than in x-direction. The initial condition and the final location and size of the bubble are presented on Figure 7.19.

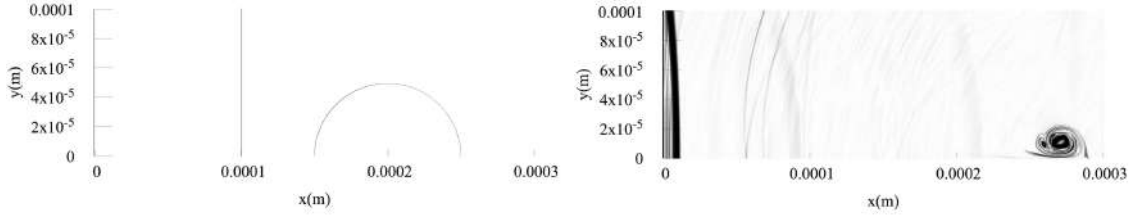

Figure 7.19: Bubble collapse near a wall, the uniform nodes box in relation to the initial condition (left) and t=0.5μs (right)

The initial location of the bubble center is set at abscissa $x = 0.0002$ m, that is, the distance from the wall is 0.0001 m. The bubble moves and changes its topology towards the wall as solution progresses. The Chapter 5 showed that the choice of the numerical scheme has a strongest effect

on the part of the bubble where the well distinguished vortex is located. This vortex occupies the bottom part of the domain along the time iterations, which is around tenth part in direction y. On the other hand, the phenomena of the wave reflection from the wall is observed and has to be reconstructed accurately. Thus, when choosing the location of the initial stretching, the latter has to be included into consideration.

Taking into the consideration the topology of the problem, the following initial mesh strategy is thought. The uniform mesh box is set on x-axis from the center of the computational domain, which includes the whole initial location of the bubble on the left. The uniformly discretized part of the domain ends at the right boundary of the domain, where the wall is located. This particular choice is made due to the interest of getting accurate solution next to the wall and catch the possible effect on the solution from the wall. On the other hand, the y-direction equally has predefined the uniform part of the domain which corresponds to the radius of the bubble, which is approximately similar to the size of the vortex which is defined as our main zone of the interest. This uniform interval is set on the interval $y = [0, 0.00005]$ m.

The size and geometry of this particular problem, however, requires a careful consideration about the degree of the stretching, β. The previous study showed that a CPU time of more than five days for the mesh 1908×3180 with CFL=0.1. Assuming similar initial configuration being used for the stretching method, considerably high stretching factor has to be applied in x-direction to achieve affordable CPU time. This computational time 'taste' is relatively conservative due to the extension of this problem to 3D computations, which is extremely expensive without mesh stretching or without the considerate reduction of the number of points required to achieve accurate computations. Hence, two additional mesh stretching strategies have been defined to understand the effect of, on one hand, the strong stretching factor in x-direction, and on the another hand, the location of the size of the uniform mesh area.

The comparison of the alternative location of the uniform mesh areas are shown on Figure 7.20. The first area, A_1, is located as such, that the whole bubble is included into the uniform mesh interval. The second area, A_2, is set to include the vortex of the bubble as it is moving towards the wall and the reflection wave on the left hand side of the bubble. The final area, A_3, includes only the internal well distinguished vortex next to the wall. The third area with uniform mesh is also reduced in direction y to the position $y = 0.00004$ m. The mesh stretching is applied starting from initialised uniform mesh areas by using $tanh$ function in both, x- and y-directions.

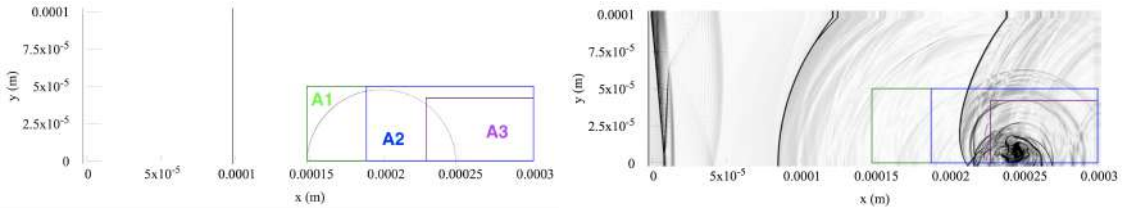

Figure 7.20: Bubble collapse near a wall, the uniform nodes box in relation to the initial condition (left) and t=3.3μs (right)

The mesh distribution is presented on Figure 7.21. The stretching factor has been applied to reduce the number of points in x- and y-directions to reduce the size of the problem as much as to achieve the CPU time around 24h. Hence, the resulting number of points is approximately similar between all three areas. The strategy where the area A_1 is set has the highest increase of dx-value outside the uniform mesh interval, which results in the value $dx_{max} = 3.6\,10^{-6}$m. The distribution of the dy-values stays approximately similar to all set areas with max value of dy equal to $5.6\,10^{-6}$ m. Hence, by taking into account that the highest variation between three chosen stretching comes from x-direction, the solution is mostly affected by the choice of stretching in x-direction.

The computations presented here are done with fixed CFL=0.1 with minimal dx-value according to the uniform mesh 1908×3180, which is also used for the reference solution computed on the uniform mesh. The scheme WENO5-IS is used for all computations unless stated otherwise. This is due to the similarity of the stretching mesh effect on the numerical schemes. The analysis starts by comparing the solutions of P_{max} and $Pwall_{max}$ presented on Figure 7.22. All three stretching strategies led to very similar solutions and the curves have been reconstructed correctly overall

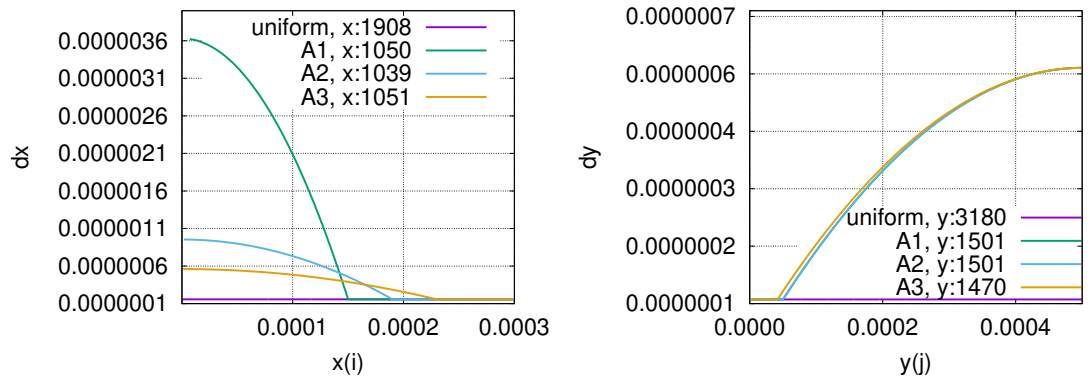

Figure 7.21: Bubble collapse next to a wall, comparison of the dx (left) and dy (right) distribution

with pressure peaks occurring at similar times. However, the loss of intensity of the highest peak in both components of the solution is observed (see Figure 7.5). The highest pressure peak at time t=0.28 μs has been reduced by approximately 6% for both, A_2 and A_3, and 3% by using the stretching with A_1. The reduction of the peak of $Pwall_{max}$ at time t=3.3μs is noted to be around 5% for all three strategies.

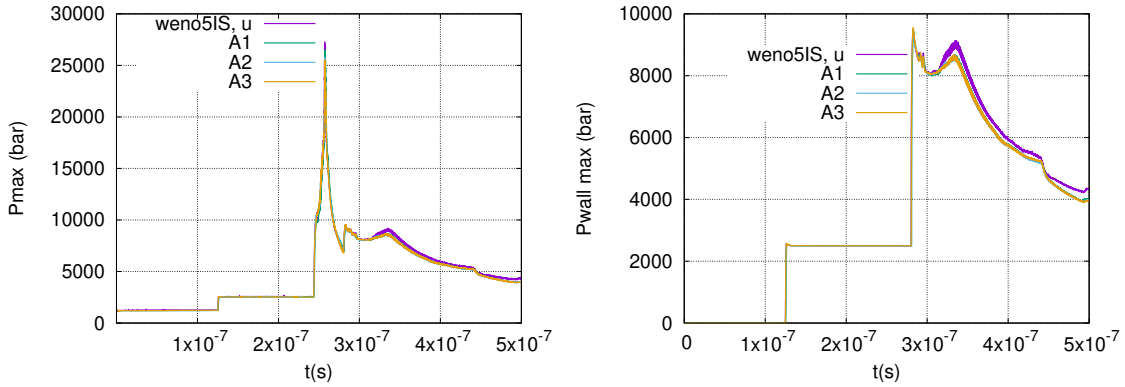

Figure 7.22: Bubble collapse near a wall, hybrid approach, P_{max} (left), $Pwall_{max}$ (right)

method	t1, μs	P, bar	Pwall, bar	t2, μs	Pwall, bar
uniform	2.8	27,301	9,456	3.35	9,138
A1	2.8	26,532	9,417	3.3	8,675
A2	2.8	25,755	9,466	3.3	8,651
A3	2.8	25,544	9,544	3.3	8,660

Table 7.5: Bubble collapse next to a wall, comparison of the maximum pressure occurrence times and intensity (bar) depending on the mesh stretching degree using $tanh$ function from interior point in x-direction. WENO5-IS, CFL=0.1

The qualitative assessment of the density gradient and pressure profiles at time of the highest pressure jump and biggest variation in its intensity as a result of the mesh stretching are presented on Figure 7.23. The main focus of this assessment is the accuracy of the bubble reconstruction and, particularly, its internal vortex which has the highest variation when different numerical schemes are used. Nevertheless, the strong stretching effect on the left boundary of the strategy A_1 is observed, where the high values of dx resulted in visible spacing. While this would be critical assuming some important phenomena take place at this part of the computational domain, these high values of dx have weak effect on the bubble reconstruction. The clear shape of the bubble and its internal structure is visibly similar to the gradient computed on the uniform mesh. Moreover, the high values of pressure profile are identically distributed. On the other hand, the strategies A_2

and A_3, where the shorter interval of the uniform mesh is used but lower degree of stretching has been applied, eliminated the visible large spacing in x direction on the left boundary, with only slight smearing of the structure noticeable. The overall bubble shape and structure are correctly reconstructed. However, the smearing of the bubble interface is observed and the slight oscillation on the left interval part of the bubble are visible, which is not present on the reference solution. The oscillations increase as the interval of the uniform mesh shortens and includes less of the bubble (see the bottom left and bottom right on Figure 7.23). Furthermore, the internal structure is somewhat tilted to the left, which is probably a result of smaller velocity values due to the mesh stretching. The pressure profiles are recovered similarly to the uniform mesh solution.

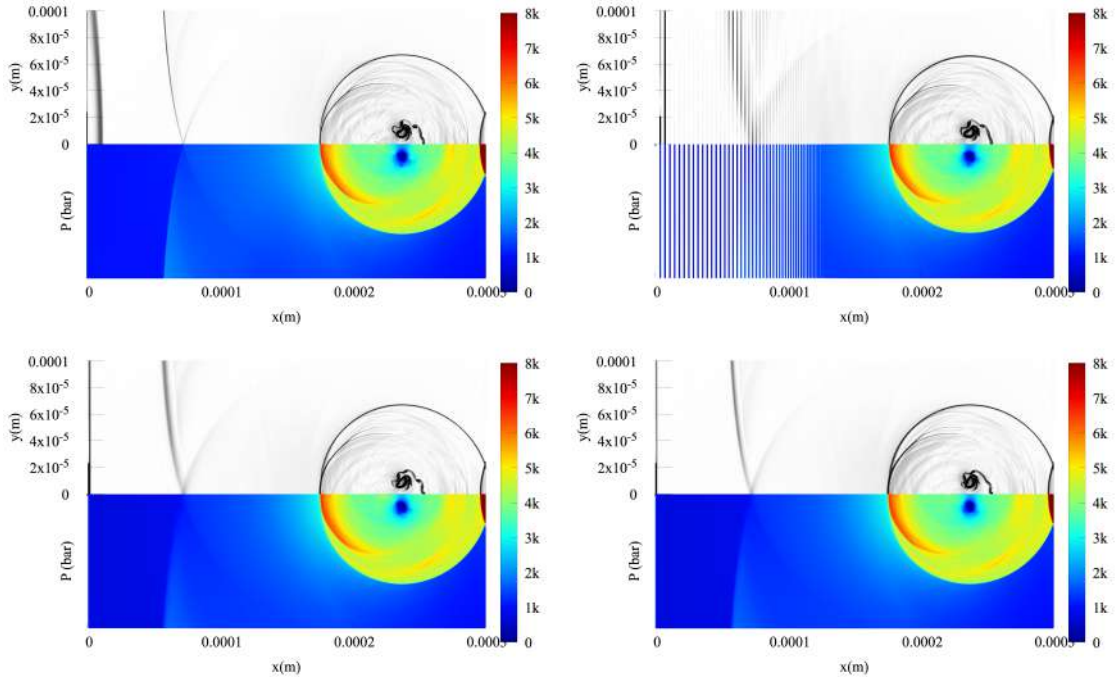

Figure 7.23: Bubble collapse next to a wall, zoom of the gradient of the density (top) pressure (bottom), WENO5-IS, uniform 1909×3181 (left top), A_1, stretch 1050×1501 (right top), A_2, stretch 1039×1501 (left bottom), A_3 stretch 1051×1470 (left right), t=2.8μs, zoom in y-direction

In order to confirm these observations, an enlargement of the internal vortex of the bubble of the size of the biggest uniform mesh area (A_1 area) at time t=3.3μs is plotted on Figure 7.24. This time of the solution illustrates stronger variations, particularly the discrepancy of the internal vortex reconstruction. The deformation of the shape and angle of this vortex increases with the decrease of the uniform mesh area. For instance, the stretching strategy A_1 led to the vortex to be nearly identical to the solution obtained on the uniform mesh, while smaller uniform box A_3 resulted in the vortex being poorly resolved and missing elements around it. Moreover, the bubble part where the mesh is stretched is more diffused, i.e. the interface on the left hand side to the vortex. Furthermore, the disturbances in the higher values of the pressure profiles with A_2- and A_3-strategies are noted. These observations show that the shorter interval of the uniform mesh, which does not include the whole bubble yields to stronger solution deterioration inside the zone of the interest. While, the larger uniform mesh box results in considerably lower accuracy of the solution on the left boundary, the result of the bubble reconstruction and its collapse next to the wall is well recovered.

7.3.1 Hybrid approach

The mesh stretching implementation demonstrated an effective way of computational cost reduction. An appropriate choice of the location of the stretching function initialization leads to the retained accuracy of the solution of the prioritised part of the computational domain, i.e. the whole bubble or its part. Even though the required CPU time can be achieved by using solely the

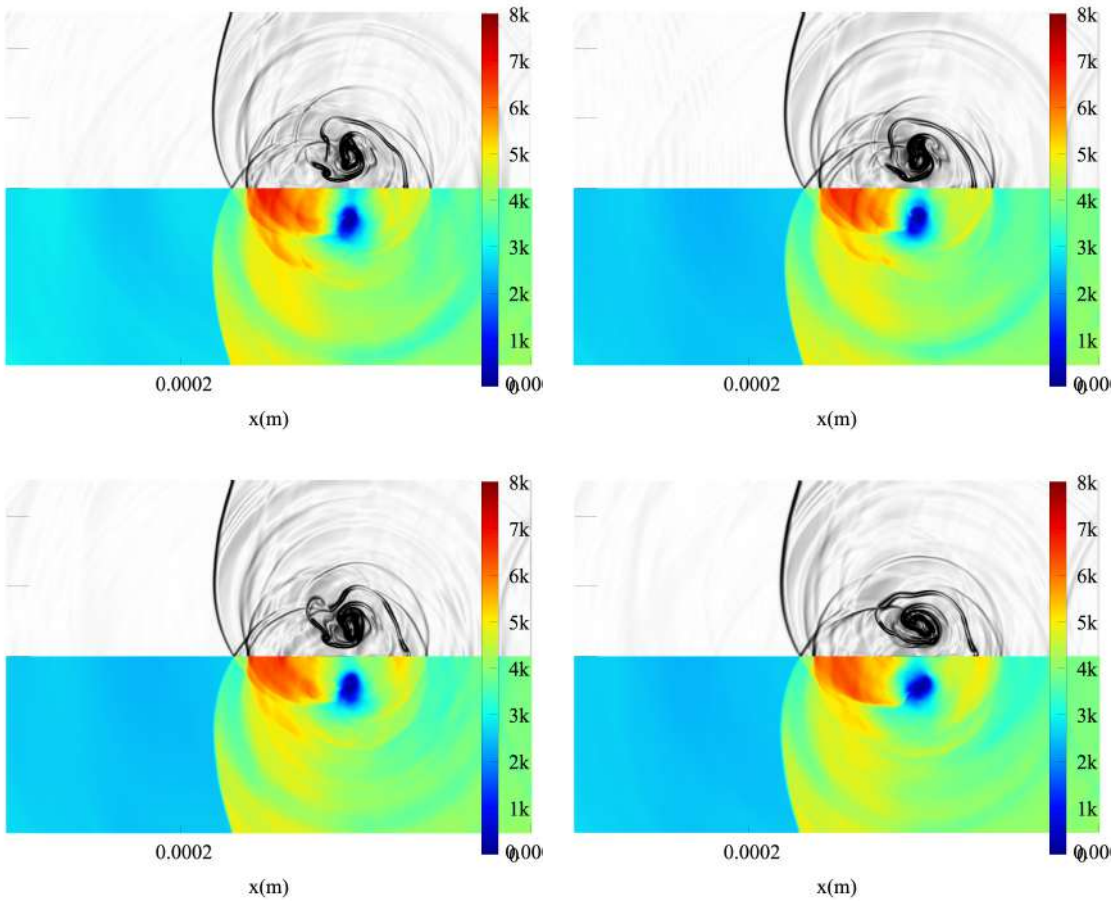

Figure 7.24: Bubble collapse near a wall zoom of the gradient of the density (top) pressure (bottom), WENO5-IS, uniform 1909×3181 (left top), A_1, stretch 1050×1501 (right top), A_2, stretch 1039×1501 (left bottom), A_3 stretch 1051×1470 (left right), t=3.3μs, zoom in y-direction

mesh stretching strategy, the extension of the computations to 3D space might need some further reduction.

The CPU cost can be affected by many things such as code optimization, implementation methods, etc. However, two crucial parts of the contribution to the computational time in present solver is the size of the problem (i.e. number of discretization points in all directions) and the size of the computational stencil. Perspectively, the fifth order scheme requires 2.5 times more nodes in the stencil than the second order scheme. Moreover, the solution obtained by using the only two-points stencil (see Section 5), have not a too big variation at the part of the domain without the bubble. Hence, one of the ways to achieve further CPU decrease is an introduction of the lower order of the scheme outside the zone where the high order of accuracy is required. The result of this is a combination of the higher order scheme and uniform mesh inside the zone of the interest and reduced order of the scheme with stretched mesh elsewhere.

In order to demonstrate this idea, the bubble collapse next to a wall is computed by using mesh stretching following configuration A_1 with similar parameters: fixed CFL=0.1, the initialisation of the mesh is done based on the 1908×3180 points. However, two more numerical methods are involved in the results presented. While the most accurate result has been achieved with WENO5-IS, MUSCL and WENO3-Z are used in order to examine different effects of the new hybrid approach. Saying that, the following combinations of the schemes are tested:

- WENO5-IS inside the zone A_1, WENO3-Z elsewhere
- WENO5-IS inside the zone A_1, MUSCL elsewhere
- WENO3-Z inside the zone A_1, MUSCL elsewhere

Firstly, the solutions for P_{max} and $P_{wallmax}$ are examined and compared with the solutions obtained on the uniform grid computed with above mentioned schemes. The results are presented on Figure 7.25. The overall correct curves reconstruction is noted. However, the intensity reduction of the maximum pressure P_{max} at time $t = 2.8\mu$s is observed as well as the decreased value of the peak at time t=3.3μs of $Pwall_{max}$. The values of these solution components are recorded in Table 7.6. The comparison between the values of P_{max} and $P_{wallmax}$ computed on the uniform mesh and on the stretched mesh coupled with hybrid schemes approach is proposed. While there is a decrease of around 3% in highest pressure peak between WENO5-IS computed on uniform mesh and all other schemes, this reduction is nearly identical among all solutions obtained on the non-uniform mesh, including those where the order reduction is used outside the zone of our interest. Similar pattern is noted for the peak of wall pressure at time t=3.3μs, i.e. the reduction of approximately 6% is observed across all solutions compared to result obtained on the homogeneous grid by using WENO5-IS.

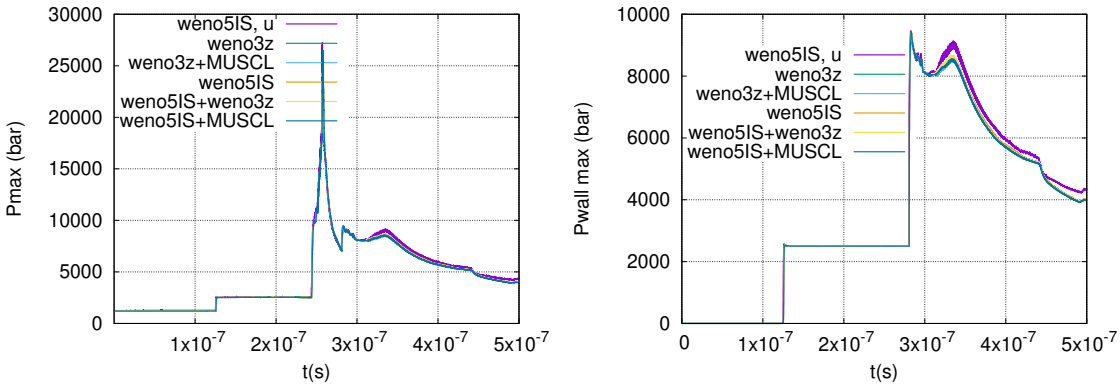

Figure 7.25: Bubble collapse near a wall, hybrid approach, P_{max} (left), $P_{wallmax}$ (right), bar

method	t1, μs	P, *bar*	Pwall, *bar*	t2, μs	Pwall, *bar*
WENO5-IS uniform	2.8	27,302	9,456	3.3	9,138
WENO5-IS	2.8	26,532	9,417	3.3	8,675
WENO5-IS+WENO3-Z	2.8	26,536	9,414	3.3	8,664
WENO5-IS+MUSCL	2.8	26,533	9,406	3.3	8,530
WENO3-Z uniform	2.8	26,000	9,453	3.3	8,938
WENO3-Z	2.8	26,199	9,409	3.3	8,637
WENO3-Z+MUSCL	2.8	26,225	9,407	3.3	8,530

Table 7.6: Bubble collapse next to a wall, comparison of the maximum pressure occurrence times and intensity (bar) depending on the mesh stretching degree using *tanh* function from interior point in x-direction. hybrid formulation, CFL=0.1

The present analysis is concluded by qualitative assessment of the gradient of the density and pressure profiles corresponding to the occurrence of the wall pressure peak at time t=3.3μs. This time has been chosen due to the advanced development of the internal vortex of the bubble and, thus, the variation in the solution can be seen. The comparison between the density gradients obtained from the uniform mesh computations are compared with those computed on the stretched mesh coupled with hybrid approach where the combinations of two schemes, lower and higher order, is used. The results zoomed on the uniform mesh area are presented on Figures 7.26 and 7.27. The bubble shape, its interface and internal vortex have been accurately reconstructed inside the zone of the interest. The solutions obtained from computations on the non-uniform mesh are nearly identical to those computed on the stretched mesh coupled with lower order scheme outside the area uniform mesh.

The final CPU cost by using mesh stretching approach with and without coupling with order reduction outside the interest zone is presented in Tables 7.7-7.8. The reduction of the size of

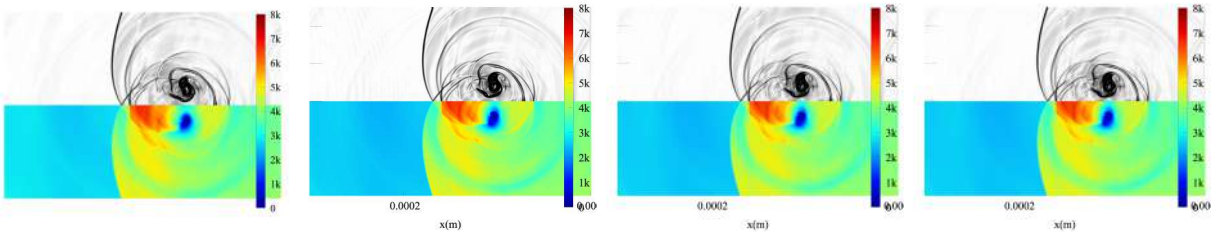

Figure 7.26: Bubble collapse next to a wall, zoom of the gradient of the density (top) pressure (bottom), WENO5-IS uniform mesh (left), WENO5-IS stretched mesh (middle left), WENO5-IS+WENO3-Z (middle right), WENO5-IS+MUSCL (right), time t=3.3μs

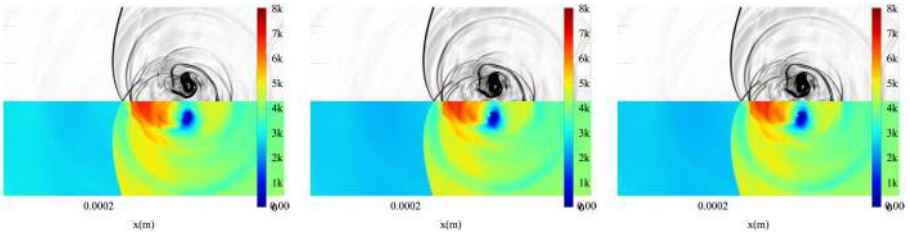

Figure 7.27: Bubble collapse next to a wall, zoom of the gradient of the density (top) pressure (bottom), WENO3-Z uniform mesh (left), WENO3-Z stretched mesh (middle), WENO3-Z+MUSCL (right), time t=3.3μs

the problem by using the stretching strategy A_1 is about 70% and the consequent decrease of computational time by using only stretched mesh approach is observed to be proportional to this value. i.e. the CPU gain is similarly about 70% between WENO5-IS solution obtained on the fully uniform mesh and same scheme used on the stretched grid. This gain is improved by further 5% and 10% by reducing the computational stencil to three and two points, respectively. Similar tendency is recorded with the scheme WENO3-Z. The CPU gain obtained by using only stretched mesh and stretched mesh coupled with order reduction is about 80% and 83%. Overall, the computational time has been improved by almost six times by using fifth order scheme.

Scheme	mesh	CPU (h)	ratio
weno5IS+MUSCL	1050×1502	23.1	1
weno5IS+weno3z	1050×1502	32.1	1.4
weno5IS	1050×1502	37.4	1.6
weno5IS	1908×3181	133.7	5.8

Table 7.7: CPU cost, bubble collapse near a wall, mesh stretching+hybrid approach based on WENO5-IS, CFL=0.1

Scheme	mesh	CPU	ratio
weno3z+MUSCL	1050×1502	20.7	1
weno3z	1050×1502	30.0	1.4
weno3z	1908×3181	121.6	5.9

Table 7.8: CPU cost, bubble collapse near a wall, mesh stretching+hybrid approach based on WENO3-Z, CFL=0.1

7.4 Synthesis

This Chapter addressed mesh stretching strategies based on the analytical presentation of stretching functions in Chapter 6. The strategies of stretching function location have been discussed and those suitable for each problem were defined. The CPU cost analysis was proposed.

Ultimately, an appropriate non-uniform mesh was introduced for the problem of shock-induced bubble collapse in vicinity to a wall. We defined a suitable location of the domain where the solution varies the most and used fine uniform spacing in this region. This mesh spacing was then used as initial value to create a continuous mesh stretching outside the zone of solution variation. We determined the degree of stretching which is necessary to achieve the required CPU cost. Moreover, the hybrid methods were implemented and tested as a way of further computational time reduction. Overall, the CPU reduction is proportional to the reduction of number of points in computational domain and we managed to speed up the computations by five times for the problem of shock-induced bubble collapse next to a wall.

Yet, the question of communication cost arises when extending these methods to 3D computations, where parallelization techniques are needed. As such, a trade-off between the highest accuracy of the method and acceptable computational time has to be made. For instance, the difference of CPU between the method of WENO3 and WENO5 is considerable even in 2D, while the difference in results is probably not huge. It is a case at least for a given number of points in computational domain, which could be afforded on our computational resources. Hence, one has to consider if the method of third order is not more suitable in terms of its complexity than a method of fifth order. Similar assessment has to be made regarding the hybrid approach which complexity is also increased by introducing two methods together. These questions will be partially clarified in the next Chapter.

Chapter 8

3D computations on non-uniform mesh

This Chapter addresses an extension of the previously discussed high-order numerical methods and mesh stretching techniques to 3D computations. Due to the complexity of implementation of high-order methods on non-uniform mesh, only WENO3-Z method is considered at this moment. Two test cases are presented.

The first problem is a direct extension of the shock-bubble collapse in vicinity to a wall detailed in Chapter 7. Due to the limits of computational resources, the solutions are obtained by using the stretched mesh and compared to the results in Goncalves & Parnaudeau (2021) and Dubois *et al.* (2021). The mesh stretching strategy has to be altered to include the location of the shock wave.

The second problem considers yet another shock-induced bubble collapse near a wall with lower value for P_{sh} for which the high-fidelity computation has been performed Wermelinger *et al.* (2018). The computations are done on the uniform and stretched mesh by using MUSCL and WENO methods. The dependence of the maximum pressure next to the wall on the stand-off distance of the bubble is proposed. All solutions presented here are obtained from computations in parallel solver SCB on supercomputer Jean Zay JeanZay (2019).

8.1 3D SCB solver

SCB is an efficient and simple parallel multi-phase solver developed to simulate various compressible multiphase flows, in particular bubble collapse. The parallelisation of the solver is based on hybrid approach of using OpenMP and MPI libraries. Recently the parallelisation strategy of combination of MPI and OpenACC has been performed given large developments of CPU and GPU-based supercomputers, see Dubois *et al.* (2021).

The distributed memory parallelisation is based on the MPI library. The computational stencil of SCB is based on five points per direction, which implies that each unknown is computed by using 13 neighbours. The HLLC Riemann solver is parallelised by using global arrays distribution between the processes. A 3D block partitioning of the matrix is used in order to perform a decomposition. This technique is based on the introduction of "ghost" cells at each subdomain and data communication between neighbouring cells of one subdomain. A Cartesian processor topology is used to organise the subdomains.The computations are coupled by using two layers of auxiliary cells which are defined on the boundaries of each subdomain. The better performance can be achieved if the subdomains has equal size and square topology.

Accelerator parallelization model is based on the OpenMP library. Three main principles have been used in order to distribute the loops across the threads (i.e. a fine grained programming). The first principle is an estimation of the problem size which allows to avoid the irrelevant data sharing should the problem size becomes too small. The second principle is a choice of appropriate scheduling. The better load around the threads can be achieved by switching between four different types of OpenMP loop scheduling. These are *static, dynamic, guided* and *runtime*. The former one is meant to switch between three previous types when a run which uses a variable system environment is executed. The final principle addresses a merging of internal loops, *COLLAPSE*, which leads to an enlargement of the iteration space and a consequent improved distribution of iterations. A simplified example with OpenMP implementation in SCB is given in Appendix B.

The non-uniform mesh is generated by separately developed program, which takes as inputs initial location and size of space steps dx, dy and dz. Since the mesh stretching is a problem-dependent, every strategy has to be implemented based on the test case in consideration. All problems and mesh stretching strategies discussed in this thesis are included into this software. The non-uniform mesh is generated and written into the data file, which is then used by SCB. The distribution of the grid coordinates values is required for the parallel computations.

An introduction of the high order schemes in SCB requires a communication of additional neighbours per unknown. This is particularly the case for the schemes of fifth order where the high communication cost is questionable in terms of its proportionality to the solution improvement. At this stage WENO3-Z with uniform and non-uniform mesh has been introduced in the framework of OpenMP and MPI. The implementation of the method on the uniform mesh does not require an enlargement of the existing stencil. However, the new communication is required for the non-uniform mesh, where we have to share the values for the non-uniform mesh coefficients required for the scheme. While this does not enlarge a number of neighbours for MUSCL method, it certainly does for WENO3 reformulated for the non-uniform grid, where two additional nodes have to be defined at the first time iteration to compute the coefficients. This can increase a communication cost. In order to avoid this, we note that due to the smooth mesh stretching function used in this study, the variation of coefficients values needed for the non-uniform mesh is very small. Thus, the last coefficients computed for WENO3 at the boundaries of the domain are set equal to its neighbour. An example of this implementation in x-direction is presented in Appendix C. Similar manner is used for all directions.

8.2 Bubble collapse near a wall, $P_{sh} = 1200$ bar

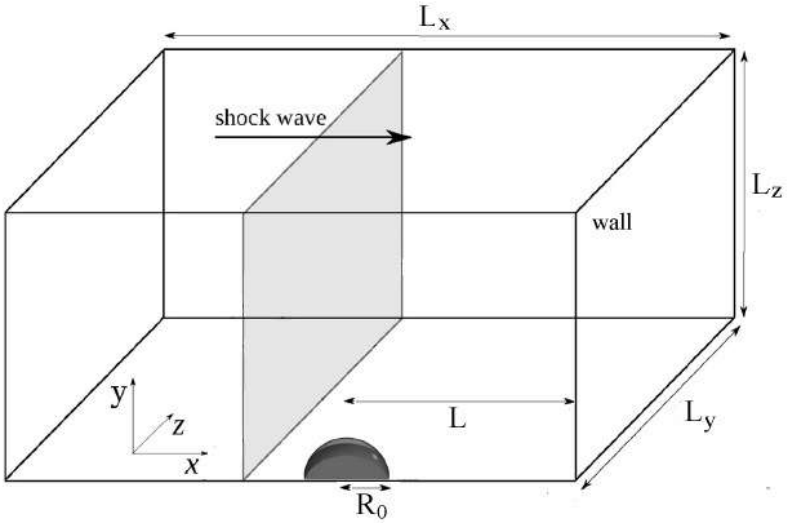

Figure 8.1: Configuration at initial time, P_{sh}=1200 bar

We consider a spherical bubble collapse with a stand-off distance from the wall L/R_0=2. The test case is similar to the bubble collapse near a wall presented in previous Chapter with extension to 3D. Exploiting the symmetry of the problem, only a quarter of the bubble is computed. The configuration at initial time is presented on Figure 8.1.

The time evolution of maximum pressure inside the fluid and along the wall is presented on Figure 8.2. We introduce a 2D result computed on the corresponding uniform mesh for comparison. As noted in Goncalves & Parnaudeau (2021) the collapse of spherical bubble develops faster and its intensity is stronger. Indeed, the same observation is confirmed in our computations. The intensity of maximum pressure peak is of factor 5 compared to 2D solution and it occurs approximately 0.5μs faster. However, the wall pressure (the right part of the plot) has very similar intensity at maximum peak, as observed in Goncalves & Parnaudeau (2021).

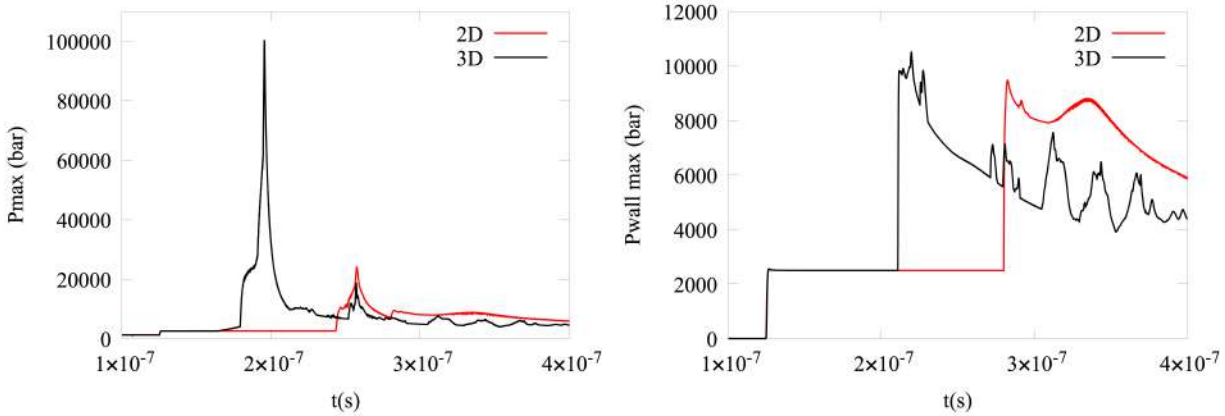

Figure 8.2: Time evolution of the maximum pressure inside the fluid (left) and near the wall (right). WENO3-Z. 2D, uniform mesh: 1500×2500; 3D, stretched mesh: 1050×850×850. P_{sh} = 1200 bar

The 3D mesh stretching strategy is firstly examined by means of coarser mesh computations. These computations illustrated a solution discrepancy by using the mesh stretching strategy similar to 2D computations. Precisely, the time of the pressure peaks is shifted depending on the stretching factor β. We demonstrate this discrepancy on Figure 8.3 (left) by using the example of solution for maximum pressure along the wall. The mesh stretching is applied only in x direction while keeping y and z directions uniform. The solutions are compared with corresponding uniform mesh 150×250×250. We observe the solution being shifted in time depending on the degree of stretching.

The variation of the time is thought to occur for two reasons. The first reason is a very coarse mesh and, hence, less accurate stretched mesh spacing at the boundaries. The second one is inappropriate strategy of the mesh stretching in x-direction. Indeed, the 3D problem has an increased complexity and difference in the shock topology and might require an alternative thinking about non-uniform grid generation. Thus, slightly different non-uniform mesh is generated for 3D computations. The difference in our new approach is an expansion of the uniform mesh area to the left hand side along x-direction. The new uniform mesh area includes the location of the incident shock wave. This change has improved the solution obtained by using the coarse stretched mesh. (see the right part of Figure 8.3). All computations results discussed below follow similar idea of mesh stretching in x direction. The mesh stretching in directions y and z stays unchanged.

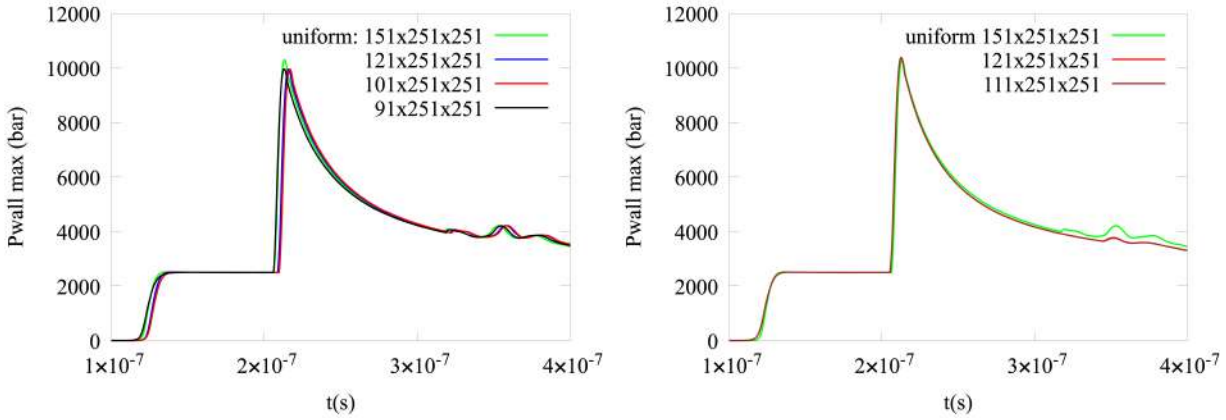

Figure 8.3: Time evolution of the maximum pressure near the wall with uniform mesh area occupying 1/2 of the domain in x-direction (left) 2/3 of the domain in x-direction (right). MUSCL. $P_{sh} = 1200$ bar

The high-order scheme effect on solution is then analysed on finer uniform mesh (750×1250×1250). The comparison is performed between MUSCL and WENO3-Z methods. The solutions of maximum pressure inside the fluid and on the wall are presented on Figure 8.4. The highest peak of pressure inside the fluid occurs at approximate time t=0.2 μs and reaches almost 70,000 bar. This value is in close agreement for both obtained solutions, with lower intensity result by WENO3-Z (reduced by around 1.5%). Similarly, the solution for the wall pressure is characterised by highest pressure intensity at t=0.22 μs and is about 10,400 bar. This value is varied by less than 1% between both methods. However, overall the WENO3-Z scheme led to the higher pressure intensity values at later times of the solution.

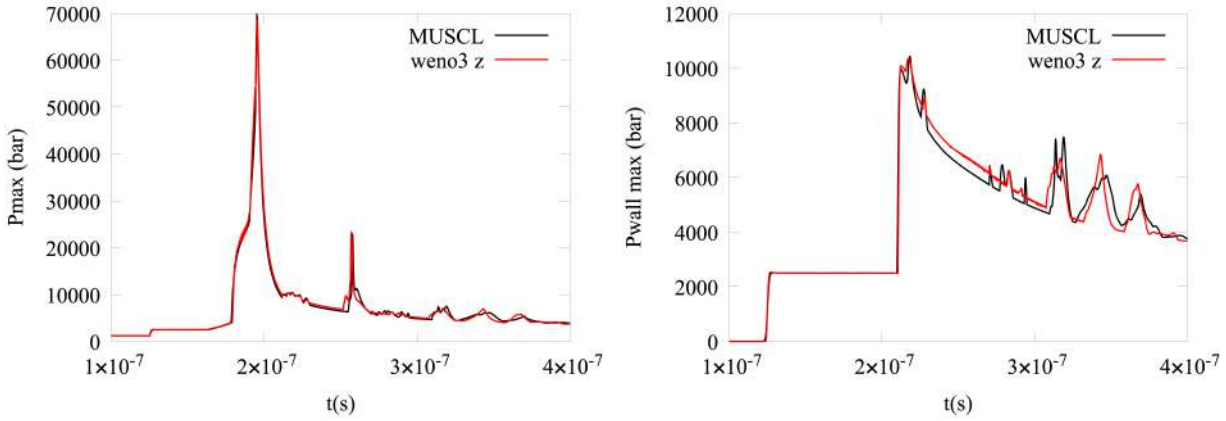

Figure 8.4: Time evolution of the maximum pressure inside the fluid (left) and near a wall (right). Comparison between MUSCL and WENO3-Z. $P_{sh} = 1200$ bar

Further comparison is performed by means of qualitative assessment of 3D visualisations where longitudinal velocity component, wall pressure, density gradient and isosurface of void ratio are presented (Figure 8.5). The solutions are compared at following times: t=0.20μs, t=0.24μs and t=0.28μs. The key components of the solution are in very close agreement between each other. This only small difference between the obtained results can be explained by relatively coarse mesh which has been employed in these tests. Due to the negligible variation between the results of second and third order formal accuracy, the stretching mesh strategy is thus initially examined by using the scheme with smaller computational stencil, i.e. MUSCL method.

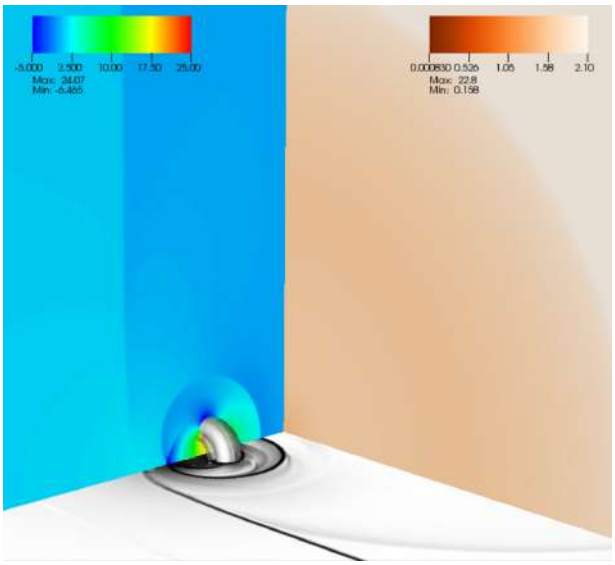

(a) t=0.2 μs, MUSCL

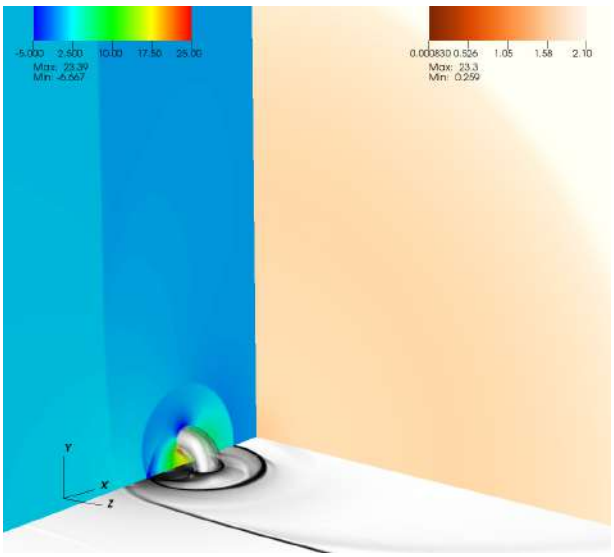

(b) t=0.2 $\mu s, WENO3-Z$

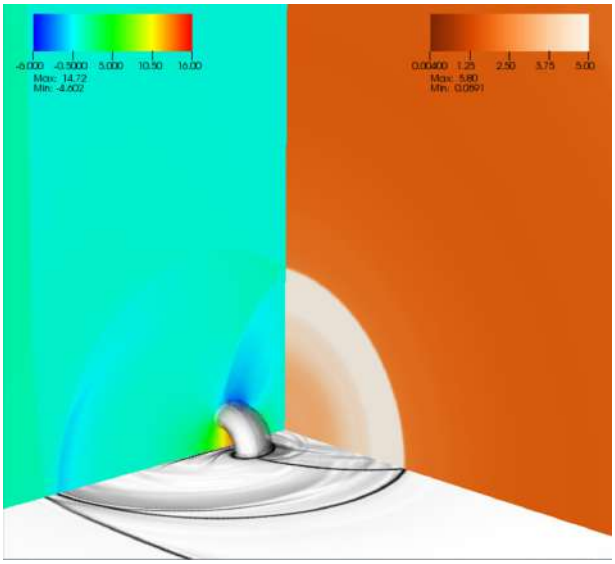

(c) t=0.24 $\mu s, MUSCL$

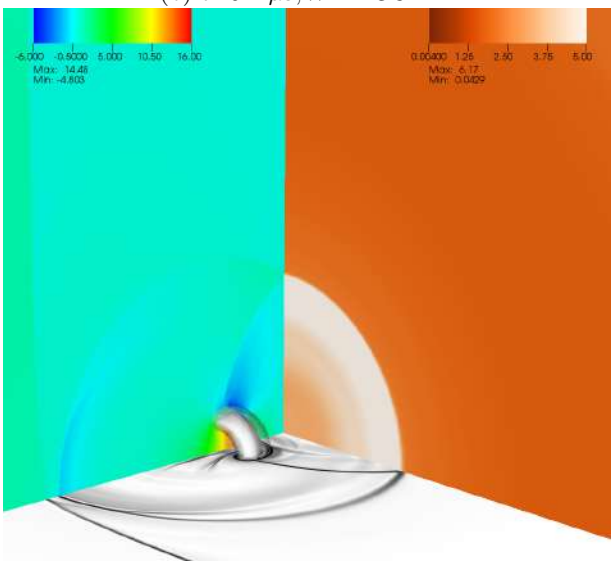

(d) t=0.24 μs, WENO3-Z

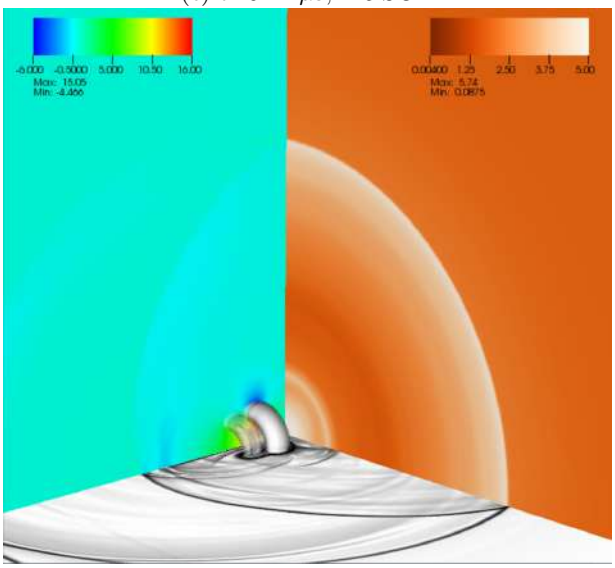

(e) t=0.28 $\mu s, MUSCL$

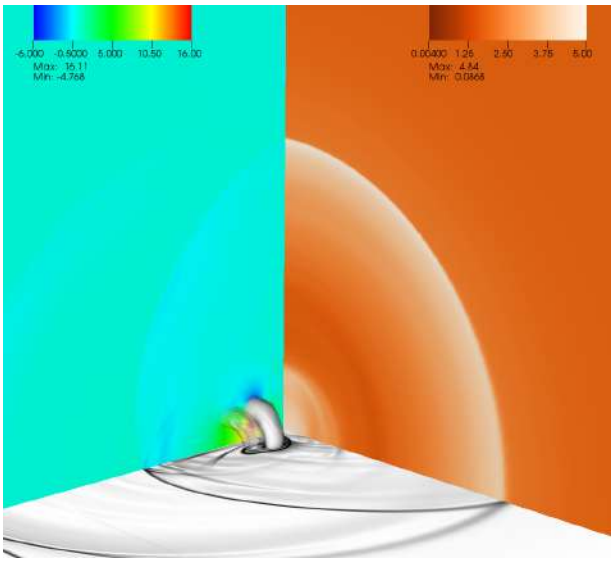

(f) t=0.28 μs, WENO3-Z

Figure 8.5: Visualisation of 3D bubble collapse at different times for a stand-off distance $L/R_0 = 2$. Dimensionless longitudinal velocity component u/u_{sh}, dimensionless wall pressure P/P_{sh}, Schlieren-like representation and isosurface of void ratio. WENO3-Z, stretched mesh: 750×1250×1250. $P_{sh} = 1200$ bar

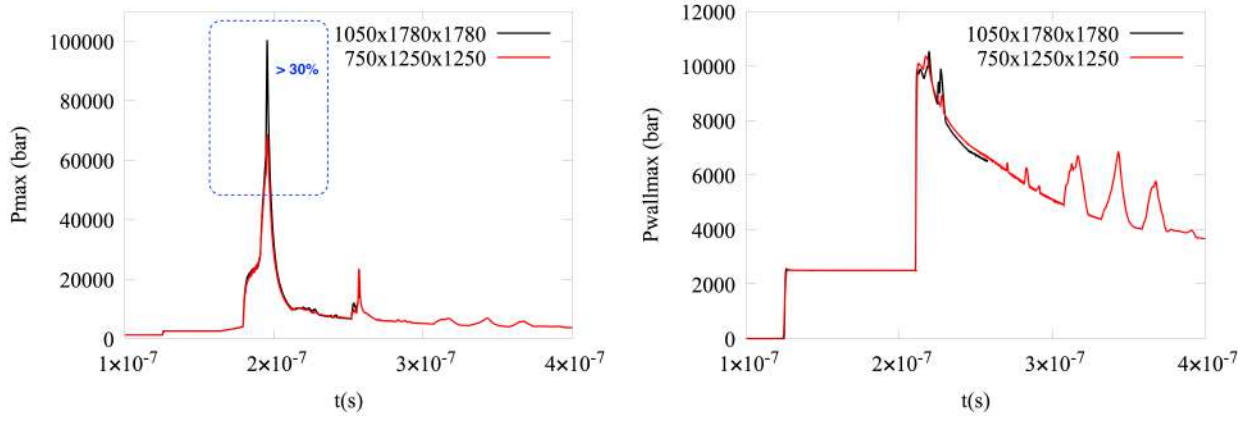

(a) P_{max} (b) $P_{wallmax}$

Figure 8.6: Time evolution of pressure. Comparison between coarse and fine mesh. $P_{sh} = 1200$ bar

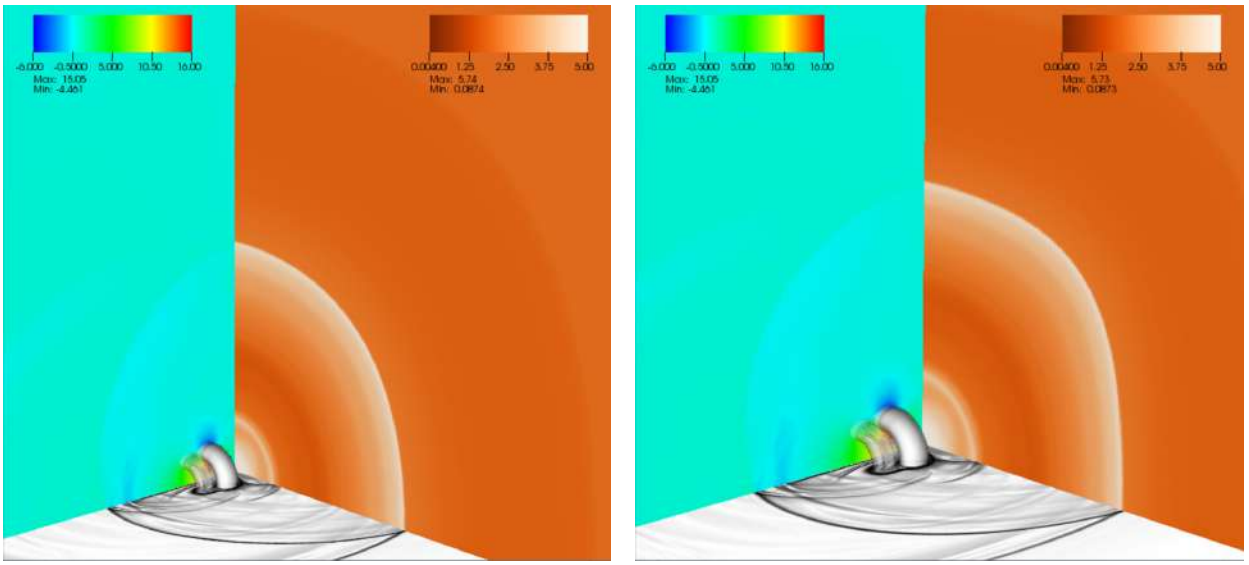

(a) t=0.28 $\mu s, 550\times900\times900$ (b) t=0.28 $\mu s, 550\times625\times625$

Figure 8.7: Visualisation of 3D bubble collapse at different times for a stand-off distance $L/R_0 = 2$. Dimensionless longitudinal velocity component u/u_{sh}, dimensionless wall pressure P/P_{sh}, Schlieren-like representation and isosurface of void ratio. MUSCL, t=0.28 μs. $P_{sh} = 1200$ bar

The computations presented in what is to follow are performed by using stretched mesh in all directions by using hyperbolic tangent function. The stretching strategy is similar to 2D case with only change being an extended uniform mesh area in x-direction to include the location of shock wave. The initialisation of dx, dy and dz values is based on the uniform mesh of $750\times1250\times1250$ corresponding to 250 points per bubble diameter for the coarser mesh or on the uniform mesh of $1500\times2500\times2500$ corresponding to 500 points per bubble diameter for finer mesh.

Different degree of stretching is examined by using MUSCL scheme and the initial spacial interval corresponding to the mesh of $750\times1250\times1250$ nodes. The uniform mesh box is set similarly in all computations. The 3D visualisations presented on Figure 8.7 illustrate the deviation of the solution with increased stretching factor. This is especially the case for the wall pressure component where the distribution values are not smoothly propagated and have a square pattern. However, the solution around the bubble, where the uniform mesh is set remains accurate and similar in all tests. This raises the need of proper definition of how much stretching can be applied to obtain the solution of required quality if the uniform accuracy everywhere in the domain is searched. These tests show that the solution accuracy for this particular problem and corresponding stretched mesh configuration is dependent on the ratio between dy_{max}/dy_{min} and dz_{max}/dz_{min}. We limit the consideration on these two directions since the uniform mesh area set in these two directions is

relatively small. Saying that, this ratio for the first stretched mesh configuration (550×900×900) is 1.7 and the obtained solution is not visually deteriorated, while the second stretched mesh configuration (550×600×600) with approximate ratio equal to 3.2 yield to the deformation of the pressure values distribution. Thus, the initial finer stretched mesh computations are following the first ratio between maximum and minimum spacing in directions of y and z.

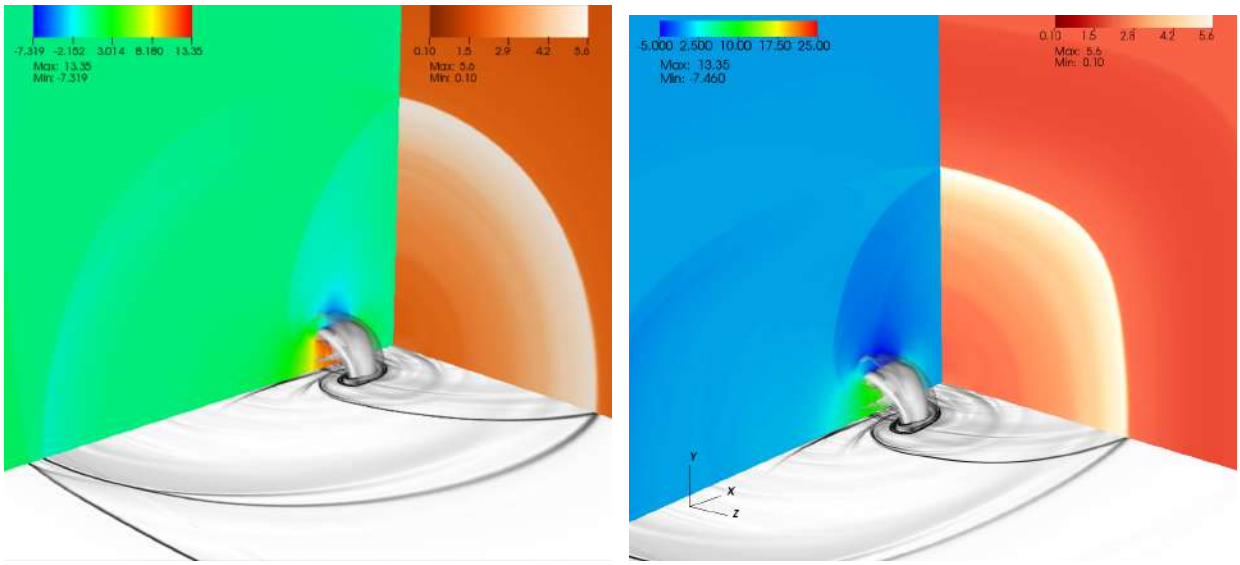

(a) t = 0.25 μs, 1050×1780×1780 (b) t = 0.25 μs, 1050×850×850

Figure 8.8: Visualisation of 3D bubble collapse at different times for a stand-off distance $L/R_0 = 2$. Dimensionless longitudinal velocity component u/u_{sh}, dimensionless wall pressure P/P_{sh}, Schlieren-like representation and isosurface of void ratio. WENO3-Z. Comparison of stretched mesh factor. $P_{sh} = 1200$ bar

We now show the reason for general finer mesh requirement inside the zone of our interest. The two key components of the solution are examined on Figure 8.6, i.e. maximum pressure inside the fluid and on the wall. The obtained maximum pressure curve next to a wall does not have a critical variation at highest intensity peak. However, the pressure inside the fluid has a gain of more than 30% in highest peak. This increase of intensity which is a result of increasing number of nodes in computational domain shows the need of certain spacing size in order to obtain an accurate reconstruction of physical phenomena.

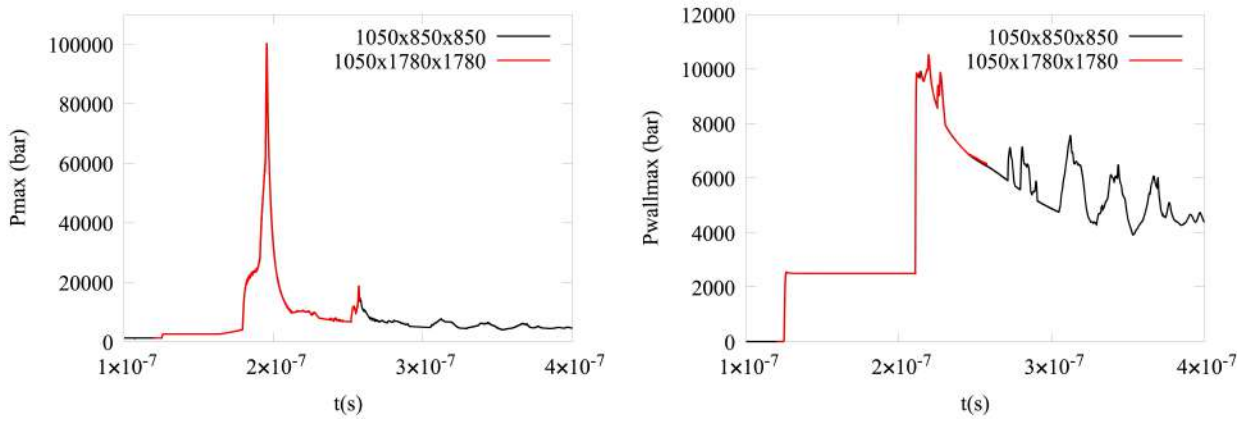

(a) P_{max} (b) $P_{wallmax}$

Figure 8.9: Time evolution of pressure. Comparison between stronger and weaker stretching. $P_{sh} = 1200$ bar

An illustration of the bubble collapse evolution is proposed on Figure 8.10. We present normalised longitudinal velocity by $u_{sh} = 75.07$ m/s on the vertical symmetry plane, normalised pressure by $P_{sh} = 1.2 \times 10^8$ Pa on the wall, the density gradient on the horizontal symmetry plane

and void ratio inside the volume. The incident shock wave reaches the wall and reflected wave is generated. At time $t = 0.15\mu$s, the reflection wave is located near the bubble. We note the bubble deformation compared with its initial spherical shape at $t = 0.12\mu$s. This happens due to the difference in pressure between two sides. The water jet penetrating the bubble causes its toroid-like shape at $t = 0.18\mu$s and the reflected shock wave has reached the bubble interface. The spherical intense blast wave is generated at time $t = 0.20\mu$s as the water-jet impacts the opposite side of bubble interface. The high velocity values are generated and reach 1500 m/s. The occurrence of strong pressure peak caused by the blast wave reaching the wall is observed at $t = 0.23\mu$s. The reflected wave propagates in direction of toroid-like bubble. Finally, this wave impacting the bubble leads to its recollapse at $t = 0.25\mu$s. Consequently, another pressure peak is generated as can be observed on Figure 8.10.

The next step has been set to apply stronger stretching factor. Figure 8.8 presents side-by-side comparison of 3D visualisation at the time of bubble recollapse under the incidence of reflections wave. A square-shaped reconstruction of pressure profile is noted away from the bubble. It is certainly due to the stretching mesh since the computations on uniform mesh and on stretched mesh with lower factor do not exhibit it. While the effect of such strong stretching has been also seen in 2D computations, it did not affect the pressure region around the bubble. Similarly in 3D, the pressure profile close to the bubble has a correct shape and starts to be more squared further away from the bubble as the grid spacing continues to increase. This can be corrected by using weaker stretching factor or larger area of uniform mesh. The way of determining this factor would depend on the final CPU cost one can acquire and the initial size of dy and dz.

The comparison of maximum pressure inside the fluid and next to a wall is proposed by using similar configuration of stretching mesh on Figure 8.9. The highest and most critical peaks of pressure have not been affected by stronger degree of stretching.

The CPU cost for present problem (Table 8.1) is recorded to be 6 hours for the stretched mesh of 1050×850×850 and 34 hours for the stretched mesh of 1050×1780×1780 by using 4,000 processors. In comparison, the computational time of similar problem in 3D with uniform coarser spacing of 750×1250×1250 and dt-value twice higher, is only 0.7 h less. We believe that given computational cost and solution accuracy inside the critical area of physical phenomena, stronger mesh stretching (i.e. stretched mesh of 1050×850×850) can be used to recover key characteristics of the bubble collapse process.

Table 8.1: CPU cost, 3D bubble collapse near a wall, WENO3-Z, $P_{sh} = 1200$ bar. JeanZay 4,000 processors

Problem	Mesh type	nb points	$\mathrm{dx_{min}}$ ($\times 10^{-7}$)	dt ($\times 10^{-11}$)	CPU (h)
$P_{sh} = 1200$ bar	uniform	750×1250×1250	4	1	5.2
$P_{sh} = 1200$ bar	stretched	1050×1780×1780	2	0.5	34.9
$P_{sh} = 1200$ bar	stretched	1050×850×850	2	0.5	5.9

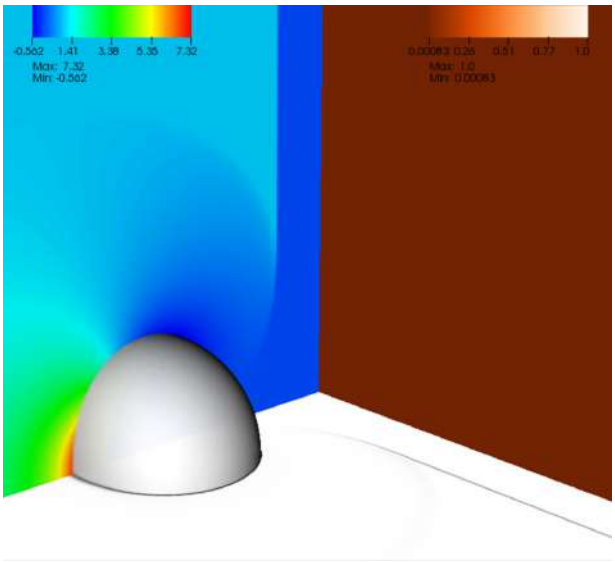

(a) t = 0.12 μs

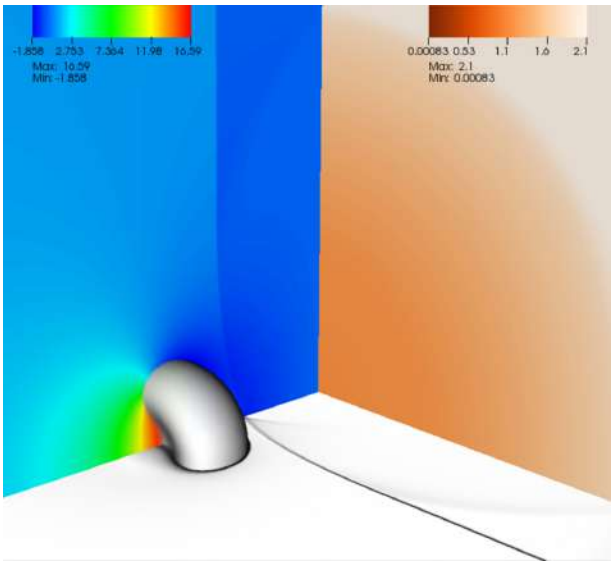

(b) t = 0.15 μs

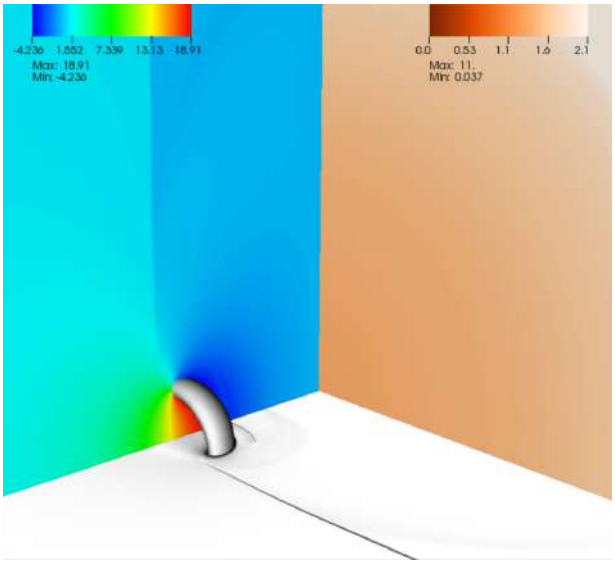

(c) t = 0.18 μs

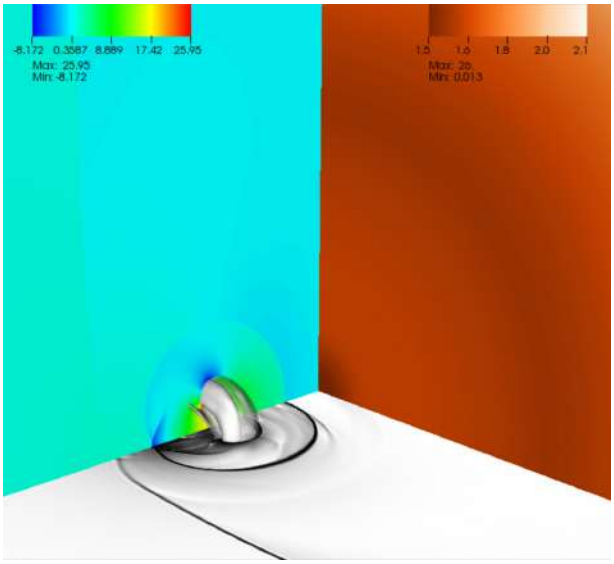

(d) t = 0.20 μs

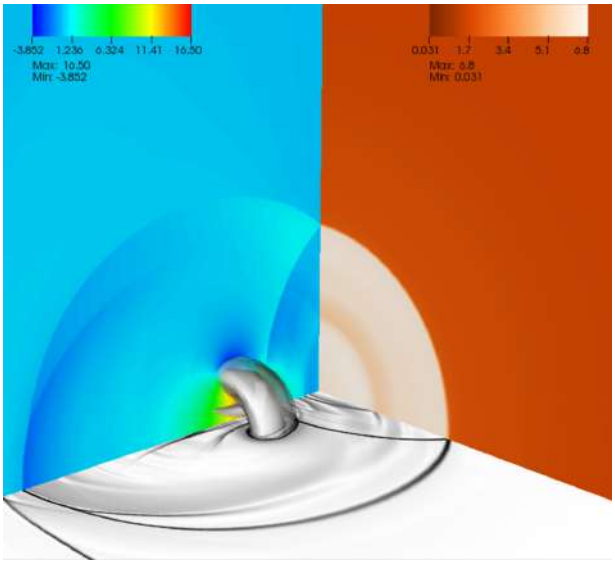

(e) t = 0.23 μs

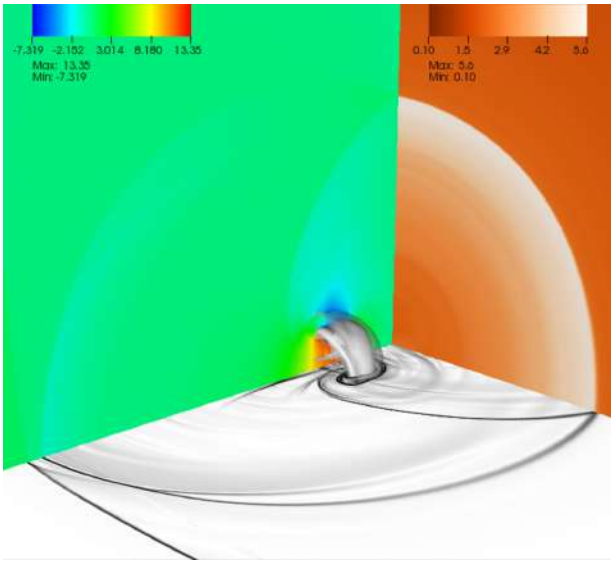

(f) t = 0.25 μs

Figure 8.10: Visualisation of 3D bubble collapse at different times for a stand-off distance $L/R_0 = 2$. Dimensionless longitudinal velocity component u/u_{sh}, dimensionless wall pressure P/P_{sh}, Schlieren-like representation and isosurface of void ratio. WENO3-Z, stretched mesh: 1050×1780×1780. $P_{sh} = 1200$ bar

8.3 Bubble collapse near a wall, $P_{sh} = 353$ bar

The present test case considers a gas spherical bubble of radius R_0 immersed in water in vicinity to a wall and impacted by a shock wave, which has a downstream pressure of $P_{sh} = 353$ bar. This problem has been studied before in Johnsen & Colonius (2009), Wermelinger *et al.* (2018) and most recently in Dubois *et al.* (2021). The initialisation and EOS parameters are stated in Tables 8.2 and 8.3.

Table 8.2: Initialisation parameters

	ρ	**u**	P
air	1 kg/m^3	0 m/s	10^5 Pa
water	998 kg/m^3	0 m/s	10^5 Pa

Table 8.3: Water-air EOS parameters

	γ	P_∞	C_p
air	1.4	0 Pa	1487 J/K.kg
water	6.68	4.103×10^8 Pa	1650 J/K.kg

The spatial domain is set $[L_x \times L_y \times L_z] = [8R_0 \times 12R_0 \times 12R_0]$ and the position of the bubble center is at $x = 6R_0$. The incident shock wave is set at $x_{sh} = 3.15R_0$. The initial stand-off distance between the bubble and the wall, a parameter which we aim to examine in some detail, is L/R_0=2. Only a quarter of the bubble is computed due to the symmetry of the problem. The wall is set by means of slip condition. Two configurations are tested. Firstly, the computations on the uniform mesh of 900×1200×1200 points are performed and solutions of maximum pressure inside the fluid and near the wall obtained by using MUSCL and WENO3-Z are compared. Secondly, the stretched mesh by using hyperbolic tangent stretching function with initialised dx, dy, dz-values corresponding to the uniform mesh of 900×1200×1200 is initialised in the framework of uniform fine mesh area which starts at the location of the shock wave and includes the whole interval in x-direction to the right hand side and bubble radius R_0 in directions y and z. This results in a new mesh of 612×600×600 points. Both configurations of the mesh correspond to 225 points per bubble diameter.

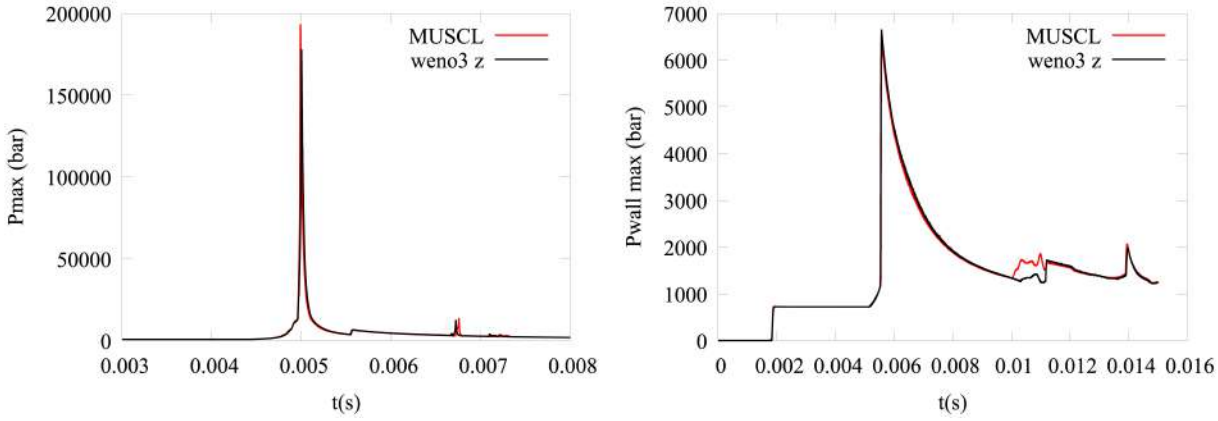

Figure 8.11: Time evolution of the maximum pressure inside the fluid (left) and near a wall (right), comparison of numerical schemes: MUSCL and WENO3-Z, uniform mesh: 900×1200×1200. $P_{sh} = 353$ bar

This test case starts by examination of the effect of high-order numerical scheme and stretched mesh on the solution. The maximum pressure evolution inside the fluid and along the wall is plotted on Figure 8.11. The solution has been obtained on the uniform mesh of 900×1200×1200 by using HLLC solver with WENO3-Z Hancock method. The MUSCL solution is proposed for

comparison purposes. The first pressure jump is generated due to the impact of water jet on the bubble and generation of the blast wave. This peaks reaches the value of almost 20 GPa by using MUSCL technique and slightly lower intensity by using WENO3-Z scheme, of about 18 GPa. The maximum pressure next to the wall is considered on the right part of the plot. The impact of higher order scheme is relatively low with maximum pressure intensity being recovered equally by both schemes. The solution variation between the schemes, however, is observed around the time $t = 0.01$ s, where lower values are generated by WENO3-Z.

Next, the effect of the mesh stretching is analysed. Similar quantities are presented on Figure 8.12, where maximum pressure evolution inside the fluid is plotted on the left and along the wall on the right. The effect of the mesh stretching is very weak: the most important peaks in pressure have been reconstructed equally, on uniform and stretched mesh with only slightly reduced intensity of maximum pressure along the wall on the interval between $t = [0.008, 0.015]$ s.

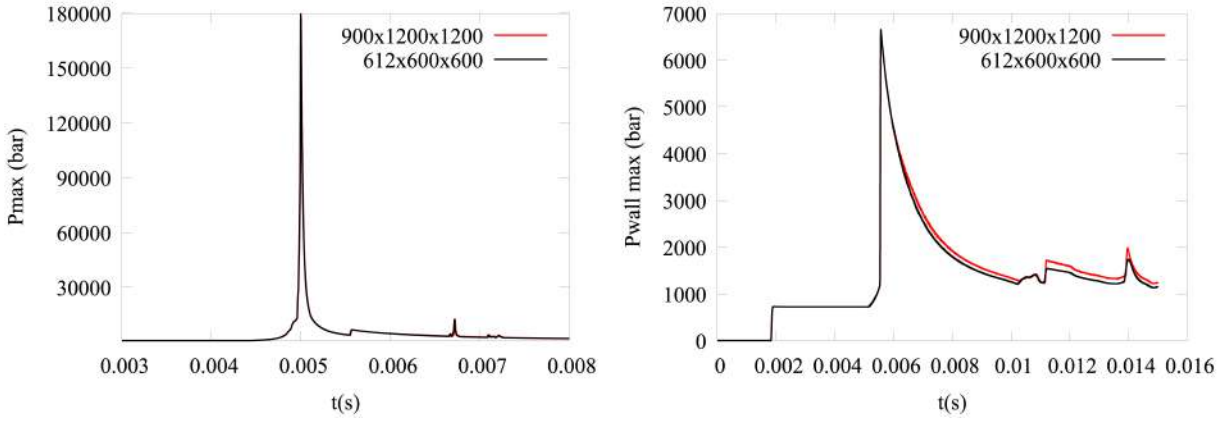

Figure 8.12: Time evolution of the maximum pressure inside the fluid (left) and near a wall (right), WENO3-Z, comparison of uniform mesh: 900×1200×1200 and stretched mesh: 612×600×600. $P_{sh} = 353$ bar

The main phenomena of the bubble collapse has been described in Johnsen & Colonius (2009) and Dubois *et al.* (2021). The pressure difference between phases causes the bubble deformation, which takes a toroid-like shape during the process. It causes a generation of water jet along the axis of flow symmetry. A high-pressure zone is generated as a consequence of the water-hammer shock formation at the time of water jet hitting the opposite side of the bubble. This results in bubble being cut into pieces. Furthermore, a consequent strong pressure peak occurs due to the impact of the blast wave to the wall. This can cause a damage of the solid material. The visualisation of this process is proposed in Figure 8.13. Computations are performed on stretched mesh with WENO3-Z scheme. The quantities presented on the plots are: the longitudinal velocity component on the vertical symmetry plane normalised with $u_{sh} = 20.77$ m/s, the pressure normalised by $P_{sh} = 3.53 \times 10^7$ Pa on the wall and density gradient on the horizontal symmetry plane. The isosurface of void ratio is plotted inside the volume.

At approximate time of t =0.004 s the shock wave affects the wall and generates the reflection wave which locates at the bubble. The water jet affecting the bubble and causing its toroid shape along with generation of the blast wave can be observed at $t = 0.005$ s. A strong pressure peak occurs as the blast wave hits the wall at time t =0.006 s. The reflective wave propagates in the direction of the bubble and eventually reaches the bubble pieces which results in recollapse and another pressure peak at approximate time t =0.008 s.

A discrepancy caused by mesh stretching is observed on the Figure 8.13, where the pressure profile has a somewhat squared pattern. Similar pattern is discussed for the problem in previous section. Moreover, it is not present on the solutions computed on the uniform mesh. We believe this effect is due to the strong stretching factor in y- and z-directions.

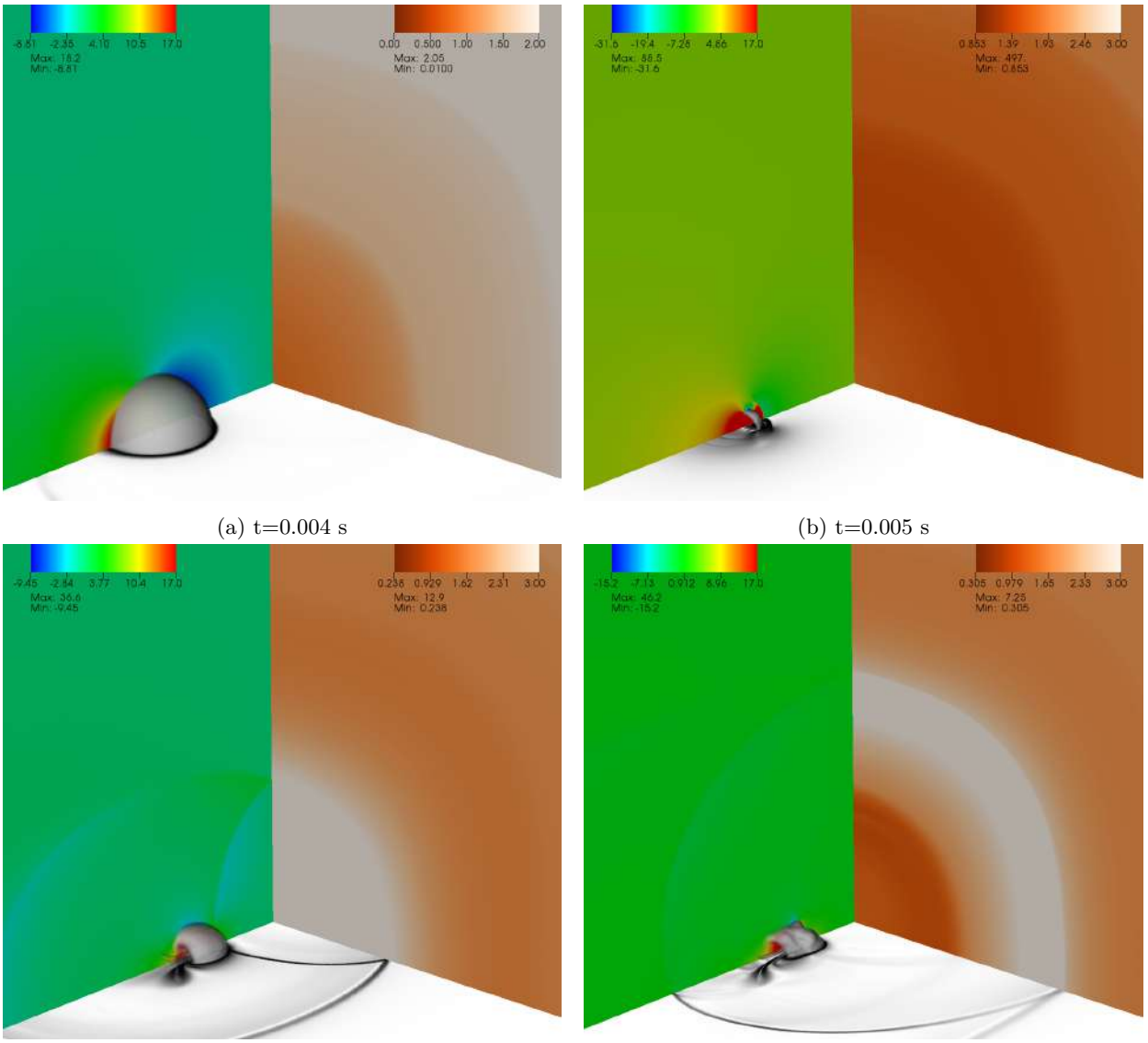

(a) t=0.004 s

(b) t=0.005 s

(c) t=0.006 s

(d) t=0.007 s

Figure 8.13: Visualisation of 3D bubble collapse at different times for a stand-off distance $L/R_0 = 2$. Dimensionless longitudinal velocity component u/u_{sh}, dimensionless wall pressure P/P_{sh}, Schlieren-like representation and isosurface of void ratio. WENO3-Z, stretched mesh: 612×600×600. $P_{sh} = 1200$ bar

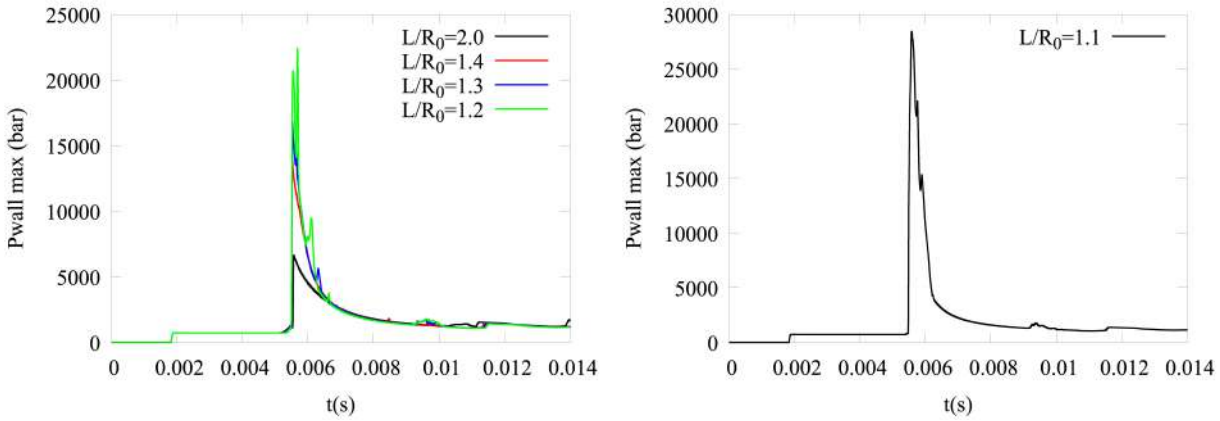

Figure 8.14: Time evolution of the maximum pressure along the wall for different values of the stand-off parameter L/R_0: from 2 to 1.2 (right), 1.1 (left), WENO3-Z, stretched mesh: 612×600×600. $P_{sh} = 353$ bar

Next, we address the effect of the initial bubble position in relation to the wall. The parameters of computations stay unchanged except the value of L/R_0, which varies from 2 to 1.1 and defines the distance of bubble center to the wall. The time evolution of the maximum pressure inside the fluid and along the wall are presented on Figure 8.14 with different L/R_0. The pressure load on the wall increases rapidly as the bubble distance from the wall decreases. The highest intensity of pressure is achieved at approximate time t = 0.006 s and it is this peak that has the biggest impact by changing the stand-off position. An intensity of almost 30,000 bar is reached when we set $L/R_0 = 1.1$ (right part of the figure), which is almost 6 times higher than the peak corresponding to $L/R_0 = 2$.

Lastly, the computational cost of this problem is proposed in Table 8.4. All computations are performed on 4,000 processors. A remarkable gain in CPU of factor 5 has been achieved by introduction of the stretched mesh. This gain is proportional to the reduction of number of points in computational domain.

Table 8.4: CPU cost, 3D bubble collapse near a wall, WENO3-Z, $P_{sh} = 353$ bar. JeanZay 4,000 processors

Problem	Mesh type	nb points	CPU (h)	ratio
$P_{sh} = 353$ bar	uniform	900×1200×1200	15	5
$P_{sh} = 353$ bar	stretched	612×600×600	3	1

8.4 Synthesis

In this Chapter we performed 3D computations based on the validated high-order numerical methods and stretching mesh techniques. The complexity of high-order numerical methods in parallel implementation limited our consideration to the third order WENO3-Z method for the moment. The implementation of the method is done in parallel framework of OpenMP and MPI. The non-uniform mesh was introduced into the solver by means of separately created mesh stretching software. The parallelization strategy of mesh coefficients required for the reformulated WENO scheme was proposed. Two problems of shock-induced bubble collapse near a wall with different post shock condition were studied.

The first problem is an extension of the 2D shock-bubble collapse in vicinity to a wall. The preliminary tests were carried out which established the main configuration of mesh stretching strategy suitable for this problem. Precisely, a suitable location of the uniform mesh area is proposed and different degree of stretching is its effect on solution accuracy is understood. It has been observed that the ratio between dy_{max} and dy_{min} and dz_{max} and dz_{min} has an effect on the solution at points away from uniform mesh area. However, this did not yield to the solution deterioration at critical points. The main physical phenomena is accurately reconstructed in comparison to similar studies. The 2D and 3D solutions were compared and faster and higher intensity of the spherical bubble collapse is confirmed in our study. We believe that the stretched mesh strategy is generally a successful idea, even though the discrepancy in pressure profile formation away from the uniform mesh zone is detected. This can be corrected by using lower factor for stretching.

The second problem has a lower value for the shock condition. The mesh stretching strategy based on different domain size is introduced. The results are validated by using the uniform mesh with MUSCL and weno3-Z methods. We found that the solutions are relatively similar. The WENO3-Z method is then used in mesh stretching framework. The effect of the non-uniform mesh is low. Similarly, the main physical phenomena is reconstructed accurately in comparison to the reference computations done in Goncalves & Parnaudeau (2021). We propose a comparison of the maximum wall pressure depending on the bubble stand-off distance from the wall. The rapidly increasing intensity of the maximum peak is noted as the distance from the wall shortens. Indeed, similar pattern has been observed for the cases with higher value of P_{sh} (see Johnsen & Colonius

(2009) and Goncalves & Parnaudeau (2021), for instance).

These computations illustrated a computation speed up of a factor five. Hence, we believe that the presented non-uniform strategy is a promising topic for further developments.

Chapter 9

General conclusion and perspectives

This Chapter concern is a general synthesis of the work presented in this manuscript and discussion about further work which can be interesting to pursue in the context of high-order numerical methods for studying shock-induced bubble collapse.

9.1 General conclusion

A shock-induced bubble collapse is an important problem, which is a part of the cavitation erosion process. The industrial applications require extensive studies of this phenomena due the occurring wall damage as a result of bubble collapse near the solid walls which can cause erosion. The physical dynamics involved into this process are characterised by high speeds and very small spatio-temporal scales. Thus, the numerical reconstruction of such phenomena requires a very fine mesh, which is around 10^6 for 2D and 10^9 in 3D computations or more. The size of the problem can be reduced by using the appropriate high-order numerical methods which can result in faster convergence and, hence, a reduction of points required to achieve the accurate reconstruction. This was defined as a main concern of this thesis.

Mathematical model and basic discretization used throughout present study were discussed in Chapter 2. A four-equation model based on one-fluid mixture approach is employed. The basic discretization is performed by using HLLC or KNP formulations for the flux and MUSCL-Hancock method for the spatial-temporal resolution of second order. The Hancock predictor-corrector scheme has been robust in our study and we believe this scheme is a good alternative to other temporal numerical methods, where the computational time is increasing along with the accuracy of the method. This is particularly important for 3D computations.

High-order numerical methods which can be used in order to improve a spatial resolution in MUSCL-Hancock algorithm were discussed in Chapter 3. Particularly, we focused on WENO-class of the schemes due its wide availability and extensive studies in the literature. Several recent variations were proposed in the Chapter. Other less popular schemes, i.e. PPM and MP5 were presented. Particularly, the PPM method has been reviewed in terms of its improved formulation for the stiffened gas EOS.

Validation methodology has been defined in Chapter 4. We note that problems we are concerned with have not analytical solutions and have discontinuities. Thus, a classical numerical validation of the solver is not possible. The validation process which has been presented in the Chapter is based on the computation of approximate reference solution which is then used to compute the relative order of accuracy. This methodology is then applied to three 1D problems, tested in hierarchical order in terms of the stiffness and complexity. The 2D problem of air-helium

shock-bubble concluded the validation.

2D shock-induced bubble collapse computations are presented in Chapter 5. We considered two problems: one, is a water-gas bubble immersed in free field and as second one, a water-gas bubble located in vicinity to a wall. These computations were meant to establish the effect of high-order numerical schemes on the accuracy of the physical phenomena reconstruction.

Non-uniform mesh techniques were discussed in Chapter 6 where we presented the stretching mesh framework. The derivation of mesh stretching functions which were thought interesting for our study were proposed. The need of reformulated versions of some high-order numerical methods was emphasised and these derivations are developed for WENO methods.

The results of 2D computations on non-uniform mesh were proposed in Chapter 7, where three problems were considered. We discussed and validated the mesh stretching strategies by using the air-helium shock-bubble, which is a suitable problem to test variety of stretched mesh techniques due to the topology of the problem. By doing so, we defined the stretching functions for the non-uniform mesh generation for the problems of shock-induced bubble collapse. In the following sections of the Chapter we developed the problem-specific mesh-stretching methods for these problems and showed the results. Furthermore, we proposed a hybrid methods approach where two numerical schemes can be used on the non-uniform mesh. These techniques are developed for the purposes of computational cost reduction.

The results of 3D computations on non-uniform mesh were presented in Chapter 8. The problem of shock-induced bubble collapse near a wall was extended to 3D and computed on non-uniform mesh with WENO3-Z method. The mesh stretching strategy has generally stayed unchanged in relation to the bubble reconstruction. The main physical phenomena of the problem were described and comparison with corresponding 2D results was shown. Lastly, a similar problem with lower value for the post-shock condition was computed on uniform and non-uniform mesh by using MUSCL and WENO3-Z methods. The effect of high-order numerical scheme in 3D computation has been verified on uniform mesh. The low impact of the non-uniform mesh on the solution accuracy was also illustrated. We showed the dependency of pressure intensity on the stand-off position of the bubble to the wall.

These developments allowed us to draw a broader picture of general numerical approach of solving a problem of shock-induced bubble collapse. Starting with a basic discretization of the mathematical model, we found that the HLLC Riemann solver is a better performer when the complexity of the problem increases and stronger shocks and discontinuities are involved. Similar conclusion was made in relation to some of the high-order numerical schemes. Generally, the WENO class of the schemes and particularly its more recent formulations were proven to be the most accurate and robust in our tests. The PPM method, which includes several algorithms to tackle the discontinuity areas of the solution, was established to work relatively well. However, in the problem of shock-bubble collapse in a free field it led to the variations in the solution which were not present by using other schemes. The MP5 method, the least popular amongst considered methods, was shown to be oscillating already in validation problems and, hence, was dropped from further analysis.

A perspective of choosing a suitable high-order numerical scheme in the framework of highly intensive computations has been thought. Considering the computational cost of the larger stencil, generally involved in high-order numerical schemes, one has to decide on the relation between the quantification of improved reconstruction and increase of CPU. This has been our concern in regard to the third and fifth order schemes. While an improvement has been clearly observed between the solution computed with MUSCL and WENO3, the same is not exactly obvious between the later and WENO5. The results which we have analysed in this thesis did not demonstrate a significant improvement between the two and, thus, the WENO3 method has been extended to 3D computations.

However, even shorter computational stencil requires a significant computational power which was thought to be reduced by using the full parallelized solver SCB and introduction of mesh stretching techniques. We found that the most suitable mesh stretching approach is the one based on the introduction of the uniform mesh area in the domain where the zone of high variation of the solution is located. In our case this is a zone of the bubble and its interaction with the shock-wave and the wall. The stretching function based on the hyperbolic tangent is determined to be the most suitable in our computations. However, the choice between hyperbolic tangent and sine can be more problem-related.

The mesh-stretching methods allowed us to reduce the cost of computations by five times in 2D for the problem of shock-induced bubble collapse. Hence, its extension has been successfully applied to 3D computations. Moreover, WENO3-Z scheme led to the accurate reconstruction of physical phenomena in 3D problems with higher and lower post-shock conditions where similar CPU gain has been observed. We believe that this method is an appropriate choice to achieve a high accuracy reconstruction for the challenging computations of shock-induced bubble collapse.

9.2 Perspectives

The present thesis developed the methods which allowed to achieve better accuracy of the solution without encountering a high computational cost. However, this work could be pursued further and be improved in one or several direction. This sections discusses these choices.

The first immediate area of further investigation is underlying mathematical model which could be changed in order to examine its effect on the solution. For instance, Goncalves & Parnaudeau (2020) has performed an extensive study of several models in 2D and this study could be extended to 3D with computational cost reduction by means of non-uniform mesh. Additionally, the viscous effects can be studied in the same framework.

Undoubtedly, the domain of high-numerical schemes can be extended almost infinitely. The variations of yet other formulations of WENO methods and its derivatives continue to appear. Thus, this part can be extended to further developments by using specifically the WENO class. The most recent publications in this regard is, for instance, Luo & Wu (2021). Furthermore, the higher methods of WENO might be examined but with care.

Another big part of improvement of present work concerns the non-uniform mesh introduction. This thesis presented only arbitrary problem-related mesh stretching techniques which are initialised once at the first time iteration. The process of finding a suitable strategy has been based on testing. This could be turned to different direction and address a problem of adaptive mesh methods. For instance, the mesh stretching could be redefined at certain time periods when the bubble is changing its topology and location the most or when the strongest solution variation is detected. The adaptive mesh stretching, however, can be a challenging and highly computationally expensive task. As such, the cost of its implementation in sequential and parallel frameworks, the numerical schemes reformulations and further analytical derivations have to be carefully examined.

Lastly, but not least importantly, a study of solid-fluid coupling in the context of the wall damage caused by the bubble collapse can be performed. The wall pressure load analysis based on the stand-off distance of the bubble from the wall is a good starting point for this type of study. For instance, it was already examined in Johnsen & Colonius (2009) and Goncalves & Parnaudeau (2021) in 2D and 3D computations. These studies can be pursued by testing different configurations of the bubble collapse to confirm the pressure load laws suggested by authors. Partly, the part of this analysis for different test configurations is presented in this thesis.

Generally, the domain of research concerning the shock-induced bubble collapse is a broad one and many numerical improvements can be and will be made in the future as we observe a constant

technological growth. This will allow to solve even more computationally extensive problems on extremely fine mesh. We hope that this study provides a step forward in these persuasions.

Appendices

Appendix A

Analytical solution for the inverse of stretching function

The two-sided stretching function for $B > 1$ and one-sided stretching function for $s_0 > 1$ require the inverse of the function

$$y = \sinh(x)/x \tag{A.1}$$

An approximate analytical solution for inverse function $x = f(y)$ as derived in Vinokur (1980). We define $\bar{y} = 1 - y$, $v = \log(y)$ and $w = 1/y - 0.028527431$.
For $y < 2.7829681$:

$$\begin{aligned} x =& \sqrt{6\bar{y}}(1 - 0.15\bar{y} + 0.057321429\bar{y}^2 - 0.024907295\bar{y}^3 \\ &+ 0.0077424461\bar{y}^4 - 0.0010794123\bar{y}^5) \end{aligned} \tag{A.2}$$

For $y > 2.7829681$:

$$\begin{aligned} x =& v + (1 + 1/v)\log(2v) - 0.02041793 + 0.24902722w \\ &+ 1.9496443 * w^2 - 2.6294547w^3 + 8.56795911w^4 \end{aligned} \tag{A.3}$$

The two-sided stretching function for $B < 1$ and one-sided stretching function if $s_0 < 1$ requires the inversion of

$$y = \sin(x)/x \tag{A.4}$$

We denote $\bar{y} = 1 - y$ and an approximate analytical representation is following.
For $y < 0.26938972$,

$$\begin{aligned} x =& \pi(1 - y + y^2 - (1 + \pi/6)y^3 \\ &+6.794732y^4 - 13.205501y^5 + 11.72609y^6) \end{aligned} \tag{A.5}$$

For $y < 0.26938972$,

$$\begin{aligned} x =& \pi(1 - y + y^2 - (1 + \pi/6)y^3 \\ &+6.794732y^4 - 13.205501y^5 + 11.72609y^6) \end{aligned} \tag{A.6}$$

For $0.26938972 < y < 1$,

$$\begin{aligned} x =& \sqrt{6\bar{y}}(1 + 0.15\bar{y} + 0.057321429\bar{y}^2 + 0.048774238\bar{y}^3 \\ &- 0.053337753\bar{y}^4 + 0.07584513\bar{y}^5) \end{aligned} \tag{A.7}$$

Appendix B

SCB simplified example of OpenMP implementation

```
! OpenMP implementation example.
DO ndt=1,ndtmax
!$OMP PARALLEL IF(ijmax.gt256) default(none)
!$OMP DO SCHEDULE (runtime) PRIVATE (i,j,k) COLLAPSE(2)
DO k=kmin,kmax
DO j=jmin,jmax
DO i=imin,imax
  RI1=w1(i,j,k)-w1(i-1,j,k)
  sl=dmax(0.0,dmin(Ri1,1.0))+dmin(0,dmax(1,Ri1))
  W1(i,j,k)=W1(i-1,j,k)&
  +1/4*sl*(W1(i-1,j,k)-W1(i-2,j,k))+1/4*sl(W1(i,j,k)-W1(i-1,j,k))
ENDDO
ENDDO
ENDDO
!$OMP END DO
CALL BOUNDARY (W1)
!$OMP END PARALLEL
CALL MPI_SENDRECV(W1,imax*kmax,MPI_DOUBLE_PRECISION, &
&neib_mpi(N),tag,W1,imax*kmax,MPI_DOUBLE_PRECISION, &
&neib_mpi(S),tag,cpmm,status,err_mpi)
ENDDO
```

Appendix C

SCB implementation of WENO3-Z on non-uniform mesh.

An example of implementation for WENO3-Z coefficients on the boundaries for non-uniform mesh. Similar manner is used for all directions.

```
! \MakeUppercase{weno}3-Z mesh coefficients.
SUBROUTINE distribute_weno3_x
#if defined key_mpi
if ((neib_mpi(WEST) == MPI_PROC_NULL).and. &
   (neib_mpi(EST) /= MPI_PROC_NULL)) then
   DO i=3,imax-2
      coef=0.5d0*(x(i)+x(i+1))
   ENDO
   i=2
   coef(i)=coef(3)
   i=imax+1
   coef(i)=coef(imax)
endif

if ((neib_mpi(EST) ==  MPI_PROC_NULL).and. &
   (neib_mpi(WEST) /= MPI_PROC_NULL)) then
   DO i=1,imax-2
      coef=0.5d0*(x(i)+x(i+1))
   ENDO
   i=0
   coef(i)=coef(1)
   i=imax-1
   coef(i)=coef(imax-2)
endif

if ((neib_mpi(WEST) /= MPI_PROC_NULL).and. &
   (neib_mpi(EST) /= MPI_PROC_NULL)) then
   DO i=1,imax
      coef=0.5d0*(x(i)+x(i+1))
   ENDO
   i=0
   coef(i)=coef(1)
   i=imax+1
   coef(i)=coef(imax)
endif
```

```
if ((neib_mpi(WEST) == MPI_PROC_NULL).and. &
   (neib_mpi(EST) == MPI_PROC_NULL)) then
#endif
   DO i=3,imax-2
      coef=0.5d0*(x(i)+x(i+1))
   ENDO
   i=2
   coef(i)=coef(3)
   i=imax-1
   coef(i)=coef(imax-2)
#if defined key_mpi
endif
#endif
return
END SUBROUTINE distribute_weno3_x
```

References

Abgrall, R. 1996 How to prevent pressure oscillations in multicomponent flow calculations: a quasi conservative approach. *J. Comput. Phys.* **125** (1), 150–160.

Baer, M.R. & Nunziato, J.W. 1986 A two-phase mixture theory for the deflagration-to-detonation transition (DDT) in reactive granular materials. *Int. J. Multiphase Flow* **12**, 861–889.

Baeza, A., Burger, R., Mulet, P. & Zorio, D. 2013 An efficient third-order WENO scheme with unconditionally optimal accuracy. *SIAM Journal on Scientific Computing* **42** (2), A1028–A1051.

Berger, M.J. & Colella, P. 1989 Local adaptive mesh refinement for shock hydrodynamics. *Journal of Computational Physics* **82** (1), 64–84.

Berger, M.J. & Joseph, O. 1984 Adaptive mesh refinement for hyperbolic partial differential equations. *Journal of Computational Physics* **53** (3), 484–512.

Berthon, C. 2005 Stability of the muscl schemes for the euler equations. *Comm. Math. Sciences* **3**, 133–158.

Berthon, C. 2006 Why the muscl-hancock scheme is l1-stable. *Numer. Math.* **104**, 27–46.

Borges, R., Carmona, M., Costa, B. & Don, W.S. 2008 An improved weighted essentially non-oscillatory scheme for hyperbolic conservation laws. *J. Comput. Phys.* **227**, 3191–3211.

Bourne, N.K. & Field, J.E. 1992 Shock-induced collapse of single cavities in liquids. *Journal of Fluid Mechanics* **244**, 225–240.

Castro, M., Costa, B. & Don, W.S. 2011 High order weighted essentially non-oscillatory weno-z schemes for hyperbolic conservation laws. *J. Comput. Phys.* **230** (5), 1766–1792.

Chung, T.J. 2002 Computational fluid dynamics. *Cambridge University Press* .

Colella, P. & Sekora, M. 2008 A limiter for PPM that preserves accuracy at smooth extrema. *J. Comput. Phys.* **227**, 7069–7076.

Colella, P. & Woodward, P.R. 1984 The piecewise parabolic method (PPM) for gas-dynamical simulations. *Commun. Comput. Phys.* **54** (1), 174–201.

Coralic, V. & Colonius, T. 2014 Finite-volume WENO scheme for viscous compressible multicomponent flow. *J. Comput. Phys.* **274**, 95–121.

Daude, F., Galon, P., Gao, Z. & Blaud, E. 2014 Numerical experiments using a HLLC-type scheme with ALE formulation for compressible two-phase flows five-equation models with phase transition. *Comput. Fluids* **94**, 112–138.

Dubois, R., Goncalves, E. & Parnaudeau, P. 2021 High performance computing of stiff bubble collapse on cpu-gpu heterogeneous platform. *Computers and Mathematics with Applications* **99**, 246—-256.

Gallouet, T., Herard, J.M. & Seguin, N. 2002 A hybrid scheme to compute contact discontinuities in Euler systems. *Math. Modell. Numer. Anal.* **36** (6), 1133–1159.

Goncalves, E. & Charriere, B. 2014 Modelling for isothermal cavitation with a four-equation model. *Int. J. Multiphase Flow* **59**, 54–72.

Goncalves, E. & Parnaudeau, P. 2020 Comparison of multiphase models for computing shock-induced bubble collapse. *Int. J. Numer. Methods Heat Fluid Flow* **30** (8), 3845–3877.

Goncalves, E. & Parnaudeau, P. 2021 Numerical study of pressure loads generated by a shock-induced bubble collapse. *Physics of fluids* .

Goncalves, E. & Zeidan, D. 2018 Simulation of compressible two-phase flows using a void ratio transport equation. *Commun. Comput. Phys.* **24** (1), 167–203.

Gong, S.W. & Klaseboer, E. 2016 Interaction between collapsing bubble and viscoelastic solid: Numerical modelling and simulation. *Applied Mathematical Modelling* **40**, 4746–4764.

Gough, D.O., Spiegel, E.A. & Toomre, J. 1975 Highly stretched meshes as functionals of solutions. *Proceedings of the fourth international conference on numerical methods in fluid dynamics* pp. 191–196.

Haas, J.-F. & Sturtevant, B. 1987 Interaction of weak shock waves with cylindrical and spherical gas inhomogeneities. *J. Fluid Mech.* **181** (1), 44–76.

Harten, A. 1983 High resolution schemes for hyperbolic conservation laws. *Journal of Computational Physics* **49**, 357–393.

Harten, A., Engquist, B., Osher, S. & Chakravarthy, S.R. 1987 Uniformly high-order accurate essentially non oscillatory schemes. *J. Comput. Phys.* **71**, 3–47.

Henrick, A.K., Aslam, T.D. & Powers, J.M. 2005 Mapped weighted essentially non-oscillatory schemes: achieving optimal order near critical points. *J. Comput. Phys.* **208**, 206–227.

Jameson, A., Schmidt, W. & Turkel, E. 1981 Numerical solution of the euler equations by finite volume methods using Runge-Kutta time stepping schemes. *AIAA J.* **81**.

JeanZay 2019 Hpe sgi 8600 (jean zay) .

Jiang, G. & Shu, C.-W. 1996*a* Efficient implementation of weighted ENO schemes. *J. Comput. Phys.* **126**, 202–228.

Jiang, G-S. & Shu, C-W. 1996*b* Efficient implementation of weighted ENO schemes. *J. Comput. Phys.* **126** (1), 202–228.

Johnsen, E. & Colonius, T. 2006 Implementation of WENO schemes in compressible multicomponent flow problems. *J. Comput. Phys.* **219** (2), 715–732.

Johnsen, E. & Colonius, T. 2009 Numerical simulations of non-spherical bubble collapse. *J. Fluid Mech.* **629**, 231–262.

Kapila, A., Menikoff, R., Bdzil, J., Son, S. & Stewart, D. 2001 Two-phase modelling of deflagration-to-detonation transition in granular materials: reduced equations. *Phys. Fluids* **13** (10), 3002–3024.

Kitamura, K., Liou, M-S. & Chang, C-H. 2014 Extension and comparative study of AUSM-family schemes for compressible multiphase flow simulations. *Commun. Comput. Phys.* **16** (3), 632–674.

Lax, P. & Mock, M. 1978 The computation of discontinuous solutions of linear hyperbolic equations. *Commun. Pure Appl. Math* **31**, 423–430.

Lax, P. D. 2005 Hyperbolic systems of conservation laws ii. *Selected Papers Volume I, Springer-Verlag* pp. 233–262.

Layes, G., Jourdan, G. & Houas, L. 2009 Experimental study on a plane shock wave accelerating a gas bubble. *Phys. Fluids* **21**.

van Leer, B. 1977 Towards the ultimate conservative difference scheme. III. Ustream-centered finite difference schemes for ideal compressible flow. *J. Comput. Phys.* **23** (3), 263–275.

van Leer, B. 1984 On the relation between the upwind-differencing schemes of Godunov, Engquist- Osher and Roe. *SIAM Journal on Scientific and Statistical Computing* **5**, 1–20.

van Leer, B. 2003 Upwind and high-resolution methods for compressible flow: from donor cell to residual-distribution schemes. *16th AIAA Computational Fluid Dynamics Conference* .

van Leer, B. 2006 Upwind and high-resolution methods for compressible flow: from donor cell to residual distribution schemes. *Comm. Computational Physics* **1** (2), 192–206.

LeMétayer, O., Massoni, J. & Saurel, R. 2004 Elaborating equations of state of a liquid and its vapor for two-phase flow models. *Int. J. Therm. Sci.* **43** (3), 265–276.

Leonard, B.P. 1991 The ultimate conservative difference scheme applied to unsteady one-dimensional advection. *Comput. Meth. Appl. Mech. Eng.* **88** (1), 17–74.

Liu, X.-D., Osher, S. & Chan, T. 1994 Weighted essentially non-oscillatory schemes. *Commun. Comput. Phys.* **115**, 200–212.

Luo, X. & Wu, S. 2021 An improved weno-z+ scheme for solving hyperbolic conservation laws. *Journal of Computational Physics* **445**.

Majda, A. & Osher, S. 1977 Propagation of error into regions of smoothness for accurate difference approximations to hyperbolic equations. *Commun. Pure Appl. Math* **30**, 674–705.

Middlecoff, J.F. & Thomas, P.D. 1979 Direct control of the grid point distribution in meshes generated by elliptic equations. *Proceedings of the AIAA fourth computational fluid dynamics conference* pp. 175–179.

Murrone, A. & Guillard, H. 2005 A five equation reduced model for compressible two phase flows problems. *J. Comput. Phys.* **202** (2), 664–698.

Nessyahu, H. & Tadmor, E. 1990 Non-oscillatory central differencing for hyperbolic conservation laws. *J. Comput. Phys.* **87** (2), 408–463.

Nourgaliev, R.R., Dinh, T.N. & Theofanous, T.G. 2006 Adaptive characteristics-based matching for compressible multifluid dynamics. *J. Comput. Phys.* **213**, 500–529.

Paquette, Y., Fivel, M., Ghigliotti, G., Johnsen, E. & Franc, J-P. 2018 Fluid-structure interaction in cavitation erosion. In *10th International Symposium on Cavitation CAV2018, Baltimore, USA*.

Peer, A.A.I., Dauhoo, M.Z. & Bhuruth, M. 2009 A method for improving the performance of the weno5 scheme near discontinuities. *Applied mathematics letters* **22**, 1730–1733.

Pierson, B.L. & Kutler, P. 1980 Optimal nodal point distribution for improved accuracy in computational fluid dynamic. *AIAA J* . **18** (1), 49–54.

Roberts, G.O. 1971 Computational meshes for boundary layer problems. *Proceedings of the second international conference on numerical methods in fluid dynamics* pp. 171–177.

Saurel, R., Petitpas, F. & Abgrall, R. 2008 Modelling phase transition in metastable liquids: application to cavitating and flashing flows. *Journal of Fluid Mechanics* **607**, 313–350.

Savitzky, A. & Golay, M.J.E. 1964 Smoothing and differentiation of data by simplified least squares procedures. *Analytical Chemistry* **36**, 1627–1639.

Schidmayer, K., Bryngelson, S.H. & Colonius, T. 2020 An assessment of multicomponent flow models and interface capturing schemes for spherical bubble dynamic. *Journal of Computational Physics* **402**, 109080.

Shen, Y. 2009 Improvement of the WENO scheme smoothness estimator. *Int. J. Numer. Methods Fluids* **64**, 653–675.

Spina, G. La & Vitturi, M. 2012 High-resolution finite volume central schemes for a compressible two-phase model. *SIAM Journal on Scientific Computing* **34** (6), 861–80.

Suresh, A. & Huynh, H.T. 1997 Accurate monotonicity-preserving schemes with Runge-Kutta time stepping. *J. Comput. Phys.* **136**, 83–99.

Thompson, J. 1972 Numerical solution for three-dimensional inviscid supersonic flow. *AIAA J.* **10** (7), 887–894.

Thompson, J. 1983 A survey of grid generation techniques in computational fluid dynamics .

Thompson, J.F., Thames, F.C. & Mastin, C.W. 1977 Tomcat - a code for numerical generation of boundary-fitted curvilinear coordinate systems on fields containing any number of arbitrary two-dimensional bodies. *J. Comp. Phys* **24** (3), 274–302.

Thompson, J., Warsi, Z.U.A. & Mastin, C. 1985 *Numerical grid generation: foundations and applications*. Elsevier Science Ltd.

Toro, E.F. 1999 *Riemann solvers and numerical methods for fluid dynamics*. 2nd edition, New York: Springer.

Toro, E.F., Spruce, M. & Speares, W. 1994 Restoration of the contact surface in the HLL Riemann solver. *Shock Waves* **4** (1), 25–34.

Vinokur, M. 1980 On one-dimensional stretching functions for finite-difference calculations. *NASA CR 3313* .

Vinokur, M. 1983 On one-dimensional stretching functions for finite-difference calculations. *Journal of computational physics* **50** (2), 215–234.

Wang, B., Xiang, G. & Hu, X.Y. 2018 An incremental-stencil WENO reconstruction for simulation of compressible two-phase flows. *Int. J. Multiphase Flow* **104**, 20–31.

Wang, R., Feng, H. & Spiteri, R. 2007 Observations on the fifth-order weno method with non-uniform meshes. *Preprint submitted to Elsevier Science* .

Wang, R., Feng, H. & Spiteri, R.J. 2008 Observations on the fifth-order wENO method with non-uniform meshes. *Appl. Math. Comput.* **196**, 433–447.

Wermelinger, F., Rasthofer, U., Hadjidoukas, P.E. & Koumoutsakos, P. 2018 Petascale simulations of compressible flows with interfaces. *Journal of Computational Science* **26**, 217—-225.

Wu, X. & Zhao, Y. 2013 A high-resolution hybrid scheme for hyperbolic conservation laws. *Int. J. Numer. Methods Fluids* **78** (3).

Xu, W. & Wu, W. 2017 An improved third-order WENO-Z scheme. *Journal of Scientific Computing* **75** (3), 1808–1841.

Zheng, J. G. & Lee, T. S. 2013 A high-resolution method for compressible two-fluid flows and simulation of three-dimensional shock–bubble interactions. *Int. J. Numer. Methods Fluids* **72**, 206–230.

High-order numerical methods for shock-bubble interaction computations

The importance of modelling two-phase flows involving shock waves arises from many engineering and medical applications. The presence of strong shock waves, their interactions with bubble interfaces and the large variation of material properties make the resolution of such problems a complicated task for the numerical methods. While the variety of numerical techniques to solve these problems exist, e.g. the sharp interface or the diffuse interface methods, these strategies can lead to spurious oscillations of the solution near the interface. It is well known that it is difficult to achieve both a high order accuracy of the scheme and the monotonicity of the solution.

In this thesis a four-equation mixture model is employed and integrated in an explicit finite-volume solver with different numerical schemes and reconstruction methods. The construction of a high-order numerical tool for solving stiff 2D and 3D shock-bubble interactions is proposed. The numerical validation of the methods is performed on various 1D problems (shock-tube problems) and on air-helium shock-bubble case in 2D. The study is then ex- tended to the collapse of a gas bubble immersed in water and located in the vicinity of a wall.

While the high-order numerical schemes lead to the high-accuracy reconstruction, the question of computational cost emerges. The physical phenomena involved into considered problems require a fine grid to achieve the detailed solution. For instance, a computational isotropic grid can reach over 1 billion nodes in 3D, leading to a huge cost. Thus, there is a need of CPU reduction techniques. Different mesh-stretching techniques have been studied and implemented in the code, leading to a reduction of the computational cost by a factor of 5 for the problem of shock-bubble collapse.

Finally, the computations of the latter problem have been successfully extended to 3D with implementation of parallel paradigms (OpenMP and MPI). The solutions computed on one billion points with third order accuracy are presented and discussed. The evolution of the maximum wall pressure is analysed when the stand-off distance varies, suggesting potential wall damages.

Keywords : Numerical analysis, Bubbles–Dynamics, Two-phase flow, Equations, Simultaneous–Numerical solutions, Shock waves, Simulation methods, Shock tubes, bubble collapse, high-order scheme, WENO reconstruction, non-uniform mesh

Méthodes numériques d'ordre élevé pour la simulation d'interactions choc-interface

La modélisation des écoulements diphasiques en présence d'ondes de choc est d'une importance majeure pour de nombreuses applications d'ingénierie et médicales. La présence d'ondes de choc de très forte intensité, leurs interactions avec les interfaces entre phases et la grande variation des propriétés des matériaux rendent difficile la résolution numérique de tels problèmes. Bien qu'il existe une large variété de méthodes numériques pour résoudre ces problèmes comme les méthodes à interface raide ou à interface diffuse, ces stratégies peuvent conduire à des oscillations numériques de la solution au voisinage de l'interface. Il est bien connu qu'il est difficile d'obtenir à la fois une précision d'ordre élevé du schéma et la monotonie de la solution.

Dans cette thèse, un modèle de mélange à quatre équations est utilisé et intégré dans un solveur aux volumes finis explicite avec différents schémas numériques et méthodes de reconstruction. La construction d'un outil numérique d'ordre élevé pour résoudre des problèmes d'interactions choc-interface 2D et 3D est proposée. La validation numérique des méthodes est effectuée sur différents problèmes en 1D (problèmes de tube à choc) et sur un cas choc-bulle air-hélium en 2D. L'étude est ensuite étendue aux problèmes de collapse de bulle de gaz immergée dans de l'eau et située à proximité d'une paroi.

Alors que les schémas numériques d'ordre élevé conduisent à une reconstruction précise, la question du coût de calcul se pose. Les phénomènes physiques impliqués dans les problèmes considérés nécessitent des maillages très fins pour être bien calculés. Par exemple, une grille isotrope de calcul peut atteindre plus d'un millard de nœuds en 3D, ce qui entraîne un coût énorme. Des techniques de réduction du CPU sont donc nécessaires. Des stratégies de maillage étiré sont ainsi étudiées et implantées dans le solveur, conduisant à une réduction du coût de calcul d'un facteur 5 pour le problème du collapse de bulles par choc.

Enfin, les calculs ont été étendus en configuration 3D avec la mise en œuvre de paradigmes parallèles (OpenMP et MPI). Les solutions calculées sur une grille d'un milliard de points avec une précision du troisième ordre sont présentées et discutées. La pression maximale à la paroi est analysée en fonction de l'emplacement initial de la bulle, permettant d'évaluer le potentiel endommagement du matériau.

Mots clés : Analyse numérique, Bulles–Dynamique, Écoulement diphasique, Équations, Systèmes d'–Solutions numériques, Ondes de choc, Simulation, Méthodes de, Tubes à choc, collapse de bulle, schéma d'ordre élevé, reconstruction WENO, maillage non uniforme